

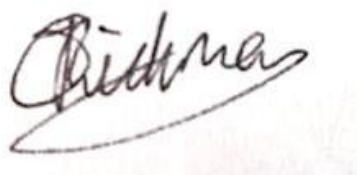
Defining new molecules and biological pathways underlying neurodegenerative disease

Submitted by Olivia Jordan Rickman to the
University of Exeter
as a thesis for the degree of
Doctor of Philosophy in Medical Studies, April 2020.

This thesis is available for Library use on the understanding that it is copyright material and that no quotation from the thesis may be published without proper acknowledgement.

I certify that all material in this thesis which is not my own work has been identified and that no material has previously been submitted and approved for the award of a degree by this or any other University.

Signature:

A handwritten signature in black ink, appearing to read 'Olivia Rickman', written over a faint, light-colored background.

Acknowledgements

I would like to express my sincerest gratitude to my supervisors Prof Andrew Crosby and Dr Emma Baple for giving me the opportunity to undertake my PhD in such an exciting research area, for the scientific guidance and patience, and for all the great experiences that this PhD has provided me with. My sincerest thanks to my supervisor, Dr John Chilton for his experimental guidance and introducing me to techniques that have made the last three years so interesting. Importantly, I wish to thank the wonderful Hereditary Spastic Paraplegia Support Group for their support and funding throughout this project.

A special thanks to all the lovely people in the RILD that have made my PhD such an enjoyable experience. In particular, to those in the level 4 labs for the experimental advice and the best TC chats. I am also extremely grateful to the volunteers who kindly donated blood for the experiments carried out in my PhD. Additionally, I need to extend my thanks to the Dr Oguro-Ando and Crosby groups for the support, experimental guidance and friendship.

Finally, my utmost thanks and appreciation to those closest to me. The continual support from my family, without whom I would not have been able to embark on this challenge. To my friends whom I have shared so many fun times with over the last three years and thanks for making many trips down to Exeter! I could never have sanely got to the end of this PhD without the incredible support from Mark Wells, I will be eternally grateful for the constant encouragement with welcomed distractions and adventures that he has given me.

Abstract

Motor neurone diseases (MNDs) are a group of disorders characterised by the degeneration of upper and/or lower motor neurones. Unlike communicable diseases in which frequency is decreasing due to improved healthcare provision, the prevalence of neurodegenerative disorders such as MND are increasing proportionally, particularly in Western countries, placing a substantial burden on healthcare services. The hereditary spastic paraplegias (HSPs) are a form of upper motor neurone disease in which the cardinal features involve progressive spasticity of the lower limbs, which may be accompanied by other neurological or non-neurological abnormalities. To date there are >80 distinct genetic causes of HSP, involving genes encoding proteins with a plethora of proposed cellular roles.

The overarching aim of the work described in this thesis involves the exploration of the role of disordered lipidomic metabolism in HSP. Chapter three describes studies stemming from an Amish individual that was originally diagnosed with neurodegeneration with brain iron accumulation (NBIA). Genetic studies defined *de novo* mutation in *C19orf12*, encoding a protein thought to be involved in lipid metabolism, as the likely cause of disease. Gene variants in *C19orf12* have previously been associated with both autosomal dominant as well as recessive forms of NBIA, as well as with HSP. This chapter defines a new mechanistic explanation as to why variants in this gene may be inherited in either a recessive or dominant state, involving *C19orf12* isoform-specific haploinsufficiency.

Mast syndrome is a complicated form of HSP at high frequency amongst the Amish community, due to mutation(s) in the *SPG21* gene encoding maspardin.

Chapter four involves deeper exploration of the biomolecular role of maspardin, and the cellular consequences that result due to loss of function of the molecule. This work determines that maspardin colocalises with rab7 and localises to endosomes and lysosomes which interact with mitochondria. Using CRISPR-Cas9 gene technology to knockout maspardin, these studies determined that maspardin loss results in altered cell bioenergetics, increased cell death and altered endosomal/lysosomal size.

Lipid imbalance is a pathological hallmark among a wide range of neurodegenerative disorders. Similarly, lipid-related proteins associated with HSP entail a notable theme within this heterogeneous group of disorders. To further explore lipid imbalance in HSP, chapter five details the development of a method whereby extremely small amounts of specific lipids can be detected from subcellular fractions obtained from 10ml blood samples, and cultured cell samples. This chapter also describes oxysterol profiles in peripheral blood mononuclear cells (PBMCs) and SH-SY5Y cells, and identifies altered lipid profiles due to maspardin loss.

Together, the findings and data presented in this thesis significantly contribute to the understanding of the subcellular role and pathomolecular basis of *C19orf12* and maspardin, both responsible for complex forms of HSP-spectrum disorders. Additionally, the new methodologies established in this work to profile lipidomic content in subcellular compartments obtained from blood and cultured cell samples will be applied in future studies to potentially develop revolutionary new approaches to testing in HSPs, and confirm the specific lipid profile imbalances highlighted in this thesis as key lipidomic biomarkers of disease.

Contents

Acknowledgements.....	2
Abstract.....	3
Contents	5
List of Figures	10
List of Tables	13
Abbreviations	14
Chapter 1.....	17
Introduction.....	18
1.1 Neurodegenerative Disorders	18
1.1.1 Cellular Hallmarks of Degeneration.....	19
1.1.2 Neuronal Cell Death and the Neuromuscular Junction.....	20
1.2 Motor Neurone Diseases	24
1.2.1 Amyotrophic Lateral Sclerosis.....	27
1.2.2 Lower Motor Neurone Disease.....	27
1.2.3 Upper Motor Neurone Disease.....	29
1.2.4 Hereditary Spastic Paraplegia.....	29
1.3 Common Pathomolecular Themes in Neurodegenerative Disorders	31
1.3.1 Abnormalities in Lipids	31
1.3.2 Mitochondrial Dysfunction	33
1.3.3 Reactive Oxygen Species	36
1.3.3.1 Lipid Peroxidation.....	38
1.3.3.2 Ferroptosis	39
1.3.3.3 The Antioxidant System	40
1.4 Pathomolecular Themes in Hereditary Spastic Paraplegia.....	43
1.4.1 Myelination	43
1.4.2 Endoplasmic Reticulum Morphology	44
1.4.3 Mitochondrial Structure and Function.....	45
1.4.4 Subcellular Transport	46
1.4.5 Lipid Metabolism and Biosynthetic Pathways.....	47
1.5 Treatment in Hereditary Spastic Paraplegia and other Motor Neurone Diseases	49
1.6 The Amish.....	50
1.6.1 History and Way of Life	50
1.6.2 The Genetic Architecture of the Amish.....	52
1.6.3 The Windows of Hope Project (WoH).....	54
1.7 Hereditary Spastic Paraplegia in the Amish.....	55
1.8 Aims of this Thesis.....	58

Chapter 2.....	59
Materials and Methods	60
2.1 Buffers, Reagents and General Consumables.....	60
2.2 General Cell Culture	61
2.2.1 Cell Storage	62
2.3 Immunocytochemistry	63
2.3.1 Cell Seeding and Transfection	63
2.3.2 Nucleofection	63
2.3.3 Cell Fixing	64
2.3.4 Cell Staining.....	64
2.4 Single Cell Sorting	65
2.5 Live Cell Imaging Cell Preparation.....	66
2.6 Microscopy.....	66
2.7 Western Blotting	68
2.7.1 Cell Lysate Preparation	68
2.7.2 Protein Quantification	69
2.7.3 Sample Preparation.....	69
2.7.4 SDS-PAGE Protein Separation	70
2.7.5 Protein Transfer.....	70
2.7.6 Antibody Incubation and Detection.....	71
2.8 Binding Partner Analysis.....	72
2.8.1 Cell Lysate Preparation	72
2.8.2 Co-immunoprecipitation	72
2.8.3 Mass Spectrometry	73
2.9 PCR and Sequencing	74
2.9.1 Primer Design	74
2.9.2 PCR Master Mixture Preparation.....	75
2.9.3 PCR Cycling Conditions	76
2.9.4 Agarose Gel Electrophoresis.....	76
2.9.5 PCR Product Clean-up.....	77
2.9.6 Sequencing	77
2.9.7 Whole Exome Sequencing	78
2.10 Nucleic Acid Extraction	78
2.10.1 DNA Extraction.....	78
2.10.2 RNA Extraction.....	79
2.10.3 cDNA Synthesis	80
2.10.4 cDNA Sequencing.....	80
2.10.5 Determining Nucleic Acid Concentration	80
2.11 Plasmid Preparation.....	80

2.11.1 General Bacterial Handling	81
2.11.2 Bacterial Stab Cultures.....	81
2.11.3 Selecting and Growing Single Colonies	81
2.11.4 Miniprep	81
2.11.5 Restriction Digest	82
2.11.6 Colony Expansion	83
2.11.7 Glycerol Stocks	83
2.11.8 Midiprep	83
2.12 Constructing a Fluorescently Tagged SPG21 Plasmid	84
2.12.1 DNA Insert and Vector Isolation	84
2.12.2 Ligation.....	86
2.12.3 Transformation of Plasmids into Competent Bacteria	87
2.13 CRISPR-Cas9 Plasmid Preparation	87
2.14 Cell Assays	89
2.14.1 Measuring Cell Viability	89
2.14.2 Measuring ROS.....	90
2.14.3 Measuring Cell Death.....	90
Chapter 3.....	93
Mitochondrial Membrane Protein-Associated Neurodegeneration.....	94
3.1 Introduction	94
3.1.1 Neurodegeneration with Brain Iron Accumulation	94
3.1.2 NBIA Disease-Associated Genes.....	94
3.1.3 NBIA Overlaps with HSP	96
3.1.4 C19orf12	97
3.2 Results.....	100
3.2.1 C19orf12 c.278del (p.Pro93Leufs*26) Alteration is Associated with AD-MPAN.....	100
3.3 Discussion	104
3.3.1 Future Work	107
Chapter 4.....	110
Defining the Biomolecular Role of Maspardin	111
4.1 Introduction	111
4.1.1 Mast Syndrome	111
4.1.2 Maspardin	114
4.1.3 CRISPR Technology	116
4.1.4 Defining the Biomolecular Role of Maspardin	119
4.2 Results.....	120
4.2.1 Creating an SPG21 Knockout SH-SY5Y Cell Line: gRNA Design .	120
4.2.2 SPG21 Knockout Cell Line Validation	123

4.2.2.1 SPG21 Knocked-out Region Confirmed by PCR.....	123
4.2.2.2 SPG21 Knockout Confirmed by DNA Sequencing.....	126
4.2.2.3 Maspardin Knockout Confirmed by Western Blotting	129
4.2.2.4 Immunocytochemistry in Cell Models	131
4.2.2.5 Knockout Colonies Confirmed by RNA Sequencing	135
4.2.2.6 SPG21 Knockout Cell Line Conclusion	137
4.2.3 Generation of SPG21 Gene Constructs	137
4.2.4 Subcellular Localisation Studies Indicate Possible Mitochondrial/ER Localisation	139
4.2.5 Maspardin Molecular Binding Partners Determined by Mass Spectrometry	142
4.2.5.1 Binding Partner Validation by Immunocytochemistry	149
4.2.6 Live Cell Imaging.....	153
4.2.6.1 Maspardin Surrounds Vesicular Structures.....	153
4.2.6.2 Maspardin Vesicles are not Lipid Droplets.....	159
4.2.6.3 Maspardin Colocalises with Rab7 Vesicles.....	161
4.2.6.4 Maspardin Surrounds Lysosomes	166
4.2.6.5 Maspardin Vesicles Appear to Interact with Mitochondria	169
4.2.7 Maspardin Amino Acid Sequence Contains Candidate Lysosome Localisation Signals	171
4.2.8 Analysis of Maspardin and Rab7 Interaction and Expression	172
4.2.9 Comparing SPG21 Knockout to Wildtype Cells.....	174
4.2.9.1 Analysis of Metabolism and Viability in SPG21 Knockout Cells	174
4.2.9.2 Endolysosomal Vesicles Morphology are Altered in SPG21 Knockout Cells	177
4.3 Discussion	184
4.3.1 Future Work	190
Chapter 5.....	193
Investigating Lipid Profiles in Motor Neurone Disease.....	194
5.1 Introduction	194
5.1.1 Cholesterol and the Bile Acid Pathway.....	194
5.1.2 Oxysterol Function	197
5.1.3 Oxysterols and Apoptosis.....	198
5.1.4 Oxysterol Imbalance and Motor Neurone Disease	199
5.1.5 The Role of Mitochondria and ER in Bile Acid Synthesis	200
5.1.6 Mutations in the Mitochondria-Associated ER Membrane Tethers Associated with Motor Neurone Disease.....	203
5.1.7 Lipidome imbalance in MNDs.....	203
5.2 Method and Results	205
5.2.1 Method Development	205
5.2.1.1 Obtaining Enriched Mitochondrial Fractions	205

5.2.1.2 Starting Cellular Material	205
5.2.1.3 First Mitochondrial Extraction Protocol	206
5.2.1.4 Second Mitochondrial Extraction Protocol: Purity Matters	209
5.2.1.5 Reducing Blood Volume	212
5.2.1.6 Antibodies to Assess Purity of Mitochondrial Fraction	213
5.2.1.7 The Optimised Mitochondrial Extraction Protocol	215
5.2.2 Oxysterol Analysis.....	219
5.2.2.1 PBMC Oxysterol Analysis.....	219
5.2.3 Oxysterol Profiling	223
5.2.3.1 Whole Cell and Mitochondrial Fractions.....	223
5.2.3.2 Increased Blood Storage Time Impacts Oxysterol Levels due to Autoxidation	225
5.2.4 Oxysterol Imbalance is Observed Between SPG21 Knockout and Control Cells.....	229
5.3 Discussion	233
5.3.2 Future Work	235
Chapter 6.....	239
Closing Comments	240
Appendices	243
Appendix A:	243
Appendix B	246
Appendix C	248
Appendix D	251
Appendix E	252
Appendix F.....	255
Bibliography	257

List of Figures

Figure 1.1 Common pathological hallmarks of a degenerating motor neurone.	20
Figure 1.2 Structure of motor and sensory neurones and the transmission of an action potential across the neuromuscular junction.	23
Figure 1.3. Simplified schematic of the primary motor pathway	25
Figure 1.4. The structure of the human brain	26
Figure 1.5. A simplified schematic representation of the proteins involved in mitochondrial transport and anchoring	34
Figure 1.6. The production of ROS from the ETC and antioxidant enzymes.	38
Figure 1.7. Schematic representation of a motor neurone showing the subcellular localisation/pathways of proteins associated with HSP	42
Figure 1.8. Genetic bottleneck resulting in the founder effect	53
Figure 2.1. Flow cytometry cell population gating.	92
Figure 3.1. Schematic representation of the cellular localisation of NBIA-associated proteins	96
Figure 3.2. Schematic representation of the four isoforms and genomic organisation of C19orf12.	98
Figure 3.3. Pedigree of Amish family with a single child affected with MPAN.	101
Figure 3.4. Dideoxy sequencing of identified c.278del variant in affected child and wildtype parents and siblings.	102
Figure 3.5. Schematic of the C19orf12 protein, displaying reported dominant and recessively acting variants (A) and missense variants (B) in relation to gene exons, transmembrane domain and isoforms.	103
Figure 4.1. An MRI image of an individual with Mast syndrome.	112
Figure 4.2. Schematic representation of the three known SPG21 mutations associated with Mast syndrome in Amish, Italian and Japanese families.	113
Figure 4.3. A schematic of CRISPR-Cas9 gene editing using two gRNAs.	118
Figure 4.4. A schematic representation of the gRNA positions and the PCR product sizes with each corresponding genetic outcome.	121
Figure 4.5. Sequencing validation of the gRNA containing plasmids.	122
Figure 4.6. Genetic outcome from 100 cell sorted colonies.	124
Figure 4.7. Exon 3 gRNA combination genetic outcome from single cell colonies.	125
Figure 4.8. Exon 3 and 5 gRNA combination genetic outcome from single cell colonies.	126
Figure 4.9. DNA sequencing results for control, heterozygous and SPG21 knockout cell lines.	128
Figure 4.10. Genetic outcome of single cell colonies and the time taken for each to reach plate confluency.	129
Figure 4.11. Expression of maspardin and GAPDH (A) and densitometry (B) of control, heterozygous and knockout colonies.	130
Figure 4.12. Schematic representation of the three epitope regions from the commercially available maspardin antibodies used.	132
Figure 4.13. Maspardin expression in control wildtype, heterozygous and SPG21 knockout colonies probed with maspardin 407, 883 and 436	133
Figure 4.14. Gel image showing the cDNA outcomes in control and SPG21 knockout colonies.	135
Figure 4.15. cDNA sequencing results for control and SPG21 knockout cell lines	136
Figure 4.16. Endogenous maspardin colocalises with YFP-SPG21 plasmid.	138

Figure 4.17. Endogenous maspardin colocalises with SPG21-myc-FLAG plasmid.....	138
Figure 4.18. Maspardin localisation with endosomal, ER and mitochondrial markers in 3T3 cells	142
Figure 4.19. Immunoprecipitation of endogenous and overexpressed maspardin.....	143
Figure 4.20. Common subcellular localisation of endogenous (A) and overexpressed (B) maspardin binding partners.....	147
Figure 4.21. Subcellular localisation (A) and function (B) of maspardin binding partners common to endogenous and overexpressed samples..	148
Figure 4.22. Binding partner colocalisation with endogenous maspardin	150
Figure 4.23. Binding partner colocalisation with SPG21-myc-FLAG	152
Figure 4.24. Maspardin localises to vesicular structures	154
Figure 4.25. Maspardin surrounded vesicles identified in SH-SY5Y and HEK 293 cells.....	155
Figure 4.26. Fixed YFP-SPG21 imaging	156
Figure 4.27. Fixed YFP-SPG21 imaging with no permeabilisation.....	158
Figure 4.28. Time lapse imaging of YFP-SPG21 and Nile Red lipid droplet stain	160
Figure 4.29. Maspardin colocalises with Rab7 surrounded vesicles.	161
Figure 4.30. Maspardin and Rab4 surrounded vesicles interact.....	163
Figure 4.31. Maspardin and Rab5 surrounded vesicles interact.....	164
Figure 4.32. Maspardin and Rab9 surrounded vesicles interact and colocalise	165
Figure 4.33. Time lapse imaging of maspardin and lysosomes.....	167
Figure 4.34. Maspardin, Rab7, and lysotracker (ab176824) imaging, indicate the three colocalise in 3T3 cells	168
Figure 4.35. Time lapse imaging of maspardin and mitotracker in 3T3 cells indicate transient interaction.....	170
Figure 4.36. Candidate subcellular localisation signals identified by LocSigDB at specific maspardin amino acid positions.	171
Figure 4.37. Maspardin and Rab7 co-immunoprecipitation (A) and SPG21 knockout Rab7 expression (B).	173
Figure 4.38. Increase in cell death, metabolic activity and ROS in SPG21 knockout cells.....	176
Figure 4.39. Rab4, 5, 7 and 9 vesicles in SH-SY5Y control and SPG21 knockout cells.....	178
Figure 4.40. Vesicle diameter of Rab surrounded vesicles in control and SPG21 knockout cells.....	179
Figure 4.41. Lysosome size and distribution in control and SPG21 knockout SH-SY5Y cells.....	180
Figure 4.42. Lipid droplet size and interaction in control and SPG21 knockout cells.....	182
Figure 4.43. Mitotracker stained control and SPG21 knockout SH-SY5Y cells.	183
Figure 5.1. The classical and alternative bile acid pathways.....	195
Figure 5.2. The multifunctional CYP27A1 enzyme in cholesterol and oxysterol metabolism.....	197
Figure 5.3. The mitochondria-associated ER membrane (MAM).....	202
Figure 5.4. The separation of PBMCs from whole blood.....	206
Figure 5.5. Diagram outlining the protocol to obtain mitochondria from homogenised cellular material.....	208

<i>Figure 5.6. Western blot of cellular fractions obtained from mitochondrial extraction of HEK 293 cells</i>	209
<i>Figure 5.7. Comparative mitochondrial isolation techniques</i>	210
<i>Figure 5.8. Identifying the portion of the ultracentrifugation tube containing cellular material.</i>	212
<i>Figure 5.9. Mitochondrial detection and extraction reliability from low volumes of blood</i>	213
<i>Figure 5.10. Mitochondrial and ER detection in whole cell lysate and mitochondrial fractions from PBMCs and SH-SY5Y cells.</i>	215
<i>Figure 5.11. Diagram outlining the main steps of the optimised protocol to obtain a mitochondrial pellet from blood or cultured cell lines</i>	218
<i>Figure 5.12. Oxysterol levels in PBMC whole cell lysate and mitochondrial fractions extracted from fresh and one day old blood stored at 4°C.</i>	221
<i>Figure 5.13. Oxysterol profiles in SH-SY5Y and PBMC whole cell and mitochondrial fractions</i>	225
<i>Figure 5.14. The effect of storage time on PBMC lysate (A) and mitochondrial (B) oxysterols.</i>	228
<i>Figure 5.15. Oxysterol variation between control and SPG21 knockout SH-SY5Y cell fractions</i>	232

List of Tables

<i>Table 2.1. Buffers and solutions.</i>	60
<i>Table 2.2. Antibody incubation conditions.</i>	67
<i>Table 2.3. Acrylamide gel composition.</i>	70
<i>Table 2.4. Primer sequences.</i>	74
<i>Table 2.5. PCR reaction mixture.</i>	75
<i>Table 2.6. PCR cycling conditions.</i>	76
<i>Table 2.7. Plasmids used in this study and their corresponding use.</i>	81
<i>Table 2.8. Components of a single and double restriction digest</i>	83
<i>Table 2.9. PCR reaction for obtaining an SPG21 cloning insert.</i>	85
<i>Table 2.10. PCR programme for obtaining an SPG21 cloning insert.</i>	85
<i>Table 2.11. Ligation reaction.</i>	87
<i>Table 2.12. Reaction mixture to anneal gRNA oligos.</i>	88
<i>Table 2.13. Thermocycler conditions to anneal gRNA oligos.</i>	88
<i>Table 2.14. Reaction mixture to ligate gRNA oligos into vectors.</i>	88
<i>Table 3.1. NBIA-associated genes.</i>	96
<i>Table 3.2. Reported autosomal dominant C19orf12 variants.</i>	109
<i>Table 4.1. SPG21 CRISPR-Cas9 plasmid composition</i>	120
<i>Table A1. HSP associated proteins, the assigned SPG designation and mode of inheritance.</i>	243

Abbreviations

°C	Degrees Celsius
aa	Amino acid
AD	Autosomal dominant
ALS	Amyotrophic lateral sclerosis
APS	Ammonium persulfate
AR	Autosomal recessive
ATP	Adenosine triphosphate
BCA	Bicinchoninic acid
bp	Base pair
BSA	Bovine serum albumin
Ca²⁺	Calcium ion
cDNA	Complementary deoxyribonucleic acid
CMT	Charcot-Marie-Tooth
CNS	Central nervous system
CRISPR	Clustered regularly interspaced short palindromic repeats
CSF	Cerebrospinal fluid
CTX	Cerebrotendinous xanthomatosis
CYP	Cytochrome P450
DAPI	4,6-diamidino-2-phenylindole, dihydrochloride
DiOH	Dihydroxycholesterol
DC	Density centrifugation
DCFDA	2',7'-dichlorofluorescein diacetate
ddH₂O	Double distilled water
dHMN	Distal hereditary motor neuropathy
DMEM	Dulbecco's modified eagle's medium
DMSO	Dimethyl sulfoxide
DNA	Deoxyribonucleic acid
dNTP	Deoxyribonucleotide triphosphate
DSB	Double stranded break
ECL	Enhanced chemiluminescence
EDTA	Ethylenediaminetetraacetic acid
EGF	Epidermal growth factor
ER	Endoplasmic reticulum
ESCRT	Endosomal sorting complex required for transport
ETC	Electron transport chain
FA2H	Fatty acid-2 hydroxylase
FBS	Foetal bovine serum
FACS	Fluorescence-activated cell sorting
g	Grams
GAPDH	Glyceraldehyde 3-phosphate dehydrogenase
GFP	Green fluorescent protein
GnomAD	Genome aggregation database
GPX	Glutathione peroxidase
H₂O₂	Hydrogen peroxide
HBSS	Hanks' balanced salt solution
HCL	Hydrochloric acid
HEK	Human embryonic kidney

HMSN	Hereditary motor sensory neuropathy
HSP	Hereditary spastic paraplegia
HRP	Horseradish peroxidase
IMM	Inner mitochondrial membrane
IP	Immunoprecipitation
Kb	Kilobase
kDa	Kilodalton
KCl	Potassium chloride
KO	Knockout
LB	Luria-Bertani
LC-MS/MS	Liquid chromatography tandem-mass spectrometry
LXR	Liver X receptor
M	Molar
mA	Milliamps
MAM	Mitochondria-associated ER membrane
Mg	Milligrams
MICOS	Mitochondrial contact site and cristae organising system
ml	Millilitres
mM	Millimolar
MND	Motor neurone disease
mOMP	Mitochondrial outer membrane pore
MPAN	Mitochondrial membrane protein-associated neurodegeneration
mPTP	Mitochondrial permeability transition pore
MTT	3-(4,5- dimethylthiazol-2-yl)-2,5-diphenyltetrazolium bromide
MW	Molecular weight
NaCl	Sodium chloride
NBIA	NBIA
ng	Nanograms
nm	Nanometer
OH	Hydroxycholesterol
OMM	Outer mitochondrial membrane
OPA1	Optic dominant atrophy 1
ORP	OSBP-related proteins
OSBP	Oxysterol binding protein
PAM	Protospacer adjacent motif
PBMC	Peripheral blood mononuclear cell
PBS	Phosphate buffered saline
PCR	Polymerase chain reaction
PFA	Paraformaldehyde
pH	Potential hydrogen
PLS	Primary lateral sclerosis
PUFAs	Poly-unsaturated fatty acids
PVDF	Polyvinylidene difluoride
RBC	Red blood cell
RFP	Red fluorescent protein
RNA	Ribonucleic acid
ROS	Reactive oxygen species
RPM	Revolutions per minute
SAP	Shrimp alkaline phosphatase

SBMA	Spinobulbar muscular atrophy
SD	Standard deviation
SDS	Sodium dodecyl sulphate
SDS-PAGE	Sodium dodecyl sulphate polyacrylamide gel electrophoresis
SEM	Standard error of the mean
SMA	Spinal muscular atrophy
SNP	Single nucleotide polymorphism
SOC	Super optimal broth
SOD	Superoxide dismutase
SREBPs	Sterol regulatory element-binding proteins
StAR	Steroidogenic acute regulatory protein
StarD	StAR-related lipid transfer domain
TAE	Tris-acetate-EDTA
TBE	Tris-borate-EDTA
TBHP	Tert-butyl hydrogen peroxide
TBS	Tris-buffered saline
TBS-T	Tris-buffered saline + Tween-20
TEMED	N,N,N',N'-tetramethylethane-1,2-diamine
TRAK	Trafficking kinesin
U	Units
UC	Ultracentrifugation
V	Volts
v/v	Volume per volume
WBC	Whole blood cell
WC	Whole cell
WoH	Windows of Hope
w/v	Weight per volume
YFP	Yellow fluorescent protein
µg	Micrograms
µl	Microlitres
µm	Micrometres
µM	Micromolar

Chapter 1

Introduction

Introduction

1.1 Neurodegenerative Disorders

Neurodegenerative disorders are an expansive and diverse group of largely incurable diseases associated with the death or impaired function of neurones. More common neurodegenerative diseases include dementias such as Alzheimer's diseases and frontotemporal dementia, and movement disorders such as Parkinson's disease, Huntington's disease and motor neurone disease (MND). These disorders are a leading source of disability and are growing in prevalence proportionally, attributable to the increase in lifespan globally. As such these conditions represent an ever-increasing healthcare burden. The number of individuals living with dementia worldwide doubled from 20.2 million in 1990 to 43.8 million in 2016, with an age-standardised prevalence increase of 1.7%. However, there is evidence indicating that the incidence of dementia is decreasing in Western high-income countries [1, 2]. Globally the number of individuals with Parkinson's disease has more than doubled from 2.5 million in 1990 to 6.1 million in 2016, with a 21.7% increase in age-standardised prevalence [3]. MNDs affect fewer individuals with a global prevalence of 331,000 in 2016 and an age-standardised increase of 4.5% since 1990; this percentage is much higher in Western countries, in particular the United Kingdom which had 13,249 individuals living with MND in 2016 with an age-standardised increase of 34.5% since 1990 [4]. Taken together these figures demonstrate the pressing need to notably improve knowledge of the pathomolecular basis of these conditions in order to develop effective therapies and treatments to address this healthcare burden.

1.1.1 Cellular Hallmarks of Degeneration

It is widely accepted that neurodegeneration is a multifactorial and complex process which likely involves a series of cellular disturbances that accumulate over time. However, it is not clear how dysfunction on a molecular level leads to the degeneration at the cellular level. The pathological hallmarks of neurodegeneration are the accumulation of misfolded proteins, oxidative stress, mitochondrial dysfunction and lipid imbalance, illustrated in Figure 1.1 [5]. While these disturbances may affect many neuronal cell types, the degeneration of motor neurones is of particular relevance in MND. There are two overarching hypotheses to define the neurodegeneration of motor neurones; the 'dying-forward' and the 'dying-back' concepts. Here, the dying-forward theory involves toxicity arising in the cortical motor areas of the brain which triggers anterograde degeneration of neurone. Conversely the dying-back theory implicates degeneration beginning distally at the nerve terminal or neuromuscular junction, which progresses towards the cell body [6]. It has been suggested that the underlying cause of each specific type of neurodegenerative disease may have its own individual cause, which then converges into a common conserved degenerative mechanism [7]. The fact that many forms of neurodegenerative disease exhibit similar pathological hallmarks supports the idea that neurodegenerative disorders share common final pathways leading to cell death. The variation in symptoms between neurodegenerative disorders may reflect the type and location of the cell populations that degenerate and/or malfunction [8].

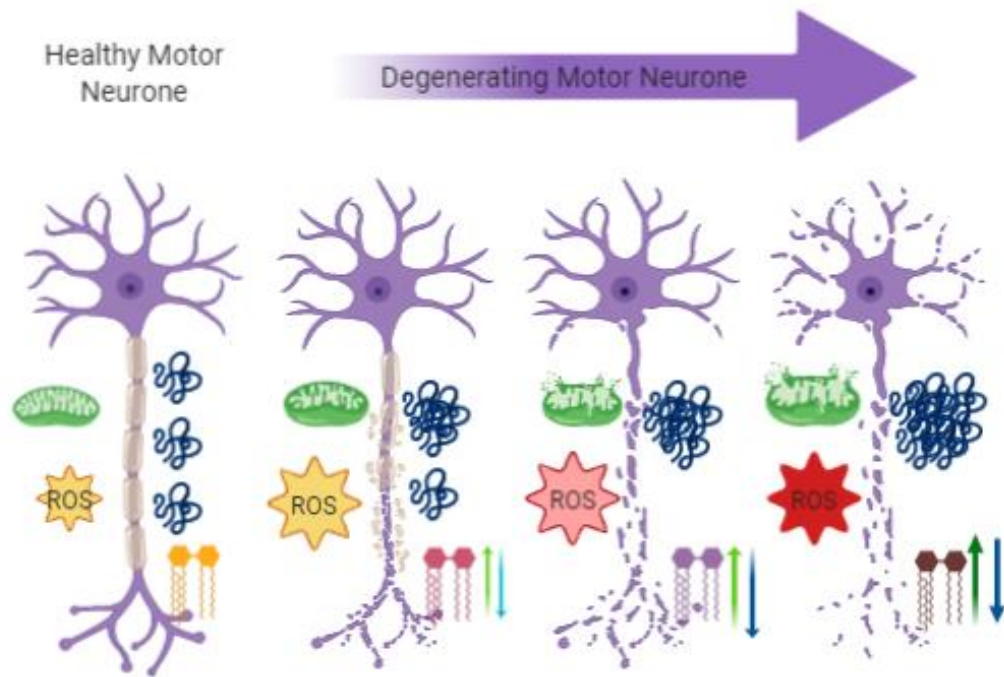


Figure 1.1 Schematic illustrating common pathological hallmarks of a degenerating motor neurone. During disease progression mitochondria become increasingly dysfunctional, reactive oxygen species (ROS) build-up, lipid levels are altered and in many cases proteins aggregate and become toxic. These pathological hallmarks are noted in most neurodegenerative diseases, however the rate and order at which they progress differs between disease types depending on the initial degenerative trigger. This build-up of cellular stress ultimately results in the death of the neurone. Illustration made using BioRender.

1.1.2 Neuronal Cell Death and the Neuromuscular Junction

While during aging a progressive but limited loss of neurones is observed, in the mature CNS of a healthy individual extensive neuronal loss is rarely seen, unlike that of an individual with a neurodegenerative disorder [9]. While motor neurone loss results in a lack of muscular innervation, other surviving motor neurones may sprout new branches and reinnervate previously denervated muscle fibres. Neurones are very robust cells as they are equipped to maintain cellular homeostasis in order to last an individual's lifetime, but prolonged cellular stress can lead to cell death [9]. Furthermore, previous studies have shown that neurones transplanted from mice to rats survived the rat's lifetime,

which is longer than that of mice. This suggests that neurones do not necessarily have an 'internal clock' predetermining cell death, but that their longevity may be determined by the lifetime of the animal [10]. The same pathways that trigger neuronal cell death during aging are active in individuals with neurodegenerative disorders, although particular pathological hallmarks are typically not observed in healthy brains, Figure 1.1 [9].

During the development of the nervous system programmed neuronal cell death is important to maintain proportionality between distinct cell types and generate a functional nervous system. In addition to complete cell death, axonal death also occurs during development to remodel and refine the neural circuit. This remodelling and axon pruning eliminates neurones that innervate incorrect targets and axons that have migrated to abnormal positions, to create the mature nervous system which is long-lived [11]. In neurodegenerative disease there is a more substantial loss of neurones resulting in an ineffective and compromised nervous system.

Apoptosis and necrosis are the major death pathways in neurones. They were once considered to be the only forms of neuronal cell death, however in recent years many forms of necrosis have been discovered including oncosis, necroptosis, parthanatos, ferroptosis, sarmoptosis, autosis, autolysis, paraptosis, pyroptosis, phagoptosis, and mitochondrial permeability transition [11]. Apoptosis is a form of programmed cell death where cells are characterised by chromosome condensation, DNA fragmentation and shrinkage [9]. Apoptosis is triggered by two primary pathways, the intrinsic or extrinsic pathways, which then converge into the common effector pathway. The extrinsic pathway is activated by the binding of extracellular tumour necrosis factor death receptors on the cell surface, whereas the intrinsic pathway is

activated by internal stimuli such as biochemical stress or DNA damage. Both pathways eventually lead to the release of pro-apoptotic factors including cytochrome c from the mitochondria to the cytoplasm, leading to apoptosis via a caspase cascade that ultimately degrades cellular proteins [9, 11]. Necrosis is characterised by cellular swelling and the unregulated 'leaking out' of its contents; DNA is also fragmented but chromosomes do not condense. Necrosis is further sub-divided into regulated and non-regulated forms depending on stimuli. The best characterised form of necrosis is the regulated necroptosis dependent on the activity of specific receptor interacting kinases which form a necrosome leading to membrane rupture [11].

Motor neurones carry signals from the brain and spinal cord to the muscles, organs and glands. Conversely sensory neurones carry information from the periphery to the brain for processing. While sensory and motor neurones have differing structures, Figure 1.2A, they both receive signals through dendrites which travel along axons where they synapse with their target cell [12]. In humans a typical lower motor neurone branches into 100-200 nerve endings that synapse with skeletal muscle and form a neuromuscular junction synapse that has fast and reliable transmission due to its specialised structure [13]. It is one of the largest types of synapse in the body, in which the post synaptic membrane is a thickened portion of sarcolemma containing a series of shallow folds packed with nicotinic cholinergic receptors forming a structure called the motor end plate. This aligns with the presynaptic active zone, which itself is an area of membrane thickening [14, 15]. These structures ensure that the neurotransmitters released from the presynaptic membrane are directed at a large surface, Figure 1.2B. The synaptic vesicles in the axon terminal of motor neurones contain 5000-10000 molecules of acetylcholine, the neurotransmitter

present in the neuromuscular junction [13]. The synaptic cleft of a neuromuscular junction is around 50nm across containing basal lamina where acetylcholinesterase, the enzyme responsible for acetylcholine breakdown, resides to catabolise the neurotransmitter thereby ensuring its' receptors do not have prolonged activation. Upon the activation of nicotinic cholinergic receptors, which are gated ion channels, they open and allow the influx of sodium ions into the muscle membrane subsequently generating and transmitting the action potential [13, 14].

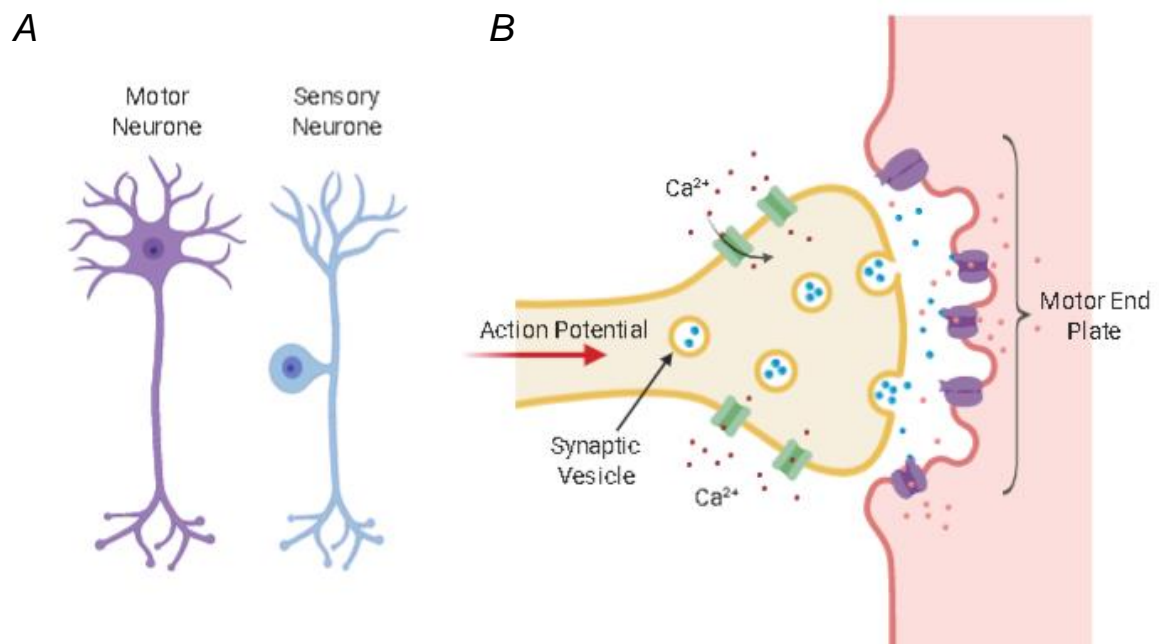


Figure 1.2 Structure of motor and sensory neurones (A) and the transmission of an action potential across the neuromuscular junction (B). **A)** The cell body of a motor neurone is at one end within the CNS and they also have a long axon whereas sensory neurones have a cell body to one side and a shorter axon. **B)** The neuromuscular junction has the unique structure of the motor end plate in the muscle to increase the chance of neurotransmitter detection. The received action potential at the axon terminal activates the Ca²⁺ channels and the subsequent Ca²⁺ (red spheres) influx triggers the release of the neurotransmitter acetylcholine (blue spheres) to the synaptic cleft. This neurotransmitter then activates the opening of nicotinic cholinergic receptor ion channels located on the postsynaptic membrane which then allows the influx of sodium ions (pink spheres) to the muscle cell to initiate a postsynaptic action potential. Made using BioRender.

Aging is also accompanied by the loss of muscle mass and strength, so the neuromuscular junction undergoes morphological and functional changes to adapt to the reduction in muscle mass. These changes include the increase in the size of the motor end plate with the addition of nicotinic cholinergic receptors, axon terminals become thinner or swollen, and sometimes multiple axon terminals innervate a single postsynaptic receptor [16]. Furthermore, the mitochondria that are vital to the proper functioning of the neuromuscular junction have been found to be dysfunctional in elderly rats with an increase in apoptosis triggered by cytochrome c [17].

1.2 Motor Neurone Diseases

MNDs are a large genetically and clinically heterogeneous group of incurable neurological diseases characterised by the progressive degeneration of upper and/or lower motor neurones, Figure 1.3. The clinical presentation and classification in MND is dependent on whether upper motor neurones, lower motor neurones, or both, are primarily involved [18]. The upper motor neurones originate in the motor cortex which is responsible for precise movements of voluntary motor control and it is located in the frontal lobe, illustrated in Figure 1.4. The frontal lobe is the largest lobe of the four cerebral lobes responsible for many functions: memory, personality, emotions and movement control [19]. The motor cortex is the principle brain region controlling the movement of skeletal muscle via the neurones of the corticospinal tract. These neurones cross through the corpus callosum and descend to innervate muscles on the opposite side of the body. The corpus callosum is critical for connecting the two hemispheres of the brain and allowing them to communicate with each other [15]. The motor cortex is further divided into three areas: the primary motor

cortex which contains the majority of the corticospinal neurones, the premotor area which is important in learning and goal-orientated movement, and the supplementary motor area which is critical for linking cognition to action [20, 21]. Lesions to the motor centres may cause seizures, weakness or paralysis. Lesions of the primary motor cortex are likely to cause paralysis of the affected muscle groups, whereas spasticity is likely to occur when the premotor and supplementary areas are also affected [22].

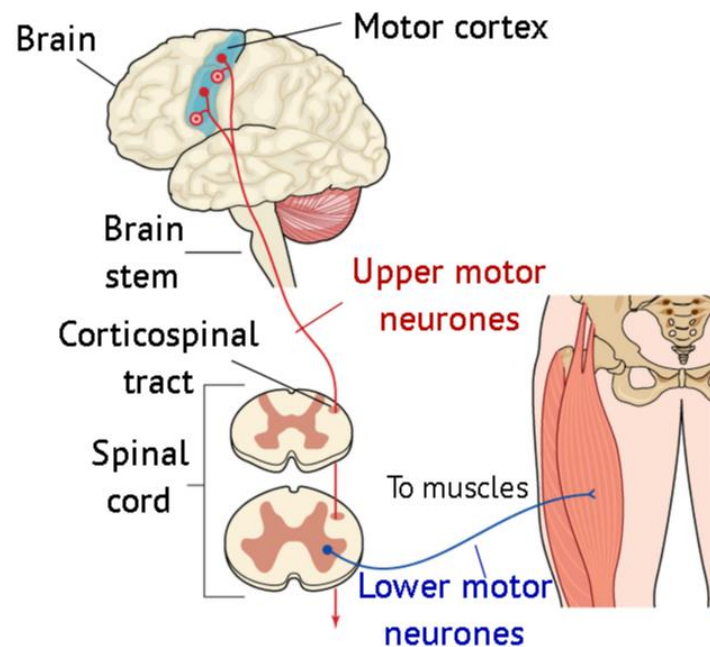


Figure 1.3. Simplified schematic of the primary motor pathway. Upper motor neurones originate in the motor cortex and convey voluntary motor activity to the spinal cord, forming the corticospinal tract. The upper motor neurones then transmit signals to the lower motor neurones in the peripheral nervous system which themselves directly innervate muscle. Figure annotated from Shutterstock.

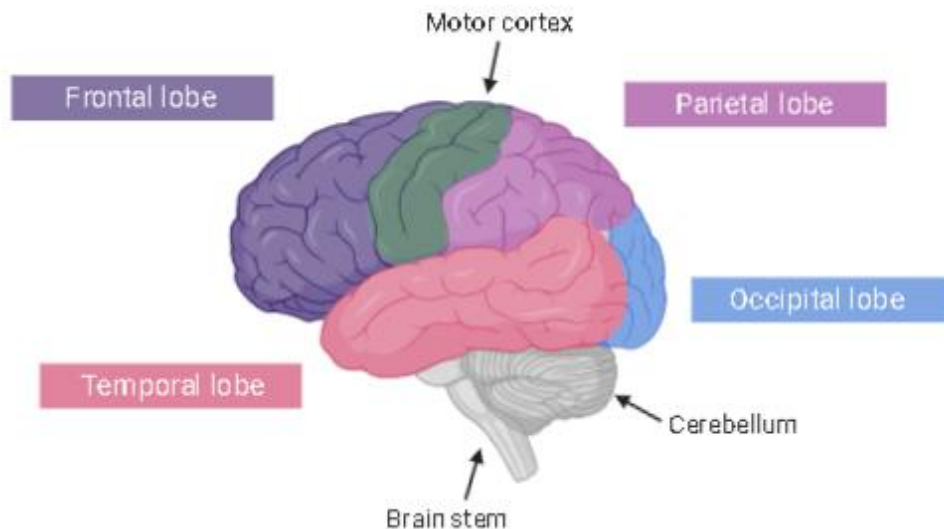


Figure 1.4. The structure of the human brain. The brain is composed of three primary structures: the cerebellum which coordinates basic voluntary functions, the cerebrum which performs higher cortical functions and the brainstem which regulates vital functions and connects the rest of the brain to the spinal cord [23]. The relative position of the four lobes (frontal, parietal, temporal and occipital) can be seen with the location of the motor cortex (green) within the frontal lobe highlighted. Made using BioRender.

Upper motor neurone malfunction primarily impairs the modulation of muscular movement resulting in muscle stiffness and spasticity, whereas lower motor neurone degeneration leads to muscle weakness and atrophy [24]. Commonly, MND presents in the sixth and seventh decade of life, although in some cases it may present much earlier. Symptoms tend to have a focal onset with three recognised patterns, limb, bulbar and respiratory, with distal limb weakness being the most common presenting symptom. If the onset is in the upper limbs, affected individuals typically notice that they start to drop things more easily accompanied by reduced dexterity and often wasting of hand muscles. If weakness commences in the legs, affected individuals often have a tendency to trip or lose balance and symptoms include the characteristic foot drop and a sensation of heaviness in the legs. Day-to-day tasks such as fastening buttons

on clothing and rising from low chairs may become harder, in addition to general fatigue. Bulbar onset MND occurs in ~20% of individuals with MND in which the first signs typically involve the slurring of speech (dysarthria) due to wasting and stiffness of the tongue, and as the condition progresses difficulties in swallowing often ensue (dysphagia). Uncommonly, respiratory muscles are first affected whereby individuals have difficulties breathing with shortness of breath and tightness of the chest [25].

1.2.1 Amyotrophic Lateral Sclerosis

The most common form of MND is amyotrophic lateral sclerosis (ALS). ALS has a prevalence of 3-5/100,000 in Europe and the United States [26] and it is associated with both upper and lower motor neurone degeneration. The primary symptom of ALS entails motor dysfunction, although ~50% of affected individuals also develop neurocognitive impairments during the course of the disease. In ALS, death typically occurs within 3-5 years of diagnosis often due to respiratory failure, although affected individuals may live up to 40 years after the onset of symptoms [26]. Up to 25% of ALS cases have a family history of the disease, with mutations in *C9orf72* and *SOD1* together accounting for ~40% of familial ALS cases [27, 28]. While the majority of individuals display no clear monogenic basis, most 'sporadic' cases are considered likely to have a more complex genetic involvement [29].

1.2.2 Lower Motor Neurone Disease

Lower motor neurone malfunction may directly compromise muscular innervation, leading to muscular atrophy, weakness and hyporeflexia which is typically observed in spinal muscular atrophy (SMA), spinobulbar muscular atrophy (SBMA) and the distal hereditary motor neuropathies (dHMNs). SMA is an autosomal recessive disorder characterised by proximal muscular weakness

which is further classified depending on the age of onset which can present at birth, childhood or in adulthood, often associated with mutations in the *SMN1* gene [30]. SBMA is an X-linked disorder caused by expansion of a polymorphic CAG repeat in the androgen receptor gene, with onset involving progressive limb and bulbar weakness usually between the third and fifth decades of life [31]. The distal hereditary motor neuropathies (dHMNs) are a heterogeneous group characterised by slowly progressing, distal weakness [32]. Weakness usually presents in the lower limb extremities in the second or third decade of life, progressing to the distal muscles of the upper limbs [33]. There are currently ~30 genes known to be responsible for dHMNs [32, 33], with many forms also displaying sensory abnormalities and/or an upper motor neurone component, and as such often overlap with other forms of MND. This overlap includes Charcot-Marie-Tooth (CMT) disease, which comprises of an additional distinct group of lower motor neurone conditions with a sensory component. CMT is the most common inherited MND with a prevalence of ~1 in 2500 with >80 distinct genetic causes identified, many of which are associated with other forms of MND [34, 35]. These genes are implicated in an array of pathways including mitochondrial function, axonal transport, myelination and endosomal function [34]. The clinical presentation of the two major subtypes of CMT; CMT1 and CMT2, are very similar with onset in the first or second decade of life where individuals present with distal weakness that slowly spreads, later accompanied by sensory loss [34]. On a pathological level the two types are distinct, CMT1 is characterised by demyelination primarily caused by mutations in myelin-specific proteins, whereas CMT2 is characterised by axonal degeneration with abnormalities in mitochondrial structure, cellular transport and chaperone activity commonly implicated [36].

1.2.3 Upper Motor Neurone Disease

Upper motor neurone dysfunction typically results in muscle rigidity and spasticity observed in primary lateral sclerosis (PLS), pseudobulbar palsy and hereditary spastic paraplegia (HSP). PLS is a mainly sporadic late-onset MND, often misdiagnosed as HSP or ALS, characterised by progressive spastic paraplegia which is also accompanied by bulbar features [37]. To be diagnosed with pure PLS the absence of lower motor neurone symptoms are required for 3-5 years as in the first few years clinical signs are the same as initial ALS presentation; some patients then progress with lower motor neurone dysfunction which presents as a classical ALS clinical phenotype [38, 39]. Pseudobulbar palsy affects the cranial nerves and is characterised by dysphagia, dysarthria and facial weakness with individuals often presenting with symptoms in the sixth and seventh decade [40].

1.2.4 Hereditary Spastic Paraplegia

HSP is an upper motor neurone degenerative disorder characterised by progressive spasticity of lower limbs, first described by Strumpell and Lorrain in the late 19th century [41]. It was first considered to be a small group of Mendelian disorders, however, subsequent advancements in our understanding of the genetic architecture of HSP have led to it being recognised as one of the most genetically heterogeneous inherited disorders. HSP subtypes were originally designated SPG prefixes (spastic paraplegia) to define genetic loci in approximate numerical order of their discovery. However, due to the large number of gene loci, the rate of gene discovery, and the complex clinical presentations associated with many spasticity-associated disorders, genes associated with HSP identified in more recent years have no longer employed

this classification system. To date there are currently over 80 distinct genetic causes of HSP, although many other disorders describe spasticity as a key diagnostic feature [42].

HSP is divided into 'pure' and 'complicated' forms where pure HSP is characterised by lower limb spasticity, whereas complex forms are also accompanied by other neurological and/or non-neurological clinical signs such as dysarthria, neuropathy, learning difficulties or seizures [43]. Autosomal dominant (AD), autosomal recessive (AR) and X-linked mode of inheritance have been reported, but ~35% of cases are considered to be sporadic and many of which have no known genetic cause [44]. The most common mode of inheritance is AD affecting 70-80% of Caucasian individuals with HSP. Most AD forms are predominantly adult onset and involve pure HSP, whereas AR forms tend to involve complicated presentations [45]. The most common form of HSP is pure AD SPG4, accounting for a third of all cases due to mutations in the *SPAST* gene encoding the microtubule severing protein spastin [46]. The second most common form of AD HSP is pure/complicated SPG3 due to mutations in the *ATL1* gene encoding the GTPase atlastin-1, which constitutes 5-15% of AD HSPs [46, 47]. The most common AR HSPs are SPG7/paraplegin (zinc metalloprotease), SPG11/spasticsin and SPG5/CYP7B1 (cytochrome P450) which collectively account for around 17% of AR HSP and are pure/complicated [47].

1.3 Common Pathomolecular Themes in Neurodegenerative Disorders

1.3.1 Abnormalities in Lipids

Lipids have three primary vital roles in cells and tissues: (i) energy storage, mostly comprised of triacylglycerol and sterol esters in lipid droplets, (ii) structural, membrane composition, formed by polar lipids, and (iii) molecular signalling pathways [48]. The brain consumes ~20% of the body's energy despite only being ~2% of the body weight, and around 20% of this energy demand is achieved by the oxidation of fatty acids [49, 50]. Furthermore, the formation of the myelin sheath comprises of 30% protein and 70% lipid [51]. The brain is the most cholesterol rich organ and cholesterol is an integral component in myelin formation, comprising 40% of the total myelin lipid content, 40% of lipids are phospholipids and the remaining 20% is comprised of glycosphingolipids [52, 53]. These lipids are crucial to enable the highly organised and tightly packed structure of myelin [52]. Moreover, synapses are enriched in lipids and cholesterol is crucial to synaptogenesis with its depletion or excess resulting in neuronal impairments; in particular, neuronal membranes are susceptible to altered structural conformation as a result of cholesterol imbalance therefore impacting neuronal firing [54]. Taken together, it is clear that lipids play a pivotal role in the brains' physiological function and structural integrity, and it is critical that the nervous system maintains lipidomic homeostasis for it to function efficiently.

Impairments in neuronal lipid homeostasis, particularly impairments in cholesterol homeostasis, result in many forms of neurological disease and neurodegeneration. Alzheimer's disease, the most common form of dementia and neurodegenerative disorder, is characterised by amyloid β peptide

aggregation which forms plaques and neurofibrillary tangles. Alzheimer's disease has several links with cholesterol imbalance. Firstly, the *APOE* 'e4' allele is the strongest genetic risk factor currently defined for developing Alzheimer's disease. This gene encodes apolipoprotein E, which is the major carrier of cholesterol in the brain [55]. Secondly, studies have shown that impairing cholesterol transport within the endo-lysosomal systems, leading to its aggregation within the vesicles, results in altered amyloid precursor protein processing and amyloid β protein generation [56]. Thirdly, a high cholesterol diet is also associated with Alzheimer's disease and patients have a ~10% increase in serum cholesterol levels [54]. It has been shown that a reduction in neuronal cholesterol levels in turn reduces the formation of amyloid β plaques highlighting the effects of abnormal cholesterol levels in Alzheimer's disease pathogenesis [57].

Parkinson's disease is the second most common form of neurodegenerative disorder characterised by the accumulation of α -synuclein, the formation of Lewy bodies and the loss of dopaminergic neurones in the substantia nigra. Examination of the composition of Lewy bodies has revealed a crowded lipid enriched environment containing membranes, vesicular structures and dysmorphic mitochondria [58]. It has been shown that α -synuclein binds to lipids and an increase in lipid levels promotes α -synuclein to aggregate [59]. Furthermore, the levels of cholesterol and its oxysterol derivatives have been shown to be altered in Parkinson's disease, and more specifically 27-hydroxycholesterol oxysterol has been shown to increase α -synuclein levels [60]. Mutations in phospholipases, which are phospholipid hydrolysing enzymes that convert phospholipids to poly-unsaturated fatty acids (PUFAs) and

lysophospholipids, have also been found to be associated with the formation of Lewy bodies [61].

Huntington's disease is an autosomal dominant disorder caused by the extension of a CAG trinucleotide repeat in the huntingtin gene. Lipid dysregulation and a reduction in cholesterol levels has been observed in individuals with Huntington's disease. The proposed molecular mechanism resulting in this dysregulation is due to mutant huntingtin protein binding to sterol regulatory element-binding proteins (SREBPs), rendering them unable to enter the nucleus and promote the synthesis of cholesterol and fatty acids; a ~50% reduction in the amount of SREBPs has been observed in the nucleus of Huntington's disease cells [62]. This is further supported as post-mortem tissues from deceased Huntington's disease patients show a reduction in mRNA transcription of key genes in the cholesterol and fatty acid biosynthetic pathways [63]. Interestingly, the length of the CAG extension has been found to be directly proportional to the amount of cholesterol and its precursors where the longer the length of the extension the lower the amounts of cholesterol are observed [64].

1.3.2 Mitochondrial Dysfunction

Mitochondrial dysfunction has been observed in many neurological disorders and it significantly contributes to disease progression [65]. While the majority of mitochondrial proteins are encoded by nuclear DNA, mitochondria also contain their own DNA housing genes important for mitochondrial function. Both mitochondrial and nuclear encoded proteins are incorporated into mitochondria whilst the organelle is within the soma [66]. Mitochondria are found in either a static or motile state, by which damaged mitochondria are transported back to the cell body for repair and healthy mitochondria are transported to where they

are required in the cell [66]. In neurones many mitochondria are located at synapses where they provide the energy required for rapid and repetitive neuronal firing. At any time 10-40% of mitochondria are on the move within the cell which, given the unique morphology and architecture of neurones, requires an efficient transport system [66]. This transport system comprises a complex network of kinesins, dyenins and mitochondria linking proteins, illustrated in Figure 1.5. The movement of mitochondria along microtubules is mediated by the anterograde kinesin motor and the retrograde dynein motors. These motors recognise mitochondria by binding to the trafficking kinesin (TRAK) protein which itself associates with the Rho GTPase Miro which is anchored to the outer mitochondrial membrane (OMM) [66]. In animal models, when either Miro or TRAK are disrupted the mitochondria are unable to travel along axons and one study has shown that loss of Miro in mouse models results in upper MND [67]. *TRAK1* mutations have also been associated with fatal encephalopathy, in which patients also present with progressive limb spasticity [68]. Static mitochondria are anchored to microtubules via the molecular brake syntaphilin, syntaphilin abnormalities have been associated with mitochondrial stress and neurodegeneration [69].

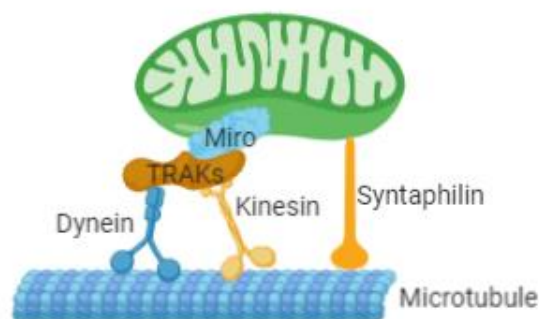


Figure 1.5. A simplified schematic representation of the proteins involved in mitochondrial transport and anchoring. Made using BioRender.

In order to maintain functional mitochondria, they continually undergo fission and fusion, particularly when cells are experiencing metabolic or environmental stress [70]. Mitochondrial fusion enables stressed and partially damaged mitochondria to be rescued and mitigate stress by the sharing of proteins and lipids with another mitochondrion. While mitochondrial fission is essential for growth, it also acts as a quality control mechanism whereby damaged mitochondria are removed. Fusion is predominately mediated by the proteins optic dominant atrophy 1 (OPA1), mitofusin 1 (Mfn1) and mitofusin 2 (Mfn2), whereas fission is mediated by Drp1, in addition to accessory proteins [71]. Sequence alterations in the *Mfn2* gene result in a range of phenotypes including spasticity in CMT type 2A disease [72] whereas mutations in the *OPA1* and *Drp1* genes are associated with distinct ophthalmological and neurological diseases; *OPA1* sequence alterations are associated with optic atrophy, and *Drp1* alterations are associated with neonatal death with impaired brain development [70, 73]. Furthermore, defects in mitochondrial fission and fusion have been noted more widely in all major forms of neurodegenerative disorders [70, 74].

Mitochondrial bioenergetic failure due to the depletion of ATP has been implicated in neurodegeneration. This energy failure may result in a range of subcellular outcomes including impaired synaptic transmission; profound energy failure may also result in the triggering of apoptosis, however in extreme energy failure apoptosis may be unable to proceed so other pathways would be triggered [75]. Further evidence for energy failure due to mitochondrial malfunction being important among neurodegenerative disorders includes the reduction of respiratory chain complexes from post-mortem brain tissue of Parkinson's, Alzheimer's and Huntington's disease patients [75]. Furthermore,

mutations in mitochondrial DNA, which encode members of the respiratory chain, may result in neurodegenerative disease. A mitochondrion contains around 1400 proteins, the vast majority being nuclear-encoded with 13 mitochondrial DNA-encoded molecules all involved in oxidative phosphorylation. These mitochondrial encoded proteins are particularly susceptible to mutation upon cellular stress, therefore resulting in the reduction of ATP production [76].

Taken together, this demonstrates the crucial requirement for maintenance of mitochondrial function in order for neurones to survive. The disruption to mitochondrial integrity can result in the opening of pores within the mitochondrial membrane allowing the release of cytochrome c and therefore initiating apoptosis of the cell [77]. Furthermore, abnormal mitochondrial function can lead to the increase in oxidative stress due to overproduction or inefficient clearance of reactive oxygen species (ROS) [78].

1.3.3 Reactive Oxygen Species

The post-mitotic nature of neurones means that they are much more susceptible to cellular stress such as ROS. Cellular ROS are mostly produced in the ER, peroxisomes and mitochondria, with the three organelles forming a redox triangle to regulate ROS signalling and homeostasis [79]. The electron transport chain (ETC) is responsible for a large proportion of cellular ROS production, mostly superoxide anion ($O_2^{\cdot-}$), which is a natural by-product of oxidative phosphorylation, Figure 1.6 [80]. The majority of $O_2^{\cdot-}$ is produced from complex I and complex III of the ETC, however complex II does also produce low levels of ROS. Interestingly, the production of $O_2^{\cdot-}$ from each ETC complex varies between organs and disease conditions. Under normal conditions complex I is the most prominent producer of $O_2^{\cdot-}$ in the brain whereas complex III is the main source of $O_2^{\cdot-}$ in the heart and lungs [81]. Under pathological

conditions complex I is most responsible for the increase in ROS production. $O_2^{\cdot-}$ is not the only ROS or the strongest oxidant but it is the precursor to most other ROS and it is involved in the propagation of oxidative chain reactions. The reactive hydroxyl radical ($OH\cdot$) is responsible for most cytotoxic effects, generated from either $O_2^{\cdot-}$ or via the Fenton reaction from hydrogen peroxide (H_2O_2) [82]. Mitochondrial ROS are subsequently released into the cytosol through an inner mitochondrial permeability transition pore (mPTP) and a mitochondrial outer membrane pore (mOMP) that are opened in response to ROS accumulation [83]. When regulated, ROS are signalling molecules that are essential for many cellular processes, such as cell protection, the cell cycle, mitochondrial fission and autophagy [80]. Excessive levels of ROS may lead to a plethora of cellular problems such as DNA damage, protein aggregation, lipid damage and subsequent cell death. Mitochondria are particularly vulnerable to damage due to ROS build-up and the mitochondrial DNA is susceptible to damage due to the lack of mitochondrial DNA repair mechanisms [84]. ROS imbalance has been associated with many diseases, such as diabetes, cardiovascular disease, cancer and neurodegenerative disease [82, 85-87].

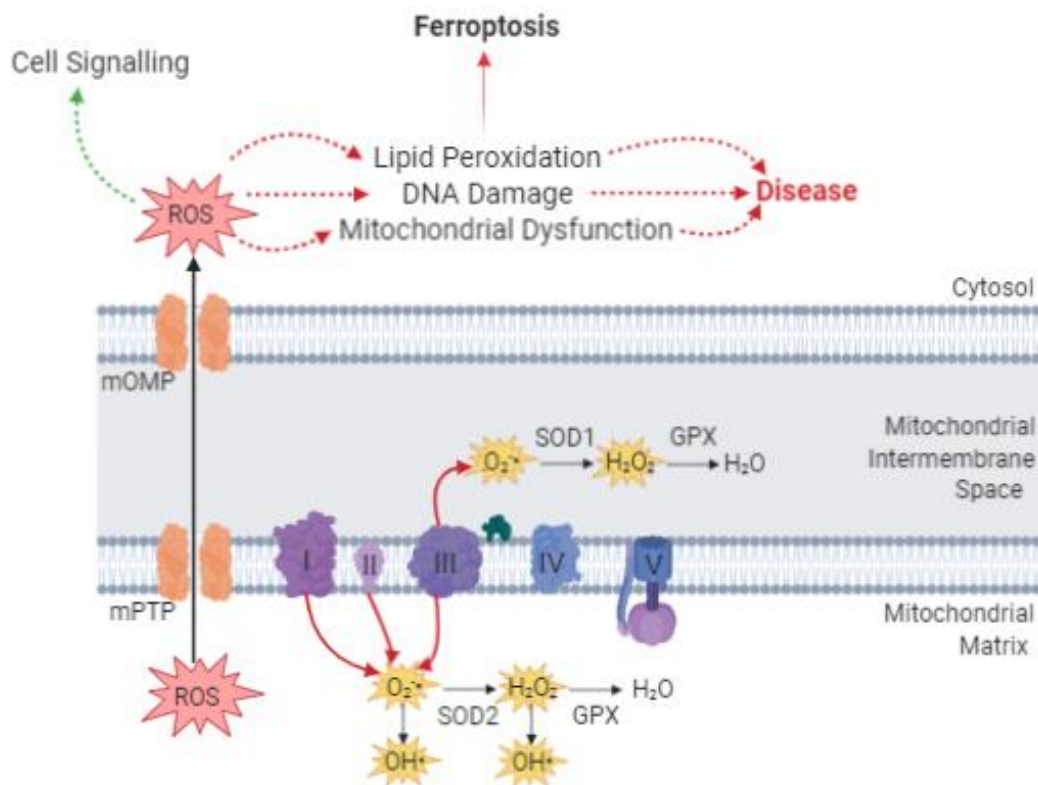


Figure 1.6. The production of ROS from the ETC and antioxidant enzymes. ROS are produced from complex I, II and III which can be released into the cytosol via the mPTP and mOMP. The mitochondrial antioxidant system includes SOD1 in the mitochondrial intermembrane space, and SOD2 within the mitochondrial matrix; in addition to GPX enzymes to convert ROS to H₂O.

1.3.3.1 Lipid Peroxidation

The nervous system is particularly susceptible to the adverse effects of ROS because of its high energy demand and lipid composition which is vulnerable to lipid peroxidation. Lipid peroxides have been identified as mediators of pathological states, including cancer, inflammation, kidney degeneration and neurodegeneration. Lipid peroxides are synthesised through enzymatic and non-enzymatic processes and the lipids most susceptible to peroxidation are PUFAs due to the carbons with double bonds being prone to oxidation. Lipid peroxides are toxic through two mechanisms, disrupting structure and dynamics of cellular membranes, and through their ability to propagate and further

generate toxic ROS [88]. The peroxidation of lipid bilayers has been shown to significantly alter its physical properties, including ion gradients, membrane fluidity and permeability. Previous studies have shown that the introduction of oxidised functional groups within the lipid bilayer leads to substantial conformational change, the oxidised tail group bends towards the water phase and forms hydrogens bonds with the lipid hydrophilic head group, subsequently resulting in a reduction of the overall lipid bilayer thickness [89]. Another study has shown that this lipid bilayer conformational change in certain phospholipid families triggers the innate immune system, leading to the phagocytic removal of the oxidatively damaged cells [90]. The brain is vulnerable to lipid peroxidation as it is enriched in PUFAs and as the brain consumes a large volume of oxygen, in turn creating ROS, therefore making it the perfect environment for lipid peroxidation to occur [91].

1.3.3.2 Ferroptosis

As previously mentioned (section 1.1.2) there are many forms of necrosis, including ferroptosis which is a recently recognised form of regulated cell death dependent on ROS and intracellular iron [92]. Ferroptosis is distinct from other forms of regulated cell death and it is characterised by the accumulation of lipid peroxides, and small mitochondria with condensed, ruptured membranes with a reduction in mitochondrial cristae. Ferroptosis can be initiated by various molecules, the first molecules discovered being erastin and RSL3 [93, 94]. Previous studies have shown that motor neurone-like cells are more sensitive to ferroptosis [95], therefore in order to maintain the proper functioning of the CNS it is crucial to maintain an equilibrium between oxidant and antioxidants to prevent the adverse effects of ROS and lipid peroxidation.

1.3.3.3 The Antioxidant System

The primary cellular defence mechanism against elevated levels of ROS is the antioxidant system, either via antioxidant enzymes or small molecule antioxidants. Superoxide dismutases (SOD) are vital to the antioxidant system as they transform $O_2^{\cdot-}$ into the more stable H_2O_2 which is then catalysed into H_2O and O_2 by glutathione peroxidase (GPX) [82]. There are three mammalian SOD isoforms each with similar functions but different protein structures, metal cofactors and cellular compartmentalisation: cytosolic and mitochondrial intermembrane space copper-zinc SOD, encoded by the *SOD1* gene; mitochondrial manganese SOD, encoded by the *SOD2* gene; and, extracellular SOD, encoded by the *SOD3* gene [96]. The GPX family contains 8 GPXs each with different subcellular and tissue localisation, but all catalyse the reduction of H_2O_2 by using glutathione as an electron donor [97]. The loss of the lipid repair enzyme GPX4 has been shown to drive ferroptosis and the ferroptosis initiator RSL3 has been shown to inhibit GPX4, further supporting GPX4 as a central regulator of ferroptosis [98]. Antioxidant systems are crucial to maintain the healthy balance of cellular ROS, when these systems are disrupted ROS production can quintuple, and the cell enters a state of oxidative stress. Conversely, antioxidant systems can also be over active resulting in too little ROS, therefore unable to carry out its crucial role efficiently and the cell also enters oxidative stress [80].

Mutations in enzymes crucial to the antioxidant system have been described to cause different forms of MND. Mutations in the *SOD1* gene associated with ALS have been well documented, with over 180 different mutations being described [99]. A hallmark of *SOD1* associated ALS is the deposition of large insoluble *SOD1* protein aggregates in motor neurones as a consequence of structural

destabilisation and oxidative damage [100]. Misfolded wildtype SOD1 has been found widely in the cerebral spinal fluid of sporadic ALS, suggesting that SOD1 dysfunction is central to ALS pathogenesis [101]. Relatively few studies have been conducted on mitochondrial SOD2, due to it being vital for mitochondrial ROS defence as superoxide is unable to cross the mitochondrial membrane. Previous studies have shown that SOD2 mutant mice die in early postnatal life [102]. Another study investigated 77 sporadic ALS patients for mutations in *SOD2*, no mutations were found in the coding region of the gene, suggesting SOD2 mutations are not commonly associated with ALS [103]. The extracellular SOD3 is highly expressed in blood vessels and the lungs, and previous studies have shown that *SOD3* ablated mice lead to a 5-fold increase in lung superoxide and 85% mortality [104].

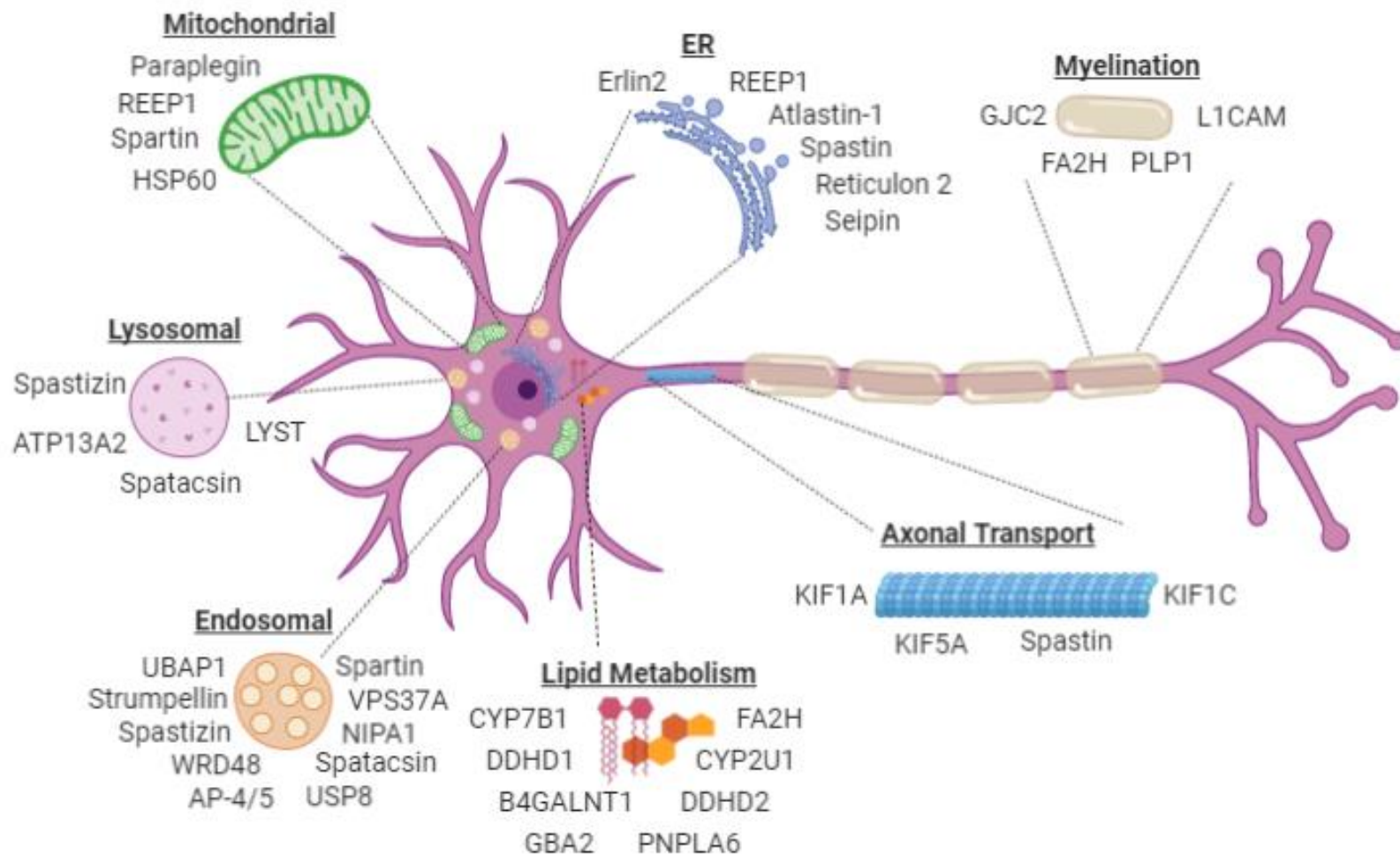


Figure 1.7. Schematic representation of a motor neuron showing the subcellular localisation/pathways of proteins associated with HSP. Made using BioRender.

1.4 Pathomolecular Themes in Hereditary Spastic Paraplegia

The genes responsible for HSP encode proteins localised to a range of organelles which function in a plethora of cellular roles. Figure 1.7 illustrates the subcellular localisation of some of these proteins which includes the ER, mitochondria, endosomes and lysosomes [44]. Despite HSP being extremely heterogeneous there are a few themes in which many known HSP proteins are commonly involved, including myelination, ER morphology, mitochondrial function, vesicular transport and lipid metabolism. While some genetic causes of HSP are well defined, the molecular basis of many forms of the condition remains unknown. A summary of the HSP associated genes mentioned in this section is in Appendix A.

1.4.1 Myelination

Neurones are the longest cell in the body with a length of up to 1m, providing a notable challenge for neuronal homeostasis involving the efficient and proper distribution of proteins, lipids and organelles whilst also executing their primary cellular function to transmit action potentials. The nervous system consists of two main cell types, neurones and glia for which there is thought to be ~85 billion of each in the human brain. The former are responsible for the majority of brain functioning, whereas the latter support the functioning of neurones by insulating them, and providing them with critical nutrients [12]. The insulation of axons is achieved by the covering of a lipid rich membrane called myelin that is produced by oligodendrocytes in the CNS, and Schwann cells in the peripheral nervous system. The term 'myelin' was first coined in 1854 by Rudolf Virchow derived from the Greek work 'myelos' (meaning marrow) [105]. The myelin sheath is divided into ~1mm long segments with 1nm in between the segments,

these 1nm long gaps are the nodes of Ranvier which increase the conduction velocity of action potentials along the axon [15]. Defects in myelination result in the inability to transmit action potentials as efficiently and mutations in genes encoding myelin proteins are known to cause HSP [106].

SPG1 (complicated, X-linked) was the first described HSP, found to be associated with mutations in the *L1CAM* gene encoding the L1 cell adhesion molecule glycoprotein that mediates cell-cell contacts crucial to promoting myelination [107]. The membrane proteolipid protein (PLP1), one of the major components of myelin, gives rise to SPG2 (complicated, X-linked) when mutated. A third HSP associated with myelin formation is SPG35 (complicated, AR) due to sequence alterations in the fatty acid-2 hydroxylase (FA2H) gene, FA2H converts free fatty acid into hydroxylated fatty acids which are then able to be incorporated into the myelin sheath, and its loss results in demyelination and enlarged axons [108]. A fourth gene associated with HSP (SPG44; complicated, AR) is the *GJC2* gene encoding connexin 47; connexins are critical to forming gap junctions and connexin 47 is specifically expressed in oligodendrocytes which can result in dysmyelination when dysfunctional [109]. Taken together, these findings show that defects in myelination, and not just the neurones directly, may result in defects in corticospinal tract function and HSP.

1.4.2 Endoplasmic Reticulum Morphology

Maintained ER morphology is critical to ensure that it is able to undertake its' primary functional roles efficiently, and alterations in ER structure are often seen in association with neurodegeneration. Three of the most common HSPs, SPG3 (atlastin-1), SPG4 (spastin) and SPG31 (REEP1; pure/complicated, AD), in addition to SPG12 (reticulon 2; pure, AD) are involved in maintaining ER

morphology [106]. Atlastin-1, REEP1 and spastin together form a molecular complex which is able to interact with microtubules and the ER to orchestrate ER shaping. Sequence alterations of these genes giving rise to dysfunctional/abnormal proteins have been seen to be associated with altered ER morphology [110]. Reticulon 2 has been shown to interact with spastin and contribute to ER shaping [111]. Other ER resident proteins are also associated with HSP including seipin (SPG17; complicated, AD) which localises to the ER but is involved in lipid droplet biogenesis (section 1.4.5) [112] and ERLIN2 (SPG18) which is involved in ER associated degradation [113].

1.4.3 Mitochondrial Structure and Function

Defects in mitochondrial function and morphology have emerged as a common cellular theme among HSP types, even if the associated gene does not directly encode a mitochondrial protein. The inner mitochondrial membrane protein paraplegin (SPG7; pure/complicated, AR) is a mitochondrial quality control protein with a role in the degradation of misfolded proteins [114]. A second mitochondrial quality control protein, HSP60 (SPG13), acts as a chaperone to fold imported mitochondrial proteins; sequence alterations in this gene have also been associated with pure AD HSP [115]. Two further mutations in proteins that are involved in mitochondrial protein translation have been described, SPG55/C12orf65 and SPG77/FARS2. Sequence alterations causative of complicated AR HSP in both genes result in the reduction of protein synthesis and defects in the respiratory complexes [44, 116]. Of the several kinesins associated with HSP when mutated, KIF5A (SPG10) has been shown to be involved in mitochondrial transport [117]. Sequence alterations dependant on the genetic region of the KIF5A gene that is impacted are also associated with

CMT2 and ALS [118]. These studies show that impairments in mitochondrial structure and function (in particular relating to the ATP synthesis), and mitochondrial transport, are associated with HSP as well as a number of other MNDs.

1.4.4 Subcellular Transport

Aberrant vesicular transport and endosomal dynamics are another pathomolecular outcome often implicated in HSP. Neurones have no rough ER within the axonal region, therefore no protein synthesis is undertaken in these regions. Consequently all proteins that are required within the axon must be transported from the soma. Given the unique morphology and length of neurones, this requires an efficient transport system to distribute proteins throughout the neurone [119]. Spartin (SPG20), associated with a complicated AR form of HSP, is a protein with multiple functions. A primary role for spartin involves interaction with the endosomal sorting complex required for transport (ESCRT), an evolutionarily conserved machinery required for protein sorting and membrane severing to regulate endosomal budding and scission [120]. Additional genes associated with HSP encode proteins that are involved with the ESCRT complex; these proteins include spastin (SPG4), UBAP1 (SPG80; pure AD), strumpellin (SPG8; pure, AD), and VPS37A (SPG53; complicated, AR) [106]. Two further clinically similar complicated AR HSPs, SPG11 (spatacsin) and SPG15 (spastizin), share a similar cellular theme of being involved in autophagic lysosomal reformation and the proteins are thought to be functional within the same functional complex [121]. Both spatacsin and spastizin have also been found to interact with the endosomal adaptor protein 5 (AP-5) and sequence alterations in the ζ 1 subunit are associated with

complicated AR SPG48. All subunits of another adaptor protein, AP-4, are also associated with complicated AR HSP (SPG47, SPG50-52); AP-4 is involved in trans-golgi to endosome transport of specific cargo proteins [122]. Sequence alterations in *Rab3GAP2*, encoding a protein which functions as an activating protein to the rab3 GTPase which itself is involved in mediating vesicular exocytosis, is associated with complex AR SPG69 [44]. Finally, another endosomal protein NIPA1 (SPG6; pure, AD) may function as an intracellular magnesium transporter [123].

Recently peroxisomal function has also been linked with HSP as cells derived from individuals with SPG4 have revealed reduced peroxisomal movement [124]. A further study has shown that spastin forms a tethering complex with the peroxisomal ABCD1 protein and lipid droplets to mediate fatty acid transport between the two organelles [125]. Mutations in the *ABCD1* gene are associated with X-linked adrenoleukodystrophy, in which spastic paraplegia is a presenting clinical feature [126].

1.4.5 Lipid Metabolism and Biosynthetic Pathways

Abnormalities in lipid metabolism are a common pathomolecular theme among neurodegenerative disorders, this is exemplified in the HSPs. Abnormalities in lipid droplet appearance and impairments in lipidomic pathways is a growing theme associated with neurodegeneration, and gene mutations causative of HSP. These pathways require membrane contact sites to facilitate the movement of lipids (and other molecules) between organelles so they can reach their site of action in addition to the enzymes crucial to these lipidomic pathways. As previously mentioned seipin (SPG17) localises to the ER, but it is also involved in lipid droplet biogenesis; given that the ER is a major site of lipid

synthesis and metabolism it is not surprising that there is a strong link between the two organelles. This functional link is highlighted by the molecular role of seipin which mediates ER-lipid droplet contact sites and facilitates the movement of triglycerides from the ER to lipid droplets [127]. Of particular note, recessively-acting sequence alterations in the *BSCL2* gene encoding seipin are also associated with a congenital generalised lipodystrophy, while dominantly-acting mutations may also cause dHMN in addition to HSP [128]. The multifunctional protein spartin (SPG20) is also involved in regulating lipid droplet biogenesis as it has been shown to bind to and regulate their size and number; spartin knockout mice have an increase in lipid droplet numbers [129, 130].

Growing numbers of enzymes crucial to lipid biosynthetic pathways are being shown to be associated with HSP. These enzymes include DDHD1 (SPG28; pure/complicated, AR), DDHD2 (SPG54; complicated, AR) and PNPLA6 (SPG39; complicated, AR) that are involved in phospholipid biosynthesis [131, 132]. Three forms of complicated AR HSP are due to sequence alterations in genes encoding enzymes involved in sphingolipid metabolism which includes B4GALNT1 (SPG26), GBA2 (SPG46) and FA2H (SPG35) [44]. A third common lipidomic theme in HSP is disturbances to fatty acid metabolism, the CYP7B1 (SPG5; complicated, AR) enzyme is involved in cholesterol metabolism and the CYP2U1 (SPG56; complicated, AR) enzyme is involved in fatty acid hydroxylation [133, 134]. Chapter five of this thesis will explore common dysfunctional lipidomic pathways underlying HSP.

These examples of proteins associated with HSP shows that there is a vast range of cellular dysfunction that results in a similar phenotype. Despite the diverse subcellular roles of individual molecules that localise to different organelles, many coalesce around the same molecular processes commonly

implicated in HSP and MND. These molecular processes are executed in multiple subcellular regions requiring a myriad of scaffolds, chaperones, transporters, organelle contact sites and auxiliary molecules facilitating these pathways.

1.5 Treatment in Hereditary Spastic Paraplegia and other Motor Neurone Diseases

Currently, there are no treatments for MNDs that have significant clinical benefit in terms of preventing or reversing neuronal degeneration. The drugs riluzole and edaravone have been approved for the treatment of ALS, although provide only a limited improvement and may slow disease progression. Riluzole suppresses excessive motor neurone firing by blocking glutamatergic neurotransmission and edaravone suppresses oxidative stress [26]. During clinical trials riluzole was found to increase the life of patients with ALS by an average of 3 months and edaravone was shown to decrease the rate of decline in physical function by 33% [135].

Currently treatment for HSP is largely symptomatic. An individual's day-to-day quality of life may be improved by the management of spastic symptoms including physiotherapy and oral antispasmodics such as baclofen and tizanidine, and botulinum toxin injections may be utilised to target specific muscle groups [46]. Functional electrical stimulation has been shown to improve gait disturbances with an increased walking speed and a reduction in falls [136].

The lack of MND therapies and its increasing prevalence has instigated many areas of therapeutic research. CuATSM is an orally administered compound that delivers copper to the SOD1 enzyme in unhealthy cells to subsequently

increase ROS elimination. It has had promising results in animal studies where SOD1 mutant mice have a significantly extended lifespan and now the drug is in stage II of ALS clinical trials in Australia [137, 138]. Due to mitochondrial dysfunction being common to many neurodegenerative disorders, protecting mitochondrial function has become a potential therapeutic target. To protect mitochondria both oxidative stress and mitochondrial apoptotic pathways have been highlighted for therapeutic intervention [139]. Motor neurone replacement and stem cell transplants are another area of research, however due to the long distances that the neurones cover this is an ambitious therapeutic option. Although, the generation and transplantation of support cells to protect existing motor neurones from undergoing degeneration may be more realistic [140].

A better understanding of the biological pathways underlying MNDs is crucial to pave the way for the development of new therapeutic targets and drug discovery.

1.6 The Amish

1.6.1 History and Way of Life

The Amish are a group of Anabaptist (a belief in adult baptism) Christians whose history dates back to the 16th century. The Anabaptist movement began in 1525 in Switzerland by a small group of Christians who insisted on adult baptism; this movement soon spread into neighbouring countries and many followers of this movement called themselves Mennonites after one of the leaders, Menno Simons. In 1693 the Amish diverged from this group under the leadership of Jakob Ammann who implemented innovative and stricter practices due to his belief that the Mennonites displayed a lack of discipline. These practices

included the prohibition of trimming of beards, or the wearing of fashionable clothes, and the shunning of individuals who had been excommunicated from the church. The practice of shunning includes avoiding the individual, refusing goods and not sharing meals with them; shunning is not intended to be a punishment, instead used to show an individual that they need to repent for their sins. Those who decided to follow Jakob Ammann were known as the Amish, and referred to as the 'plain people' based on their appearance [141].

The spread of Anabaptism in Europe unfortunately led to widespread persecution and isolation of these communities. This persecution subsequently resulted in the Amish and other Anabaptists wanting to start afresh in the New World. The migration of the Amish community from Europe to the United States of America and Canada started in the early 18th century. The first significant wave was in 1737 with 21 Amish families setting sail on the Charming Nancy ship from Rotterdam to Philadelphia. The positive reports from these original families paved the way for the Amish in Europe to follow in their footsteps and migrate to North America. By the mid-19th century around 3000 Amish individuals had settled in America, predominantly in the states of Pennsylvania, Ohio and Indiana. Today although there are Mennonite communities in Europe, there are no Old Order Amish and the last Amish church in Europe closed in 1937 [142].

Since the first Amish migrated to North America there has been a huge population expansion with 126,000 Amish in 1992 compared to >325,000 in 2018; the population roughly doubles every 20 years [143]. The reason for the rapid population expansion is due to large family sizes with parental couples typically having 5-10 children, and the Amish faith has a high retention rate of ~90% [144]. The Amish mostly live in small tightly-knit church groups typically

consisting of up to 20-30 families [144]. In the last few decades the population expansion has led to many settlements being formed in states outside of the MidWest, and the Amish now also have settlements in South America and Canada [143].

Today's Amish population are primarily farmers who live lives of simplicity, resisting modern advancements including electricity and motorised vehicles, instead opting for the horse and buggy as their primary mode of transport [145]. While the use of telephones is becoming increasingly popular (although mostly associated with employment) the possession of televisions, bicycles, and modern vehicles are forbidden as they detract from their beliefs [142]. Formal education within the Amish is limited to the eighth grade (age 13-14), which typically takes place in-one room parochial schools. Traditionally the Amish have not used modern medicine and instead use alternative approaches including homeopathic and natural treatments in-line with their religious beliefs [145]. In recent years the Amish have been more accepting of modern medicine and science, however, they rely on financial (community) aid to support medical costs as they do not pay taxes and they do not believe in purchasing health care insurance [142].

1.6.2 The Genetic Architecture of the Amish

The migratory bottleneck followed by subsequent population expansion of the Amish community has resulted in reduced genetic diversity and a unique genetic distinctiveness, which involves the enrichment of certain gene mutations that are otherwise rare (Figure 1.8). While this 'founder effect' may lead to a higher incidence of certain genetic diseases, other disorders present elsewhere globally may be rare or even absent in the Amish. The term founder effect was first introduced in 1942 by Ernst Mayr, who determined that the loss of genetic

variation may give rise to a genetically and phenotypically different founder population distinct to that of the original population [146].

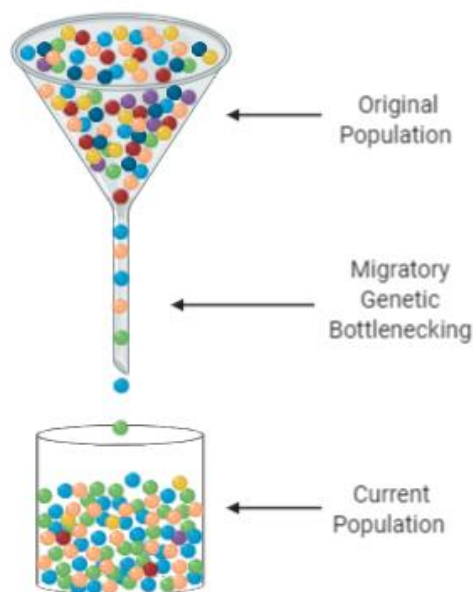


Figure 1.8. Genetic bottleneck resulting in the founder effect. The coloured balls represent genes, the genetic variation in the original European population is much greater than the American founder population and an enrichment in specific genes can be seen in the founder population. Made using BioRender.

The investigation of genetic conditions within the Amish community began in the early 1960s by Professor Victor McKusick, who was interested in understanding the frequency and causes of dwarfism which at that time were recognised to be due to inherited factors. The high incidence of dwarfism in the Amish led him to consider that there would be value in studying inherited disorders which are present in large family settings (such as in the Amish), in order to learn more about those conditions. In collaboration with his then PhD student Dr Harold Cross, McKusick subsequently investigated the types and frequencies of neurodevelopmental delay and motor neurone conditions in the Ohio Amish community, leading to their description in the medical literature of a number of new conditions [147]. This included two novel forms of HSP; Troyer syndrome

and Mast syndrome [148, 149]. It wasn't for another 25 years, during which genetic technologies advanced significantly, that the precise genetic causes of these (and other) conditions was discovered, as part of the Windows of Hope project now based at the University of Exeter (see section 1.6.3 below) [150, 151].

Importantly, almost all disorders (rare or common) originally described in the Amish community have subsequently been identified in non-Amish families globally, underscoring the importance of genomic studies in a community setting. For example, studies of cystic fibrosis in the Amish were crucial to the ultimate identification of the cystic fibrosis causative gene [147, 152].

1.6.3 The Windows of Hope Project (WoH)

The Windows of Hope Project is a non-profit research study that works alongside regional healthcare workers to define the genetic basis of genetic disorders within Anabaptist communities, in order to aid disease diagnosis and improve patient care. The roots of this project began in 2000 when Professor Andrew Crosby and Professor Harold Cross collaborated to investigate the genetic causes of Troyer and Mast syndromes first described in the 1960s by Cross/McKusick, leading to the discovery of those genes [148, 149]. Subsequently the research team identified genes responsible for many other hereditary conditions within Anabaptist communities, including other forms of HSP/spasticity and MNDs (see section 1.7 below). The current day WoH project is based in Exeter and co-led by Prof Crosby and Dr Emma Baple, and collaborates closely and is primarily based locally within regional clinics (e.g. New Leaf Centre for Special Children), aiding them in their mission to provide specialist diagnostic, counselling and healthcare services for Amish children and families with inherited disease. To date, this project has identified and

described over 20 novel genetic disorders, and identified founder gene mutations responsible for >150 other known conditions previously unrecognised in Amish communities, greatly aiding the provision of diagnostic services locally [153].

1.7 Hereditary Spastic Paraplegia in the Amish

Two forms of complex HSP, Troyer syndrome and Mast syndrome, were among the first neurological abnormalities to be described within the Amish community, by McKusick and Cross [148, 149]. Troyer syndrome is a slowly progressive autosomal recessive complicated form of HSP, characterised by spastic paraparesis, dysarthria, symmetrical amyotrophy and skeletal abnormalities, with developmental delay [154]. Within the Amish community Troyer syndrome is the result of a single nucleotide deletion (NM_015087.4: c. 1110delA; (p.Lys370Asnfs*30)) in the *SPG20* gene encoding the protein spartin [150]. Troyer syndrome due to different sequence alterations in the *SPG20* gene have since been reported in Omani, Turkish, Filipino, Saudi and Moroccan individuals [155, 156]. Subsequent studies have revealed spartin to be a multifunctional protein including a role in lipid droplet turnover and interacting with cardiolipin in the mitochondrial membrane [157, 158]. Mast syndrome is another progressive complicated autosomal recessive HSP, in which HSP is accompanied by more global neurodegeneration and dementia with symptoms often presenting in the third decade of life [151]; more details of this condition are provided in chapter four of this thesis.

A third autosomal recessive complicated form of HSP present amongst the Amish is GM2 synthase deficiency (SPG26), associated with mutations in the

B4GALNT1 gene [159]. This condition was originally described within the Amish community by WoH, and has since been widely reported worldwide [160, 161]. Affected individuals present with progressive weakness and spasticity in addition to developmental delay and cognitive impairment often within the first two decades of life [159, 162]. GM2 synthases are involved in the second step of ganglioside biosynthesis, and defects in the wider glycosphingolipid family entail a well-known group of lysosomal storage disorders [162]. Interestingly, an inherited disorder arising from defects in the first step of ganglioside biosynthesis, catalysed by GM3 synthase (*ST3GAL5*), was also discovered among the Amish by the WoH team, associated with a severe epileptic disorder and spasticity due to a substitution mutation (c.694C>T) in this gene [163].

A condition associated with mutations in the *MTPAP* gene originally described within the Amish community by the WoH team presents as a form of complex HSP. This condition presents in childhood and is characterised by cerebellar ataxia, spastic paraparesis, dysarthria, optic atrophy and learning difficulties. The *MTPAP* gene encodes the mitochondrial poly(A) RNA polymerase which is required for the regulation of mitochondrial encoded genes [164].

A final HSP within the Amish community, due to mutations in *CYP2U1*, encoding the cytochrome P450 2U1, result in a rare complicated autosomal recessive form. Mutations in *CYP2U1* were originally described in 2012 by *Tesson et al* associated with HSP in individuals with Italian, Egyptian, Spanish and Vietnamese ancestry [165]. The condition was subsequently named SPG56 in line with the then HSP naming system, and further individuals with different ancestry have been diagnosed with SPG56 [133]. Individuals present with childhood onset spastic paraplegia, upper extremity dystonia and cognitive impairments. MRI imaging shows corpus callosum thinning and white matter

lesions in some cases [165]. The CYP2U1 enzyme is predominantly found in the brain and liver, and is thought to localise to the ER and mitochondria to hydroxylate fatty acids [133]. SPG56 gene mutation has also recently been found by our group within the Amish community (Prof Crosby, personal communication and unpublished).

1.8 Aims of this Thesis

Despite the discovery of the genetic causes of many forms of HSP, a robust scientific understanding of the molecular roles of the proteins that these genes encode is often lacking. The overarching aim of this thesis is to further scientific understanding of the pathomolecular basis, in particular the role of lipidomic imbalance, in HSP. The specific aims include:

1. Defining the genetic cause of disease in an Amish individual with clinical features overlapping those of complex HSP (subsequently diagnosed as NBIA), and in doing so explain the mechanistic basis of dominantly / recessively acting genetic variants in *C19orf12*, found to be responsible for the condition,
2. Developing an SH-SY5Y knockout cell model of SPG21 (maspardin) using CRISPR-Cas9 gene editing alongside undertaking a range of molecular studies to provide more detailed understanding of the biological role of this molecule, and the pathomolecular basis of Mast syndrome,
3. To develop the methodology required to confirm lipidomic imbalance as a common pathomolecular theme in HSP, and explore the molecular basis of this disease mechanism.

Chapter 2

Materials and Methods

Materials and Methods

2.1 Buffers, Reagents and General Consumables

General purpose chemicals and reagents were purchased from Fisher Scientific and Sigma-Aldrich.

General consumables and plasticware for tissue culture were purchased from Greiner Bio-one and Fisher Scientific. Cell culture media, serum, antibiotics and trypsin were obtained from Lonza or GIBCO. Cell staining and assay kits were purchased from Abcam.

Kits from Qiagen were used for all plasmid DNA work, whereas for DNA extraction the kit was purchased from Invitrogen. All restriction digests and their relevant buffers were obtained from either Promega or New England Biolabs.

Where appropriate, all other reagents and specialist kits are indicated in text where they were acquired from.

Table 2.1 indicates the composition of buffers and solutions used in this project.

Table 2.1. Buffers and solutions.

Buffer	Composition
	Cell Culture and Staining
3T3 Medium	10% (v/v) heat-inactivated calf serum with 1% (v/v) penicillin-streptomycin solution in DMEM
SH-SY5Y Medium	10% (v/v) heat-inactivated fetal bovine serum with 1% (v/v) penicillin-streptomycin solution in DMEM/F-12 GlutaMAX Supplement
HEK Medium	10% (v/v) heat-inactivated fetal bovine serum with 1% (v/v) penicillin-streptomycin solution in DMEM
Filming Medium	10% (v/v) heat-inactivated fetal bovine serum with 1% (v/v) penicillin-streptomycin solution in phenol red free DMEM/F-12 GlutaMAX Supplement
Freezing Medium	20% (v/v) serum, 10% (v/v) DMSO in appropriate DMEM
4% PFA	4% (w/v) paraformaldehyde, in PBS adjusted to pH7.4

Lysine Block	5% (v/v) horse serum, 5% (v/v) goat serum, 50 mM poly-D-lysine, 0.2% (v/v) Triton X-100
FACS Buffer	1% FBS (v/v) in PBS
Propidium Iodide Solution	20µg/µl propidium iodide in FACS buffer
Gel Electrophoresis	
TAE	40 mM Tris-base (pH 7.6), 20 mM acetic acid, 1 mM EDTA
6x DNA loading Buffer	30% (v/v) glycerol, 0.25% (w/v) bromophenol blue, 0.25% (w/v) xylene cyanol
Western Blotting	
Lysis Buffer	20mM Tris HCl, 150mM KCl, 0.1% (v/v) Triton X-100, protease and phosphatase inhibitors
3x SDS Sample Buffer	10% (v/v) glycerol, 2% (w/v) SDS, 5% (v/v) β-mercaptoethanol, 0.002% (w/v) bromophenol blue, 0.125M Tris-Cl (pH 6.8)
Running Buffer	25 mM Tris-base, 192 mM glycine, 0.1% (w/v) SDS
Transfer Buffer	25mM Tris-base, 192mM glycine, 0.1% (w/v) SDS, 20% (v/v) MeOH
TBS	20mM Tris-Cl, 150mM NaCl
TBS-T	20mM Tris-Cl, 150mM NaCl, 0.1% (v/v) Tween-20
Blocking Solution	5% (w/v) semi-skimmed milk in TBS-T
Co-Immunoprecipitation	
Wash Buffer	20mM Tris (pH8), 150mM KCl, 0.1% (v/v) Triton X-100, protease and phosphatase inhibitors
Elution Buffer	25% 4x NuPAGE sample buffer and 2% (v/v) 10% β-mercaptoethanol.
Bacterial Culture	
LB Agar	15 g/L agar, 10 g/L tryptone, 10 g/L NaCl, 5 g/L yeast extract
LB Broth	10 g/L tryptone, 10 g/L NaCl, 5 g/L yeast extract
100x SOC	2M glucose, 1M MgCl ₂ , 250 mM KCl, sterilised by push filtration with a 0.2µm pore size
SOC Medium	1x SOC in LB broth
Ampicillin	100 U/ml
Kanamycin	50 µg/ml

2.2 General Cell Culture

The 3T3 mouse fibroblast cell line (American Type Culture Collection) was grown in Dulbecco's Modified Eagle Medium (DMEM) supplemented with penicillin (100U/ml) and streptomycin (100µg/ml) antibiotics and 10% (v/v) calf serum. The human embryonic kidney (HEK) 293 cell line (Sigma-Aldrich) was

grown in DMEM supplemented with penicillin (100U/ml) and streptomycin (100µg/ml) antibiotics and 10% (v/v) foetal bovine serum. The SH-SY5Y human neuroblastoma cell line (American Type Culture Collection) was grown in DMEM/F12 with GlutaMAX supplement further supplemented with penicillin (100U/ml) and streptomycin (100µg/ml) antibiotics and 10% (v/v) foetal bovine serum. Cells were incubated at 37°C with 5% carbon dioxide in their relevant media and passaged when confluent using 1ml trypsin for 10cm plate detachment. All media, PBS and trypsin were warmed to 37°C in either a water or bead bath prior to use. General cell culture was carried out in a class 2 biological safety cabinet with general aseptic technique adhered to.

2.2.1 Cell Storage

For long term storage of cell lines, cells were first grown to 70-80% confluency, washed with PBS, trypsinised for 5 minutes, the trypsin was neutralised by the addition of serum-containing growth medium and then centrifuged at 1,000g for 5 minutes. The cell pellet was then resuspended in 1ml freezing medium containing the appropriate serum and DMEM required for the cell line and transferred to a cryovial. Cryovials were placed into a Mr Frosty freezing container (Thermo Scientific) to allow controlled rate freezing in a -80°C freezer at -1°C per minute to ensure cell preservation. After 24 hours cryovials were then transferred to a liquid nitrogen cell storage tank for long term storage.

For cell recovery, cells were thawed in a 37°C water bath, placed into a 50ml tube with 9ml cell culture media and centrifuged at 1000g for 5 minutes. The cell pellet was then resuspended in 10ml cell culture media and transferred to a 10cm cell culture dish.

2.3 Immunocytochemistry

Immunocytochemistry is a common technique used to visualise specific proteins by using an antibody to target the protein of interest. The primary antibody that targets the protein is then bound to by a secondary antibody with a fluorophore which can be visualised by microscopy.

2.3.1 Cell Seeding and Transfection

For immunocytochemistry cells were subcultured using trypsin detachment and seeded onto acid-etched 13mm glass coverslips. The number of cells seeded varied between cell types; typically, 150-250,000 cells were seeded into a 3.5cm diameter cell culture dish.

24 hours post seeding, if transfection was required, a transfection mixture was prepared using 4.5µl of Lipofectamine LTX (Invitrogen) with 2.5µg of plasmid DNA for a single transfection or 1.5µg of each plasmid DNA for a double transfection in 500µl DMEM. This mixture was inverted several times and incubated at room temperature for 30 minutes before being added to the relevant cell culture dish. This mixture was sufficient for a 3.5cm diameter cell culture dish and it was scaled up or down for other plate sizes.

2.3.2 Nucleofection

In preparation supplement was added to nucleofector solution and reagents were warmed to 37°C. First, the cells were washed with Hanks' balanced salt solution (HBSS), trypsinised, pelleted at 1000g for 5 minutes, resuspended in HBSS and counted. The appropriate number of cells per experimental condition were then centrifuged in a microcentrifuge tube and resuspended in 100µl of nucleofector solution. 1µg of plasmid was added and mixed, and then this solution was transferred to a nucleocuvette, ensuring the sample covered the bottom of the cuvette. This cuvette was then placed into the 4D-nucleofector X

unit and nucleofected. The cuvette was incubated for 10 minutes at room temperature and then resuspended in the appropriate cell media, plated onto a cell culture dish and incubated at 37°C.

2.3.3 Cell Fixing

If cells were required to be stained with a vital dye this was performed before fixing. Mitotracker Red (Invitrogen) was diluted 1:2000 in DMEM and incubated for 15 minutes at 37°C, Nile Red (Abcam, ab228553) lipid droplet stain was diluted 1:500 in the provided staining buffer and incubated for 20 minutes at 37°C, and lysosome stains (Abcam, ab112137 and ab176824) were also diluted 1:500 in the staining buffer provided or phenol free media and incubated for 20 minutes at 37°C. Cells were washed with PBS, fixed for 15 minutes with 1ml prewarmed 4% paraformaldehyde, and then washed three times with PBS. The fixed coverslips were then kept in PBS and stored at 4°C until staining.

2.3.4 Cell Staining

Upon mounting the coverslips onto a staining dish peg, the coverslips were washed twice with 150µl PBS for 5 minutes at room temperature and all subsequent steps were carried out at room temperature. The cells were then blocked and permeabilised in lysine block for 20 minutes. The primary antibodies (Table 2.2) were diluted at the indicated concentration in 100µl lysine block then added to the coverslips for one-hour incubation. The coverslips were then washed again three times for 5 minutes with 150µl PBS before adding the appropriate Alexa Fluor secondary antibodies which were diluted 1:400 in 100µl PBS and incubated for a further hour. The secondary antibodies were then removed and replaced with 1:5000 4,6- diamidino-2-phenylindole, dihydrochloride (DAPI, Invitrogen) stain in 50µl PBS for 5 minutes. The coverslips were then washed three times for 5 minutes in 150µl PBS. Finally,

the coverslips were mounted onto microscope slides (VWR) using FluorSave mounting medium (Calbiochem) and left to cure overnight, in the dark at room temperature. Slides were then stored at 4°C until imaging.

2.4 Single Cell Sorting

Cells that were previously nucleofected with fluorescent plasmids were washed, detached with trypsin, centrifuged and the pellet was resuspended well in 1ml phenol-free media containing the appropriate amount of serum and antibiotics. 96-wells plates were also prepared with each well containing 100µl of the same phenol-free media. The cells were then single cell sorted by double positive fluorescence for cells nucleofected with two different plasmids, this was achieved by fluorescence-activated cell sorting (FACS) using a FACS Aria Flow Cytometer operated by Dr Mark Russell. Cells were sorted by double fluorescence, therefore those cells nucleofected with both a mCherry and GFP containing plasmid were individually seeded into a single well of a 96-well plate. In addition to single cells, 100 cells were seeded into three individual wells. A control plate was also prepared containing single cells that had no plasmid addition. The 96-well plates were then incubated and after 5 days 100µl of phenol red containing media was added to each well. Cells were then checked every few days and media changed until they reach 80-90% confluency where they were transferred to a 24-well plate and the DNA was extracted for genotyping. Each colony was subsequently grown into larger sized cell culture dishes until they reach a 10cm plate.

2.5 Live Cell Imaging Cell Preparation

100,000 cells were seeded onto glass-bottomed Fluorodishes (World Precision Instruments) and transfected with fluorescent plasmids 24 hours post-seeding. If cell staining was required, this was performed on the day of imaging. Half an hour before imaging, phenol-red media was replaced with phenol red-free media to prevent any interference when imaging.

2.6 Microscopy

Both fixed and live cell imaging was conducted on a Leica SP8 confocal microscope, with a cell incubation chamber at 37°C for live cell imaging. 63x oil immersion objective (numerical aperture = 1.40) and 20x dry objective (numerical aperture = 0.75) were used for imaging. Fixed images were acquired at 1024 x 1024 pixel resolution, whereas live cell time lapse images were acquired at 512 x 512 pixels. For fixed imaging the scan speed was set at 400Hz, whereas for live cell imaging it was increased to 700Hz. Both fixed and live cell imaging had the pinhole set at 1 Airy unit. For live cell imaging, images were captured at 5-9 second intervals over 2-6 minutes depending on the number of channels, in some cases images were acquired every 2 seconds for fast moving endosomes.

Table 2.2. Antibody incubation conditions.

Antibody	Host	Diluent	Stock Concentration	Western Blot Dilution	Immunocytochemistry Dilution	Supplier and Catalogue Number
Primary Antibodies						
ALDH16A1	Mouse	Milk	1mg/ml	/	1:100	Novus Biologicals (H00126133-B01P)
ATP5A	Mouse	Milk	1mg/ml	1:1000	1:100	Abcam (ab14748)
Calnexin	Rabbit	Milk	1mg/ml	1:1000	/	Abcam (ab22595)
Calreticulin	Rabbit	Milk	1mg/ml	1:1000	/	ThermoFisher Scientific (PA3-900)
Calreticulin	Mouse	Milk	1mg/ml	/	1:100	ThermoFisher Scientific (MA5-15382)
COX IV	Rabbit	BSA		1:1000	/	Cell Signaling Technology (4850P)
EEA1	Rabbit	BSA	Not specified	/	1:100	Cell Signaling Technology (C45B10)
Flag	Mouse	Milk	1mg/ml	1:1000	1:100	Sigma-Aldrich (F1804)
Flag	Rabbit	Milk	0.8mg/ml	1:1000	1:100	Sigma-Aldrich (F7425)
GAPDH	Mouse	Milk	1mg/ml	1:5000	/	Proteintech (60004-1)
Maspardin 407	Rabbit	Milk	0.2mg/ml	1:375	1:100	Atlas Antibodies (HPA040407)
Maspardin 436	Rabbit	Milk	0.4mg/ml	1:1000	1:100	Atlas Antibodies (HPA040436)
Maspardin 883	Rabbit	Milk	0.5mg/ml	1:500	1:100	Abcam (ab133883)
Mitofilin	Mouse	Milk	1mg/ml	/	1:100	ThermoFisher Scientific (45-6400)
PMP70	Mouse	Milk	1mg/ml	/	1:100	Novus Biologicals (NBP2-36770)
Rab7	Mouse	Milk	2.1mg/ml	1:2000	/	Abcam (ab50533)
Rab11	Rabbit	BSA	Not specified	1:1000	1:100	Cell Signaling Technology (D4F5)

SAMM50	Mouse	Milk	0.5mg/ml	/	1:100	Novus Biologicals (H00025813-M04)
Tubulin Beta 4α	Mouse	Milk	0.57mg/ml	1:1000	1:100	Novus Biologicals (NBP2-00812)
Secondary Antibodies						
Alexa Fluor Rabbit 488	Goat	/	2mg/ml	/	1:400	Invitrogen (A11034)
Alexa Fluor Mouse 488	Goat	/	2mg/ml	/	1:400	Invitrogen (A11029)
Alexa Fluor Rabbit 647	Goat	/	2mg/ml	/	1:400	Invitrogen (A21245)
Alexa Fluor Mouse 635	Goat	/	2mg/ml	/	1:400	Invitrogen (A31575)
DyLight 800 Rabbit	Goat	Milk	0.5mg/ml	1:5000	/	Invitrogen (SA5-10036)
DyLight 680 Mouse	Goat	Milk	1mg/ml	1:5000	/	Invitrogen (35519)
HRP Rabbit	Goat	Milk		1:5000	/	Sigma (A0545)
HRP Mouse	Rabbit	Milk		1:5000	/	Sigma (A9044)

2.7 Western Blotting

Western blotting is a widely used technique to detect specific proteins that have been electrophoretically separated according to their molecular mass. Western blotting was developed in 1979 by Towbin *et al* who showed that proteins can be transferred from polyacrylamide gels to nitrocellulose membranes by electrophoretic transfer for probing by antibodies [166].

2.7.1 Cell Lysate Preparation

Cells were seeded onto a 10cm cell culture dish and transfected if required, as previously described. Growth media was removed, cells washed with PBS and the culture dish placed onto ice. 500 μ l of cell lysis buffer containing the appropriate amount of complete protease and phosphatase inhibitors was added ensuring complete plate coverage and incubated on ice for 10 minutes. The culture dish was then scraped to ensure all cellular material fully dissociated and the lysate was collected in a microcentrifuge tube and

centrifuged at 18,800g for 10 minutes at 4°C. The supernatant was transferred to a fresh microcentrifuge tube and frozen.

2.7.2 Protein Quantification

Sample protein quantification was calculated using the Pierce bicinchoninic acid (BCA) Protein Assay Kit (Thermo Scientific) using bovine serum albumin (BSA) as a standard. This assay is based on colorimetric detection where proteins can reduce copper ions that chelate with BCA forming a purple-coloured complex that absorbs light at 562nm.

Protein standards ranging from 0.2-1.2µg/ul were prepared in a 96-well plate in triplicate by diluting 2mg/ml BSA in PBS. Samples were also prepared in triplicate and diluted 1:5 in PBS. A working reagent was prepared by mixing 50 parts of BCA Reagent A with 1 part of BCA Reagent B. 200µl of this working reagent was added to each well containing standards and samples. The plate was incubated for 10 minutes at room temperature whilst shaking on an orbital shaker (Grant). The absorbance was then measured at 562nm using a PHERAstar FS microplate reader (BMG Labtech). For data analysis the triplicate values were averaged, and the concentrations of each sample were calculated against the BSA standard curve.

2.7.3 Sample Preparation

Whilst on ice the samples were mixed with 3x SDS sample buffer and diluted with lysis buffer accordingly depending on the protein quantification and subsequent desired amount of protein. If protein normalisation was not required, the samples were diluted 2:1 with 3x sample buffer. Diluted samples were then briefly vortexed, boiled for 5 minutes at 95°C, briefly vortexed again and stored on ice until gel loading.

2.7.4 SDS-PAGE Protein Separation

Up to 30µl of samples were then loaded onto a 4% stacking and either a 10% or 12% separating sodium dodecyl sulphate polyacrylamide gel electrophoresis (SDS-PAGE) gel depending on the size of the protein of interest. Gels were often prepared the day before according to the recipe in Table 2.3 using a Mini-PROTEAN Tetra Handcast System and stored in running buffer at 4°C until use where they were allowed warm to room temperature. 5µl of BLUeye Pre-Stained Protein Ladder (Geneflow) was loaded as a protein size reference. The electrophoresis was performed in running buffer at 80V until the samples had run into the stacking gel and then 200V for the remainder of the run until the dye front reached the bottom of the gel. The gel tank was placed in a polystyrene box and packed with ice to ensure the gel would not melt while running.

Table 2.3. Acrylamide gel composition. These recipes are sufficient to make 2 gels.

Stock Solution	4% Stacking Gel	10% Separating Gel	12% Separating Gel
40% (w/v) acrylamide	0.7ml	6.3ml	7.5ml
1 M Tris-HCl pH 6.8	0.88ml	-	-
1.5M Tris-HCl pH 8.8	-	6.25ml	6.25ml
10% (w/v) SDS	0.07ml	0.25ml	0.25ml
10% (w/v) APS	0.07ml	0.125ml	0.125ml
ddH ₂ O	5.28ml	12.1ml	10.9ml
TEMED	7µl	17µl	17µl

2.7.5 Protein Transfer

After protein separation, gels were equilibrated in transfer buffer for 10 minutes. During this time an Immobilon-P polyvinylidene difluoride (PVDF) transfer membrane (Merck) was activated in methanol and equilibrated. The gel and membrane were sandwiched between Hybond blotting paper (GE Healthcare)

and sponges and placed into a transfer cassette. The transfer cassette was placed in the tank, filled with transfer buffer and run for 2 hours at 250mA to enable the efficient transfer of protein to bind to the PVDF membrane.

2.7.6 Antibody Incubation and Detection

After transfer, membranes were immediately incubated for one hour in 5% milk in TBS-T blocking solution to prevent non-specific binding of the antibodies.

Primary antibodies were diluted accordingly (Table 2.2) and incubated with the membrane rolling overnight at 4°C. Membranes were then washed with TBS-T three times for 5 minutes. After washing the membranes were then incubated with the appropriate secondary antibody for 1 hour at room temperature in the same diluent used for the primary antibody incubation. Blots were then washed 3 times for 15 minutes in TBS-T and immediately imaged if fluorescent DyLight secondary antibodies were used. Some blots were detected using the Pierce enhanced chemiluminescence (ECL) Western blotting substrate (Thermo Scientific). The ECL detection method was used with horseradish peroxidase conjugated secondary antibodies. To prepare the chemiluminescent substrate equal parts of Detection Reagents 1 and 2 were mixed; 350µl of this mixture was required for each blot. The blots were placed in a plastic autoclave bag, the ECL substrate added, the bag was then sealed and incubated for 5 minutes before immediately visualising the blot. In some cases blots were then re-probed with GAPDH, a commonly used control for normalising protein expression.

Fluorescent blots were visualised using the CLx imaging system scanner (LI-COR Bioscience). Blots detected with ECL first had the protein ladder marked using a Glow Writer pen (Diversified Biotech) and visualised on a C-DiGit scanner (LI-COR Bioscience).

2.8 Binding Partner Analysis

The binding partners of both endogenous and overexpressed transfected maspardin was analysed in duplicate by first performing co-immunoprecipitation and then these samples were analysed by liquid chromatography-mass spectrometry.

2.8.1 Cell Lysate Preparation

For each experimental condition three 10cm plates of HEK 293 cells were grown to 80% confluency, and each condition was carried out in duplicate. For the overexpressed maspardin group these cells were transfected with SPG21-Myc-FLAG plasmid, as detailed in the immunocytochemistry method section. For cell lysis, each plate was washed with PBS, trypsinised, and each experimental condition pooled into a 50ml tube and centrifuged for 5 minutes at 1000g. The cell pellet was then resuspended in 1.2ml of chilled lysis buffer containing the appropriate amount of complete protease and phosphatase inhibitors, transferred to a microcentrifuge tube and rotated for 30 minutes at 4°C. The cell lysates were then centrifuged at 21,000g for 15 minutes at 4°C. The supernatant was transferred to a fresh microcentrifuge tube and frozen at -80°C until required for co-immunoprecipitation.

2.8.2 Co-immunoprecipitation

Magnetic Dynabeads (Invitrogen) were used to bind the relevant antibody which themselves bind to the protein of interest. The antibody's Fc region binds to the Dynabeads Protein G which is attached to the beads. First, the Dynabeads were prepared by resuspending the beads and transferring 50-100µl of beads, per sample, to a fresh microcentrifuge tube. The tube was placed onto a magnet and the supernatant removed. Antibodies were diluted in 200µl of PBS containing 0.02% Tween and added to the beads, then incubated with rotation

for 1 hour at room temperature to allow the antibodies to bind. The tube was then again placed onto the magnet and supernatant removed and discarded. The tube was removed from the magnet and beads washed with 200µl of PBS containing 0.02% Tween by gentle pipetting and wash solution discarded.

The next step was to immunoprecipitate the target antigen. The cell lysates that were previously prepared were added to their respective tubes and incubated for 2 hours, with rotation, at 4°C to allow the antigen to bind the magnetic bead-antibody complex. The tube was then placed onto the magnet once again and the supernatant was removed and stored at -20°C to use as a negative control in order to assess the efficiency of protein binding. The beads were washed three times with 200µl of washing buffer with a final resuspension in 100µl of washing buffer and transferred to a fresh microcentrifuge tube.

The final step was to elute the target protein from the antibody and magnetic beads. The tube was placed onto the magnet and supernatant removed. 50µl of denaturing elution buffer was added and the beads were carefully resuspended. This solution was then heated to 70°C for 10 minutes to dissociate the Dynabead-antibody-antigen complex. The tube was placed on the magnet, and supernatant transferred to a clean tube and stored at -20°C. The eluted samples were then probed by Western blot, alongside the collected negative controls.

2.8.3 Mass Spectrometry

Samples for binding partner analysis were sent to the University of Bristol Proteomics Facility for liquid chromatography-mass spectrometry and the data obtained was filtered at a 5% false discovery rate. The returned data included a score for each protein detected by mass spectrometry based upon the number of that protein, the number of unique peptides sequences and the number of

peptide fragments detected in each sample. For data analysis the samples were analysed for common protein hits in the duplicate samples and then any hits found in the control samples were removed.

2.9 PCR and Sequencing

Polymerase chain reaction is an *in vitro* method first developed in the 1980's for amplifying specific regions of DNA [167]. Three main steps, denaturation, primer annealing and extension, are involved in the amplification of DNA where a minute starting material can be amplified to millions of copies.

2.9.1 Primer Design

The genetic region of interest was first obtained from Ensemble Genome Browser using the Genome Reference Consortium human genome 38 [168]. For PCR amplification primers were designed using the Primer3Plus software version 2.4.2 [169]. Primers were chosen to have similar melting temperatures, a length of 18-24 bases and where possible a guanine-cytosine base content lower than 60%. The UCSC Genome browser was then used to ensure the primers would not bind elsewhere in the human genome by using the BLAT genome search tool, in addition to checking that there were no significant SNPs within the primer binding region [170, 171]. A list of all primers used, and their relevant annealing temperatures are in Table 2.4.

Table 2.4. Primer sequences.

Application	Primer Orientation	Sequence	Annealing Temperature
SPG21 cDNA	Forward Primer	TTTCAGCTAATCATGGGAGAGA	58°C
	Reverse Primer	AAAAAGCCTCCCAAAGAAGC	
SPG21	Forward	GGTGTGAGCTCCAGGTTACC	59°C

Exon 3	Primer		
	Reverse Primer	CTCTGTGTGACCGTGGACTC	
SPG21 Exon 5	Forward Primer	TGAAGCAACTTTTTAATACTCAGGT	59°C
	Reverse Primer	TCCCTTCCTAATGTACCAAACACT	
YFP-SPG21 Cloning	Forward Primer	ATATAGATCTATGGGAGAGATTAAA GTCTCTC	63°C
	Reverse Primer	ATTAGTCGACTGCTCCTCCTGGCTG ATGCC	
C19orf12	Forward Primer	ATCATACTGGATCTCGGCC	62°C
	Reverse Primer	CTCATGGTGATGGTGGTGTG	

2.9.2 PCR Master Mixture Preparation

A mixture containing all the vital components needed for DNA amplification other than the DNA itself were first assembled into a 'master mix'. This mix consisted of forward and reverse primers, Dream Taq Green buffer, Dream Taq DNA polymerase and distilled water, a standard mix for one reaction is shown in Table 2.5. In some cases, Pfu DNA polymerase with its complimentary buffer was used instead of Taq polymerase. This master mix was then aliquoted into 0.2ml PCR tubes and DNA added to give an overall volume of 10 μ l. At least one tube substituted DNA for water as a negative control to confirm the absence of contamination.

Table 2.5. PCR reaction mixture.

Component	Volume	Source
Forward Primer (100μM)	0.4 μ l	IDT
Reverse Primer (100μM)	0.4 μ l	IDT
dNTP (10μM)	0.4 μ l	Solis BioDyne
Dream Taq Polymerase	0.1 μ l	Thermo Scientific
Dream Taq 10x Buffer	1 μ l	Thermo Scientific
Water	6.7 μ l	/
DNA	1 μ l	/

2.9.3 PCR Cycling Conditions

Cycling conditions were optimised for each primer pair by performing a gradient PCR to determine the optimum annealing temperature. A touchdown PCR approach was used where annealing temperatures decreased by 2°C for two PCR cycling stages until the previously optimised annealing temperature (TD) is reached for the final cycling stage which consists of 35 cycles. The denaturation and extension temperatures were kept the same for each PCR reaction at 95°C and 72°C, respectively. The extension time for each reaction was determined by the PCR product size, whereas the denaturation and annealing stages were kept constant at 30 seconds. PCR cycling conditions are in Table 2.6.

Table 2.6. PCR cycling conditions.

Stage	Step	Time	Temperature	Cycles
1	Denaturation	30 Seconds	95°C	2
	Annealing	30 Seconds	TD+4°C	
	Extension	Variable	72°C	
2	Denaturation	30 Seconds	95°C	2
	Annealing	30 Seconds	TD+2°C	
	Extension	Variable	72°C	
3	Denaturation	30 Seconds	95°C	35
	Annealing	30 Seconds	TD	
	Extension	Variable	72°C	

2.9.4 Agarose Gel Electrophoresis

Gel electrophoresis was used to determine if the PCR product that had been amplified was of the desired size, in addition to checking for contamination. The percentage of agarose was altered depending on the PCR product size, a lower percentage gel was used for larger products whereas small PCR products used a higher percentage gel, typically containing 0.8% or 1.8% agarose. Either 0.8g or 1.8g of agarose powder was added to 100ml of 1xTAE and heated in a microwave until the agarose had dissolved. 5µl of ethidium bromide (Fisher

Scientific) or SYBR Safe (Invitrogen) was added to the mixture before pouring into a gel tray with a well comb until set.

If Pfu DNA polymerase was used then a 6x DNA loading buffer was added to the PCR mixture, whereas with Dream Taq Polymerase this was not needed as the buffer contained a density reagent and tracking dye. 2-5µl of PCR product was loaded into the gel with one lane containing an appropriately sized DNA ladder. The loaded gel was then run in 1xTAE buffer at 150V for around 30 minutes. After electrophoresis the gel was visualised under ultra-violet light and photographed.

2.9.5 PCR Product Clean-up

In order to sequence the PCR product, it first needs to be cleaned up by removing excess primers and dNTPs. This clean-up was achieved by ExoSAP, an enzymatic mixture containing both exonuclease I and shrimp alkaline phosphatase that degrade leftover primers and dNTPs. 2µl of ExoSAP was added to 5µl of PCR product and incubated at 37°C for 30 minutes. The PCR-ExoSAP mixture was then heated to 95°C for 5 minutes to deactivate the enzymes.

2.9.6 Sequencing

DNA sequencing was carried out by Source Bioscience using the dideoxy chain termination method to analyse the gene of interest. The 7µl post-ExoSAP purified PCR product in addition to 5ul of primers (10µM) was sequenced. The returned sequencing data was analysed using the sequence viewer software Chromas 2.6.

2.9.7 Whole Exome Sequencing

Trio exome sequence analysis was performed by in-solution hybridisation to biotin-labelled VCRome (version 2.1) on an Illumina GAIx sequencer or the Illumina HiSeq 2000 platform [172]. Reads were aligned to the human genome reference sequence (hg19) using BWA-MEM (v0.7.17), mate pairs were fixed and duplicates removed using Picard (v2.15). Insertion/deletion realignment and base quality recalibration were performed using GATK (v3.7.0). Single nucleotide variants and insertion/deletion polymorphisms were detected using GATK HaplotypeCaller and annotated using Alamut batch (v1.10). Read depth was determined for the whole exome using GATK DepthOfCoverage, conforming to GATK Best Practices. Called variants were filtered on call quality, population database allele frequency, presence in databases of pathogenic variants and inheritance pattern. Copy number variants were detected using both `ExomeDepth` (<https://cran.r-project.org/web/packages/ExomeDepth/vignettes/ExomeDepth-vignette.pdf> and <https://github.com/vplagnol/ExomeDepth>) and `SavyCNV` (<https://www.biorxiv.org/content/10.1101/617605v1> and <https://github.com/rdemolgen/SavvySuite>). Genome-wide single nucleotide polymorphism microarray analysis was performed, in order to assess candidate copy number variants and large scale genomic rearrangements, using Illumina's HumanCytoSNP-12 v2.1 beadchip array.

2.10 Nucleic Acid Extraction

2.10.1 DNA Extraction

DNA extraction from cell cultures was performed using a PureLink Genomic DNA Kit (Invitrogen) according to manufacturer's instructions. Cells were

harvested, centrifuged at 1000g for 5 minutes and resuspended in 200µl of PBS. 20µl of proteinase K and 20µl of RNase A was added, mixed and incubated for 2 minutes, followed by 200µl of Purelink Genomic Lysis/Binding Buffer which was added, mixed and incubated at 55°C for 10 minutes to lyse cells, digest proteins and remove RNA. 200µl of ethanol was added to the solution to precipitate the DNA. The lysate was added to a PureLink Spin Column and centrifuged at 10,000g for 1 minute to allow DNA binding to the silica-based membrane. The DNA was then washed with 500µl of Wash Buffer 1 and centrifuged at 10,000g for 1 minute, followed by 500µl of Wash Buffer 2 and centrifuged at full speed for 3 minutes to remove impurities. The DNA was then eluted in 50µl of Elution Buffer and DNA quantified.

2.10.2 RNA Extraction

Cultured cells were washed with PBS, trypsinised, suspended in 9ml media and pelleted by centrifugation at 1000g for 5 minutes. RNA extraction was performed using a Qiagen RNeasy Plus Mini Kit according to manufacturer's instructions. First, the cells were resuspended in 600µl Buffer RLT Plus containing β-mercaptoethanol, vortexed and the lysate was added to a gRNA Eliminator spin column and centrifuged at 8000g for 30 seconds to remove genomic DNA. 600µl of 70% ethanol was added to the RNA containing flow-through, mixed, and centrifuged in an RNeasy Mini spin column at 8,000g for 15 seconds to allow RNA to bind to the column's membrane. The column was then washed with 700µl Buffer RW1 and centrifuged at 8,000g for 15 seconds. The wash step was then repeated twice with 500µl Buffer RPE. Finally, the RNA was eluted by adding 40µl of RNase-free water to the membrane and centrifuged for 1 minute at 8,000g. RNA concentration was subsequently determined, refer to section 2.10.5.

2.10.3 cDNA Synthesis

Complementary DNA was synthesised from the previously extracted RNA using random primers and reverse transcriptase. First, 1µl RNA, 0.5µl random primers (500µg/µl, Promega) and 12.5µl nuclease free water was added to a PCR tube. This reaction mixture was heated in a thermocycler to 70°C for 5 minutes, followed by 4°C for 5 minutes to denature RNA secondary structures. To this mixture 5µl M-MLV buffer, 1.25µl dNTPs (10mM), 1µl M-MLV Reverse Transcriptase (200 U/µl) and 3.75µl ddH₂O was added. This mixture was left at room temperature for 10 minutes then incubated in a thermocycler at 55°C for 50 minutes followed by 70°C for 15 minutes. cDNA was stored at -20°C.

2.10.4 cDNA Sequencing

cDNA samples were diluted to a final concentration of 20-50ng/µl, amplified by PCR (using exonic primers), run on an agarose gel, cleaned-up by ExoSap and sent for sequencing as previously described.

2.10.5 Determining Nucleic Acid Concentration

Nucleic acids were quantified spectrophotometrically using a NanoDrop 8000 (Thermo Scientific) by measuring absorbance at 260nm in 1µl of sample and the quantity of nucleic acid was calculated by the Nanodrop software.

2.11 Plasmid Preparation

The use of plasmids as a tool in molecular biology made their mark in the 1970's when restriction enzymes and DNA ligases were discovered allowing us to insert genes into a vector, and insert this recombinant DNA into cells to promote the desired protein production [173-175]. The plasmids used in this study are outlined in Table 2.7.

Table 2.7. Plasmids used in this study and their corresponding use.

Plasmid	Function	Source
SPG21-myc-FLAG	Protein Expression	Gift from Dr John Chilton
Rab4-RFP	Protein Expression	Gift from Dr Giles Cory
Rab5-RFP	Protein Expression	Gift from Dr Giles Cory
mCh-Rab7A	Protein Expression	Addgene - 61804
Rab9-RFP	Protein Expression	Gift from Dr Giles Cory
Rab11-RFP	Protein Expression	Gift from Dr Giles Cory
pEYFP-N1	Cloning Vector	Clontech - 6006-1
pEGFP-C1	Cloning Vector	Clontech - 6084-1

2.11.1 General Bacterial Handling

Live bacterial cultures were handled within a designated category 2 biological safety cabinet using standard aseptic technique. When incubated all bacteria were incubated in a designated bacterial Innova 42 incubator at 37°C. Bacterial cultures and streak plates were stored at 4°C. When disposing of bacteria they were first decontaminated in ~1% Virkon overnight.

2.11.2 Bacterial Stab Cultures

Plasmids ordered from Addgene were shipped as transformed bacteria in a stab culture. Cultures were streaked out onto a LB agar plate containing the appropriate selection antibiotic and incubated overnight to allow single bacterial colonies to form.

2.11.3 Selecting and Growing Single Colonies

Single colonies were then selected and picked up using a pipette tip and the pipette tip was then put into individual bacterial culture tubes containing 5ml of LB broth with the appropriate selection antibiotic. The tubes were incubated at 37°C overnight, whilst shaking to allow bacterial cultures to grow.

2.11.4 Miniprep

A miniprep was performed using the QIAprep Spin Miniprep Kit to extract a small amount of plasmid DNA in order to identify colonies that contain the

correct recombinant clone. 1.5ml from the grown single colony was removed and centrifuged at 16,200g for 1 minute at room temperature. The supernatant was discarded, and the pellet was resuspended in 250µl of Buffer P1 (50 mM Tris-HCl, pH 8.0; 10 mM EDTA; 100 µg/ml RNase A, without LyseBlue reagent). To lyse the bacterial cells 250µl of Buffer P2 (200 mM NaOH; 1% w/v SDS) was added and then the microcentrifuge tube inverted 4-6 times. The DNA was precipitated by the addition of 350µl of Buffer N3 (a proprietary acetate-buffered solution containing chaotropic salt) and mixed immediately by inverting a further 4-6 times until the solution became evenly cloudy. This solution was centrifuged for 10 minutes at 16,200g. The supernatant was added to a QIAprep spin column and centrifuged for 1 minute at 16,200g to allow the plasmid DNA to bind to the silica membrane and the flow-through discarded. The spin column was then washed with 750µl of Buffer PE (proprietary solution with high ethanol and low salt concentrations), centrifuged for 1 minute at 16,200g, and the flow-through was discarded. The spin column was then centrifuged for a further minute at the same conditions to remove residual wash buffer. The spin column was then transferred to a clean microcentrifuge tube and the DNA was eluted by the addition of 55µl of molecular biology grade water, incubated for 1 minute, and finally centrifuged for 1 minute at 16,200g.

2.11.5 Restriction Digest

The plasmid DNA obtained by miniprep was digested by restriction enzymes to identify the colony with the desired plasmid clone. Restriction digests were performed using restriction enzymes and their appropriate buffer with the standard mixture components outlined in Table 2.8. The mixture was incubated in a water bath at 37°C for 1 hour. This digested plasmid DNA mixture was then mixed with 6x DNA loading buffer and visualised by gel electrophoresis.

Table 2.8. Components of a single and double restriction digest. Top: single digest. Bottom: double digest.

Component	Volume
Plasmid DNA (1µg/µl)	3µl
Enzyme	0.4µl
Buffer	1µl
ddH ₂ O	5.6µl

Component	Volume
Plasmid DNA (1µg/µl)	3µl
Enzyme A	0.4µl
Enzyme B	0.4µl
Buffer	1µl
ddH ₂ O	5.2µl

2.11.6 Colony Expansion

A colony that was confirmed to contain the desired plasmid, as determined by restriction digest was then grown on a larger scale in order to obtain a larger quantity of plasmid DNA for future applications. 50µl of bacterial culture was transferred to 50ml of LB broth containing the appropriate selection antibiotic and incubated overnight at 37°C overnight, whilst shaking.

2.11.7 Glycerol Stocks

800µl of the bacterial culture from colony expansion was transferred to a microcentrifuge tube combined with 200µl of glycerol and mixed by vortexing. This was then stored at -80°C for long term storage and when required the culture could be streaked out onto an agar plate and the plasmid DNA obtained once again.

2.11.8 Midiprep

To extract a larger quantity of plasmid DNA a HiSpeed Midi Prep Kit was used. The bacterial suspension grown in the colony expansion was transferred to a

50ml tube and centrifuged at 4700g for 15 minutes at room temperature to harvest the bacteria. The supernatant was discarded, and the bacterial pellet resuspended in 6ml Buffer P1. 6ml Buffer P2 was added, the mixture was inverted 4-6 times and incubated for 5 minutes at room temperature to lyse the bacterial cells. The lysed bacterial cellular debris was precipitated by the addition of 6ml Buffer P3 (3 M potassium acetate, pH 5.5), and again inverted 4-6 times. This solution was transferred to a QIAfilter Cartridge and incubated at room temperature for 10 minutes. During this incubation step a HiSpeed Tip was equilibrated with 4ml Buffer QBT (750 mM NaCl; 50 mM MOPS, pH 7.0; 15% v/v isopropanol; 0.15% v/v Triton X-100) which flowed through the tip and was discarded. A plunger was then inserted into the QIAfilter Cartridge and the cell lysate was filtered into the HiSpeed Tip and allowed to flow through. The HiSpeed Tip was washed with 20ml of Buffer QC (1 M NaCl; 50 mM MOPS, pH 7.0; 15% v/v isopropanol). The plasmid DNA was eluted into a fresh 50ml tube by the addition of 5ml Buffer QF (1.25 M NaCl; 50 mM Tris-HCl, pH8.5; 15% v/v isopropanol). The DNA was precipitated by the addition of 3.5ml isopropanol, mixed by inversion, and incubated at room temperature for 5 minutes. The precipitated DNA mixture was poured into a syringe with a QIAprecipitator Module attached to allow DNA binding and the alcohol removed by pushing air through the module with a syringe. The DNA was then eluted in 750µl of Buffer TE (10 mM Tris-HCl, pH 8.0; 1 mM EDTA) to protect the DNA from degradation.

2.12 Constructing a Fluorescently Tagged SPG21 Plasmid

2.12.1 DNA Insert and Vector Isolation

The SPG21 DNA fragment was obtained by PCR amplification from the SPG21-myc-FLAG plasmid, using the cloning primers outlined in Table 2.4 and Pfu

polymerase with a 2 minute extension time. The forward primer contains a BglII restriction site and the reverse primer contains a Sall restriction site for cloning; a gradient PCR was first performed to determine the optimal annealing temperature. The PCR reaction mixture is outlined in Table 2.9 and programme in Table 2.10.

Table 2.9. PCR reaction for obtaining an SPG21 cloning insert.

Component	Volume
Forward Primer (100µM)	1µl
Reverse Primer (100µM)	1µl
dNTP (10 µM)	1µl
Pfu Polymerase (3U/µl)	0.5µl
Pfu 10x Buffer	5µl
ddH ₂ O	40.5µl
DNA	1µl

Table 2.10. PCR programme for obtaining an SPG21 cloning insert.

Stage	Time	Temperature	Cycles
Initial denaturation	2 minutes	95°C	
Denaturation	30 Seconds	95°C	35
Primer annealing	30 Seconds	63°C	
Extension	3 minutes	72°C	
Final Extension	5 minutes	72°C	

The PCR product was then mixed with 6x DNA loading buffer, run on a 0.8% agarose gel containing SyberSafe at 90V to ensure the PCR was successful and the product was of the expected size. The remainder of the PCR product was then cleaned up using a Qiagen QIAquick PCR purification kit according to manufacturer's instructions. In brief, Buffer PB was added to the PCR reaction at a 5:1 ratio, and the pH was adjusted if required with 3M sodium acetate. The solution was centrifuged at 16,200g for 1 minute in a QIAquick column to allow the DNA to bind. The column was then washed with 750µl Buffer PE and

centrifuged again at 16,200g for 1 minute, with a further centrifugation step to remove residual buffer. The sample was then eluted with 50µl of molecular biology water and once again centrifuged at 16,200g for 1 minute. The purified PCR product was then run on an agarose gel and the band visualised under UV light and excised using a scalpel to ensure the correct PCR product would be selected. The DNA from the excised portion of gel was then extracted using the QIAquick Gel Extraction Kit according to manufacturer's instructions. 3 volumes of Buffer QG (5.5 M guanidine thiocyanate; 20 mM Tris HCl pH 6.6) were added to 1 volume gel fragment and incubated at 50°C until the gel had dissolved. If required, the pH was adjusted using with 3M sodium acetate. 1 gel volume of isopropanol was added and mixed. The samples were then added to a QIAquick spin column and washed as described using a PCR purification kit. The DNA was finally eluted with 30µl molecular biology water.

The next stage was to prepare sticky ends of both the DNA insert and backbones. They were digested overnight using BglII (10U/µl) and Sall (10U/µl) enzymes to generate overhanging ends in preparation for ligation. The pEYFP-N1 and pEGFP-C1 vectors were opened with overhanging ends by overnight digestion with the same enzymes.

The DNA inserts and fluorescent vectors with sticky ends were again isolated by gel electrophoresis and gel extraction to remove contaminants using the same conditions mentioned above.

2.12.2 Ligation

The DNA insert and fluorescent vector was then ligated using a T4 DNA ligase at an 8:1 ratio of insert to backbone overnight at 14.5°C. The ligation reaction mixture is outlined in Table 2.11.

Table 2.11. Ligation reaction.

Component	Volume
Backbone	8 μ l
DNA Insert (1μg/μl)	1 μ l
T4 DNA Ligase (400U/μl)	0.8 μ l
10x Ligation Buffer	1 μ l
ddH₂O	0.2 μ l

2.12.3 Transformation of Plasmids into Competent Bacteria

The chemically competent *Escherichia Coli* strain DH5 α (NEB) was used for transformation of the fluorescent plasmids. 40 μ l of competent bacteria was mixed with 1 μ l of ligation reaction and incubated on ice for 15 minutes. After incubation, the cells were heat shocked at 42°C for 45 seconds and then immediately incubated on ice for a further 2 minutes. 1ml of freshly prepared SOC medium was then added to the mixture and incubated at 37°C for 1 hour whilst shaking. 150 μ l of transformation mixture was spread onto an agar plate containing the appropriate selection antibiotic and incubated overnight at 37°C. Single colonies were selected and grown, plasmid DNA extracted, verified and quantified as previously outlined.

2.13 CRISPR-Cas9 Plasmid Preparation

gRNA oligos were phosphorylated and annealed together using the reaction components shown in Table 2.12 and the thermocycler programme in Table 2.13. Annealed oligos were diluted 1:200 with ddH₂O. Oligos were then ligated into either a GFP or mCherry Cas9 containing plasmid with the reaction mixture outlined in Table 2.14. This mixture was ligated on a thermocycler with six cycles of 37°C for 5 minutes then 21°C for 5 minutes.

Table 2.12. Reaction mixture to anneal gRNA oligos.

Component	Volume (μ l)
gRNA Forward (100 μ M)	1
gRNA Reverse (100 μ M)	1
T4 PNK (10U/ μ l)	1
10x T4 Ligation Buffer	1
ddH ₂ O	6

Table 2.13. Thermocycler conditions to anneal gRNA oligos.

Temperature	Time (minutes)
37°C	30
90°C	5
25°C	Ramped down 5°C per min

Table 2.14. Reaction mixture to ligate gRNA oligos into vectors.

Component	Volume (μ l)
CRISPR vector from Table 4.1(100ng)	1
Diluted gRNA Oligos	2
10mM DTT (10nM)	1
10mM ATP (10nM)	1
10x Fast Digest Buffer	2
Fast Digest Bpil (BbsI)	1
T4 DNA Ligase (400U/ μ l)	0.5
10x Ligase Buffer	2
ddH ₂ O	9.5

The plasmids were then transformed into *E.coli*, using the plain mCherry vector as a positive control. Six colonies for each experimental condition were picked and grown up, then three were selected for DNA extraction by miniprep. To

confirm gRNA insert a diagnostic restriction digest was performed using the BbsI and EcoRI enzymes, and empty vectors as controls. Two colonies' DNA for each experimental condition were sent for sequencing using the LKO1_5 forward primer to ensure the gRNA sequence had been inserted correctly. One of each plasmid was then selected, the original bacterial culture grown up by overnight culture and the DNA was extracted by midiprep, and concentrated to 1µg/µl and frozen until transfection.

2.14 Cell Assays

2.14.1 Measuring Cell Viability

Cell viability was determined by using an MTT cell proliferation assay kit (Abcam, ab211091). This kit quantifies cell viability and proliferation based on the conversion of 3-(4,5- dimethylthiazol-2-yl)-2,5-diphenyltetrazolium bromide (MTT) to formazan by mitochondrial enzymes, therefore the more metabolically active a cell is the more formazan is produced and the higher the absorbance.

Cells were washed with PBS, trypinised for 5 minutes, pelleted and resuspended in 10ml media. Cells were manually counted using a haemocytometer. Cells were then made up to 50,000 cells per ml in a tube and 200µl seeded into a 96-well plate giving 10,000 cells per well with 8 replicates for each cell line. Two plates were seeded out at a time as results were read after both 48 hours and 96 hours of incubation. After incubation cell media was aspirated and replaced with 50µl MTT Reagent and 50µl cell media, and 8 background wells were also prepared. The plate was incubated at 37°C for three hours in the absence of light before 150µl of MTT Solvent was added to each well. The plate was shaken for 15 minutes whilst wrapped in foil and then the absorbance was read at 590nm. For data analysis extreme outliers

determined by GraphPad Prism were removed, the background subtracted, and replicates averaged.

2.14.2 Measuring ROS

Cellular reactive oxygen species was determined by using a DCFDA cellular ROS detection assay kit (Abcam, ab113851). This kit quantitatively measures ROS by using the cell permeant reagent 2',7'-dichlorofluorescein diacetate (DCFDA) which is a fluorogenic dye. DCFDA is deacylated by esterases and then oxidised by ROS into the fluorogenic compound 2',7'-dichlorofluorescein which can be detected by fluorescent spectroscopy.

Cells were washed with PBS, trypsinised for 5 minutes, pelleted and resuspended in 10ml media. Cells were manually counted using a haemocytometer. Cells were then made up to 125,000 cells per ml in a tube and 200µl seeded into a 96-well plate giving 25,000 cells per well with 8 replicates for each experimental condition. All wash steps and compound dilutions were with 100µl DMEM/F-12 phenol free media containing 10% FBS. Cells were washed then stained with 25µM DCFDA, incubated at 37°C for 45 minutes and then washed. Cells exposed to ROS were treated with 50µM tert-butyl hydrogen peroxide (TBHP), whereas the non-treated cells had media added and then incubated at 37°C for 1 hour. The fluorescence was then immediately measured (Ex/Em 485/520 in end point mode) using a microplate reader. For data analysis extreme outliers determined by GraphPad Prism were removed and replicates averaged.

2.14.3 Measuring Cell Death

Propidium iodide staining was used to quantitatively assess the number of dead cells in culture, followed by flow cytometry to measure cell size and staining on an individual cell basis. Propidium iodide is a fluorescent membrane

impermeant dye, therefore unable to penetrate viable cells, that intercalates between DNA base pairs [176]. Hallmarks of cell death include membrane blebbing/degradation and nuclear fragmentation therefore propidium iodide can intercalate the DNA [177].

100,000 cells were seeded into a 3.5cm cell culture dish, with each experimental condition in triplicate, 2 days prior to staining. After 2 days the supernatant was removed and transferred to a FACS tube. The cells were detached with 200 μ l trypsin, incubated for 5 minutes, neutralised with 1ml cell culture media and transferred to the same FACS tube as the supernatant. The FACS tube was centrifuged for 5 minutes at 1000g, supernatant poured off, and samples immediately placed on ice. The pellet was resuspended in 200 μ l of FACS buffer and 200 μ l of propidium iodide solution.

To prepare the flow cytometer (BD Accuri C6 Plus) a quality control was first run to ensure the machine would run effectively. Samples were then resuspended to ensure the cells were in solution and then the FACS tubes were placed into the flow cytometer. The samples were appropriately gated to exclude debris and differentiate dead cells from live cells, as shown in Figure 2.1. 10,000 cellular events were analysed and plotted by the software for forward scatter which indicates cell size against the side scatter which indicates the cell granularity.

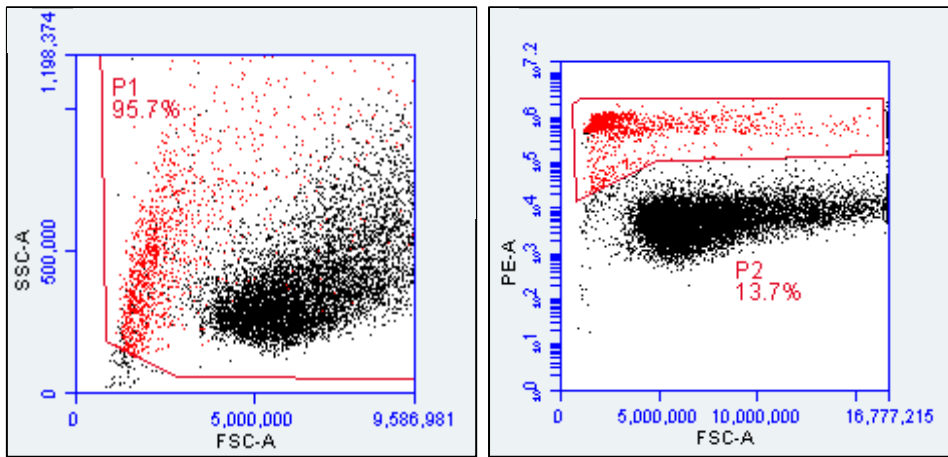


Figure 2.1. Flow cytometry cell population gating. The left-hand graph shows gating to remove pieces of cellular debris, designated P1, indicating that the cell population is 95.7% of the total events. The right-hand graph shows gating to identify the two populations, dead and viable cells, dead cells account for 13.7% of cells from the P1 gated cell population, therefore 86.3% are viable. In both graphs the red pixels indicate dead cells and black pixels indicate viable cells. Forward scatter (FSC-A) indicates cell size; side scatter (SSC-A) indicates cellular granularity; and PE-A indicates the staining intensity as PE is the red fluorescent channel used to excite propidium iodide.

Chapter 3

Mitochondrial Membrane Protein-Associated Neurodegeneration

Mitochondrial Membrane Protein-Associated Neurodegeneration

3.1 Introduction

3.1.1 Neurodegeneration with Brain Iron Accumulation

Brain iron accumulation is a pathological hallmark of a heterogeneous group of disorders collectively known as neurodegeneration with brain iron accumulation (NBIA) [178]. Excess iron in the brain is visualised by magnetic resonance imaging which primarily accumulates within the basal ganglia and in more advanced cases accumulation in the cerebellum is often observed. Clinically, NBIA is characterised by spasticity, dystonia, dysarthria, Parkinsonism, mental disability, optic atrophy and retinal degeneration [178]. While NBIA onset varies, most individuals present in childhood or early adulthood with gait and speech abnormalities. NBIA rate of progression also varies although affected individuals typically have an early death [179].

3.1.2 NBIA Disease-Associated Genes

To date, 12 disease-associated genes have been associated with NBIA, although only two of these genes are directly related to iron metabolism; *FTL* encoding ferritin light chain, and *CP* encoding ceruloplasmin [178]. Outcomes of these genetic subtypes result in altered iron homeostasis due to inefficient iron storage (ferritin light chain) and a reduction in ferrous iron oxidation (ceruloplasmin), leading to iron accumulation [178]. Other NBIA genes encode proteins that are involved in lipid metabolism, autophagic processing and lysosomal activity. Of the 10 other genes the largest metabolic group are those involved in lipid metabolism, including *PANK2* (pathothenate kinase type 2) and *COASY* (CoA synthase) that are both directly involved in coenzyme A synthesis which is required for energy production and fatty acid metabolism [178]. *PLA2G6* (phospholipase A2 group 6) and *FA2H* (fatty acid hydroxylase 2) are

involved in lipid metabolism, membrane integrity and mitochondrial function [178]. Dysfunctional PLA2G6 in mouse neurones leads to reduced mitochondrial potential and altered calcium uptake [180]. FA2H is an enzyme critical to myelin formation and mice lacking FA2H exhibit myelin sheath degeneration [181]. A fifth gene, *C19orf12*, is also thought to be involved in lipid metabolism, section 3.1.4 [182]. Two genes, *WDR45* (WD40-repeat protein 45) and *ATP13A2* (cation-transporting ATPase 13A2), are involved in autophagosome formation and lysosomal activity [178]. *SCP2* encodes a peroxisomal enzyme, sterol carrier protein x with a lipid transfer function, and patients with *SCP2* mutation have been found to have abnormal fatty acid acyl-CoA metabolism [183]. *GTPBP2* encoding GTP-binding protein 2 which may be implicated in mRNA metabolism [184]. The final disease-associated gene, *DCAF17* encodes a nucleolar protein with an unknown function [185]. Four of the 12 disease-associated genes encode mitochondrial proteins suggesting that mitochondria may be central to NBIA disease pathogenesis, Figure 3.1. NBIA can be inherited as autosomal recessive, autosomal dominant or X-linked trait, Table 3.1 [178].

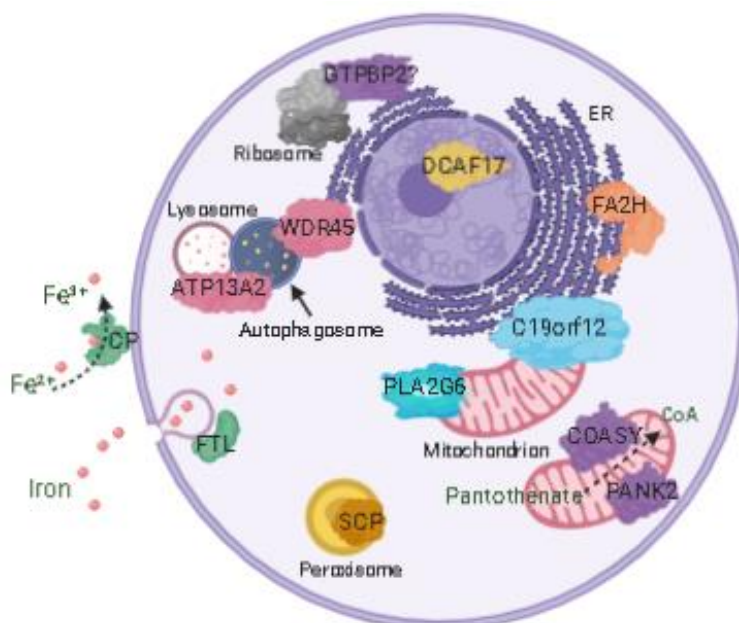


Figure 3.1. Schematic representation of the cellular localisation of NBIA-associated proteins. Figure adapted from Di Meo and Tiranti, 2018 and made using BioRender.

Table 3.1. NBIA-associated genes.

Gene	Protein	Protein Function	Mode of Inheritance	HSP Association
<i>FTL</i>	Ferritin light chain	Cellular iron storage	AD	
<i>CP</i>	Ceruloplasmin	Iron oxidation	AR	
<i>PANK2</i>	Pathothenate kinase type 2	Coenzyme A synthesis	AR	
<i>COASY</i>	CoA synthase	Coenzyme A synthesis	AR	
<i>PLA2G6</i>	Phospholipase A2 group 6	Fatty acid hydrolysis	AR	Complicated HSP
<i>FA2H</i>	Fatty acid hydroxylase 2	Fatty acid synthesis	AR	Complicated HSP
<i>C19orf12</i>	C19orf12	Unknown; possibly lipid metabolism	AR	Complicated HSP
<i>WDR45</i>	WD40-repeat protein 45	Autophagosome formation	X-linked	
<i>ATP13A2</i>	Cation-transporting ATPase 13A2	Autophagosome formation	AR	Complicated HSP
<i>SCP2</i>	Sterol carrier protein x	Lipid transport/ fatty acid breakdown	AR	
<i>GTPBP2</i>	GTP-binding protein 2	Unknown; possibly mRNA metabolism	AR	
<i>DCAF17</i>	DDB1- and CUL4-associated factor 17	Unknown; nuclear transmembrane protein with unknown	AR	

3.1.3 NBIA Overlaps with HSP

There is clear clinical overlap between NBIA and HSP primarily through spasticity which is a cardinal sign of both conditions. Moreover, several NBIA-associated genes are also associated with pure and/or complex forms of HSP, without brain iron accumulation. These genes include *FA2H*, *C19orf12* and

ATP13A2 which are respectively associated with SPG35 [186], SPG43 [187] and SPG78 [188]. *PLA2G6* has also been associated with HSP as patients with sequence alterations in the *PLA2G6* gene have been found to present with a complex form of HSP [189, 190]

Like HSP, a common biomolecular finding in NBIA involves altered lipid metabolism. Additionally, many of the proteins associated with HSP and NBIA are thought to possess a mitochondrial role. Mitochondria are hubs for cellular iron storage and utilisation for synthesis of enzyme co-factors [191]. Excess iron and increased lipid peroxidation by ROS can result in cellular death by ferroptosis [192]. Lipid peroxidation and mitochondrial structural abnormalities have also been observed in NBIA cell models suggesting ferroptosis may play a role in NBIA pathophysiology [185, 192].

3.1.4 *C19orf12*

NBIA due to mutations in the *C19orf12* gene is also referred to as mitochondrial membrane protein-associated neurodegeneration (MPAN). MPAN accounts for ~30% of NBIA cases and typically presents between the ages of 4-20 years old with a mean age of 9 years [178, 182]. Initial presentation of gait and speech abnormalities slowly progress to a typical MPAN presentation which includes dystonia and Parkinsonism, optic atrophy, axonal motor neuropathy and neurological abnormalities [182, 193]. Late-onset MPAN in the third or fourth decade is dominated by neuropsychiatric disturbances and an accelerated clinical progression [194]. Ultimately, MPAN results in severe dementia, spasticity, dystonia and Parkinsonism, frequently leading to an early death [195].

C19orf12 protein contains a transmembrane region (amino acids 51-72; Figure 3.2) which contains two glycine zippers that are thought to anchor the protein to

the mitochondrial membrane [196]. C19orf12 has been found to localise to the mitochondria and ER, in addition to the MAM [196]. Additionally, soluble regions at N- and C-termini (1-41 and 77-151aa) display homology with the N-regulatory domain of bacterial MgtE transporter indicating a potential role in magnesium transport [196].

There are four isoforms of *C19orf12* with the canonical and longest isoform containing three exons with a total length of 152 amino acids producing a 17kDa protein [196]. The other three isoforms are variations of the canonical sequence, however the third exon of isoform 4 contains the same coding sequence with a different frame, therefore different amino acids are encoded. Each isoform has differing initiation codons, apart from exon two and four (Figure 3.2).

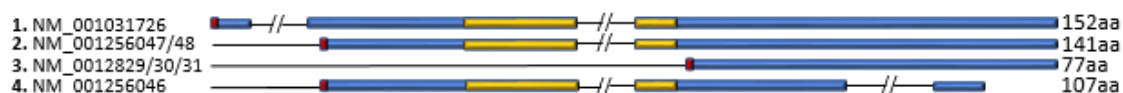


Figure 3.2. Schematic representation of the four isoforms and genomic organisation of C19orf12. Isoform 1 is the canonical sequence containing 152 amino acids and three coding exons. Isoform 2, 3 and 4 arise from differing splicing of the *C19orf12* gene and/or initiation codon usage. Transmembrane region in yellow.

C19orf12 is ubiquitously expressed with increased expression in the brain, blood cells and adipocytes [178]. While the precise functional role of C19orf12 remains to be elucidated, it is thought to be involved in lipid metabolism given its high expression in adipocytes, and transcriptional analyses which indicate that it is co-regulated with genes involved in fatty acid biosynthesis [178, 182]. Isoform expression analysis using the Genotype-Tissue Expression (GTEx)

portal indicates that isoform three is significantly more highly expressed in all tissue types than the other three isoforms [197].

Biallelic *C19orf12* variants were first associated with autosomal recessive MPAN (AR-MPAN) in 2011 in a cohort of Polish patients with NBIA [182]. Since this time many biallelic loss of function, missense and splice junction variants have been described, Figure 3.5. The majority of disease-associated mutations are pathogenic in the biallelic state and cause MPAN in an AR manner. However, more recent studies indicate that individuals may present with MPAN due to monoallelic variants in an autosomal dominant fashion (AD-MPAN) [179, 193, 198]. The phenotypic presentation of MPAN is indistinguishable regardless if the genotypic variant is AR or AD [193]. Several *de novo* mutations have also been reported [193, 198], and an additional *de novo* variant identified within an individual from the Amish community will be described in this chapter. Furthermore, this chapter will propose a mechanism to explain the differing pathological mechanisms in monoallelic and biallelic state that result in MPAN with identical clinical presentations.

3.2 Results

3.2.1 *C19orf12* c.278del (p.Pro93Leufs*26) Alteration is Associated with AD-MPAN

An Amish individual, presenting with cognitive decline, gait instability and frequent falls at 20 years of age was initially referred to the WoH Project for investigation. The disorder progressed with mood disturbances, slowed movements, ataxia, tremor and difficulty with fine motor skills, by 37 years of age, she was immobile and non-verbal. Her examination showed dystonic movements, upper and lower limb spasticity, marked hyperreflexia and extensor plantar responses bilaterally. The family history was unremarkable and developmental milestones were reportedly normal, although parents stated that she was always clumsier than her siblings. MRI neuroimaging at 26 years of age revealed abnormal signal intensity in the basal ganglia, suggestive of NBIA. Genetic testing for the Amish founder variant in *PANK2* (NM_153638.3: c.1561G>A; (p.Gly521Arg)), known to cause NBIA within the Ohio Amish and Mennonite community, and the clinically overlapping *SPG21* Mast syndrome variant (NM_016630.7: c.601dup; (p.Thr201Asnfs*13)), excluded these as causal mutations.

To investigate the cause of this condition the family were recruited and examined with the appropriate consent, pedigree in Figure 3.3. DNA samples were extracted from blood or buccal samples using standard techniques. Whole exome sequencing was performed in the affected individual (II:5) and her parents (I:1 and I:2) which detected single nucleotide polymorphisms. Genome-wide single nucleotide polymorphism mapping was also performed in the affected individual (II:5).

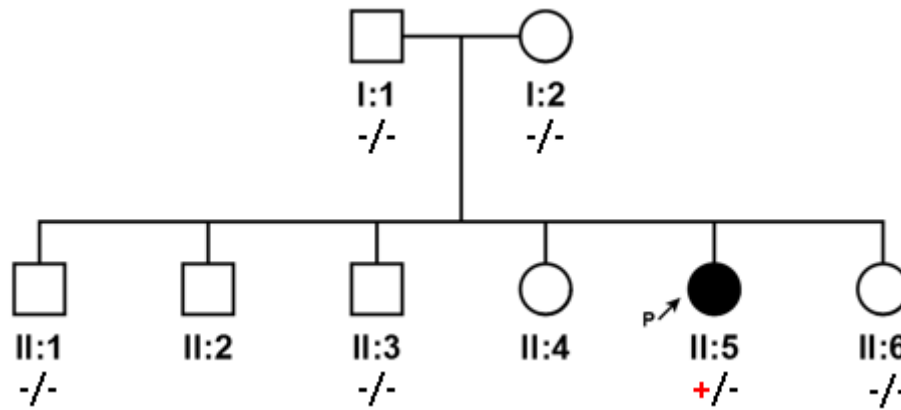


Figure 3.3. Pedigree of Amish family with a single child affected with MPAN. Shading indicates clinically affected individual (+/-) with the identified variant p.(Pro93Leufs*26) and (-/-) indicates the members of the family found to be wildtype by dideoxy sequencing.

From this data the NBIA disease-associated genes (Table 3.1) were analysed initially, which revealed a heterozygous frameshift variant in *C19orf12*; Chr19(GRCh37):g.30193800delG; NM_001031726.3:c.278del; NP_001026896.2:p.Pro93Leufs*26. This variant is absent from the gnomAD (v2.1) population database and our in-house Amish exome database with 220 individuals. No other candidate variants including copy number variants were identified in these genes. The variant was confirmed to be a *de novo* event by dideoxy sequencing and is not present in the parents or 3 of the 5 siblings in which DNA was available for testing (Figure 3.4). This single base deletion results in a frameshift predicted to result in premature termination of protein translation. As this variant is present within the final exon it is likely to result in the production of a truncated mutant protein.

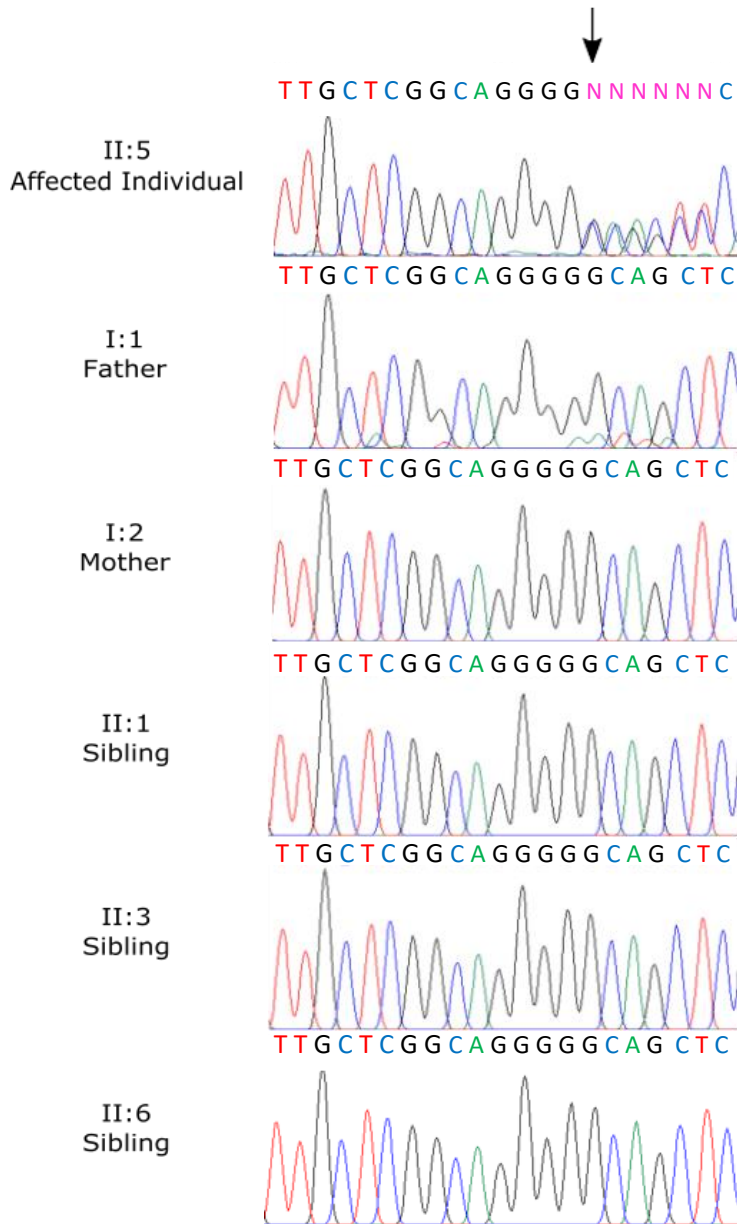
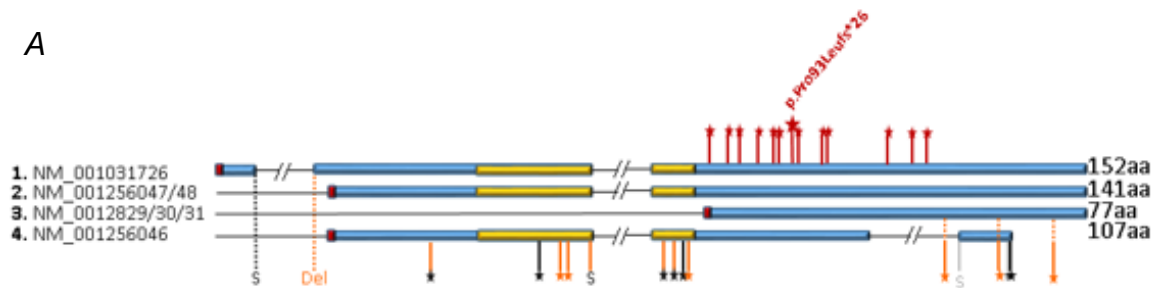


Figure 3.4. Dideoxy sequencing of identified c.278del variant in affected child and wildtype parents and siblings. The arrow indicates the position of the variant in the parents and the 3 of the 5 siblings that were tested.

A



B

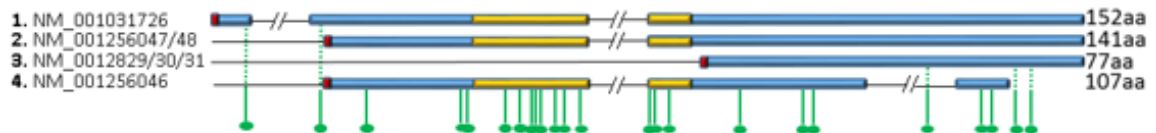


Figure 3.5. Schematic of the C19orf12 protein, displaying reported dominant and recessively acting variants (A) and missense variants (B) in relation to gene exons, transmembrane domain and isoforms. A) Red: Variants reported to be associated with AD-MPAN, which are pathogenic in heterozygous state. Orange: Protein loss of function and splice junction variants reported to be associated with AR-MPAN, which do not cause disease in heterozygous state. Black: Protein loss of function heterozygous variants present in the population database, gnomAD. Grey: Low confidence variants present in gnomAD. B) Green: Missense mutations reported in recessively acting MPAN. Variants detailed in Appendix B.

3.3 Discussion

The *C19orf12* c.278del/p.Pro93Leu*26 variant identified in the Amish individual in this study, shown to be *de novo* and dominantly acting, confirmed a diagnosis of NBIA in this individual. This *C19orf12* variant affects all four protein isoforms and all identified autosomal dominant variants (Table 3.2) are located in a clustered region of the third exon, Figure 3.5A (red pegs). Autosomal recessive variants are located in all other regions of the gene but are not present within the region where autosomal dominant variants occur. This indicates that dominant or recessive outcomes depend on the location of each variant. Gregory *et al.*, 2019 highlighted the regional genetic pattern between autosomal recessive and dominant variants, suggesting three possible mechanisms as to why this may be the case: haploinsufficiency, gain of function or a dominant negative effect. Haploinsufficiency was considered to be unlikely due to the large number of healthy parents of offspring with AR-MPAN individuals who themselves have heterozygous variants in the first or second exon, in which the protein product may be expected to undergo nonsense mediated mRNA decay. However, it is important to note that these healthy individuals would still potentially express isoform three from the mutant allele as this isoform's initiation codon is in the third exon of the canonical isoform, in addition to the other three isoforms expressed from the wild type allele.

However, in reviewing the nature and outcome of likely pathogenic variants in this gene, it appears overly simplistic to correlate dominant vs recessive outcomes with exon position alone. It is notable that a number of AR-MPAN disease-associated truncating variants occur at the start of exon three (p.Ala67Leufs*6, p.Ala67Glyfs*14, p.Gly69Argfs*10 and p.Leu72Phefs*11) [198]. Whilst being located in the third exon, these variants do not likely impact

isoform three. Thus, rather than being linked to exonic location, AR/AD-MPAN outcomes may be more likely relate to the specific *C19orf12* isoform impacted by gene mutation. *C19orf12* loss of function AD-MPAN variants are all located after amino acid 75, the precise position of the alternate initiation codon generating isoform 3 which lacks the putative transmembrane region. However, three other homozygous protein truncating variants located at the C-terminus of exon three have been associated with AR-MPAN in three families (p.Met124Ilefs*17, p.Met135Ilefs*15 and p.Ala146Glyfs*6) [199-201], although these variants do not impact isoform four. It is also important to note that three heterozygous loss of function/ gene splicing variants are present in exon three in the population database gnomAD, although with low confidence (c.291-1G>A splice variant, p.Trp107* and Val137Glyfs*15) [202]. Two of the gnomAD loss of function variants only affect the unique third exon in isoform four, while Val137Glyfs*15 is present in isoforms one, two and three with a possible explanation for this variant among the healthy population (present in one individual) being non-penetrance or variable expression, although this variant has been marked as low confidence of loss of function.

When taken together, the mechanistic basis of dominant and recessive inheritance seems more likely to relate to how each gene variant impacts *C19orf12* isoforms, rather than just exon location. Given that isoform three is the most highly expressed isoform (GTEx [197]), this may indicate that it is the most biologically important isoform for which two functional copies are required to avoid dominant pathogenicity. Thus, a 'haploinsufficiency of isoform 3' model arising from loss of function mutations affecting this isoform may better explain AD-MPAN. However, this may not account for the three C-terminal AR-MPAN variants (Figure 3.5, orange pegs), although it may be possible that frameshift

variants located toward the C-terminus retain some functionality, or are rescued by isoform 4 which is not impacted by variants in this location. This isoform-specific haploinsufficiency model would also explain why the variants at the start of exon three cause pathogenicity in the autosomal recessive state, as they do not affect isoform three. Additionally, the biological importance and role of isoforms one, two and four is also evidenced as many homozygous missense variants present upstream of isoform 3 are associated with AR-MPAN, Figure 3.5B.

In-silico domain predictions indicate that C19orf12 protein entails a transmembrane domain (amino acids 51-72), containing glycine zipper motifs important for localisation to the mitochondrial membrane in which a large number of AR-MPAN missense variants impact [196]. A functional study has highlighted the altered cellular distribution of C19orf12 due to a missense mutation at a glycine zipper amino acid, p.Gly58Ser; which results in a more cytosolic distribution of C19orf12 rather than its wildtype mitochondrial/ER localisation, likely to be due to ineffective membrane binding [196]. The cellular consequences of another missense mutation, p.Gln96Pro, in the third exon also shows altered subcellular distribution to a vesicular localisation, which the authors suggest may be due to the loss of side-chain mediated hydrogen bonds resulting in an altered 3D structure [196].

Four other NBIA disease-associated genes encode lipid related proteins and C19orf12 has also been suggested to be involved in lipid metabolism [182, 196]. The high proportion of lipid and mitochondrial associated genes suggest that altered lipid homeostasis is involved in NBIA pathophysiology, along with dysfunctional mitochondria [185]. As C19orf12 has been found to be localised to the MAM, a hub for lipid transfer between the mitochondria and ER, this may

indicate that it functions to facilitate lipid biological pathways. The MAM and lipid imbalance will be explored further in chapter five of this thesis.

3.3.1 Future Work

One area of future studies to prove our hypothesis explaining mono- and biallelic MPAN outcomes due to *C19orf12* mutations could explore the functional relevance of each of the *C19orf12* isoforms, with a particular focus on isoform 3. To do this isoform specific plasmids could be generated to explore the subcellular localisation of each isoform, and determine how isoform 3 differs to the other isoforms given that it is predicted to lack the transmembrane domain. To expand upon these studies, binding partner analyses followed by corroboratory functional studies including more detailed subcellular localisation studies of putative binding partners (such as those detailed in section 4.2.5 in this thesis), could be undertaken in parallel to give further insight into the function of each isoform.

Previous studies have outlined a potential role of *C19orf12* in lipid metabolism, in keeping with other molecules associated with NBIA and complex HSP clinical outcomes. This aspect requires further investigation to understand more specifically how protein dysfunction or depletion may impact lipid pathways. To do this, the methodology outlined in chapter five of this thesis including subcellular fraction and lipid analysis could be utilised. Furthermore, these experiments could be conducted on different cell and tissue types to investigate whether the isoforms have functional tissue specificity.

Another avenue of future work that is helpful for understanding NBIA more broadly involves the investigation of how *C19orf12* variants lead to iron accumulation, and subsequent neurodegeneration. To date, little is known

about how or if the various NBIA-associated proteins interact with one another despite all resulting in the same pathological hallmark. By investigating these interactions, alongside associated HSP molecules will likely shed light on common biomolecular pathways. To delve into this deeper, the imbalances which trigger apoptotic pathways could be investigated within this group of disorders.

Table 3.2. Reported autosomal dominant C19orf12 variants.

Autosomal Variant	Dominant	Affected Individuals; Age of Onset	Inheritance and Family Clinical Information
p.Met76Thrfs*3 [193]		4 individuals; 19-56 years	Variant segregates with disease in the 3 affected individuals available for testing. Dominant (9 affected in 3 generations), non-penetrance in some individuals in 60-80s. Mother obligate carrier died in 60s without MPAN symptoms.
p.Gln80* [193]		2 siblings; both 10 years	Inheritance unknown – adopted.
p.Gln80* [193]		Singleton; 5 years	<i>De novo</i> . Parents unaffected.
p.Lys82* [199]		Singleton; 10 years	Inherited from unaffected mother.
p.Gln86* [203]		Singleton; Cohort onset 4-30 years mean 11 years.	Inheritance unknown.
p.Gln86* [193]		Singleton; 12 years	Inheritance unknown. Parents unaffected.
p.Met89Glyfs*12 [198]		Singleton; 5 years	<i>De novo</i> . Parents unaffected.
p.Glu90* [193]		Singleton; 22 years	Inheritance unknown. Parents unaffected.
p.Pro93Leufs*26 [193]		Singleton; 18 years	Inheritance unknown. Parents unaffected.
p.Pro93Leufs*26 (reported in this paper)		Singleton; 20 years	<i>De novo</i> . Parents unaffected.
p.Pro93Profs*8 (c.278dupC) [193]		Singleton; 9 years	Inheritance unknown.
p.A94Cfs*8 [203]		Singleton, cohort onset 4-30 years mean 11 years	Inheritance unknown.
p.Ala94Profs*25 [193]		Singleton; 9 years	<i>De novo</i> . Parents unaffected.
p.Ala94Serfs*24 [193]		Singleton; 4 years	<i>De novo</i> . Parents unaffected.
p.Leu99fs*102 [204]		Singleton; Not known	Inheritance unknown.
p.Phe100Leufs*19 [193]		Singleton; 5 years	Inheritance unknown. Parents unaffected.
p.Trp112* [193]		Mother and daughter; 28 and 30 years	MPAN on maternal side. Inherited from mother.
p.Gln117* [193]		Singleton; 18 months	Inheritance unknown. Parents unaffected.
p.Ala120Glyfs*32 [203]		Singleton; Cohort onset 4-30 years, mean 11 years	Inheritance unknown. Father died aged 47 with neurodegeneration and likely signs NBIA at post-mortem.
p.Ala120Glyfs*32 [193]		Singleton; 29 years	Inheritance unknown. Parents unaffected.

Chapter 4

Defining the Biomolecular Role of Maspardin

Defining the Biomolecular Role of Maspardin

4.1 Introduction

4.1.1 Mast Syndrome

Mast syndrome is a complicated autosomal recessive form of HSP associated with cognitive decline and progressive dementia typically starting in early adulthood, first described by Victor McKusick in 1967 [149]. It currently remains unclear if or what clinical signs may be present in childhood, although parents often report that affected individuals appeared to be clumsy and found school more challenging than their unaffected siblings. However most affected individuals are usually perceived to be 'normal' through their teenage years and early adulthood, and are able to work, manage well in day to day life, establish and maintain relationships and have children, prior to the full onset of the condition. The condition typically presents in earnest in the third or fourth decade of life with initially lower and subsequently upper limb spasticity, dysarthria and swallowing difficulties, alongside significant decline in motor and mental function. The condition continues to progress, profoundly impacting on quality of life. Magnetic resonance neuroimaging findings include a thin corpus callosum with cerebral and cerebellar atrophy as shown in Figure 4.1 [151].

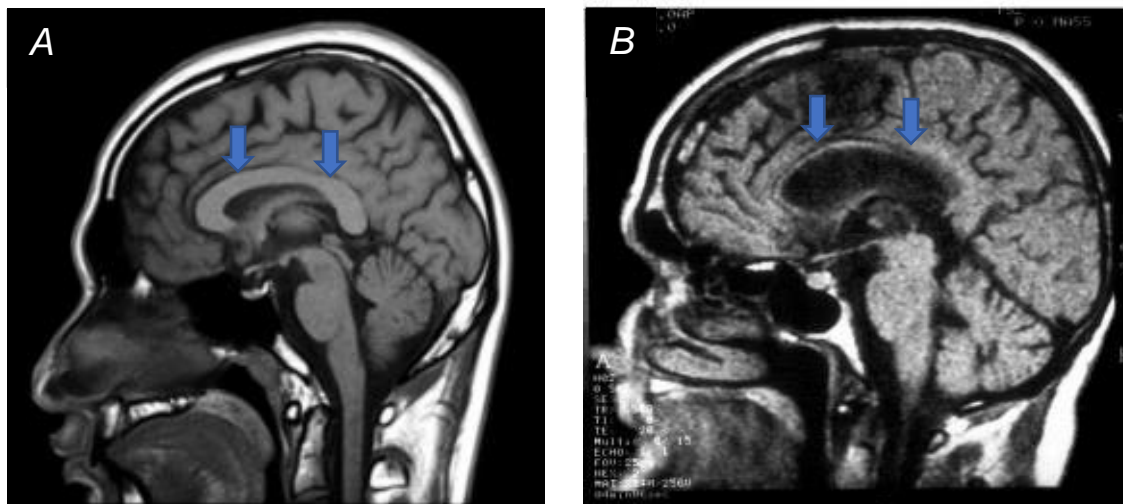


Figure 4.1. An MRI image of an individual with Mast syndrome. A) A healthy individual's MRI (Shutterstock Images) compared with that of an individual with Mast syndrome (B) showing a thin corpus callosum (indicated by blue arrows) and general cerebellar atrophy [151].

Mast syndrome is found at high frequency among the Ohio Amish community. As described in section 1.6.1, the Amish are a group of Anabaptist Christians who fled Europe to escape persecution in the 18th century. This migratory bottleneck, following population expansion, led to the enrichment of a number of founder gene mutations, including that responsible for Mast syndrome, which are now associated with a high incidence of certain inherited disorders [151]. In recent years other Mast syndrome cases have been identified in Japanese and Italian families, Figure 4.2 [205, 206]. From our group's previous work to define the causes of inherited disorders amongst the Amish, we determined that the condition results from biallelic inheritance of an *SPG21* gene mutation, encoding the protein maspardin (Mast syndrome, spastic paraplegia, autosomal recessive with dementia) [151, 207]. In the Amish population Mast syndrome is associated with a single base pair insertion (NM_016630.7:c.601dup; (p.Thr201Asnfs*13)) which results in a frameshift and a premature stop codon [151]. The cause of Mast syndrome described in an Italian family was found to

involve a single base pair deletion (NM_016630.7:c.118delC;(p.Arg40Glufs*27)) in *SPG21*, also resulting in a frameshift and a premature stop codon; the clinical presentation of the affected individual is very similar to that of affected Amish individuals [206]. Both frameshift mutations are likely to result in nonsense mediated mRNA decay, therefore complete loss of protein function. Two Japanese brothers have also been diagnosed with Mast syndrome as a result of a single base substitution (NM_016630.7:c.322G>C;(p.Ala108Pro)) [205]. This mutation impacts the 108th amino acid of maspardin, in which the 109th (serine) amino acid is a key component of the catalytic triad functional domain of maspardin, and so may disrupt protein function through impacting this molecular region [97]. However, clinically the Japanese siblings presented with milder late-onset disease with walking difficulties manifesting in the fifth and sixth decades, and the individuals do not exhibit cerebellar or bulbar signs [205].

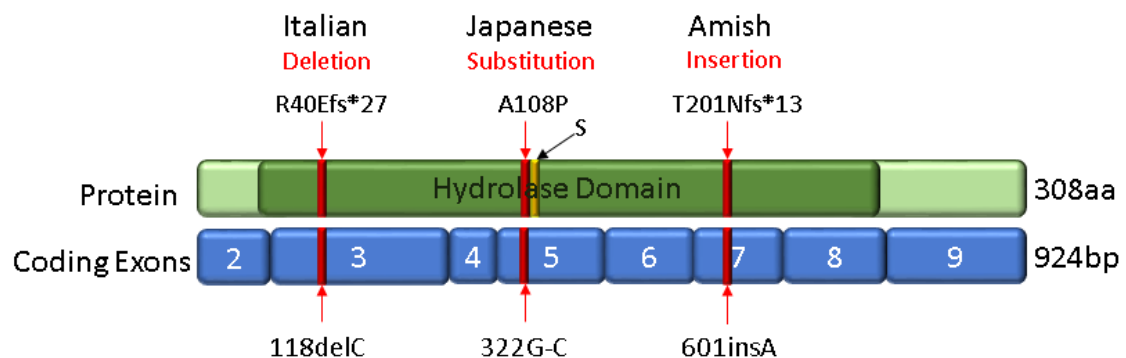


Figure 4.2. Schematic representation of the three known *SPG21* mutations associated with Mast syndrome in Amish, Italian and Japanese families. The α/β hydrolase domain is shown in dark green spanning the majority of the 308 amino acid protein. The serine amino acid is also shown which is next to the position of the Japanese mutation. The coding exons are shown and the relevant exon that each mutation occurs in. Italian deletion mutation = c.118delC, p.R40EfsTer27; Japanese substitution mutation = c.322G-C, p.A108P; Amish insertion mutation = c.601insA, p.T201Nfs.

4.1.2 Maspardin

The precise subcellular localisation and function of maspardin are unknown, however there have been several studies describing potential binding partners of maspardin and its cellular localisation.

Spg21 knockout mice have been generated which appear normal at birth, but within several months develop hind limb dysfunction which progressively worsens, representative of the human phenotype. Cultures of cortical neurones from these mice reveal increased axonal branching, however another study showed the reduction of axonal branching which the authors speculate may be due to the differing culture conditions [208, 209]. Cortical neurones from *Spg21* knockout mice showed that epidermal growth factor (EGF) did not promote the growth and maturation of neurones, unlike wildtype neurones [209].

Maspardin is known to contain a domain similar to that of the α/β hydrolase family with a characteristic nucleophilic elbow and parallel strands, however it lacks the crucial catalytic triad required for enzymatic function [151]. Maspardin also contains a G-X-S-X-G (single letter amino acid code) motif that is found in many lipases [208]. As maspardin lacks the catalytic triad it has been suggested that it may function as a peptide binding molecule. Originally, maspardin was identified as a candidate intracellular binding molecule to the cell surface CD4 protein in T-cells [210]. However, as maspardin is expressed in many cell types it may likely have functions other than mediating CD4 activity. Maspardin is also highly conserved with orthologs present in phylogenetically distant species, including plants [208]. This high conservation suggests that it is involved in critical cellular processes that are common to many cell types and species. The precise subcellular localisation of maspardin has not been fully elucidated but

previous studies have identified that it partially colocalises with markers for late endosomes and lysosomes [210, 211].

Maspardin has also been shown to interact with an aldehyde dehydrogenase (ALDH16A1), determined by mass spectrometry using HeLa cell lysates. This study also showed that maspardin localises to cytosolic and membrane fractions of the cell but not nuclear fractions [211]. Very little is known about ALDH16A1, however it has been found to be associated with gout and serum uric acid levels when mutated, and it is thought that it too lacks the critical catalytic triad in humans. However ALDH16A1 may interact with the hypoxanthine-guanine phosphoribosyltransferase protein, which is a key enzyme required for uric acid metabolism [212, 213]. Mutations in another aldehyde dehydrogenase, ALDH18A1 that encodes a mitochondrial enzyme involved in proline, ornithine and arginine synthesis has been found to be associated with SPG9 [214-216]. SPG9 is further divided into dominant and recessive, SPG9A and SPG9B, forms and the recessive form has a more severe clinical phenotype with a younger age of onset and increased disability [217]. Furthermore, ALDH18A1 was found to have differential mRNA expression in *Spg21* knockout and wildtype mouse brains [208].

Another study has highlighted an interaction of maspardin with the Rab7 GTPase which localises to late endosomes, lysosomes and other vesicular structures. This study performed mass spectrometry on HEK 293 cell lysates pulled down with Rab7 to identify potential Rab7 binding partners [218]. Rab proteins are a group of almost 70 GTPases in humans which regulate intracellular membrane trafficking. They localise to different membranes and are found in either a membrane GTP bound 'on' state or a cytosolic GDP bound 'off' state [219]. Rab7 plays a vital role in the regulation and trafficking of late

endosomes and lysosomes, and it is also crucial to the endosomal maturation process as it is involved in controlling the transition of early to late endosomes, alongside Rab5 [220, 221]. Rab7 has also been found to associate with other cellular compartments including the ER, mitochondria and trans-Golgi network [222].

Four missense mutations in *Rab7* have been described to cause the autosomal dominant neuropathy CMT type 2 B [223]. It is unknown how mutations in *Rab7* result in axonal degeneration. One study identified that the mutant Rab7 protein exhibited increased nucleotide exchange rates and the majority of mutant Rab7 protein is in the active GTP bound state [224]. Another study confirmed this by determining the crystal structure of the mutant Rab7 protein which revealed a disruption to the nucleotide binding pocket that is crucial for switching between its active and inactive state, therefore Rab7 is retained on target membranes [218]. Furthermore Rab7 has also been found to be crucial to the regulation of long range axonal trafficking and defects in axonal transport are associated with neurodegeneration [225].

4.1.3 CRISPR Technology

The CRISPR (Clustered Regularly Interspaced Short Palindromic Repeats) Cas9 gene technology is one of the newest molecular biology tools. CRISPR-Cas9 gene technology was first developed for use in mammalian cells in 2013 by the Feng Zhang lab after three decades of research by many scientific groups since CRISPR was first discovered in bacteria [226-228]. It allows the targeting of a specific region of DNA to create a double stranded DNA break (DSB) in that region, enabling the removal, addition or alteration of genetic material at a specific location in the genome.

This gene technology is utilised in this chapter to knockout a region of the *SPG21* gene in the SH-SY5Y human neuroblastoma cell line. To do this two gRNAs were designed to guide the Cas9 enzyme to specific protospacer adjacent motif (PAM) sites to create two DSBs. These DSBs then result in the removal of a section of DNA and the remaining DNA is repaired by non-homologous end joining. The DNA deletion results in nonsense mediated mRNA decay due to a frameshift, therefore a polypeptide is not produced; this mechanism is illustrated in Figure 4.3. This will provide a useful resource to study the cellular consequences due to the loss of maspardin, essentially mimicking the insertion and deletion mutations found the Amish and Japanese individuals diagnosed with Mast syndrome.

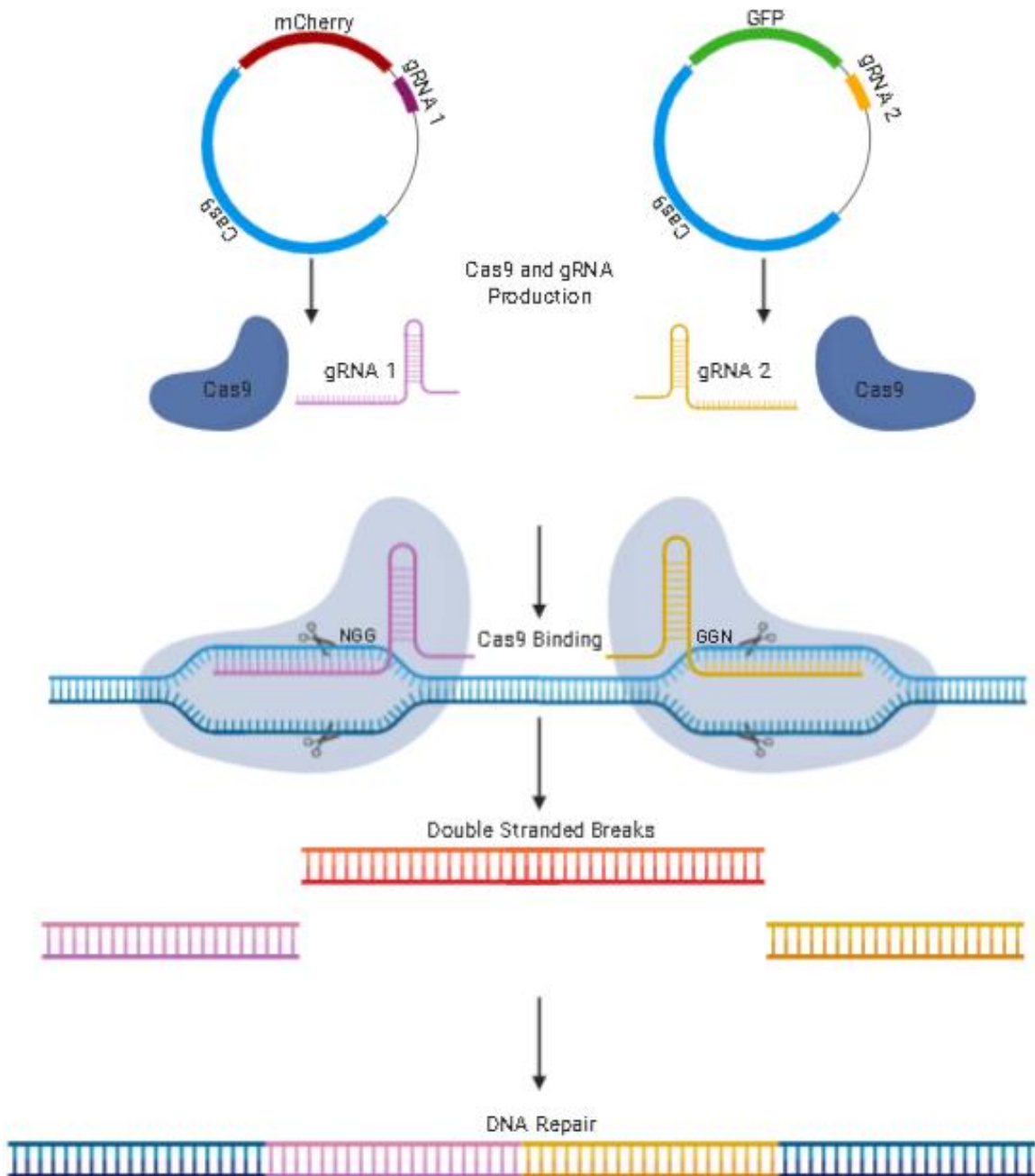


Figure 4.3. A schematic of CRISPR-Cas9 gene editing using two gRNAs. First, two individual gRNA and Cas9 containing plasmids are generated and transfected into a cell. The Cas9 enzyme and gRNA form a complex where the gRNA binds to the targeted sequence upstream of the PAM (NGG) site which the Cas9 enzyme recognises. The enzyme induces a DSB 3 bases upstream of the PAM site. This results in the deletion of the DNA region and the remaining sequence is repaired by non-homologous end joining resulting in a frameshift mutation and nonsense mediated mRNA decay, therefore no protein is translated.

4.1.4 Defining the Biomolecular Role of Maspardin

Despite the few studies surrounding maspardin characterisation the precise function and subcellular localisation of maspardin is still unclear, in particular the specific function of maspardin in neuronal cells is not known. Maspardin is expressed in many cell types [197], however the SH-SY5Y cell line was chosen for the majority of the investigations in this chapter due to them being derived from neuroblastoma cells. This chapter focuses on furthering knowledge of maspardin by in-depth subcellular localisation studies, with a particular focus on live cell studies, in addition to molecular binding partner studies. Alongside this the cellular consequences due to the loss of maspardin has been investigated via gene knockout in neuronal cell models, to identify how the specific organelles that are associated with maspardin are impacted and how this alters cellular functions in relation to wildtype control SH-SY5Y cells. As to date an *SPG21* knockout cell line has not been developed, and maspardin has not been studied in live cells, this will significantly contribute to Mast syndrome research. This chapter also highlights some of the flaws of functional studies, and how they were overcome.

By understanding where in the cell maspardin resides, and to what functional complex it may belong, will help understand the pathomolecular basis of Mast syndrome. Additionally, these findings may also be of importance to other HSPs, as well as neurodegenerative disease more widely. Improved understanding of the biomolecular basis of disease is essential to enable the identification of new molecular targets for drug development. Not only will this be of significance to the Amish community, it will also benefit individuals with this (and potentially other related) condition elsewhere.

4.2 Results

4.2.1 Creating an SPG21 Knockout SH-SY5Y Cell Line: gRNA Design

Exon 3 of the 9 exon *SPG21* gene was chosen for the gRNA target sequences due to it being conserved throughout *SPG21* transcripts, and the larger size of this exon was more suited to the two-guide approach. The guides were designed using the Benchling software (<https://benchling.com>) which ranks potential gRNA target sequences based on their 'on-target' and 'off-target' scores. Two guides were chosen in exon three (gRNA 3.1 and 3.2), however the second guide had a lower ranking so a second pair of guides were designed using the same guide at the start of exon three (gRNA 3.1), and a second in exon 5 (gRNA 5). The chosen sequences were also checked to ensure they are not present at any other position in the genome and that a BbsI enzyme restriction site was not present. BbsI cloning overhangs were added to the sequences to enable insertion into the backbone in the correct orientation. A schematic representation of the two sets of guides can be seen in Figure 4.4 to visualise the gRNA positions and the gRNA sequences with their corresponding forward and reverse sequences can be seen in Table 4.1.

Table 4.1. *SPG21* CRISPR-Cas9 plasmid composition. Construct denotes the target exon as indicated in Figure 4.4. gRNA sequences include the required bases for BbsI sticky ends (red) and corresponding cloning vector.

Construct	Strand	gRNA Sequence 5' to 3'	Vector
3.1	Forward	CACCGATATGGTCGCTCTATGACG	pU6-(BbsI) CBh-Cas9-T2A-mCherry
	Reverse	AAACCGTCATAGAGCGACCATATC	
3.2	Forward	AAACGGTTATCGCTGTAAGTATTAC	pSpCas9(BB)-2A-GFP
	Reverse	CACCGTAATACTTACAGCGATAACC	
5	Forward	CACCGCCAAGTTTGGTTGAAGATAG	pSpCas9(BB)-2A-GFP
	Reverse	AAACCTATCTTCAACCAAACTTGGC	

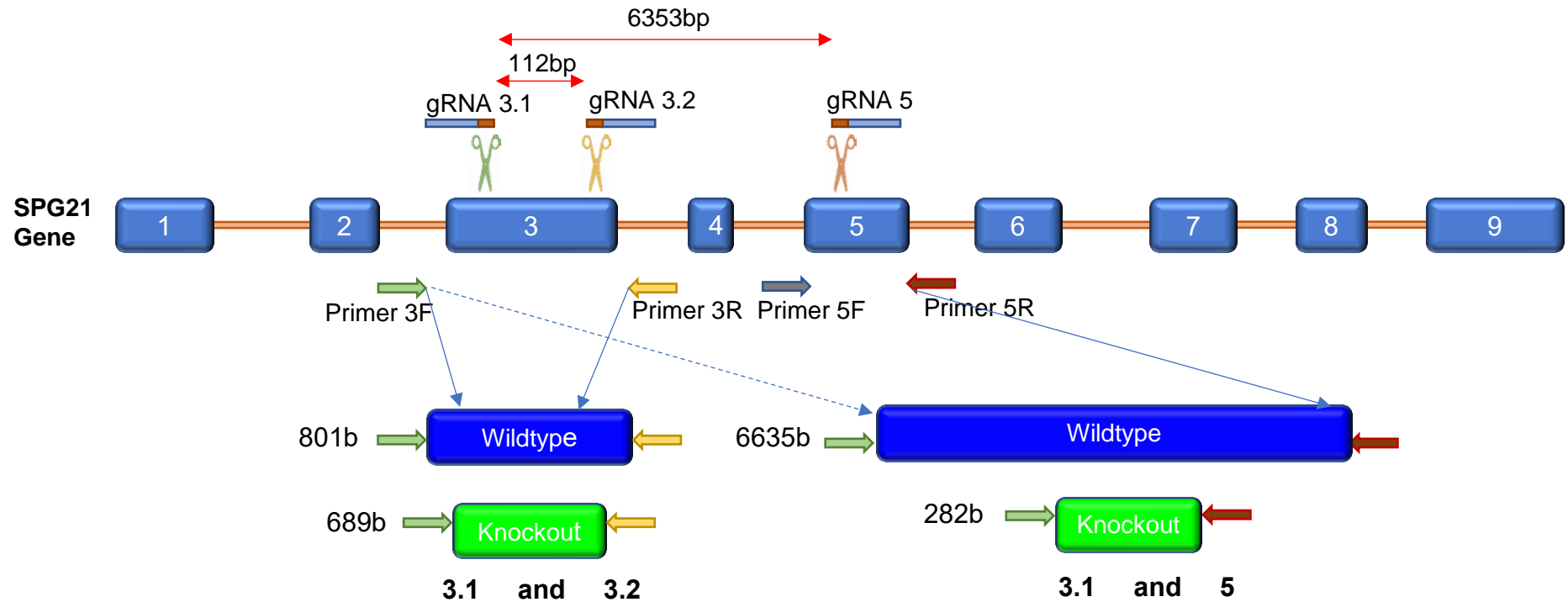


Figure 4.4. A schematic representation of the gRNA positions and the PCR product sizes with each corresponding genetic outcome. The 9 exons are shown and one set of gRNAs (gRNA 3.1 and 3.2) are within the third exon, and the second set of gRNAs use the same 3.1 gRNA in combination with another gRNA in the fifth exon. The relative positions of primers are also shown as arrows below the gene that are used for genotyping, in addition to their corresponding product size for a wildtype or knockout genetic outcome. If both gRNA 3.1 and gRNA 3.2 are successful in causing DSBs, then this will result in a 112bp deletion and a 689bp product will be amplified by PCR using primers 3F and 3R compared to the 801bp wild type product; both will be amplified for heterozygous colonies. The second set of gRNAs, gRNA 3.1 and gRNA 5 will result in a 6353bp deletion if successful, and using primers 3F and 5R will result in a 282bp product for a knockout. However as the wildtype 6635bp product is not easily distinguished by PCR both exon 3 and 5 using their respective primers need to be examined to confirm wildtype, knockout or heterozygous genetic outcomes.

CRISPR-Cas9 plasmids were prepared as outlined in the general methods (section 2.13) and Figure 4.5 indicates that all sequenced plasmids contain the expected gRNA insert.

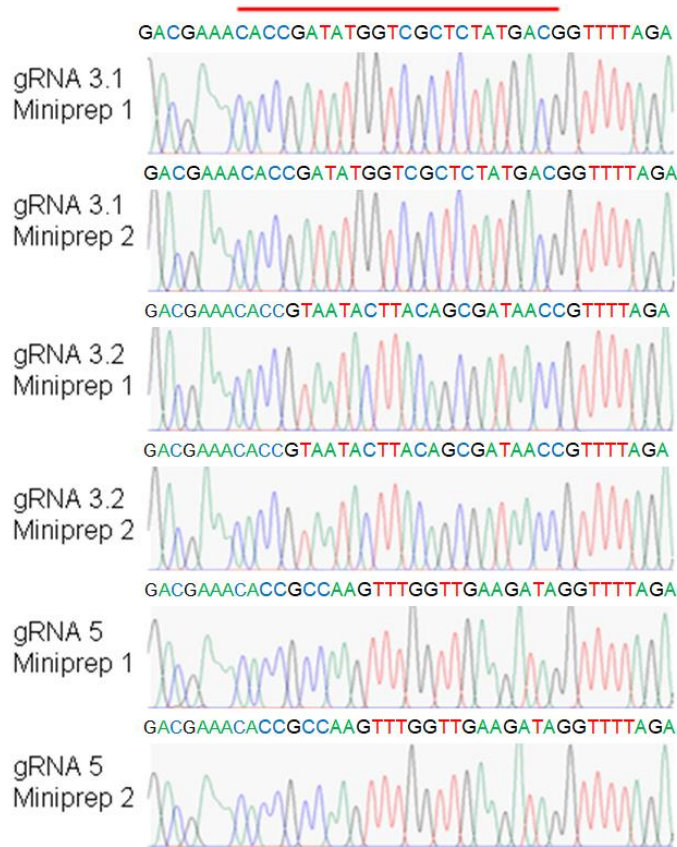


Figure 4.5. Sequencing validation of the gRNA containing plasmids. The red line indicates gRNA sequence region. Two minipreps from each experimental condition (3.1, 3.2 and 5) post restriction digest validation were chosen for sequencing to ensure the correct gRNA sequence had been inserted into the plasmid.

0.9 million cells SH-SY5Y cells were nucleofected with 1 μ g of each plasmid in their respective pairs (3.1 + 3.2 and 3.1 + 5), alongside a control sample where plasmid DNA was substituted for water. To obtain genetically identical colonies the nucleofected cells were sorted into single cells by double positive FACS, in addition to 100 cell colonies, as per the general methods. These colonies were then grown until there was sufficient cellular material for cell line validation where DNA and protein was extracted from each colony.

4.2.2 SPG21 Knockout Cell Line Validation

4.2.2.1 SPG21 Knocked-out Region Confirmed by PCR

First, the 100 cell colonies were genotyped as a preliminary screen to assess the efficiency of the two DSBs. For the exon 3 combination, primers were designed around exon 3 such that if both DSBs are successful, the PCR product expected is 112bp smaller than the 801bp wildtype product. A second pair of primers were designed around exon 5, and the forward exon 3 primer paired with reverse exon 5 primer used to study the exon 3 and 5 DSBs combination. For clarity, Figure 4.4 outlines the relative position of these primer pairs and the expected PCR products for each outcome. If both DSBs were successful, a large 6353bp deletion would result and the primers would span a 6635bp region, which is not easily amplified by PCR. However, knockout colonies would produce a 282bp product that is readily amplified by PCR. Figure 4.6 indicates that there is both wildtype and knockout DNA for the exon 3 DSBs in all three of the 100 cell sorted colonies due to the Cas9 enzyme cutting in both genetic locations, therefore it is likely that homozygous knockout colonies will be identified from the single cell sorted colonies. However, the exon 3 and 5 DSBs only produced a 282bp knockout band (highlighted by the red arrow) in one 100 cell sorted colony, indicating that this combination of gRNAs is not as successful as the exon 3 combination.

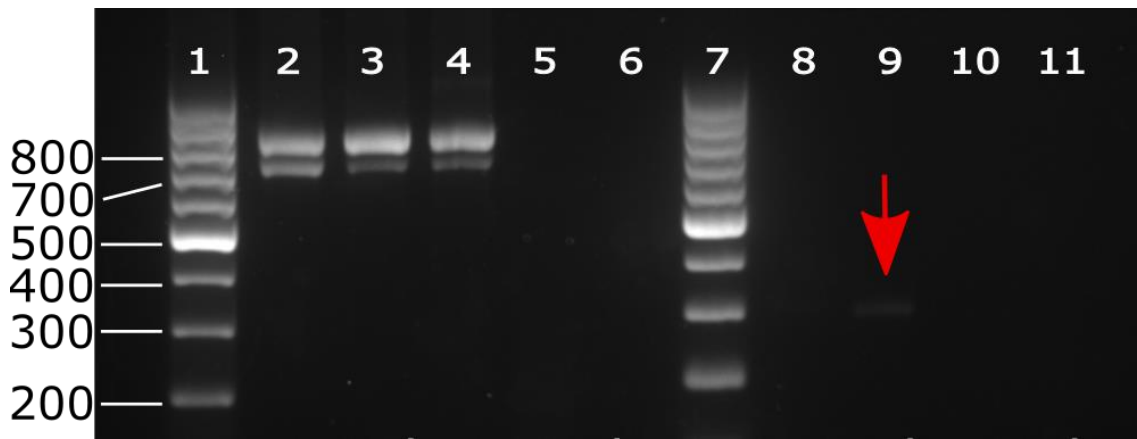


Figure 4.6. Genetic outcome from 100 cell sorted colonies. Three colonies for each experimental condition are shown, lanes 2-4 (exon 3) and 8-10 (exon 3 and 5), in addition to a negative control to confirm the absence of contamination. The colonies for the exon 3 condition indicate that at least some cells have the 112bp deletion. The exon 3 and 5 condition reveal only a faint band in the second colony (lane 9) indicating that this condition is not as successful. A 100bp ladder is in lane 1 and 7. A negative control containing water instead of DNA is included for each condition in lanes 5 and 11. Lane 6 is blank.

Next, the colonies grown from single cells were genetically assessed using the same primer pairs as the 100 cell sorted colonies. Figure 4.7 shows the genetic outcome determined by PCR from the exon 3 DSB colonies which include a mixture of wildtype, heterozygous and knockout colonies.

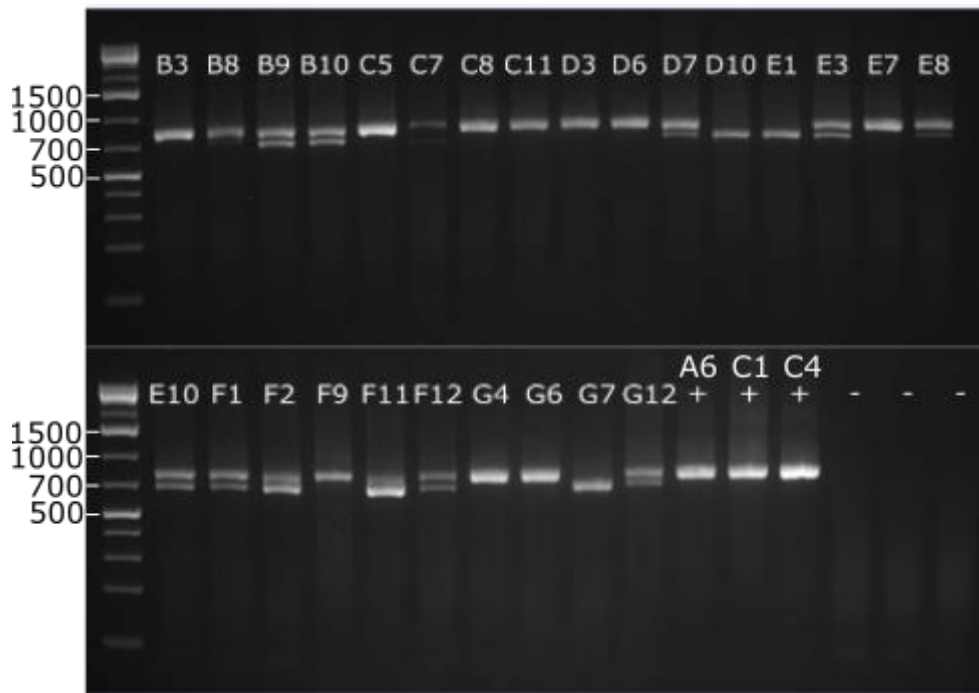


Figure 4.7. Exon 3 gRNA combination genetic outcome from single cell colonies. A mixture of wildtype, heterozygous and knockout colonies are distinguishable by gel electrophoresis. Larger 801bp bands represent a wildtype colony, knockout colonies present with a 689bp PCR product and heterozygous colonies show both bands. A 1kb ladder is in lane 1 of each gel. Three control colonies (A6, C1 and C4) and three negative controls containing water instead of DNA are included.

Figure 4.8 shows the results of the three PCR reactions to determine the genetic outcome of the exon 3 and 5 DSB colonies which reveals that G7 is heterozygous, and all other colonies are wildtype. However, it is plausible that the Cas9 enzyme created a DSB and the DNA insert was not removed, instead localised DNA repair could have occurred and this small change in bases is not distinguishable by gel electrophoresis. Due to the lack of success with this gRNA combination it was not pursued any further as the alternative exon 3 gRNA combination proved to be successful in creating knockout colonies.

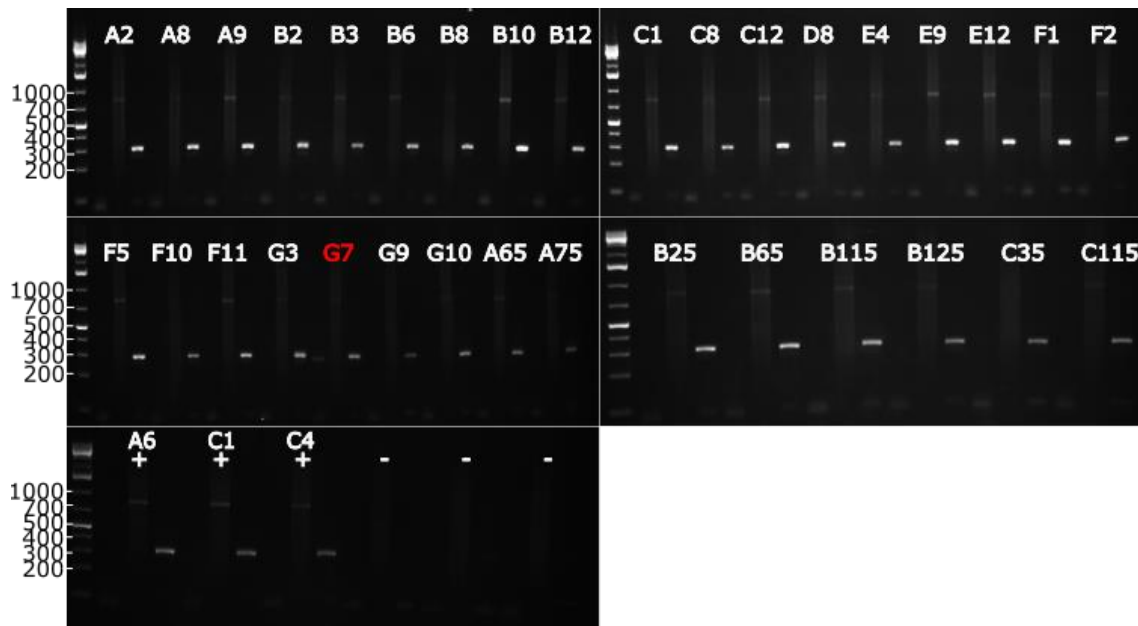


Figure 4.8. Exon 3 and 5 gRNA combination genetic outcome from single cell colonies. No knockout colonies are distinguishable by gel electrophoresis; only one colony is heterozygous as bands are present in all conditions, whereas all other colonies are wildtype. For each colony three individual PCR reactions were carried out, the forward exon three and reverse exon 5 primer pair to assess genetically recombined knockout sequences in addition to exon 3 and exon 5 individually. For each colony the first lane shows the exon 3 forward and reverse exon 5 primer pair, the second lane shows the exon 3 primer pair and the third lane shows the exon 5 primer pair. A 1kb ladder is in lane 1 of each gel. Three control colonies (A6, C1 and C4) and three negative controls containing water instead of DNA are included.

4.2.2.2 SPG21 Knockout Confirmed by DNA Sequencing

Nine (three controls, three heterozygotes and three knockouts) PCR products from the exon 3 DSBs were sequenced to confirm the knocked-out outcomes were as expected, Figure 4.9. Wildtype and heterozygous clones are as expected. Both D10 and G7 knockouts have clear outcomes that have been cleaved by the Cas9 enzyme three bases away from the PAM, subsequently resulting in the removal of the DNA fragment and the DNA sequence being repaired. This 112bp deletion results in a frameshift mutation and would be predicted to lead to nonsense mediated mRNA decay, therefore no protein will be translated. The E1 sequence is slightly different as it appears that one allele

has unexpectedly undergone cleavage three bases from the PAM site, but the second allele has been cleaved five bases downstream of the 3.2 gRNA, resulting in a 114bp deletion. This slightly larger deletion on one allele is in frame and not frameshift, therefore it is possible that this allele may still be transcribed and translated producing a truncated protein.

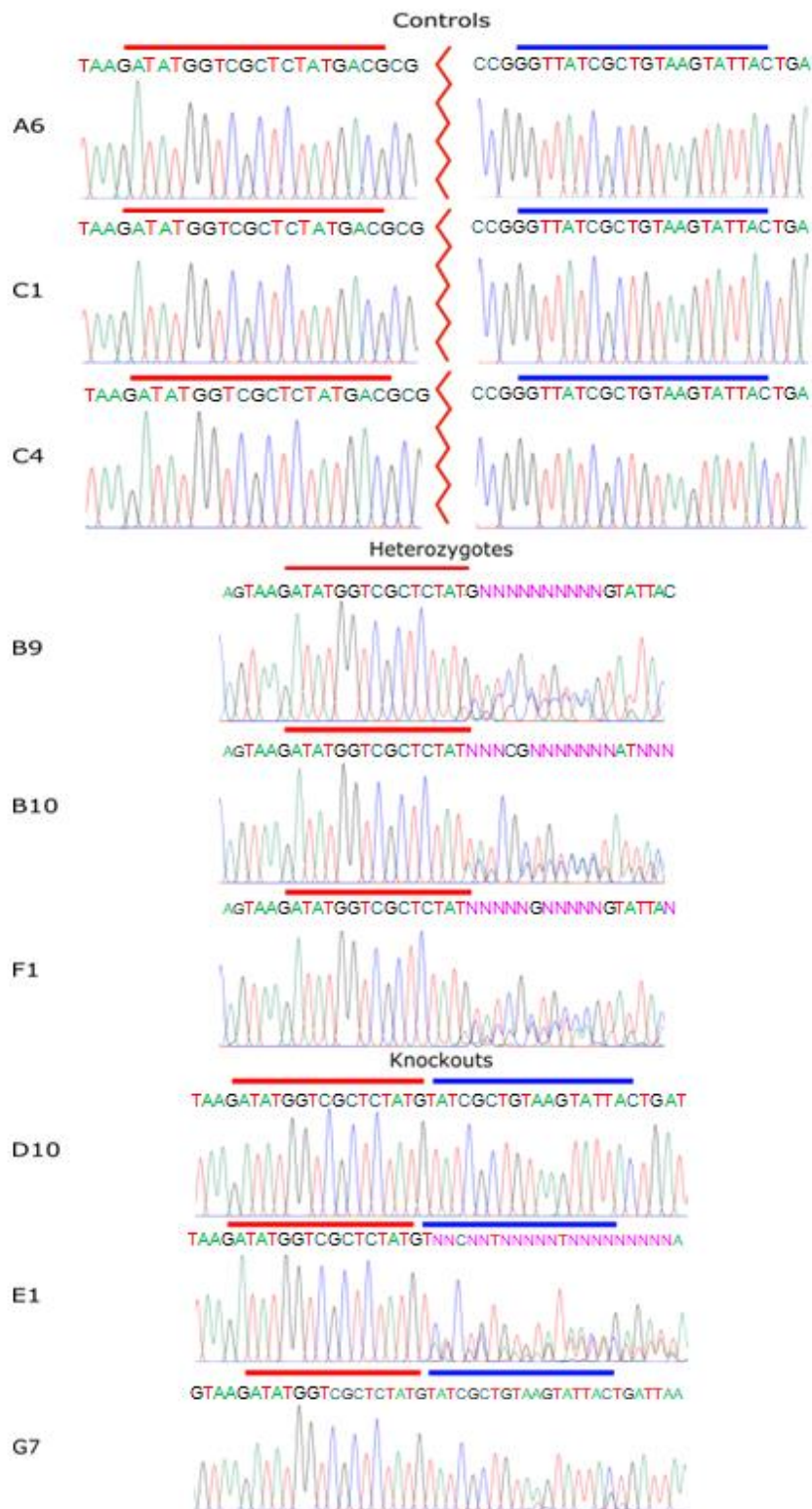


Figure 4.9. DNA sequencing results for control, heterozygous and SPG21 knockout cell lines. Red bars indicate the position of gRNA 3.1 and the blue bars indicate the position of gRNA 3.2. Three control cells sequenced show the gRNA sequence in their wildtype location with over 100bp between them, and the three heterozygous colonies show the appropriate pattern. The knockout colonies show the two gRNA regions side by side as the 112bp region was removed.

Out of the 84 mCherry and GFP double positive single cells that were sorted, only 32 were viable. Of those 32 viable colonies seven were confirmed, by PCR and gel electrophoresis, to be knockout colonies. Additionally, 14 of the colonies were wildtype and 11 were heterozygous, Figure 4.10A. The time taken for the colonies to reach ~80% confluency within the 96-well plate varied greatly from colony to colony ranging from 24-45 days after the cells were initially sorted; the knockout colonies were among the last to reach confluency as graphically represented in Figure 4.10B.

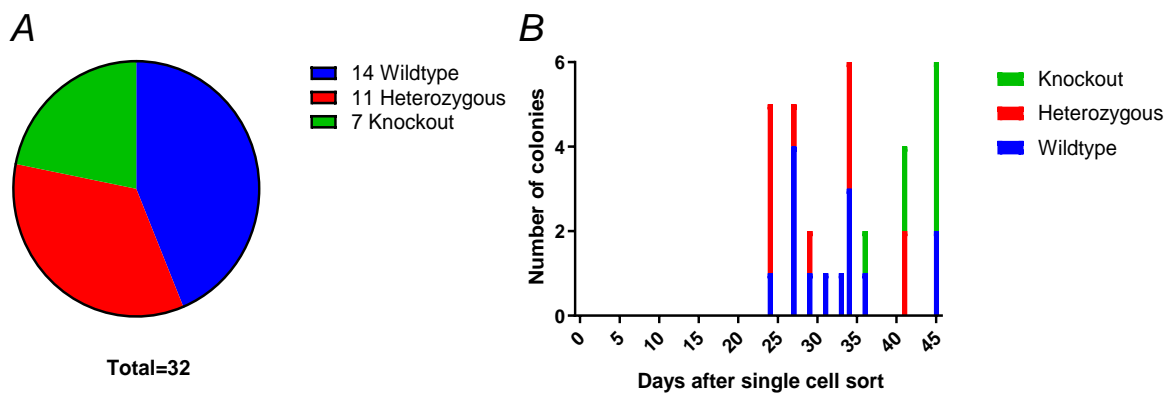


Figure 4.10. Genetic outcome of single cell colonies and the time taken for each to reach plate confluency. **A)** Total viable colonies and their genetic outcome as determined by gel electrophoresis. **B)** The time taken for each colony to reach the desired confluency post single cell sorting.

4.2.2.3 Maspardin Knockout Confirmed by Western Blotting

As the 112bp knocked-out region is predicted to result in nonsense mediated mRNA decay, maspardin protein product would not be expected. In order to validate the absence of maspardin in the cell lines, cell lysates were harvested by three independent experiments and Western blots performed, Figure 4.11. As expected maspardin is present in all control samples, and it is not present in the knockout samples. Curiously, heterozygous colonies also do not express

maspardin. This indicates these colonies may in fact be null for *SPG21* which may be due to the Cas9 enzyme having cleaved the DNA in just one location on the 'wildtype' allele rather than in both positions; just one DSB still has the potential to result in a frameshift mutation, however this is not distinguishable by PCR.

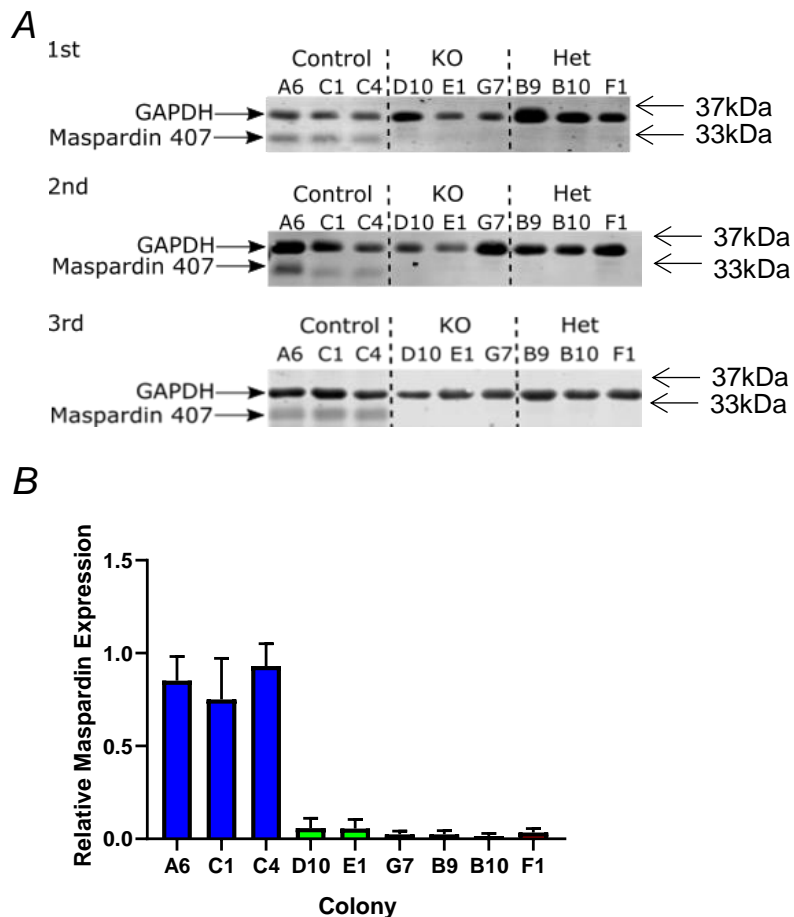


Figure 4.11. Expression of maspardin and GAPDH (A) and densitometry (B) of control, heterozygous and knockout colonies. A) Three separate blots are shown from three individual protein extractions probed with both maspardin 407 and GAPDH. Fluorescent secondary antibodies and detection was used. 33kDa bands present in control colonies indicate the expression of maspardin, however both heterozygous and knockout colonies do not. No additional smaller bands were detected by the maspardin antibody. The 37kDa bands indicate the expression of GAPDH used as a loading control to normalise maspardin expression. **B)** Quantification by densitometry with relative fold change of maspardin to GAPDH intensity determined by Image Studio Lite software.

4.2.2.4 Immunocytochemistry in Cell Models

The next stage of validation was to confirm the absence of maspardin by immunocytochemistry. The same colonies were seeded onto coverslips, stained with the previously used 407 maspardin antibody and imaged by confocal microscopy (Figure 4.13A). Immunofluorescence corresponding to maspardin protein can be seen in all control, heterozygous and knockout colonies. While there is a reduction in overall fluorescence in heterozygous and knockout colonies, clear punctate spots are present throughout the cell. An absence of fluorescence is expected in the knockout colonies, particularly as the maspardin protein is not present in Western blots using the same antibody. It is important to have a reliable antibody that can be used for immunocytochemistry, particularly to be able to reliably interpret colocalisation data. Consequently, two further maspardin antibodies with different epitopes were used, Figure 4.12 shows the epitope region of each maspardin antibody. All antibodies have the epitope towards the C-terminus of the amino acid chain, and all are downstream of the removed region in exon 3. Maspardin antibodies used in other previous studies were not commercially available [151, 211], however both the 407 and 436 antibodies were characterised by the Human Protein Atlas [229]; the 833 antibody was not supported with any references and was later discontinued.

Both the maspardin 436 and 883 antibodies were also shown to have significant fluorescence in the knockout colonies, Figure 4.13B and C. Unexpectedly, the 436 and 883 maspardin antibodies also showed a nuclear localisation, whereas the 407 antibody does not. All three antibodies detected protein dispersed throughout the cytoplasm of knockout, heterozygous and wildtype cell lines. Staining was repeated three times on three individually prepared coverslips and a DNA extraction, PCR, and gel electrophoresis was performed at the same

time to check for possible cell contamination, which there was not. Therefore, the maspardin antibodies may be detecting another protein in the cell, and are not entirely reliable to use for immunocytochemistry experiments. However, when staining 3T3 cells with just the Alexa Fluor 488 secondary antibody and imaging using a high gain there is also some cellular fluorescent detected, Figure 4.13D.

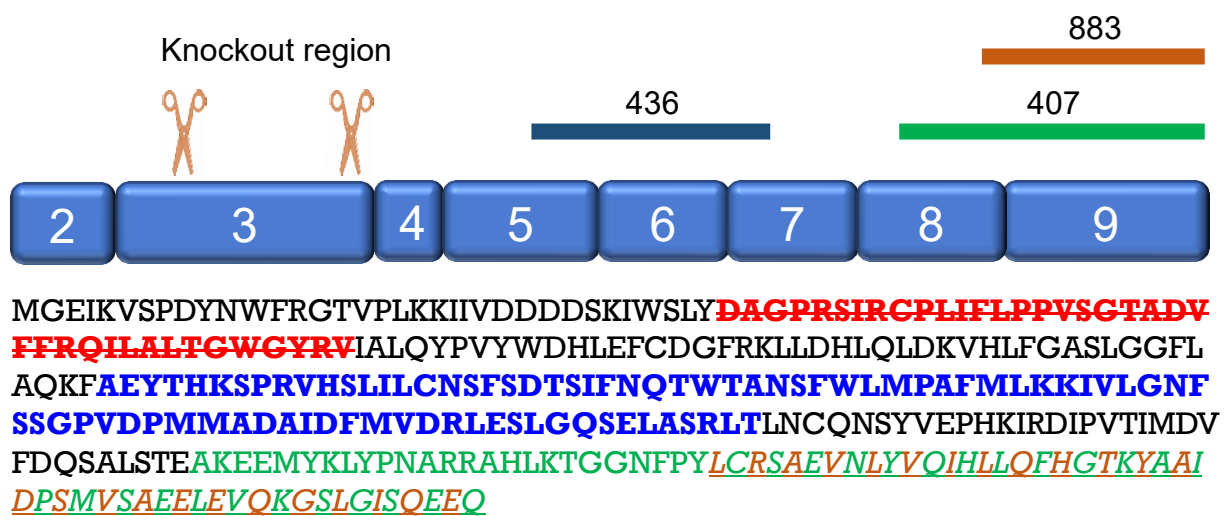
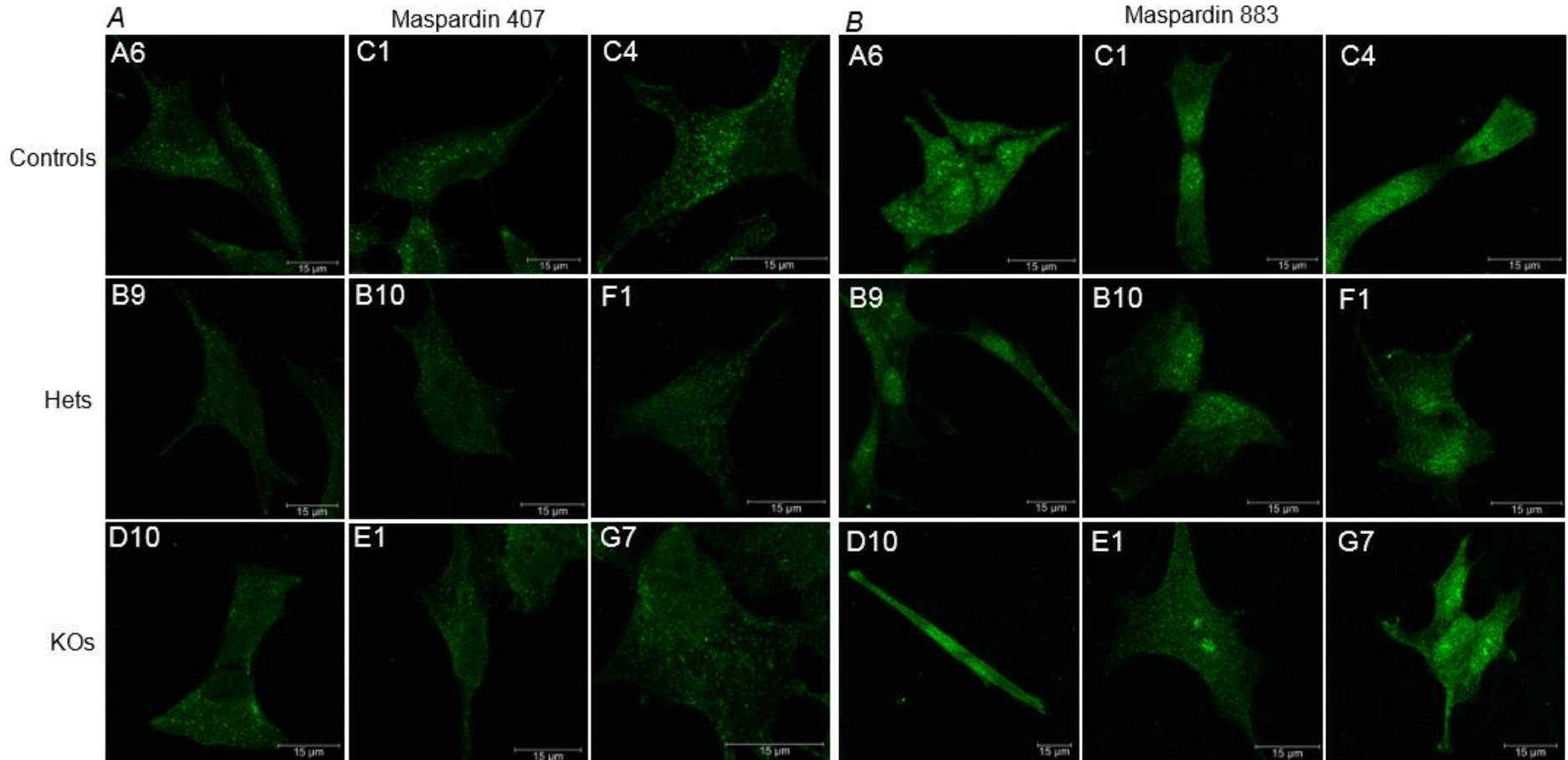
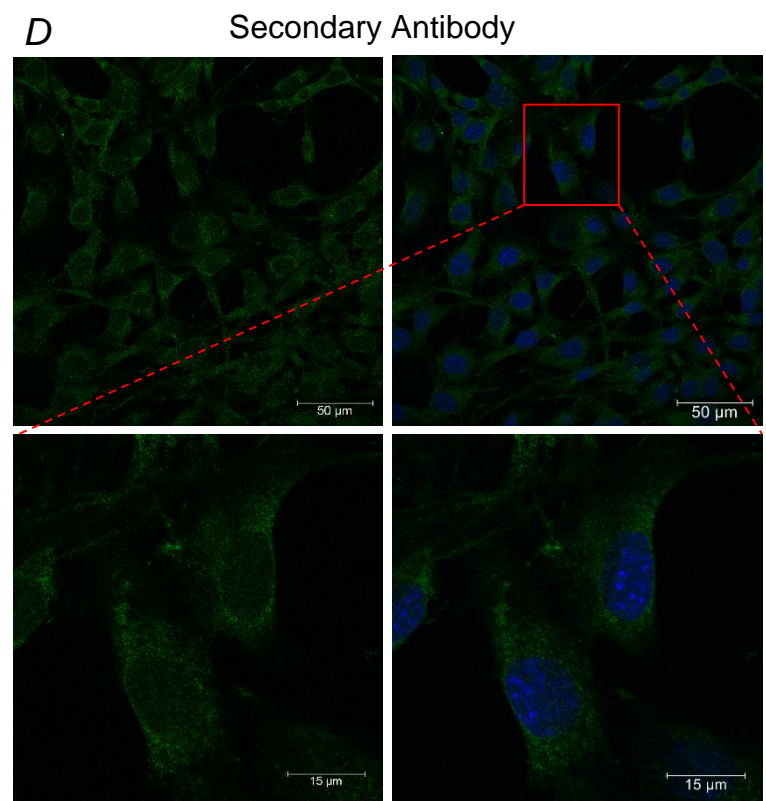
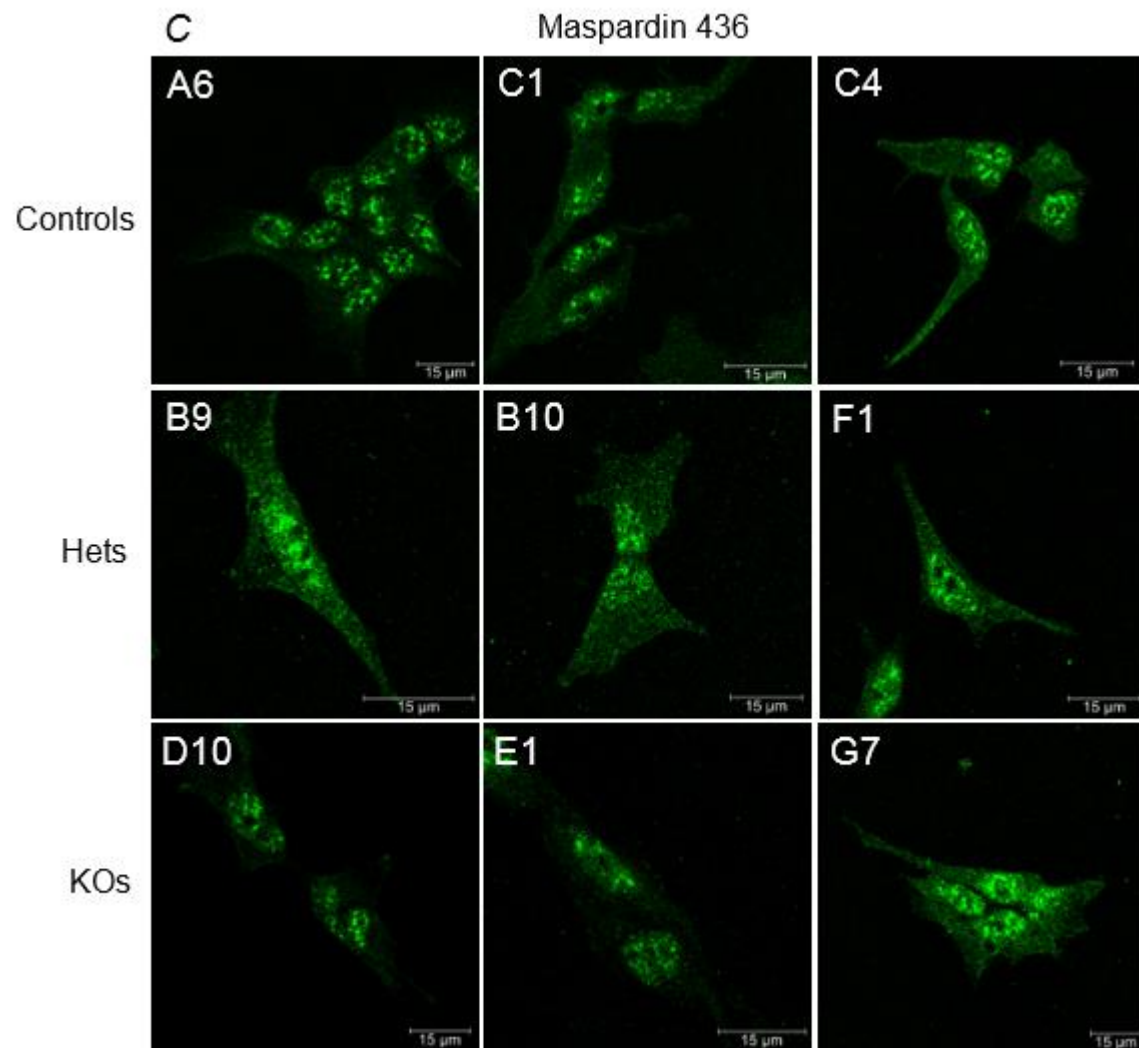


Figure 4.12. Schematic representation of the three epitope regions from the commercially available maspardin antibodies used. The schematic shows the positions of the epitopes relative to each other and the knocked-out region. The amino acid sequence details the precise epitope sequences. The epitope region for the maspardin 436 antibody is shown in blue and is towards the centre of the protein whereas the 883 (brown) and 407 (green) epitopes are at the c-terminus.

Figure 4.13. Maspardin expression in control wildtype, heterozygous and SPG21 knockout colonies probed with maspardin 407, 883 and 436. Cells were fixed with 4% PFA, stained with the appropriate maspardin antibody followed by Alexa Fluor 488 and viewed by confocal microscopy using a 63x oil immersion lens. Microscope settings were kept constant for each antibody. **A)** Maspardin 407. **B)** Maspardin 883. **C)** Maspardin 436. **D)** Secondary Alexa Fluor 488 antibody and DAPI in 3T3 cells.





4.2.2.5 Knockout Colonies Confirmed by RNA Sequencing

To further confirm knockout of *SPG21*, the RNA sequences for control and knockout cell lines were studied by isolating RNA for cDNA analysis, Figure 4.14 and Figure 4.15. Following PCR, the control wildtype band generated a 352bp product, and knockouts a 240bp product. Part of the 3.2 gRNA sequence is within the intronic region therefore this is not present in RNA as represented in Figure 4.15 with the blue bars showing the portion of the gRNA that is present within the exon and the green bars show the start of exon 4. The RNA data is as expected reflecting the DNA sequences although the G7 colony amplification was not successful. The DNA was once again extracted from all colonies to ensure there was no contamination, although the G7 colony could again not be successfully cleanly amplified; as such the clone was not taken forward for further analysis.



Figure 4.14. Gel image showing the cDNA outcomes in control and *SPG21* knockout colonies. Control bands are 352bp and knockouts are 240bp in size as expected, however G7 presents with multiple bands. 100bp ladder lanes 1 and 10, control colonies lanes 2-4, knockout colonies lanes 5-7 and negative controls containing water instead of DNA lanes 8 and 9.

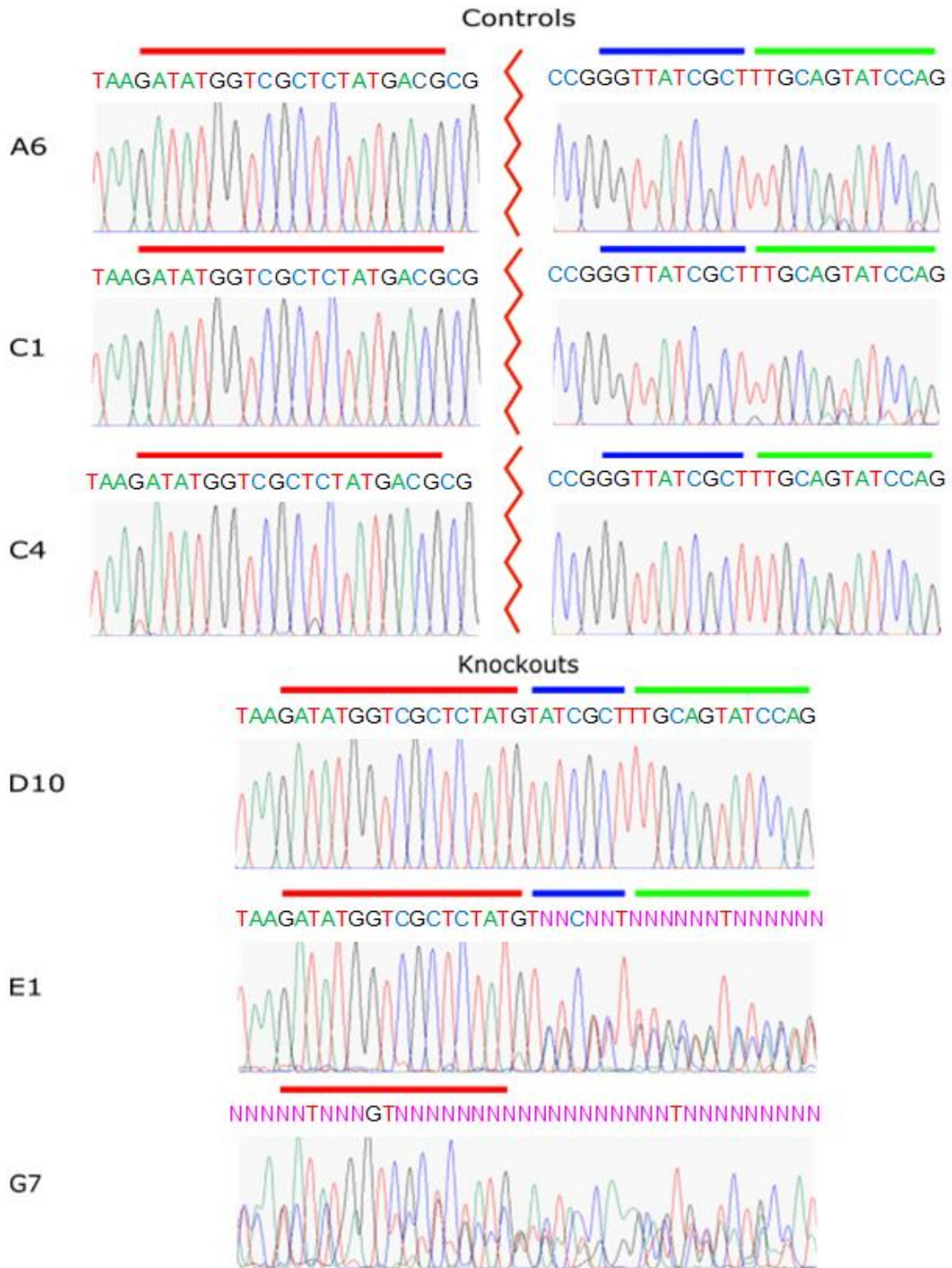


Figure 4.15. cDNA sequencing results for control and SPG21 knockout cell lines. Red bars indicate the position of gRNA 3.1, blue bars indicate the position of the gRNA 3.2 portion, green bars indicate the start of exon 4. Three control cells (A6, C1 and C4) sequenced show the gRNAs in their wildtype location with over 100bp between them. The knockout colonies (D10, E1 and G7) show the two gRNA regions side by side as the 112bp region was removed. Some of gRNA 3.2 is within the intronic region so is not present.

4.2.2.6 *SPG21 Knockout Cell Line Conclusion*

After the extensive validation of the cell lines generated by CRISPR/Cas9, control C1 and knockout D10 colonies were considered most appropriate for use in all future comparative experiments. D10 displayed clean DSBs validated by sequencing (with the 112bp *SPG21* sequence removal) and showed no maspardin expression by Western blot. As the E1 and G7 lines did not have the expected CRISPR-Cas9 outcomes, neither were taken forward for further analysis.

Additionally, no heterozygous colonies were selected as they are not certain to be true heterozygotes, and may in fact be knockouts due the lack of protein expression identified by Western blot. A knockout could also result from one Cas9 DSB on each allele, instead of two that are needed for the 112bp removal. This could still result in nonsense mediated mRNA decay and therefore no protein production, and not visualised by gel electrophoresis. In this case it is likely that DSBs have occurred in both positions on one allele as is seen by the smaller band, but the other allele has just one DSB.

4.2.3 *Generation of SPG21 Gene Constructs*

In order to overcome experimental limitations caused by the maspardin antibodies not binding specifically to maspardin, *SPG21* tagged gene constructs were generated including a C-terminal Myc-FLAG tag (kindly provided by Dr John Chilton), and a N-terminal YFP tag. The plasmids were both validated by 3T3 cell transfections and probing with a maspardin antibody against FLAG or the YFP fluorescent signal (Figure 4.16 and Figure 4.17). 3T3 cells were chosen for plasmid validation and colocalisation studies due to their large cytoplasmic area. Both maspardin constructs are expressed widely throughout the cytoplasm. A limitation with the use of plasmids is that the overexpression of

a protein is not completely representative of the function of that protein as it will be at much higher levels than the endogenous protein.

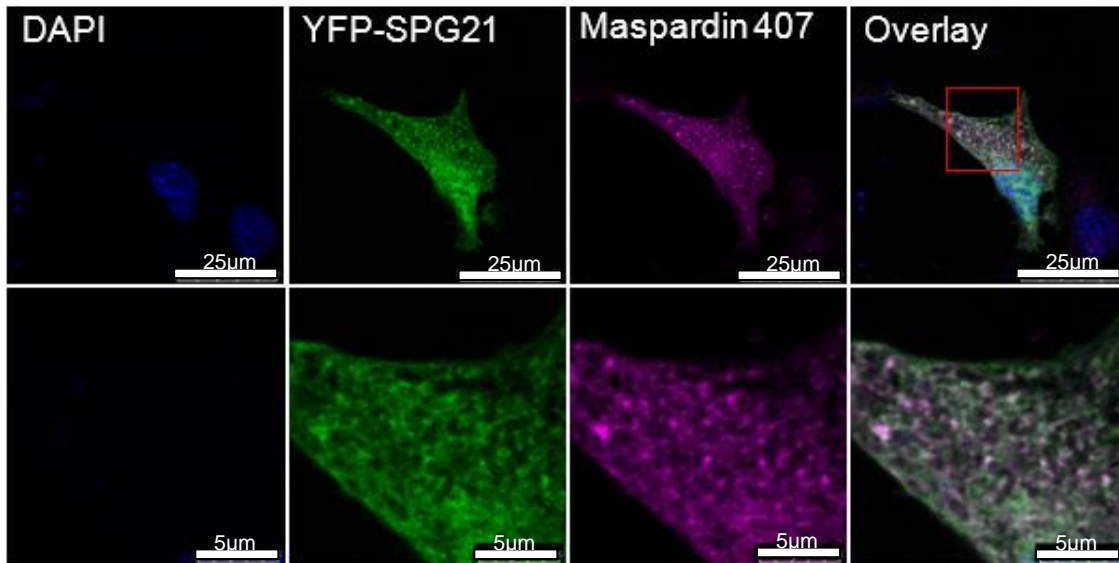


Figure 4.16. Endogenous maspardin colocalises with YFP-SPG21 plasmid. 3T3 cells were transfected with YFP-SPG21 (green), fixed and probed with the maspardin 407 (magenta) primary antibody followed by the rabbit 647 secondary antibody, and stained with DAPI (blue). Cells were viewed using a confocal microscope. Images show both whole cell (top panel) and the outlined magnification of a section of the cytoplasm (bottom panel).

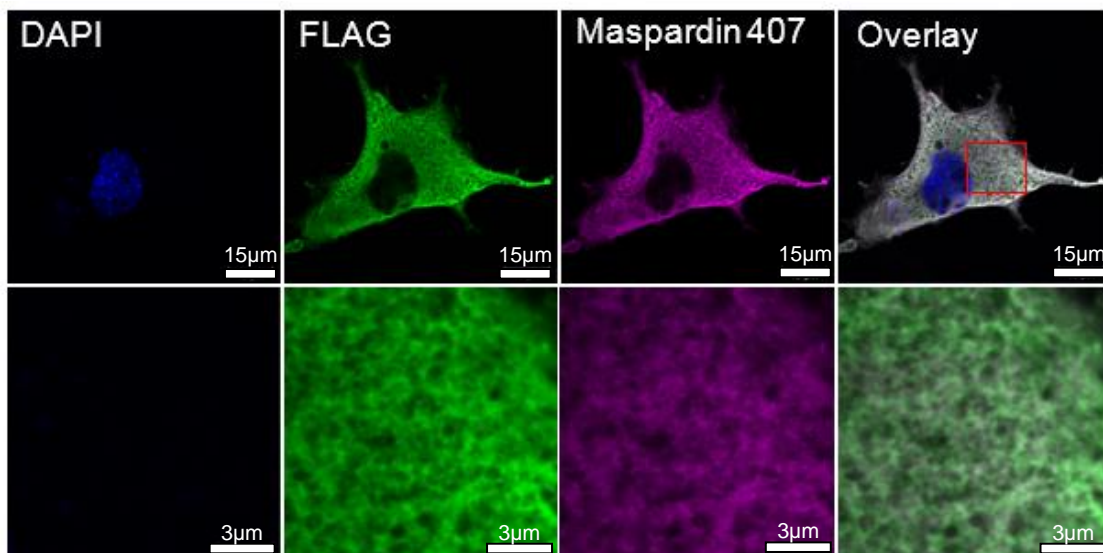


Figure 4.17. Endogenous maspardin colocalises with SPG21-myc-FLAG plasmid. 3T3 cells were transfected with SPG21-myc-FLAG (green), fixed and probed with the maspardin 407 (magenta) and mouse FLAG (F1804) primary antibodies followed by the rabbit 488 and mouse 635 secondary antibodies, and stained with DAPI (blue). Cells were viewed using a confocal microscope. Images show both whole cell (top panel) and the outlined magnification of a section of the cytoplasm (bottom panel).

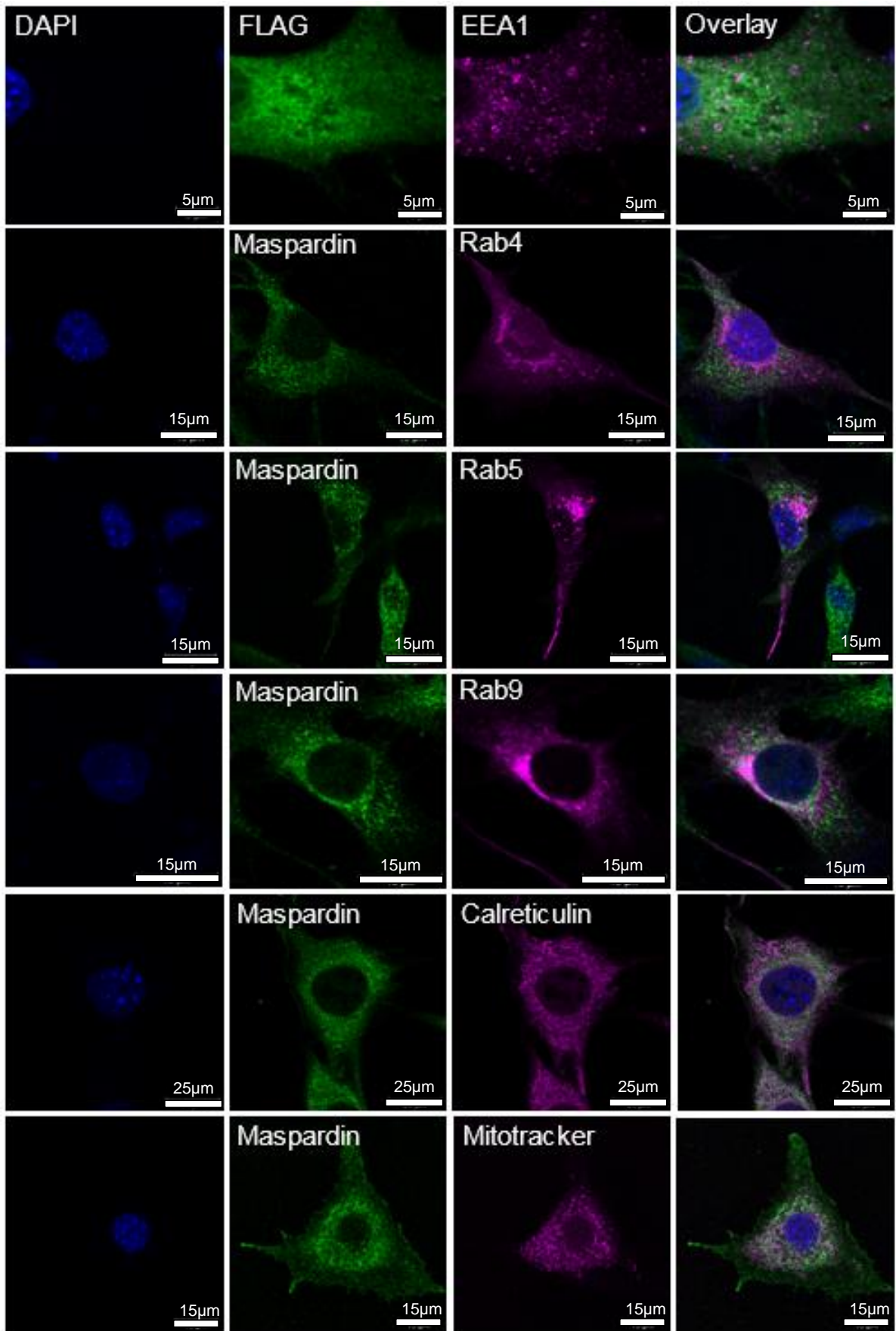
4.2.4 Subcellular Localisation Studies Indicate Possible Mitochondrial/ER Localisation

To improve understanding of the subcellular localisation of maspardin the maspardin 407 antibody was used in addition to various subcellular markers, including mitochondrial, ER and endosomal markers to investigate whether maspardin localised to a specific subcellular organelle. From these preliminary experiments maspardin was shown to not localise to a specific single organelle, with localisation more intense in the perinuclear region (Figure 4.18). Cells were transfected with SPG21-myc-FLAG and then probed with both FLAG and the early endosomal marker EEA1 to see if the two colocalised, revealing no obvious colocalisation with early endosomes. Other stages of the endosomal maturation process were also explored using Rab4, Rab5 and Rab9, none of which displayed considerable colocalisation with the maspardin 407 antibody although there is partial colocalisation with Rab9 (Figure 4.18 – fourth panel). To explore whether maspardin colocalised with mitochondria, Mitotracker and ATP5A were used. This indicated that maspardin occupies similar cellular space as the mitochondria. To investigate whether maspardin associates with the ER it was co-immunostained with calreticulin, which again revealed overlapping cellular space as this marker, similar to that seen with the mitochondrial markers.

As maspardin was revealed to be in the vicinity of both the ER and mitochondria in the perinuclear region, it could indicate that maspardin may localise to ER-mitochondria contact sites. In order to assess this hypothesis, 3T3 cells were transfected with a mCherry-KDEL containing plasmid localising to the ER, and then co-immunostained with both maspardin and the mitochondrial marker ATP5A. This showed several precise regions, as indicated by the red arrows in

Figure 4.18 (bottom panel), where all three markers are in extremely close contact, although not colocalising completely.

As data from the *SPG21* knockout cell lines indicates that the maspardin antibody may not solely detect maspardin, this imaging must be interpreted with caution. However, it does indicate that maspardin may be present in the mitochondrial/ER subcellular region.



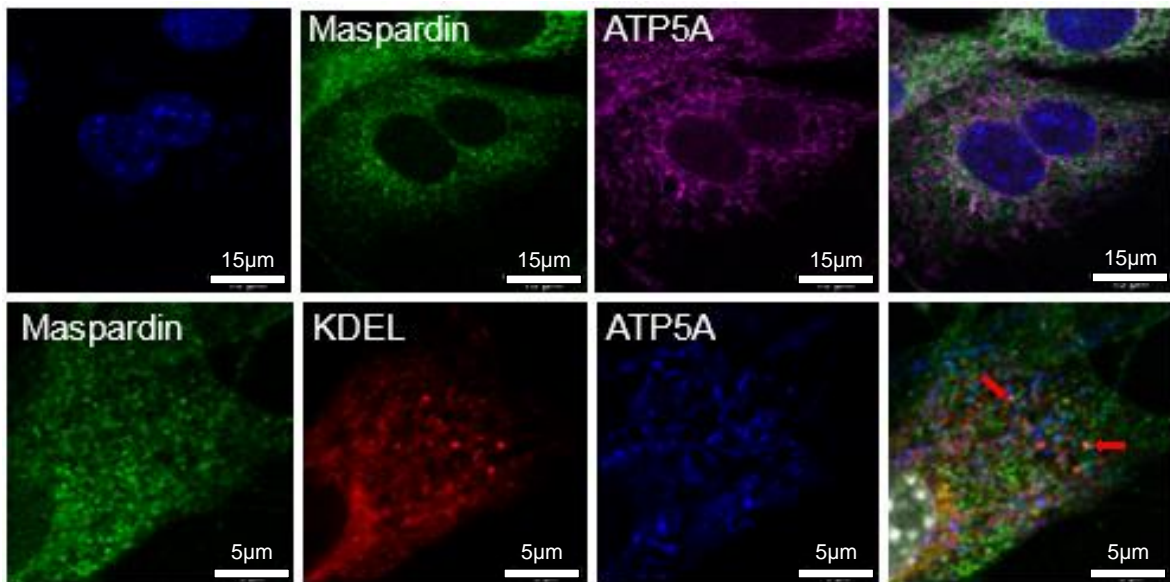


Figure 4.18. Maspardin localisation with endosomal, ER and mitochondrial markers in 3T3 cells. For EEA1 staining the cells were transfected with SPG21-myc-FLAG and probed with FLAG (F1804) and EEA1. Rab4, Rab5 and Rab9 plasmids were transfected into cells and then immunostained with maspardin 407. Maspardin 407 and calreticulin or ATP5A were co-immunostained. Mitotracker was pre-stained prior to fixing and then immunostained with the maspardin 407 antibody. For assessing ER-mitochondria contact sites, cells were transfected with the BiP-mCherry-KDEL plasmid and immunostained with maspardin 407 and ATP5A. The primary antibodies were then immunostained using the rabbit 488 and mouse 635 fluorescent secondary antibodies, as required, and viewed by confocal microscopy.

4.2.5 Maspardin Molecular Binding Partners Determined by Mass Spectrometry

To further understand the biological role of maspardin, studies were undertaken to identify molecular binding partners using co-immunoprecipitation followed by mass spectrometry analyses. The binding partners of both endogenous (407 antibody) and transfected/overexpressed (SPG21-Myc-FLAG) maspardin were assessed, in addition to controls with each undertaken in duplicate. HEK 293 cells were used for this experiment due to their high transfection efficiency.

In addition, samples were probed by Western blot to assess the efficiency of protein pull-down (Figure 4.19). As expected, maspardin protein was not detected in control samples when probed with FLAG antibody (both negative

unbound control samples detected GAPDH). Similarly FLAG was identified in SPG21-Myc-FLAG overexpressed samples in both pull-down and negative unbound samples, likely due to the overabundance of maspardin in these overexpression samples so that not all of the protein was pulled down. However, the pull-down was considered successful as GAPDH was detected only in the negative unbound samples (shown by red circles). The endogenous samples are as expected with maspardin detected only in both pulled down samples and GAPDH only detected in the negative unbound samples. A notable band (~50kDa) was detected on western blots of the endogenous samples, and detected (faintly) in the control samples, likely to be the result of non-specific binding to the immunoglobulin heavy chain which is commonly seen in co-immunoprecipitation experiments.

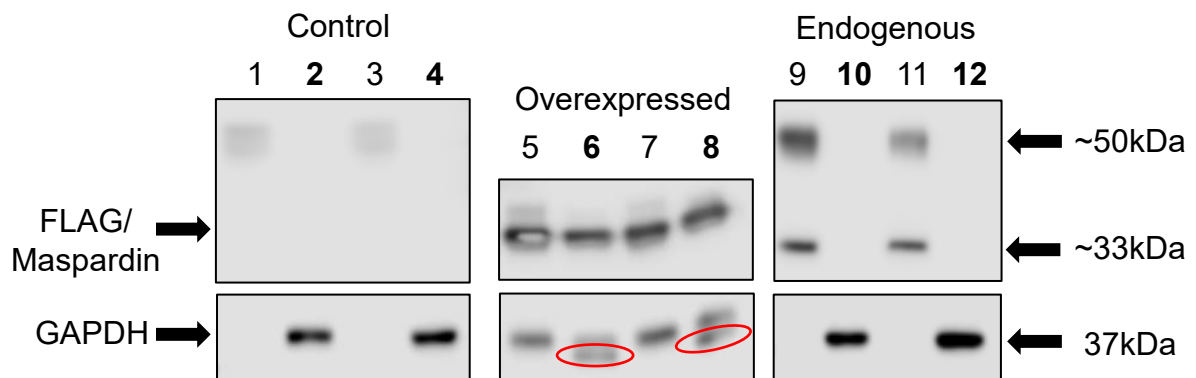


Figure 4.19. Immunoprecipitation of endogenous and overexpressed maspardin. Protein lysates from HEK 293 cells (control and endogenous) and HEK 293 cells transfected with SPG21-myc-FLAG (overexpressed) were analysed for maspardin (molecular weight: 33kDa) and FLAG (F1804). ECL used for blot detection. Immunoprecipitation of samples were performed in duplicate and a negative unbound control (indicated in bold numbers) was taken for each sample involving the remaining cellular lysate containing protein not bound to beads. GAPDH probed as a loading control (molecular weight: 37kDa), as expected GAPDH was only observed in the negative unbound controls. Numerical identification; 1&3: control samples, HEK 293 lysate with FLAG pull-down; 2&4: negative controls of 1&3; 5&7: SPG21-myc-FLAG transfected lysate with FLAG pull-down; 6&8: negative control of 5&7; 9&11: HEK 293 lysate with maspardin (407) pull-down; 10&12: negative controls of 9&11.

Mass spectrometry data from this experiment identified 966 and 838 putative binding partners for endogenous maspardin (experiment duplicates 1 and 2), and 1600 and 1636 binding partners in the overexpression experiments (duplicates 1 and 2); 291 and 210 proteins were identified in the control groups. For analysis, the control proteins were excluded from the endogenous and overexpressed samples, and molecules identified in all four samples were taken forward for further analysis initially. There were 665 molecules common to both the overexpressed experiments, and 415 common to both endogenous experiments, with 86 present in all four experiments. The proteins were ordered based on a protein score utilised by The University of Bristol Proteomics Facility, this score being based on the number of peptides identified for each particular protein.

Initial analysis consisted of molecules common to both endogenous (Figure 4.20A) and overexpressed experiments (Figure 4.20B) individually was undertaken using the STRING database, to assess potential molecular interactions and biochemical pathways [230]. The STRING analysis criteria used all evidence modes to analyse the localisation and function of each protein to give an overview of common themes among potential binding partners. Many of the proteins were identified to be nuclear related (shown in pink), however a large proportion involved molecules localised to the mitochondria and ER (blue and red) with a subset involved in membrane trafficking (yellow). While this approach is in some ways imprecise as not all protein-protein interactions are fully verified, similar pathways were identified in both endogenous and overexpressed experiments.

Next, the 86 proteins that were common to all samples were analysed to provide the highest confidence of finding true binding partners of maspardin. A

similar analysis was performed using STRING to identify protein-protein interactions and potential subcellular localisation, in addition to Reactome pathway analysis to gauge the overall function of the proteins and pathways identified [231]. Figure 4.21A shows the subcellular localisation of these proteins, which as in our initial analysis identified nuclear proteins (yellow), with a smaller percentage localised to mitochondria and ER (red and blue). Interestingly, a significant proportion are found to be vesicular, as well as being localised to the mitochondria and ER. Two protein complexes were identified as potential binding partners; the mitochondrial contact site and cristae organising system (MICOS) and associated proteins, and the ER oligosaccharyl transferase complex (OST) complex, circled in red and blue (Figure 4.21A). The Reactome pathway analysis (Figure 4.21B) indicates the function of these proteins, with the MICOS complex being involved in mitochondrial cristae formation, and the OST complex in protein glycosylation. A large proportion of the previously identified vesicular proteins are implicated in membrane trafficking (green), and a subset of these are involved in Golgi-to-ER retrograde transport (red).

To further condense this large dataset, only the top 100 hits of each sample were analysed. This identified several common proteins including tubulin beta-4a; a member of the ER OST complex, ribophorin-1; heat shock cognate 71 protein; the peroxisomal protein PMP70; and the mitochondrial MICOS protein mitofilin. Several of these proteins were selected for follow up with further experiments due to their association with neurological conditions, and potential functional overlap with maspardin. Tubulin beta 4a mutations are associated with dystonia [232]; PMP70 is a fatty acid and bile acid transporter known to cause Zellweger syndrome when mutated with symptoms including hypotonia,

seizures and skeletal abnormalities [233]; and mitofilin has recently been associated with Parkinson's disease and other MICOS proteins have been implicated in ALS [234, 235].

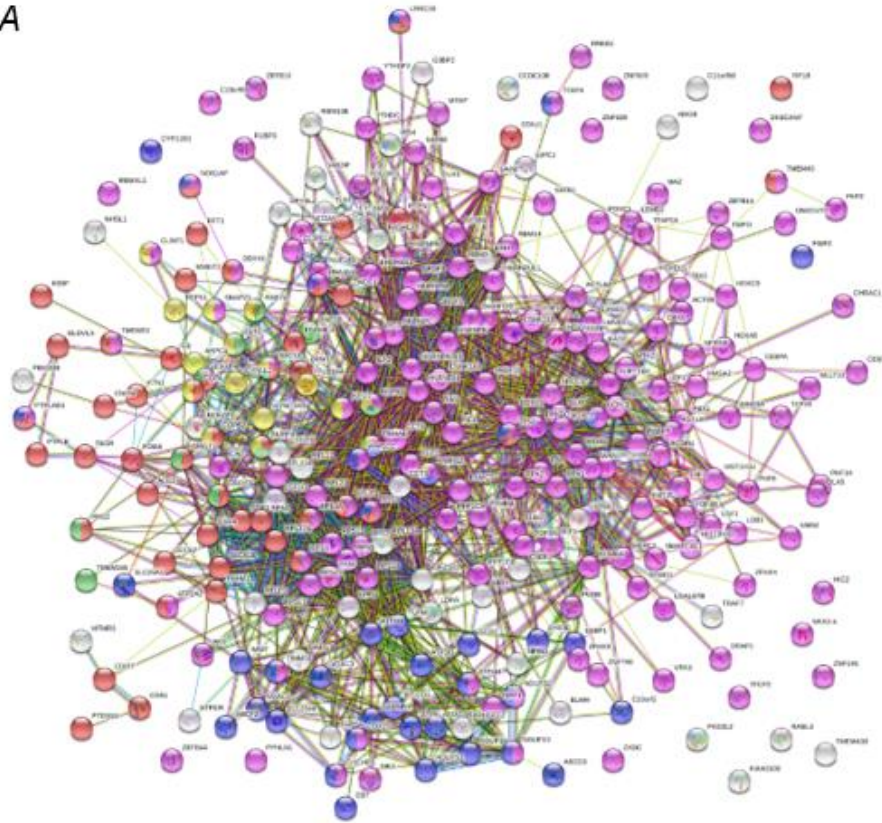
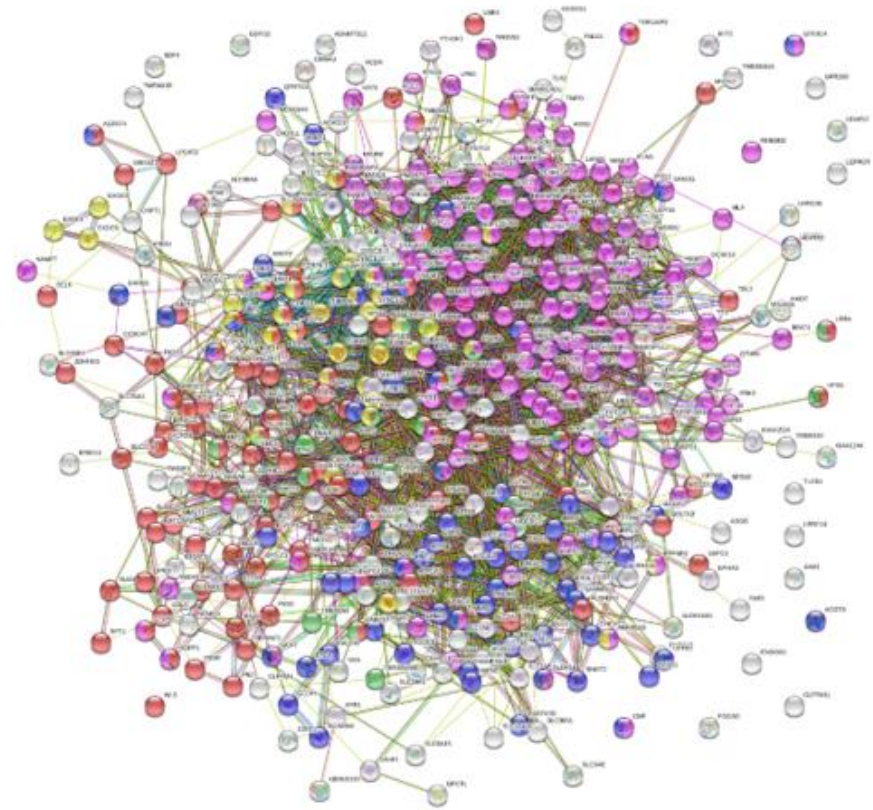
A**B**

Figure 4.20. Common subcellular localisation of endogenous (A) and overexpressed (B) maspardin binding partners. Both figures are generated and modified using the STRING database. The endogenous (A) shows 280 of the 415 accession numbers and the overexpressed (B) shows 448 of the 665 accession numbers recognised by STRING. Blue ● = mitochondrial, red ● = ER, green ● = lysosomal, yellow ● = membrane trafficking and pink ● = nuclear.

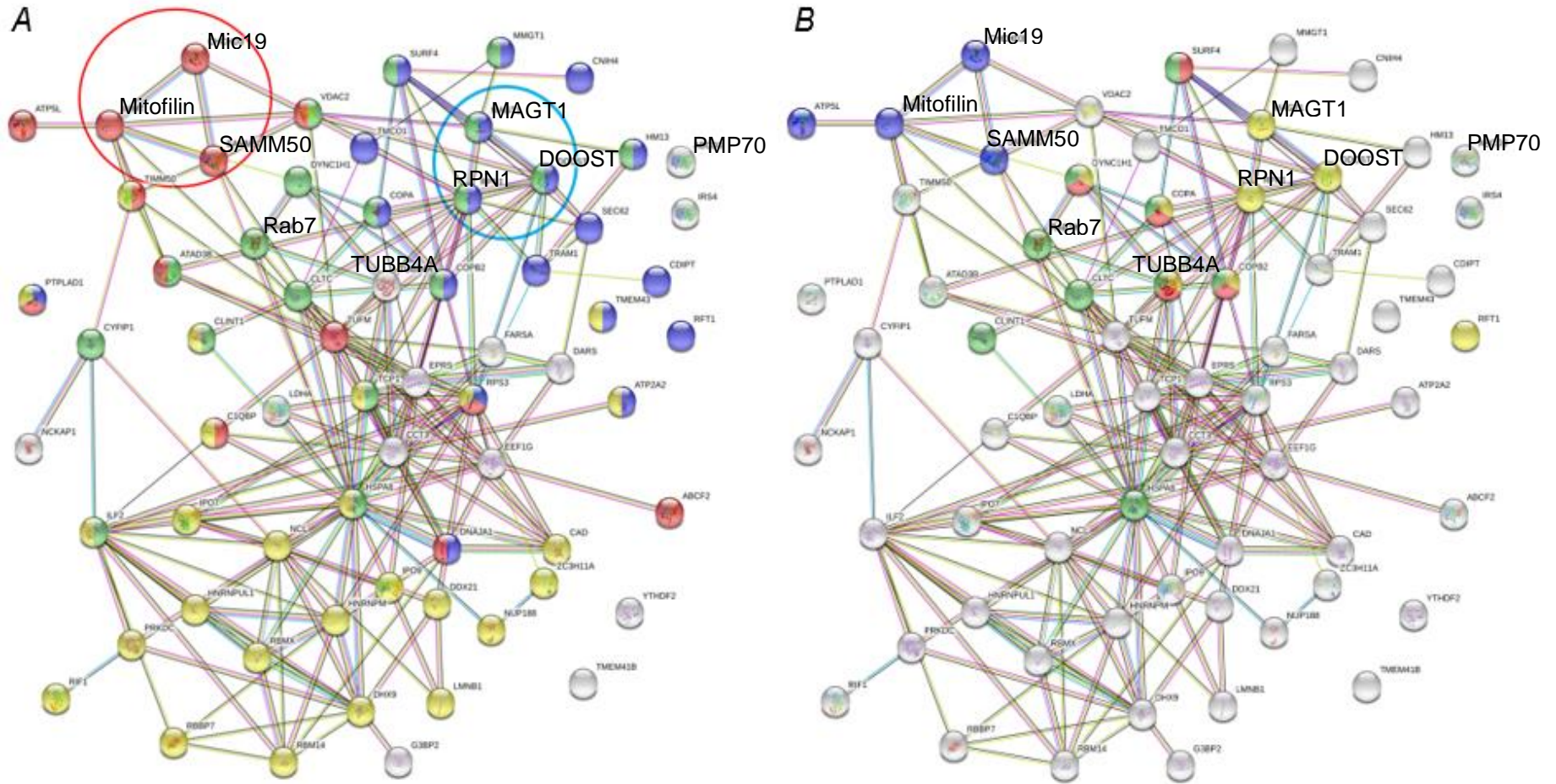


Figure 4.21. Subcellular localisation (A) and function (B) of maspardin binding partners common to endogenous and overexpressed samples. Both figures are generated and modified using the STRING database. **A)** Red ● = mitochondrial, blue ● = ER, green ● = vesicular and yellow ● = nuclear. Red circle shows MICOS complex members and associated outer mitochondrial membrane SAMM50. Blue circle shows OST complex members. **B)** Blue ● = cristae formation, green ● = membrane trafficking, yellow ● = asparagine N-linked glycosylation and red ● = Golgi-to-ER retrograde transport.

As mentioned, ALDH16A1 had previously been identified as a binding partner of maspardin from co-immunoprecipitation of HeLa cell lysates and mass spectrometry [211]. However, the binding partner analysis performed here did not identify ALDH16A1 in endogenous maspardin pull-downs, although it was identified in both overexpressed samples. Rab7 has also previously been identified as a maspardin binding partner from mass spectrometry analysis on HEK 293 cell lysates, pulled down with Rab7 [218]. A Rab7 interaction was identified here in both endogenous and maspardin overexpressed HEK 293 cells.

4.2.5.1 Binding Partner Validation by Immunocytochemistry

The MICOS complex inner mitochondrial membrane protein mitofilin, and its associated outer membrane protein SAMM50; the peroxisome protein, PMP70; tubulin beta 4a; Rab7; and ALDH16A1 were selected for further study. The antibodies for these putative binding partners (except for Rab7 where a Rab7a-mCherry plasmid was used) were co-immunostained with maspardin 407 in order to investigate cellular colocalisation, Figure 4.22. Of these Rab7 was identified to clearly localise to the same cytoplasmic perinuclear region as maspardin. The inner mitochondrial protein mitofilin and its associated outer mitochondrial membrane SAMM50 protein, revealed partial colocalisation with maspardin in the perinuclear region. Likewise, the PMP70 and ALDH16A1 displayed a degree of localisation with maspardin. The tubulin antibody identified a clear cellular tubulin network as expected, however this network did not obviously colocalise with maspardin.

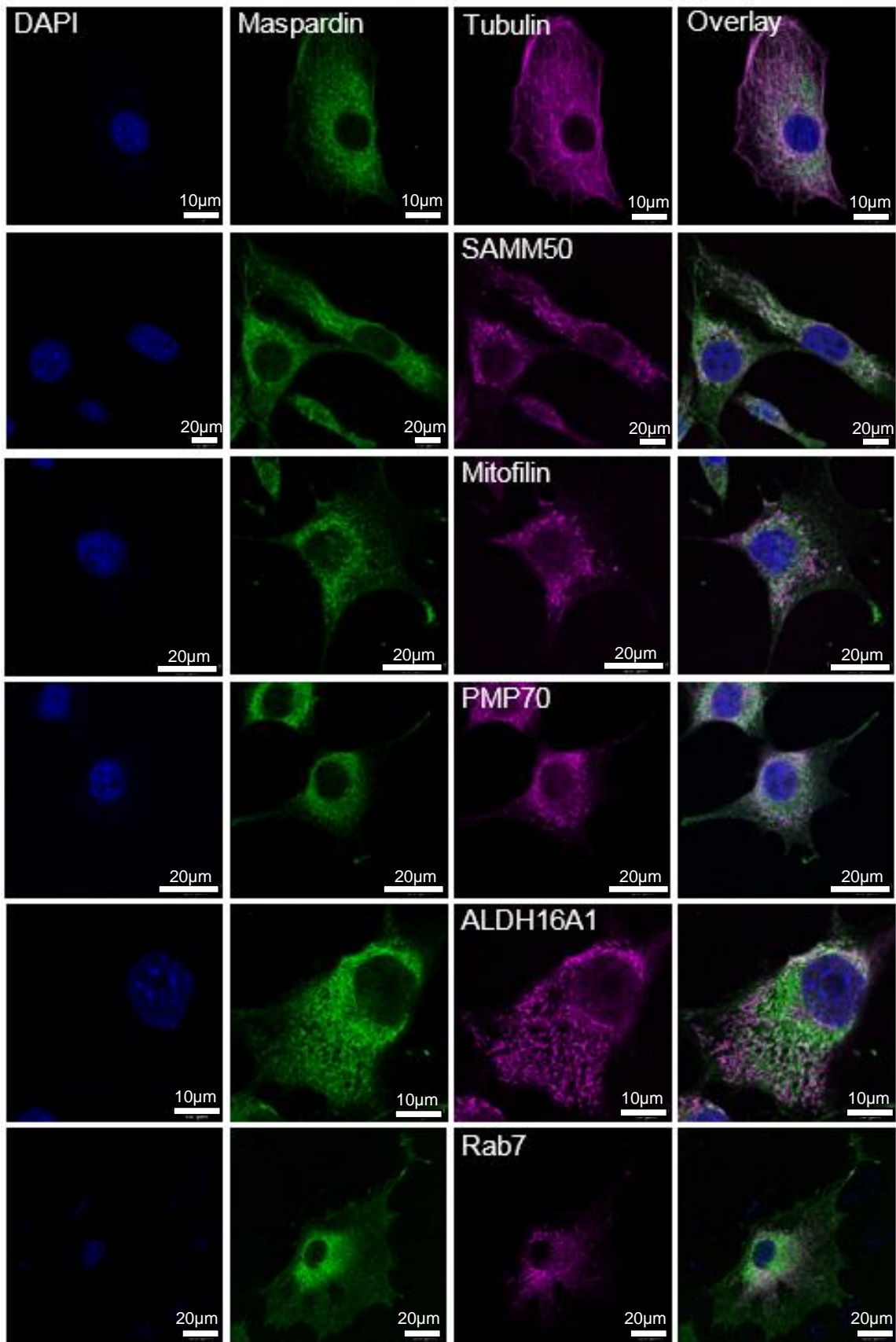


Figure 4.22. Binding partner colocalisation with endogenous maspardin. 3T3 cells stained with the maspardin 407 primary antibody in addition to the relevant binding partner antibody except for Rab7 which was transfected. The primary antibodies were then immunostained using the rabbit 488 and mouse 635 fluorescent secondary antibodies and viewed by confocal microscopy.

Given that the maspardin antibody was found to not solely detect maspardin this data set was further supported by repeating the experiment with the SPG21-myc-FLAG plasmid. The plasmid was transfected into 3T3 cells and then probed for FLAG alongside each candidate binding partner, Figure 4.23. While this data was difficult to interpret due to overexpression of the gene construct, again SAMM50 and mitofilin displayed a level of colocalisation with maspardin. The SPG21-myc-FLAG plasmid did not display the same dominant perinuclear intensity that is observed with the maspardin 407 antibody, therefore a strong overall cellular colocalisation cannot be identified with Rab7.

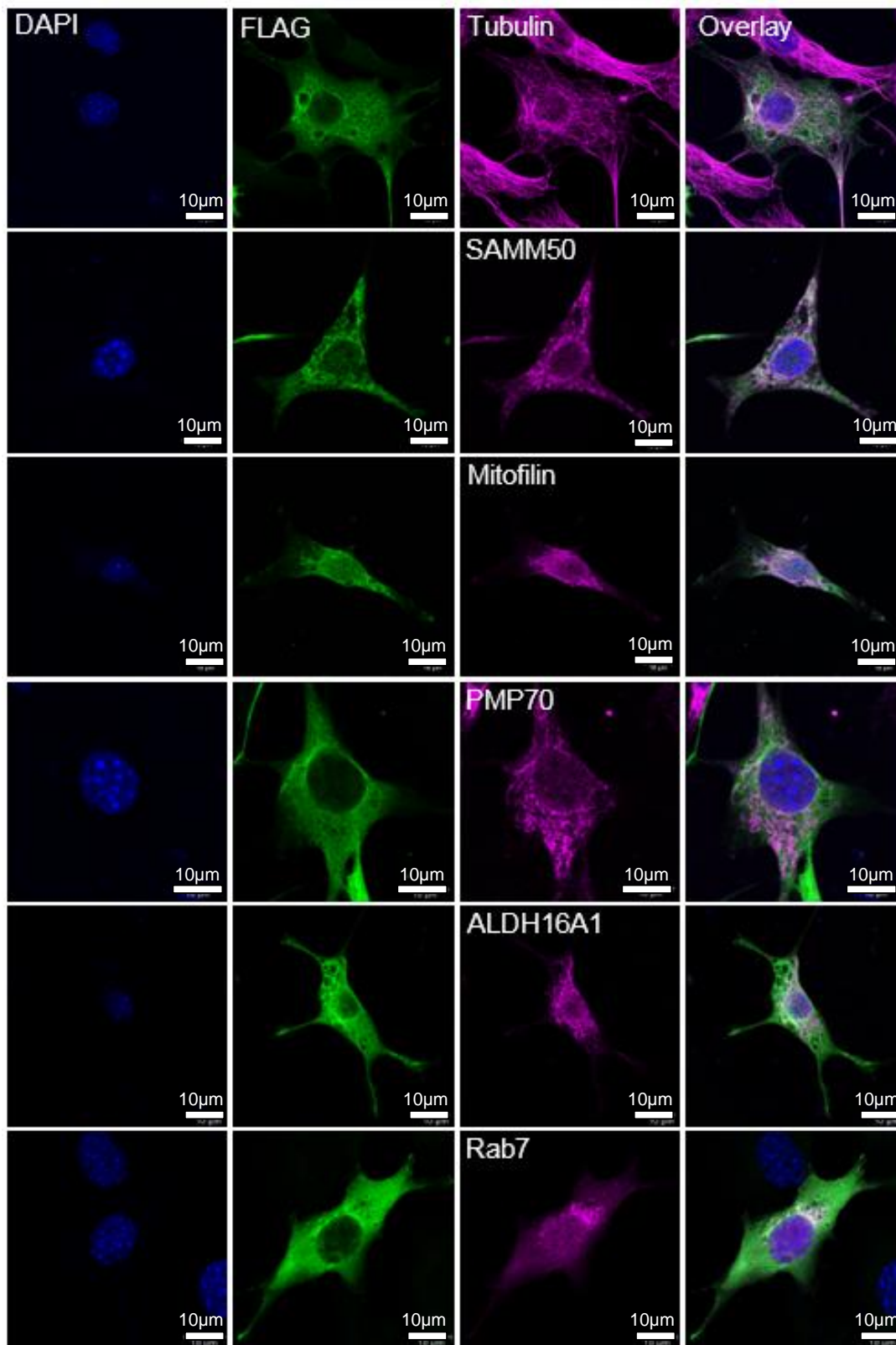


Figure 4.23. Binding partner colocalisation with SPG21-myc-FLAG. 3T3 cells transfected with the SPG21-myc-FLAG plasmid and probed with FLAG (F7425) primary antibody in addition to the relevant binding partner antibody except for Rab7 which was co-transfected alongside SPG21-myc-FLAG. The primary antibodies were then immunostained using the appropriate rabbit 488 and mouse 635 fluorescent secondary antibodies and viewed by confocal microscopy.

4.2.6 Live Cell Imaging

4.2.6.1 Maspardin Surrounds Vesicular Structures

Due to the diffuse cellular localisation with the FLAG tagged plasmid, the fluorescently tagged maspardin plasmid was prioritised for use in live cells to avoid potential issues of antibodies recognising alternate proteins. When 3T3 cells were transfected with YFP-SPG21, maspardin was clearly identified in the immediate vicinity of vesicular structures predominantly located in the perinuclear region and not at the cellular periphery (Figure 4.24A). Interestingly, other (mostly larger), circular structures are also identified that are not decorated by maspardin (blue arrows, Figure 4.24A). These vesicles were investigated further by measuring their diameter, revealing that maspardin surrounded vesicles are $\sim 0.4\text{-}2\mu\text{m}$ in diameter with an average vesicular diameter of $0.87\mu\text{m}$, Figure 4.24B. Within the control cells transfected with eYFP circular structures void of any fluorescent signal can be seen, this is likely to be that the ubiquitous and diffuse cellular YFP distribution is excluded from certain vesicles.

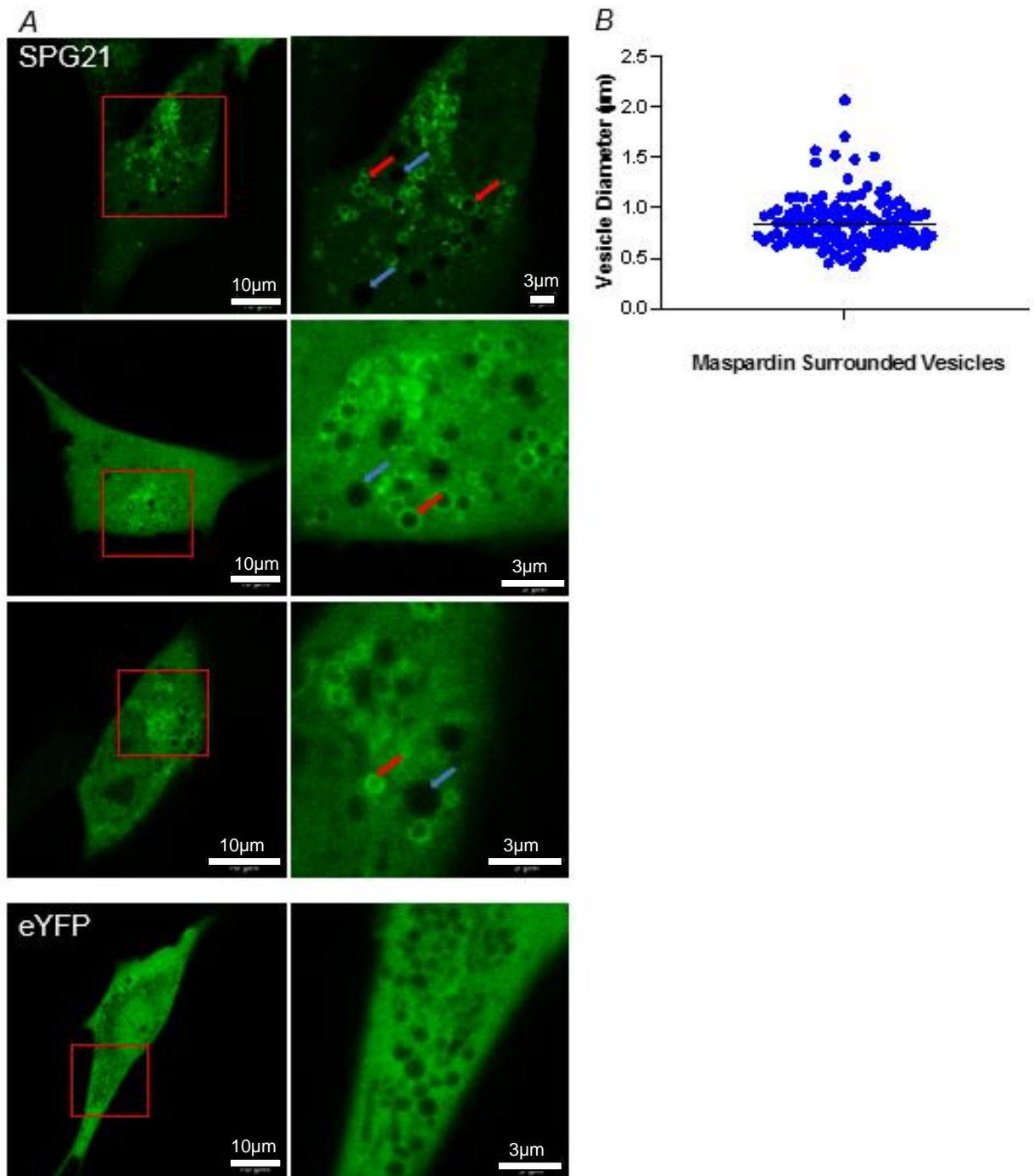


Figure 4.24. Maspardin localises to vesicular structures. A) 3T3 cells transfected with YFP-SPG21 and viewed by live cell imaging on a confocal microscope. Red arrows indicate maspardin surrounded vesicles whereas blue arrows indicate vesicles absent of maspardin. Bottom row of images shows eYFP backbone control. **B)** Maspardin surrounded vesicle diameters showing median line, $n=117$ vesicles from 14 cells from 4 individual experiments.

Human neuroblastoma SH-SY5Y as well as HEK 293 cells were used for other experiments to investigate maspardin function so these cell types were transfected with YFP-SPG21 plasmid. Figure 4.25 shows that both neuronal and non-neuronal cell types display maspardin decorated vesicles which is not identified in eYFP controls.

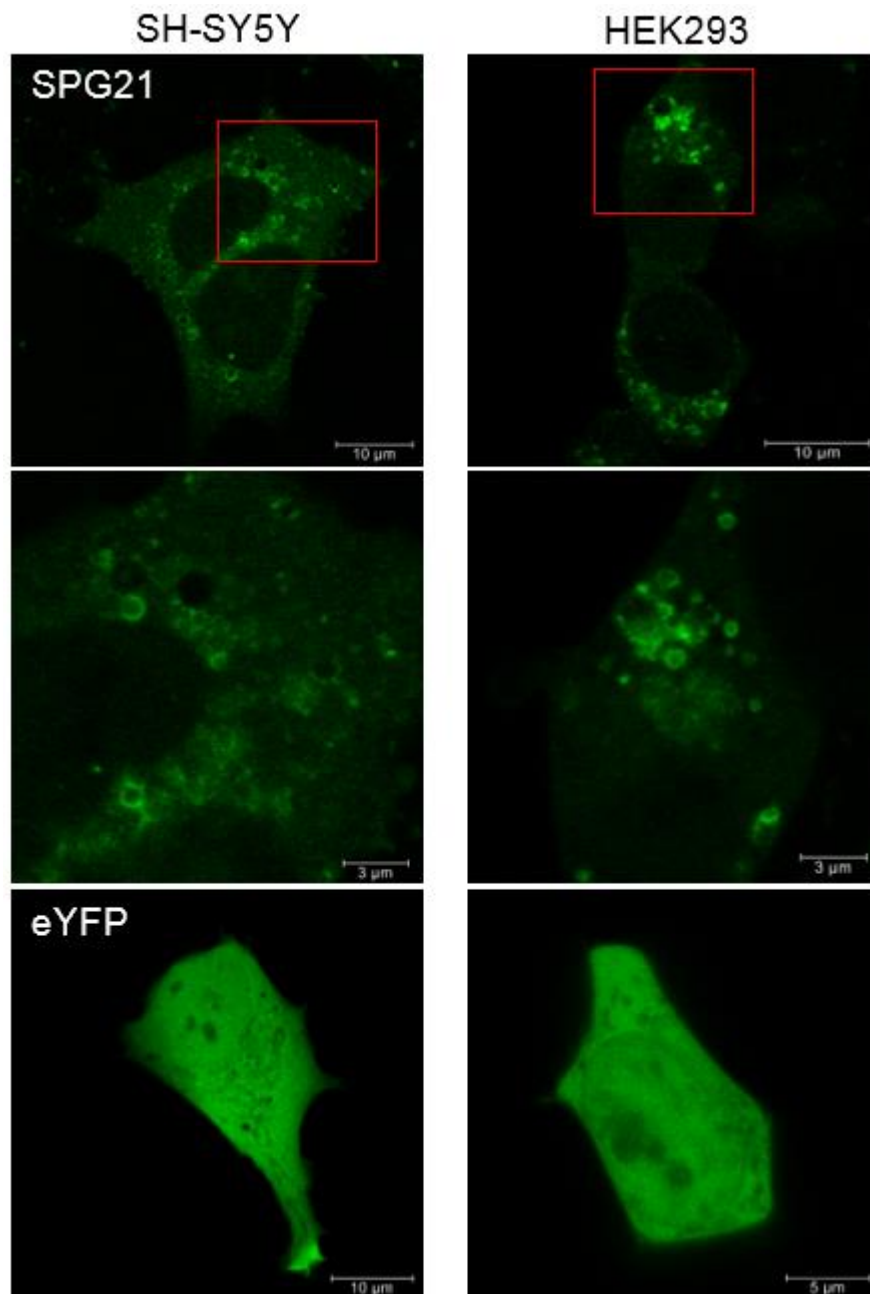


Figure 4.25. Maspardin surrounded vesicles identified in SH-SY5Y and HEK 293 cells. Cells transfected with YFP-SPG21 and viewed by live cell imaging on a confocal microscope. Bottom row of images shows eYFP backbone control.

Importantly, the YFP-SPG21 overexpressed protein is detected by the maspardin antibody (Figure 4.16), in part validating both plasmid and the antibody. Fixed cell imaging did not identify maspardin decorated vesicular structures to the same clarity as live cell imaging, but an intense expression of maspardin in the perinuclear region was observed (Figure 4.26).

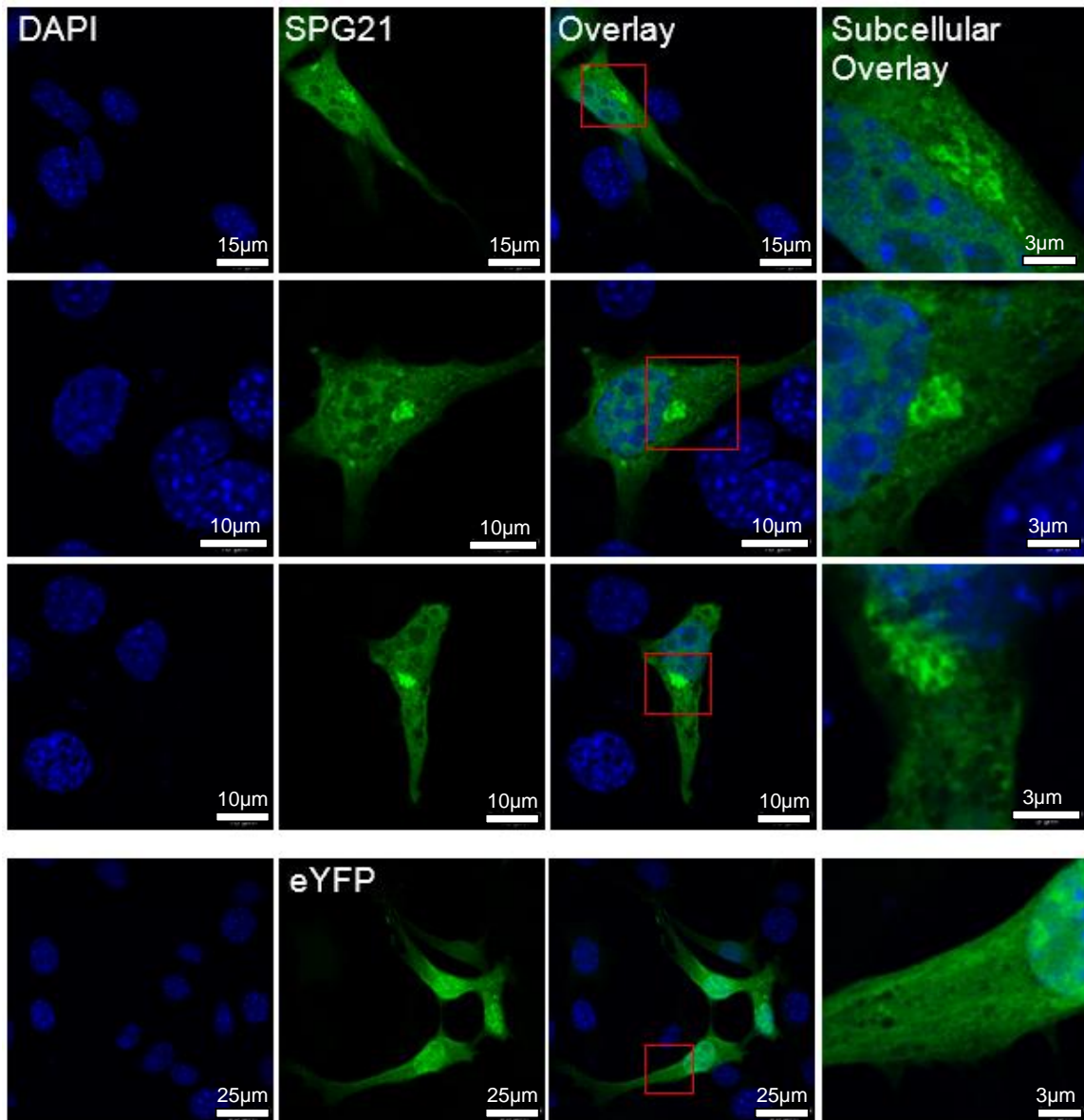


Figure 4.26. Fixed YFP-SPG21 imaging. 3T3 cells transfected with YFP-SPG21, fixed, permeabilised, DAPI stained and viewed by confocal microscopy. Images show whole cell and subcellular images of the same cell. Bottom row of images shows eYFP backbone control.

The expression of maspardin in live and fixed cell imaging was further investigated to determine whether permeabilisation of cells post fixing alters subcellular localisation. Cells were transfected and fixed onto coverslips as before but instead of permeabilising and staining them they were directly mounted onto microscope slides, Figure 4.27. This did not substantially increase the clarity, however maspardin decorated circular structures were again identified although not in the same resolution as in live cell imaging. This suggests that cell fixation may alter the subcellular distribution of maspardin when cells are transfected with the YFP-SPG21 plasmid.

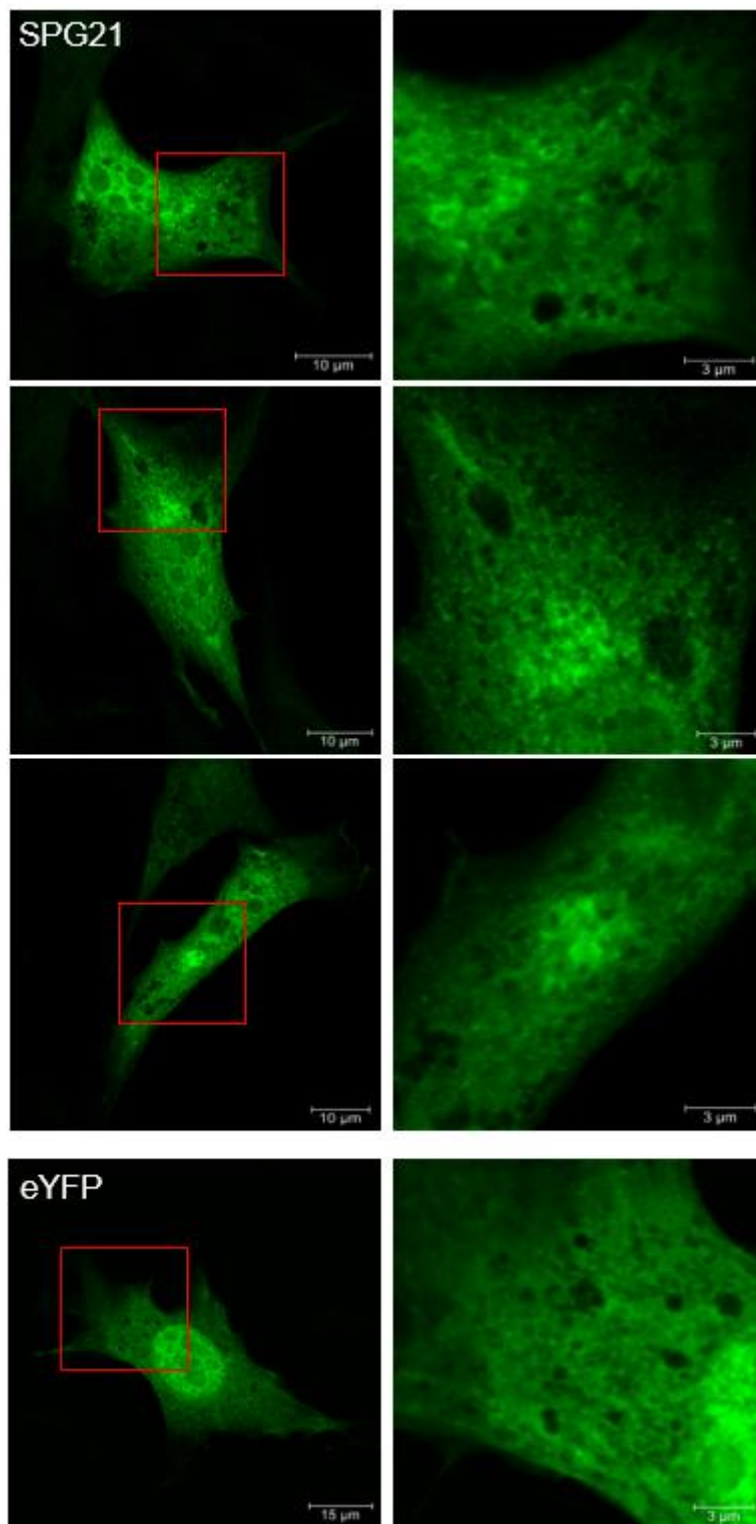


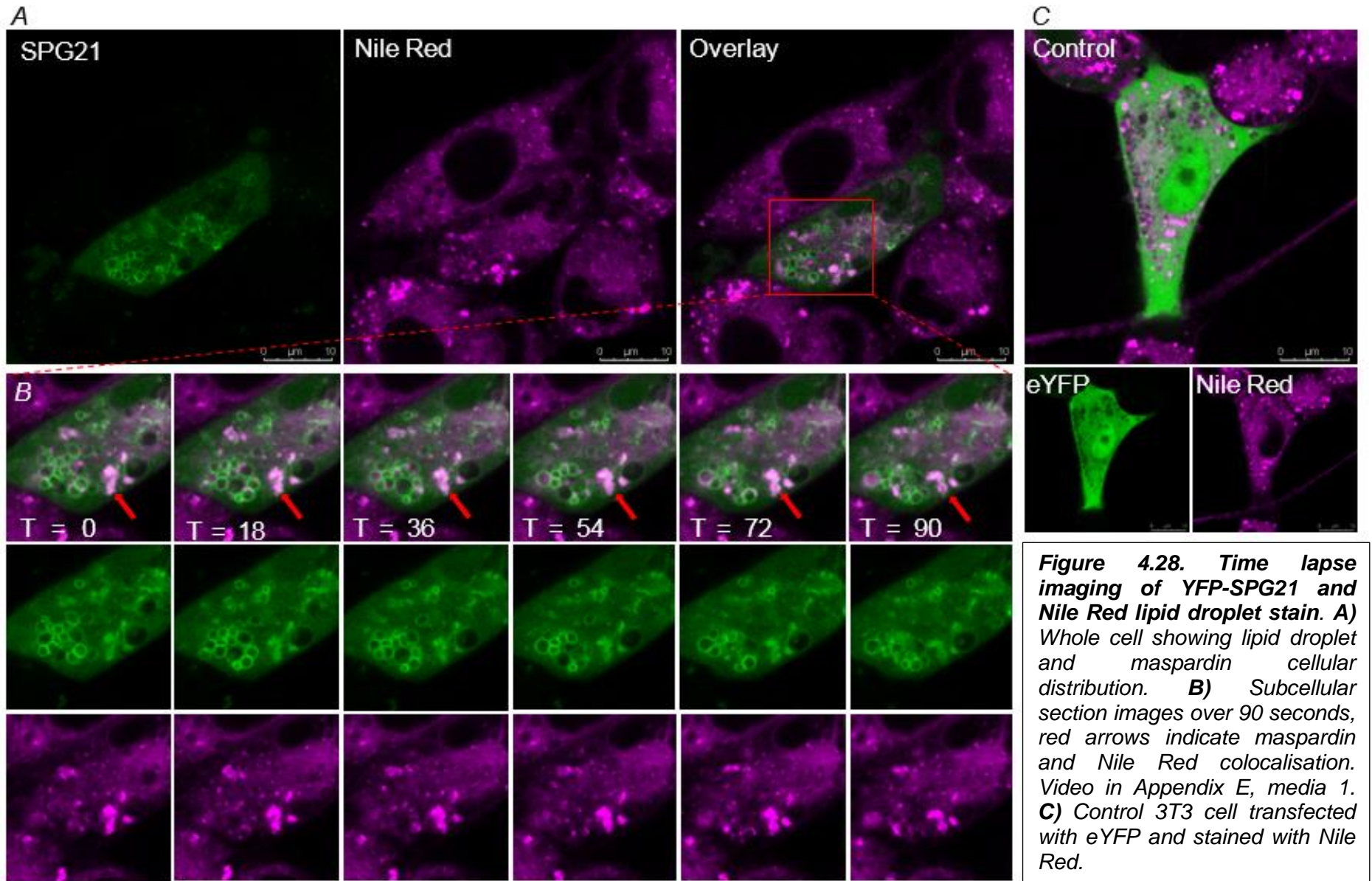
Figure 4.27. Fixed YFP-SPG21 imaging with no permeabilisation. 3T3 cells transfected with YFP-SPG21, fixed, mounted and viewed by confocal microscopy. Images show whole cell and subcellular images of the same cells. Bottom row of images shows eYFP backbone control.

Given this, subcellular localisation studies were subsequently undertaken using live cell imaging, which unfortunately limits experiments to using fluorescent vital dyes and plasmids to determine the nature of the maspardin surrounded vesicles.

4.2.6.2 Maspardin Vesicles are not Lipid Droplets

Further experiments were undertaken to determine whether maspardin decorated vesicles involved lipid droplets, which vary considerably in size and are abundant in lipases [236]. Interestingly maspardin contains a motif found in many lipases [208] and a number of HSP-associated genes are known to be involved in lipid droplet regulation [237].

Cells were firstly transfected with YFP-SPG21 and stained with the Nile Red lipid droplet stain for imaging. This showed that the maspardin surrounded vesicles were not lipid droplets, however the Nile Red lipid droplet stain and YFP-SPG21 do colocalise in some areas (Figure 4.28).



4.2.6.3 Maspardin Colocalises with Rab7 Vesicles

Maspardin was previously identified to be a binding partner of Rab7 by *McCray et al., 2010* and Rab7 was also identified as a likely binding partner in the mass spectrometry-pull down data here (section 4.2.5). To further investigate this interaction, Rab7-mCherry was co-transfected with YFP-SPG21 which visibly revealed a high degree of colocalisation on the same vesicles (Figure 4.29).

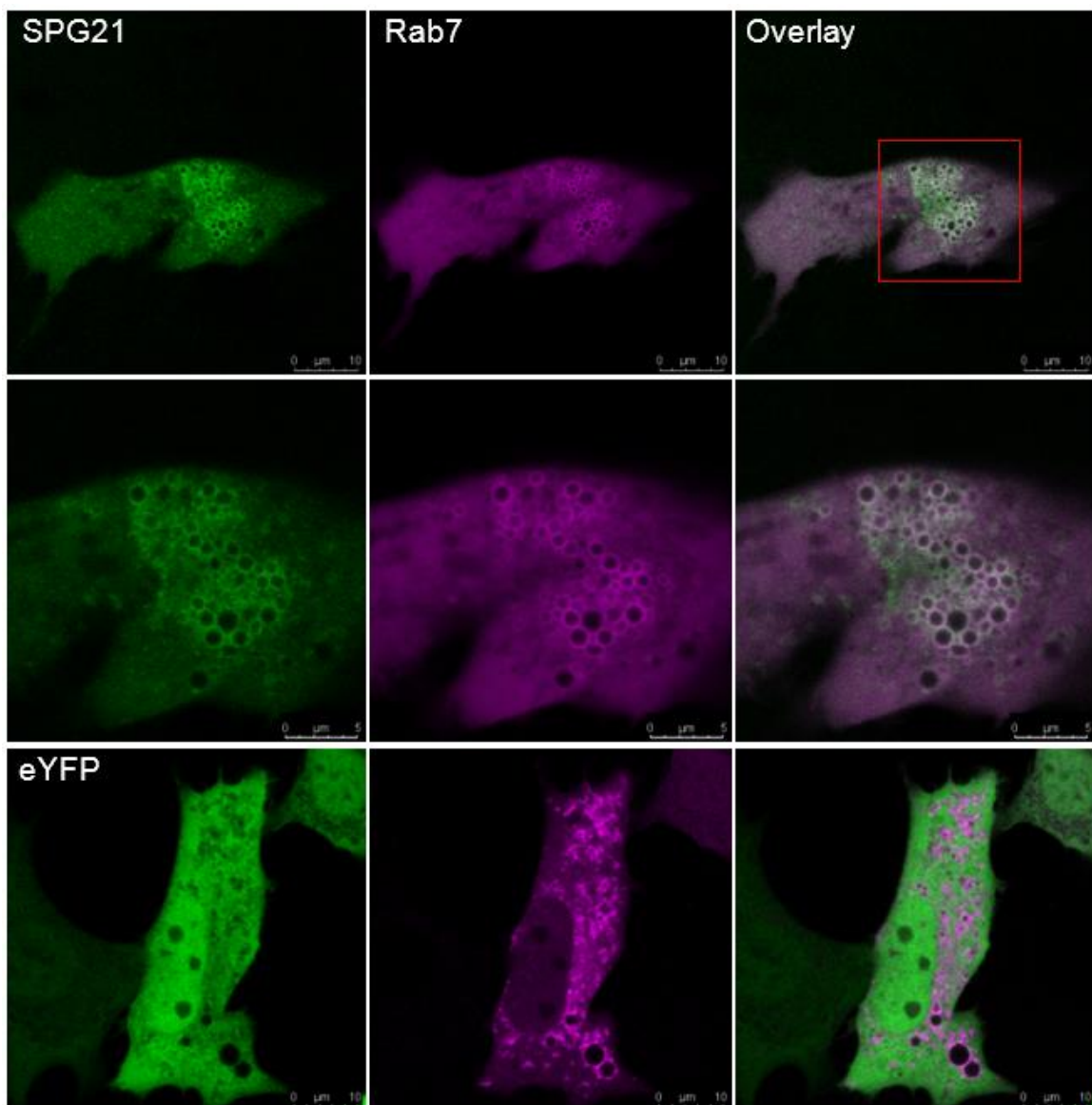


Figure 4.29. Maspardin colocalises with Rab7 surrounded vesicles. 3T3 cells co-transfected with YFP-SPG21 and Rab7-mCherry and viewed by live cell imaging on a confocal microscope. Video in Appendix E, media 2. Bottom row of images shows eYFP backbone control.

To explore the endosomal localisation of maspardin in more detail it was then compared to a panel of Rabs to provide a broader overview of the whole endosomal pathway including the early endosomal Rab5, the fast recycling endosomal Rab4, and Rab9 which mediates endosomal transport to the trans-Golgi network [238]. As endosomal maturation from early to late endosomes is marked by a transition from Rab5 to Rab7 [218], it may be expected that maspardin may also interact with Rab5 positive endosomes. To investigate the extent of maspardin localisation to the endosomal pathway YFP-SPG21 was co-transfected alongside the fluorescent Rab plasmids.

Rab4 surrounded vesicles were found to be fewer in number than maspardin surrounded vesicles, and the two markers do not decorate the same vesicles, Figure 4.30. However, the two vesicles do share the same overall cellular space and appear to contact each other as highlighted by red arrows.

Similarly, Rab5 and maspardin also decorate distinct vesicles, some of which are again in the same cellular vicinity, Figure 4.31. The video in Appendix E (media 3) indicates that both Rab5 and maspardin surrounded vesicles may interact with one another, which is highlighted in Figure 4.31. Smaller Rab5 surrounded vesicles are observed towards the cellular periphery whereas larger vesicles are towards the centre of the cell. These larger vesicles are in the same cellular region as maspardin surrounded vesicles. Rab5 localisation towards the cellular periphery is particularly evident in the control cell where smaller vesicles can be observed.

Rab9 surrounded and maspardin surrounded vesicles are in the vicinity of one another and in most cases do not colocalise, although may be located on the same vesicle on occasion (blue arrow, Figure 4.32).

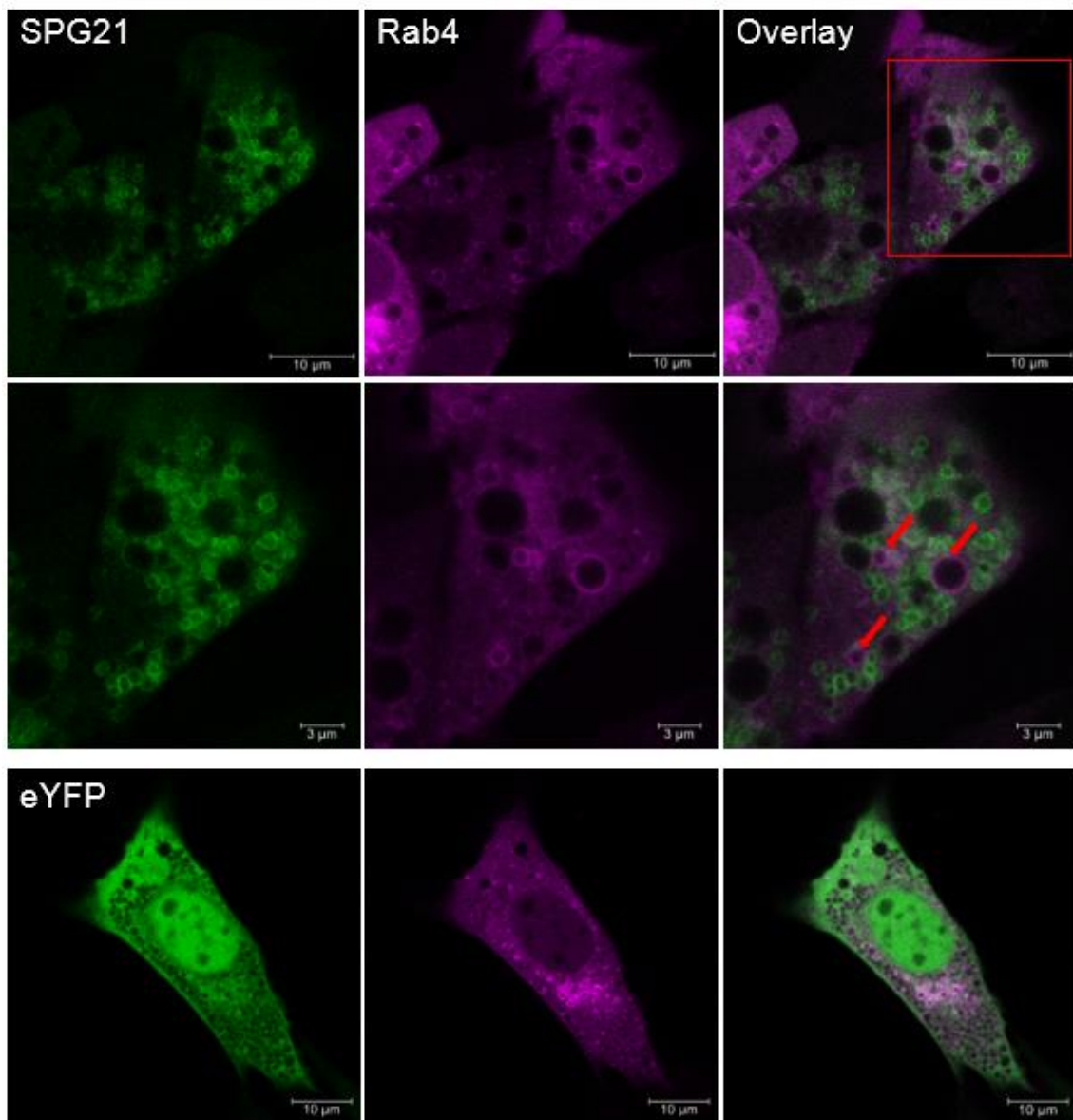


Figure 4.30. Maspardin and Rab4 surrounded vesicles potentially interact. 3T3 cells co-transfected with YFP-SPG21 and Rab4-RFP, and imaged by live cell confocal microscopy. Red arrows indicate contact between the two vesicles. Bottom row of images shows eYFP backbone control.

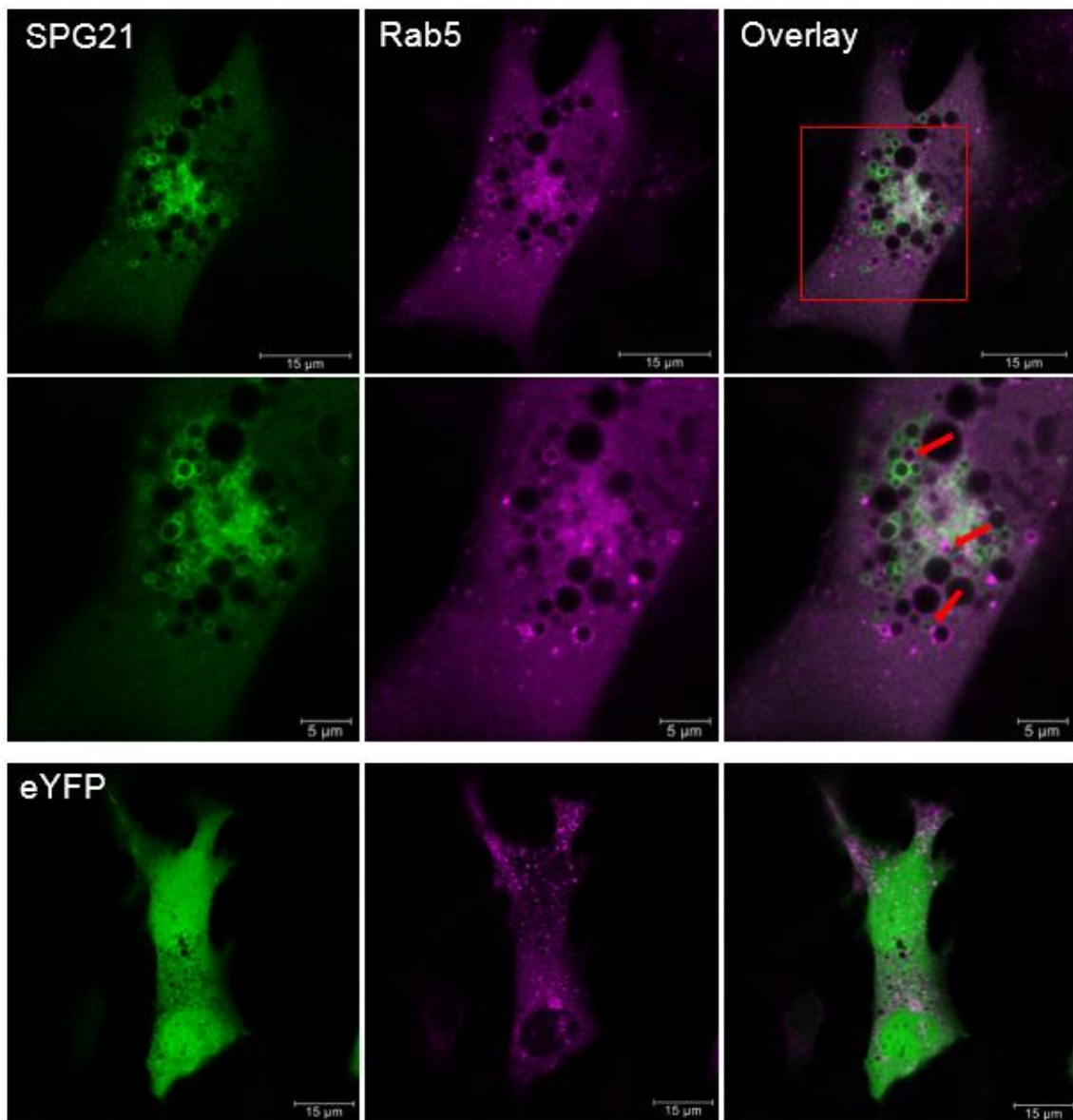


Figure 4.31. Maspardin and Rab5 surrounded vesicles potentially interact. 3T3 cells co-transfected with YFP-SPG21 and Rab5-RFP, and imaged by live cell confocal microscopy. Red arrows indicate contact between the two vesicles. Video in Appendix E, media 3. Bottom row of images shows eYFP backbone control.

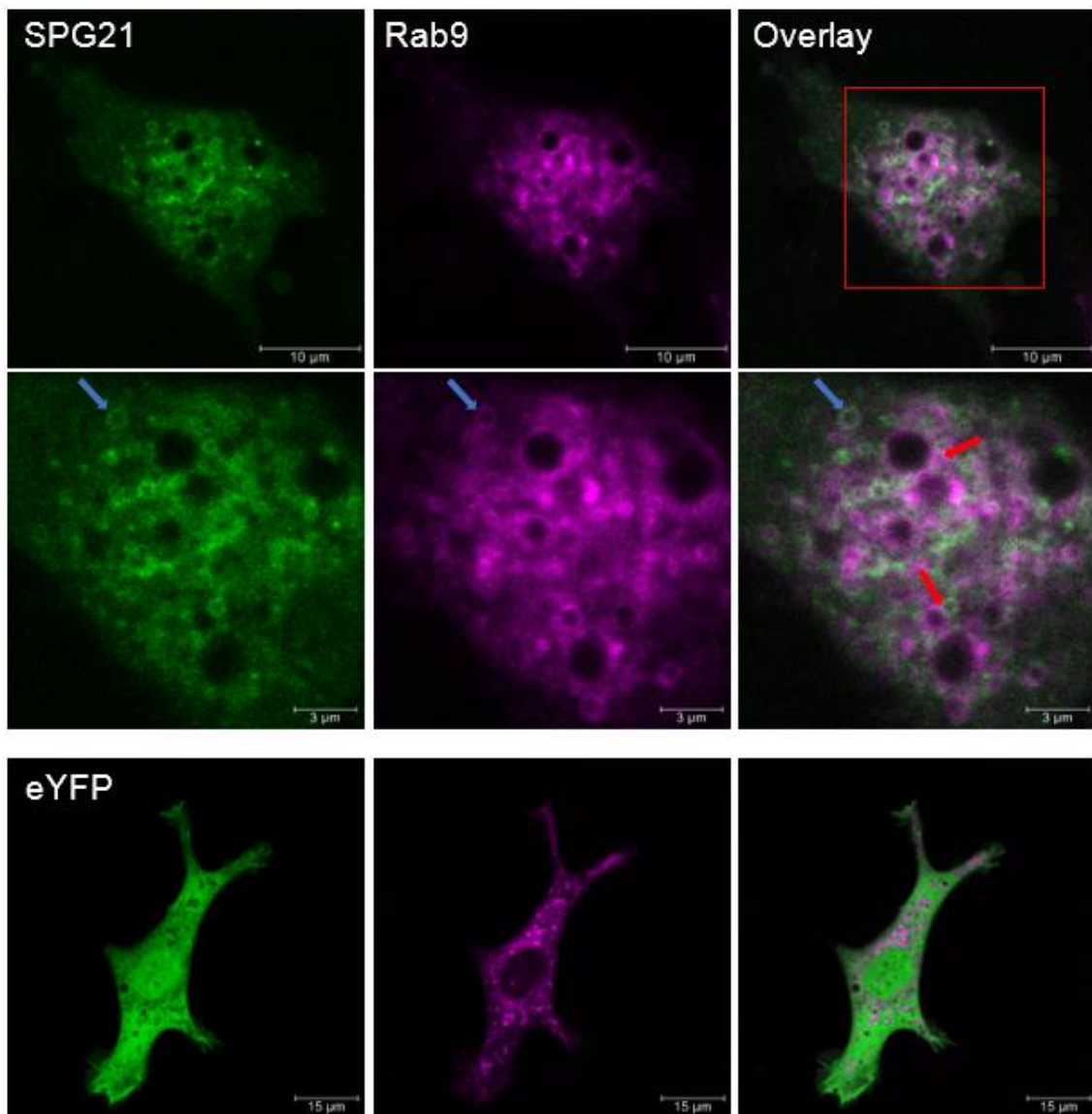


Figure 4.32. Maspardin and Rab9 surrounded vesicles potentially interact and colocalise. 3T3 cells co-transfected with YFP-SPG21 and Rab9-RFP, and imaged by live cell confocal microscopy. Red arrows indicate contact between the two vesicles whereas the blue arrows show colocalisation. Bottom row of images shows eYFP backbone control.

Taken together the live cell imaging as well as co-immunoprecipitation mass spectrometry data clearly indicates that maspardin is resident on a specific subset of likely late endosome vesicles, indicating that maspardin perhaps possesses a role in late endosomal processes.

4.2.6.4 Maspardin Surrounds Lysosomes

As one of the main roles of Rab7 is to mediate late endosomal transport and contact with lysosomes, studies were undertaken to determine whether maspardin may also interact with lysosomes. Cells were transfected with YFP-SPG21 and then stained with a lysosomal stain (ab112137; Figure 4.33), revealing overlap with lysosomes, although not all maspardin decorated vesicles were stained. Within the control eYFP cells the circular structures that were void of any fluorescent signal were stained with the lysosomal stain. This is likely to be that the ubiquitous and diffuse cellular YFP distribution is excluded from these vesicles or that within the lysosome the YFP no longer fluoresces.

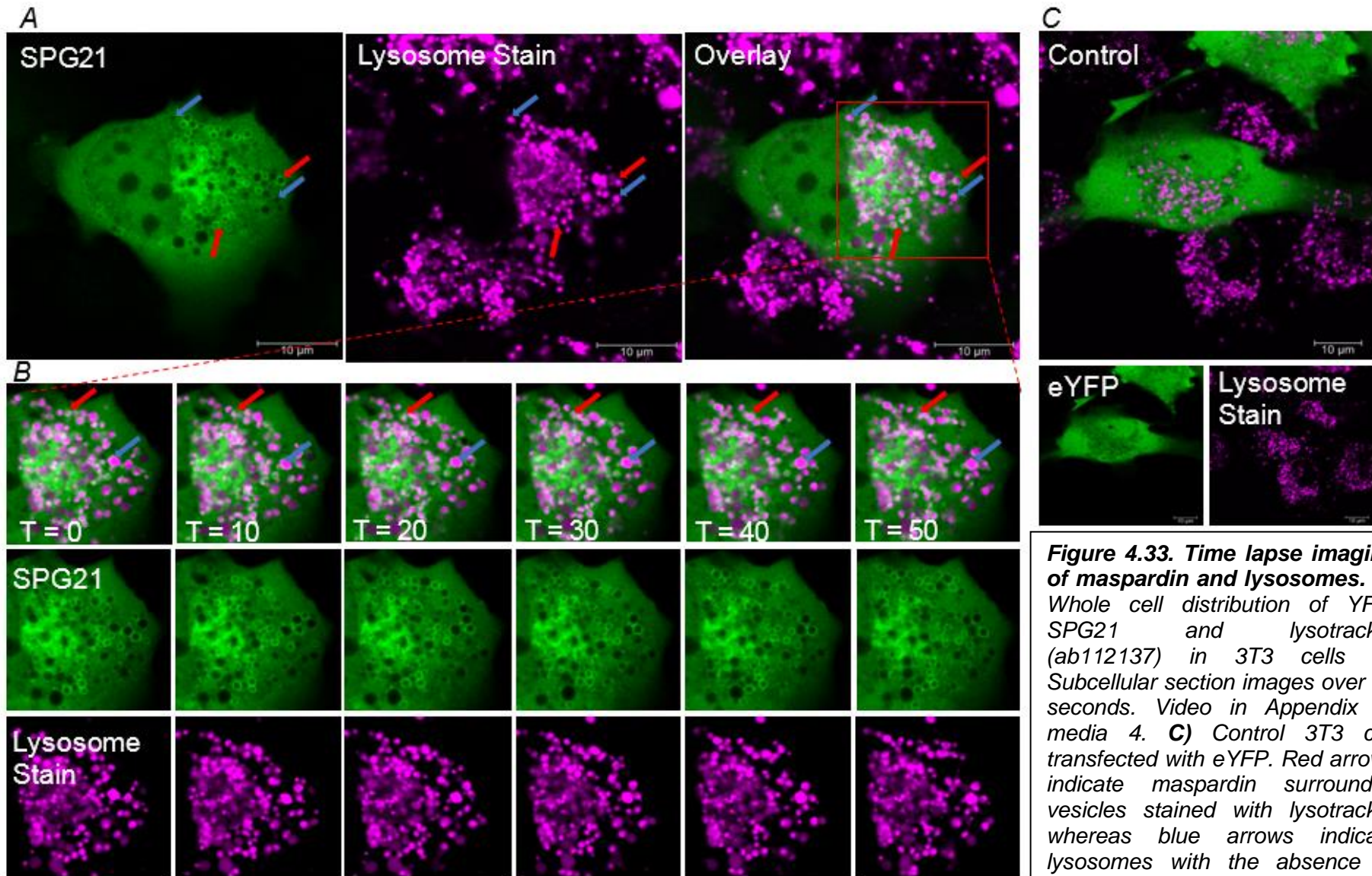


Figure 4.33. Time lapse imaging of maspardin and lysosomes. A) Whole cell distribution of YFP-SPG21 and lysotracker (ab112137) in 3T3 cells **B)** Subcellular section images over 50 seconds. Video in Appendix E, media 4. **C)** Control 3T3 cell transfected with eYFP. Red arrows indicate maspardin surrounded vesicles stained with lysotracker whereas blue arrows indicate lysosomes with the absence of maspardin.

Due to the lysosomal marker used entering lysosomes via a pH gradient, it is likely that it also labels late endosomes which are also acidic [239]. In order to further understand what portion of these organelles are lysosomes or late endosomes both the lysosomal stain and Rab7, in addition to maspardin were imaged together.

As shown in Figure 4.34, this revealed that all three reside in the same overall cellular space and that the lysosome stain does not solely stain lysosomes, but also identifies other organelles including Rab7 decorated late endosomes.

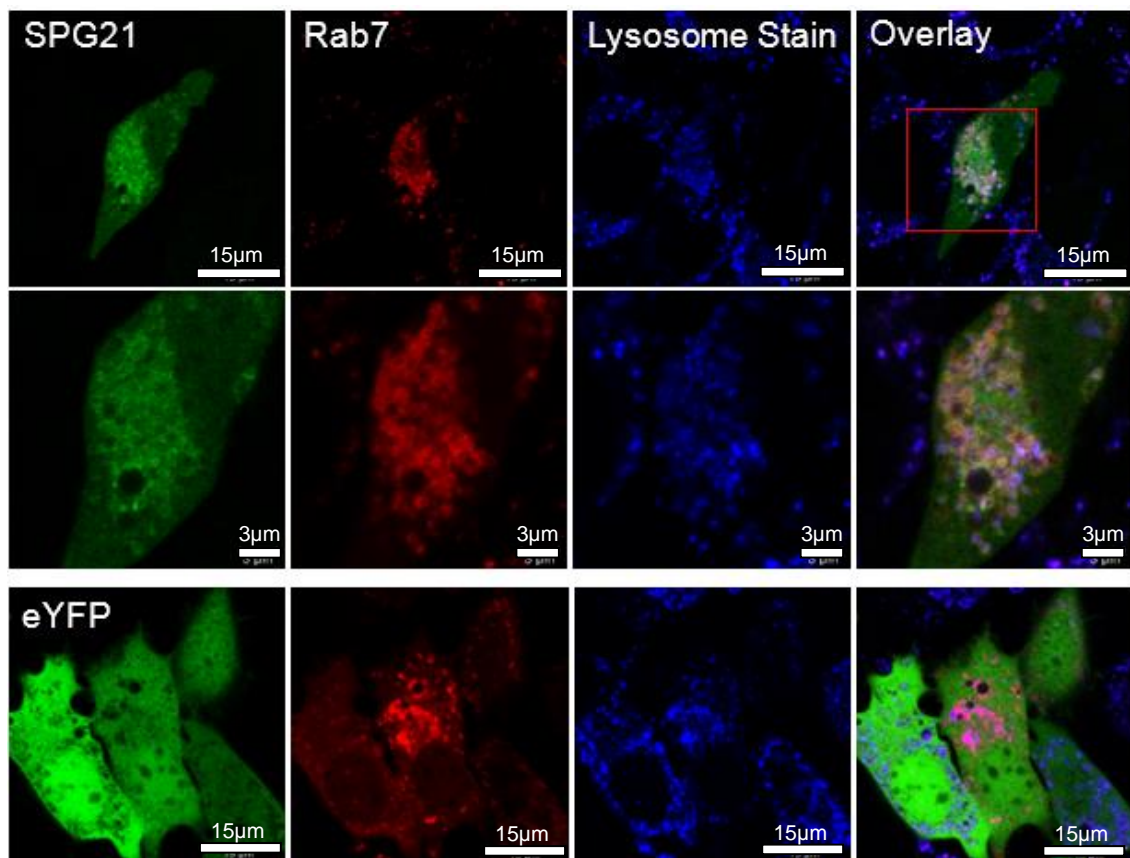


Figure 4.34. Maspardin, Rab7, and lysotracker (ab176824) imaging, indicate the three colocalise in 3T3 cells. Video included in Appendix E, media 5. Bottom row shows control 3T3 cells co-transfected with eYFP and Rab7, and stained with lysotracker.

4.2.6.5 Maspardin Vesicles Appear to Interact with Mitochondria

Previous immunocytochemistry experiments (section 4.2.4) indicate that maspardin may interact with mitochondria, which is also supported by the number of mitochondrial proteins that were identified in the mass spectrometry binding partner analysis. To further explore this, live cell imaging was used to investigate the proximity of maspardin to mitochondria. While maspardin does not appear to reside on mitochondria, a modest proportion of maspardin decorated vesicles contact mitochondria transiently. These transient interactions appear to adapt and associate with one another over a short period of time, as highlighted by red arrows in Figure 4.35.

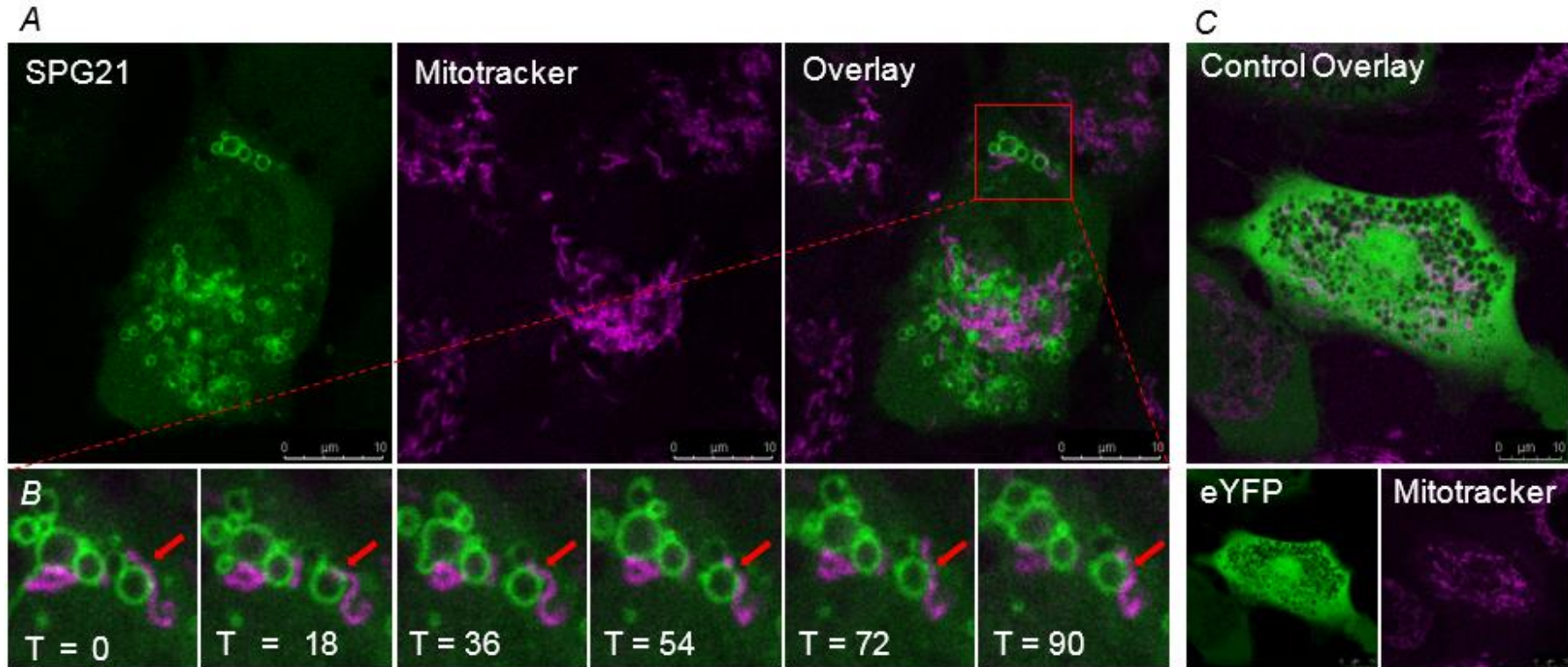


Figure 4.35. Time lapse imaging of maspardin and mitotracker in 3T3 cells indicate transient interaction. A) Whole cell showing mitochondria and YFP-SPG21 cellular distribution. **B)** Subcellular section images over 90 seconds with images shown every 18 seconds showing the interaction between maspardin surrounded vesicles and the mitochondria over time. Red arrows highlight the association of maspardin with the mitochondria. Video included in Appendix E, media 6. **C)** Control 3T3 cell transfected with eYFP and stained with Mitotracker.

4.2.7 Maspardin Amino Acid Sequence Contains Candidate Lysosome Localisation Signals

To investigate whether the maspardin amino acid sequence contained any localisation signals the full length polypeptide sequence was examined using the localisation signal database LogSigDB, which investigates candidate localisation sequences for eight distinct subcellular organelles [240, 241]. This identified five possible lysosomal localisation signals, including four YXXΦ (Φ=VILFWCM (single letter amino acid code)) at amino acid residues 9-13, 70-74, 267-271 and 280-284, and a GYXXI signal overlapping another lysosomal signal at amino acid residues 69-74. The 267-271 localisation signal was also identified as a possible Golgi signal when extended by three amino acids, YxxxxLL. A potential ER localisation signal, HLK at the 248-251 amino acid position was also identified. These localisation signals are shown on the maspardin amino acid sequence in Figure 4.36.

MGEIKVSPDYNWFRG'TVPLKKIIVDDDDSKIWSLYDAGPRSIRCPLIFLPPVSGTAD
VFFRQILALTGWCYRVIALQYPVYWDHLEFCDFRKLDDHLQLDKVHLFGASLG
GFLAQKFAEYTHKSPRVHSLILCNSFSDTSIFNQTTWTANSFWLMPAFMLKKIVLGN
FSSGPVDPMMADAIDFMVDRLESLGQSELASRLTLNCQNSYVEPHKIRDIPVTIMD
VFDQSALSTEAKEEMYKLYPNARRAHLKGTGNFPYLCRSAEVNLYVOIHLLQFHG
TKYAAIDPSMVSAEELEVQKGSLSISQEEQ

Figure 4.36. Candidate subcellular localisation signals identified by LocSigDB at specific maspardin amino acid positions. Red indicates lysosome localisation signals, blue indicates ER localisation signal and the green with the adjacent underlined sequence indicates Golgi localisation signal. Note that the orange and red underlined signal in the 69th-74th amino acid position represent two different lysosome localisation signals.

4.2.8 Analysis of Maspardin and Rab7 Interaction and Expression

To further investigate the likely interaction between Rab7 and maspardin a co-immunoprecipitation was performed where each protein was pulled down from HEK 293 cell lysates, followed by Western blotting (Figure 4.37A). Each immunoprecipitated protein did not clearly identify the presence of the other protein, however both pull-downs were successful due to the enriched presence of the respective pulled down protein with the absence of GAPDH. However, Rab7 was detected in the negative unbound fraction and a slightly higher than expected and less defined band was identified in the Rab7 IP sample, perhaps due to not all of the protein being immunoprecipitated and a large amount of protein loaded onto the gel.

Given the interaction between maspardin and Rab7 it was explored whether the absence of maspardin would alter Rab7 expression in SH-SY5Y control and *SPG21* knockout cell lysates. This revealed that Rab7 expression is not affected by the loss of maspardin, and that neither tubulin nor GAPDH expression are altered, Figure 4.37B.

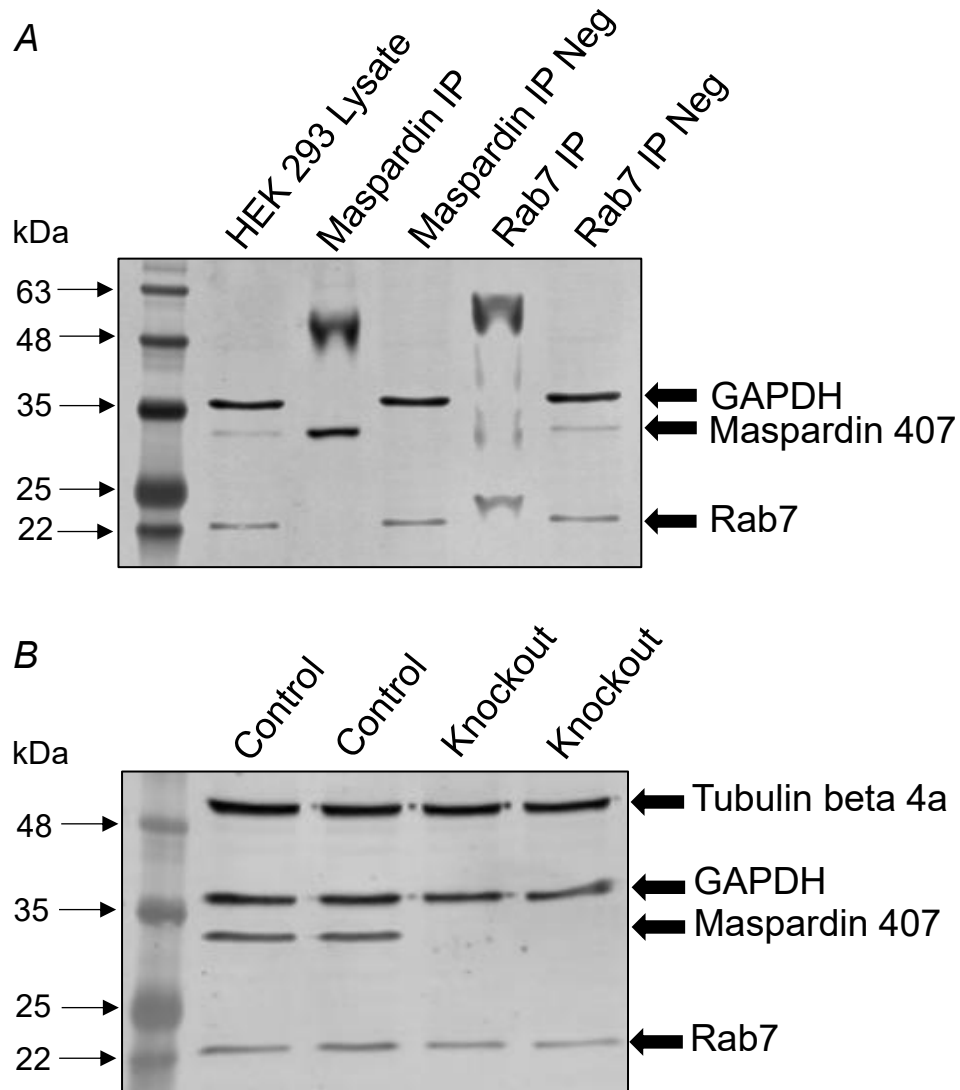


Figure 4.37. Maspardin and Rab7 co-immunoprecipitation (A) and SPG21 knockout Rab7 expression (B). **A)** Co-immunoprecipitation of HEK 293 cell lysates using maspardin 407 and Rab7 antibodies. Probed with Rab7 (22kDa), maspardin 407 (33kDa) and GAPDH (37kDa). Band at ~50kDa present in both pull-downs is likely to be the immunoglobulin heavy chain. Lane 1, molecular weight marker; lane 2, HEK 293 cell lysate; lane3, maspardin 407 pull-down; lane 4, negative unbound supernatant of maspardin 407 pull-down; lane 5, Rab7 pull-down; lane 6, negative unbound supernatant of Rab7 pull-down. **B)** Rab7 expression in SH-SY5Y control and SPG21 knockout cells from cell lysates loaded in duplicate and probed with the same antibodies in addition to tubulin beta 4a (50kDa). Fluorescent secondary antibodies and detection was used.

4.2.9 Comparing *SPG21* Knockout to Wildtype Cells

4.2.9.1 Analysis of Metabolism and Viability in *SPG21* Knockout Cells

To understand the cellular consequences as a result of maspardin loss basic experiments were undertaken to explore whether there were alterations in cell death, metabolic activity and cellular ROS between control and *SPG21* knockout cells. Motor neurone disease is known to be associated with an increase in ROS that is implicated in the pathogenesis of disease [242]. The metabolic activity was also investigated to better understand the result of maspardin loss in knockout cells which may compromise cellular functioning.

Cellular death was investigated by propidium iodide staining followed by flow cytometry to sort dead cells from viable cells based on cell size and staining intensity, with experimental repeats. This revealed a statistically significant increase in the number of dead cells in knockout (27.5%) compared to control (10.8%) cells (Figure 4.38A).

Given the increase in *SPG21* knockout cell death the metabolic activity was not directly investigated, instead the difference in metabolic activity over time was analysed using the cell proliferation MTT assay which quantifies cell viability based on the activity of mitochondrial enzymes. This data revealed a 348% increase in *SPG21* knockout cell metabolic activity over two days compared to a 263% increase in control cells (Figure 4.38B).

To explore ROS, the DCFDA cellular ROS detection assay kit was used to investigate cellular ROS upon addition of exogenous (TBHP) ROS over time. This revealed an initial increase (16.7%) in *SPG21* knockout cellular ROS after one hour of TBHP compared to a 11.2% increase in control wildtype cells. After

5 hours of TBHP exposure a 40.4% increase in *SPG21* knockout cellular ROS compared to a 30% wildtype increase was identified.

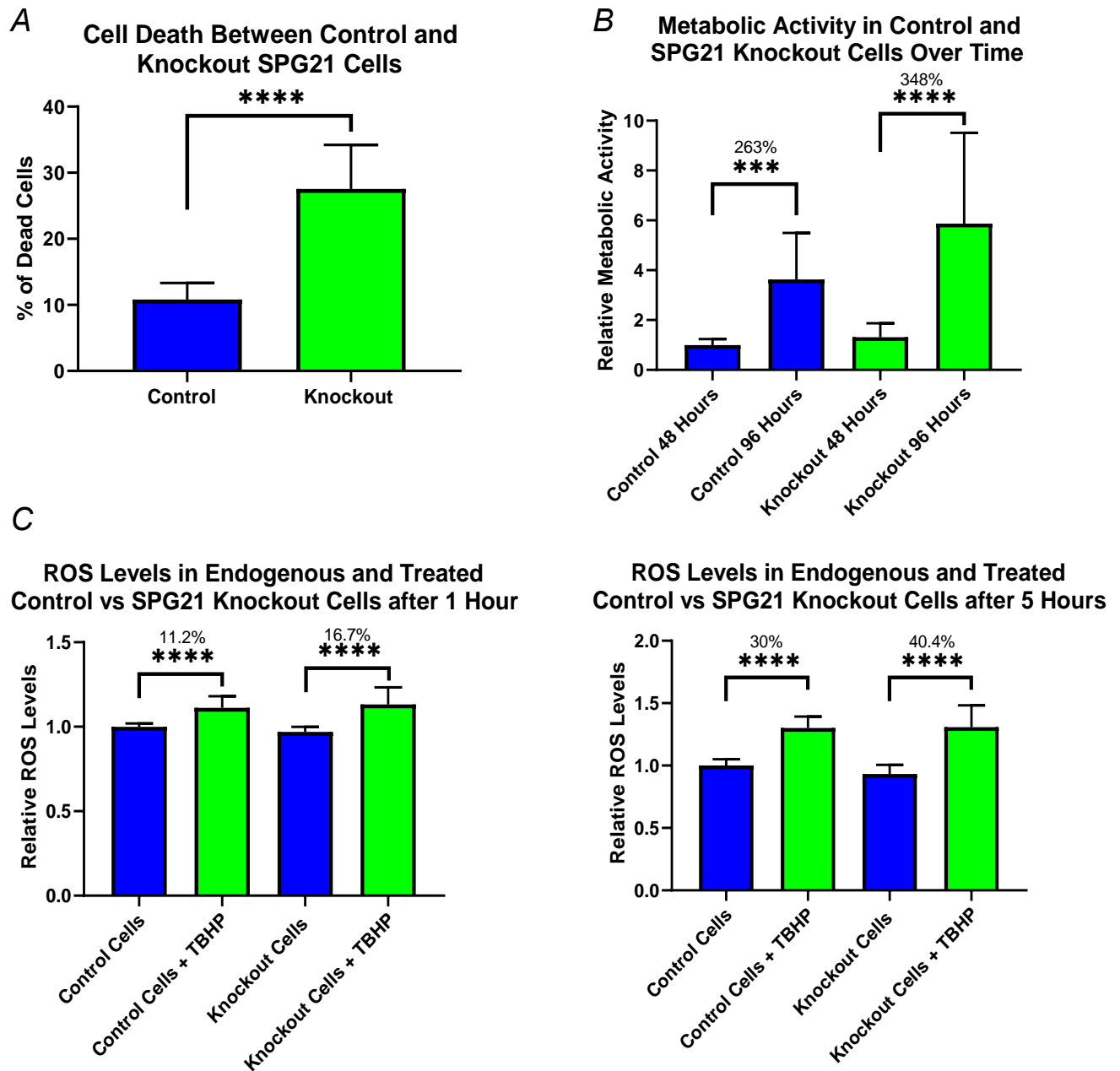


Figure 4.38. Increase in cell death, metabolic activity and ROS in SPG21 knockout cells. **A)** Cell death determined by propidium iodide staining shows a statistically significant increase in cell death in SPG21 knockout cells. **B)** Metabolic activity determined by MTT assay after both 48 and 96 hours post seeding shows a statistically significant increase in metabolic activity in SPG21 knockout cells. **C)** Graphs showing both endogenous ROS and ROS levels after the addition of exogenous ROS (TBHP) after 1 hour (left) and 5 hours (right) post treatment. Results show a larger increase in ROS in SPG21 knockout cells compared to controls when exposed to TBHP, which is more notable after 1 hour of treatment compared to 5 hours. Both graphs B and C made relative to either the mean of the control 48 hour or untreated control cells. All graphs mean values plotted with standard deviation. Significance determined by Mann-Whitney test and asterisks show statistical significance where *** = $p < 0.001$ and **** = $p < 0.0001$.

4.2.9.2 Endolysosomal Vesicles Morphology are Altered in *SPG21* Knockout Cells

Given the colocalisation between maspardin and Rab7, the impact of Rab7 vesicle size was investigated between the *SPG21* knockout and control cells by transfecting the cells with a Rab7 plasmid and imaging these cells using live cell imaging, Figure 4.39. *SPG21* knockout cells displayed a statistically significant increase in Rab7 surrounded vesicle diameter size, with the mean diameter found to be 0.84 μ m compared to the control cells with an average diameter of 0.7 μ m, Figure 4.40. This prompted subsequent experiments to explore other areas of the endolysosomal pathway, revealing that *SPG21* knockout cells also displayed a significant decrease in lysosome diameter, with an average control cell diameter of 1.02 μ m compared with 0.87 μ m in *SPG21* knockout cells Figure 4.41. Figure 4.39 and Figure 4.40; Rab5 surrounded vesicles were not found to display a difference in size. Rab4 (mediates fast recycling) and Rab9 (important for the transport of late endosomes to the trans-Golgi pathway) were also not found to display a difference in vesicle size.

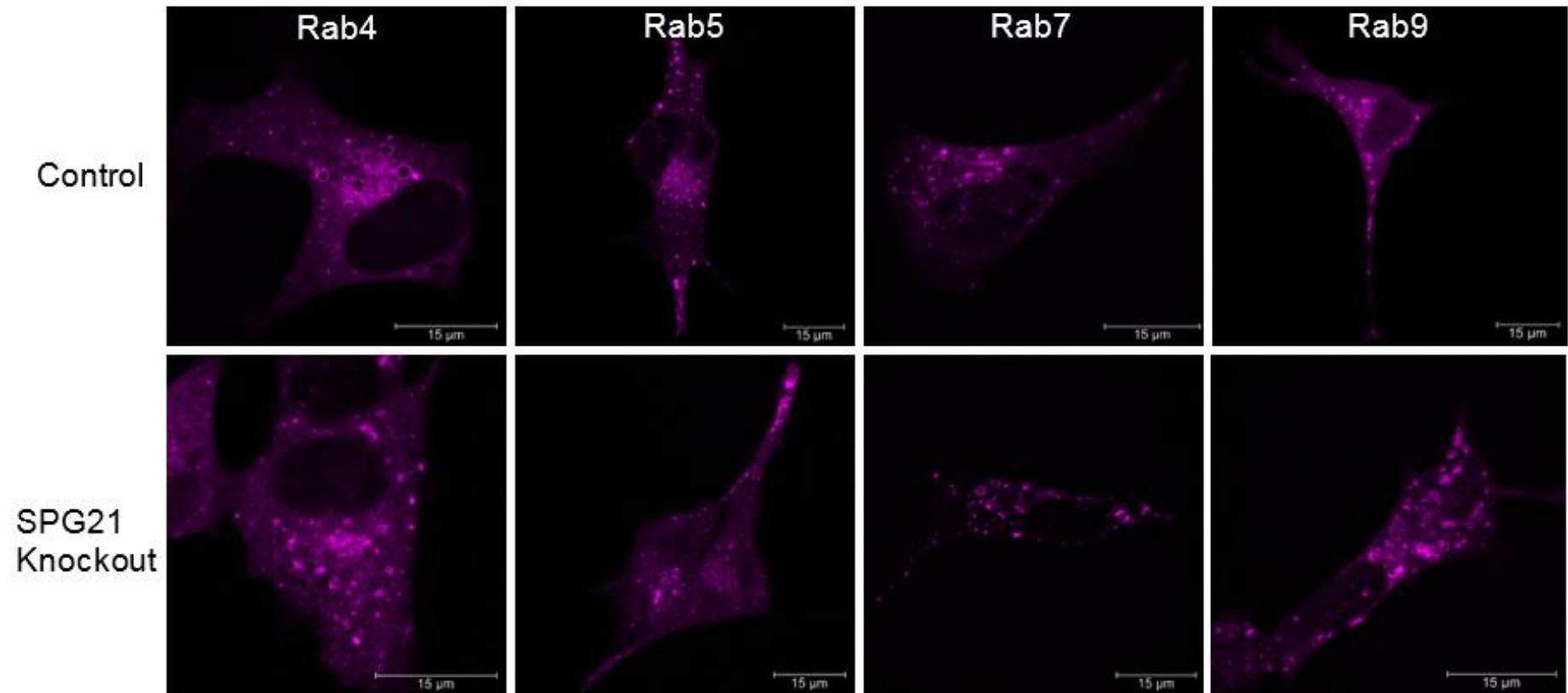


Figure 4.39. Rab4, 5, 7 and 9 vesicles in SH-SY5Y control and SPG21 knockout cells. Control and SPG21 knockout SH-SY5Y cells individually transfected with panel of Rab plasmids (Rab4-RFP, Rab5-RFP, Rab7-mCherry and Rab9-RFP) and imaged by live cell confocal microscopy.

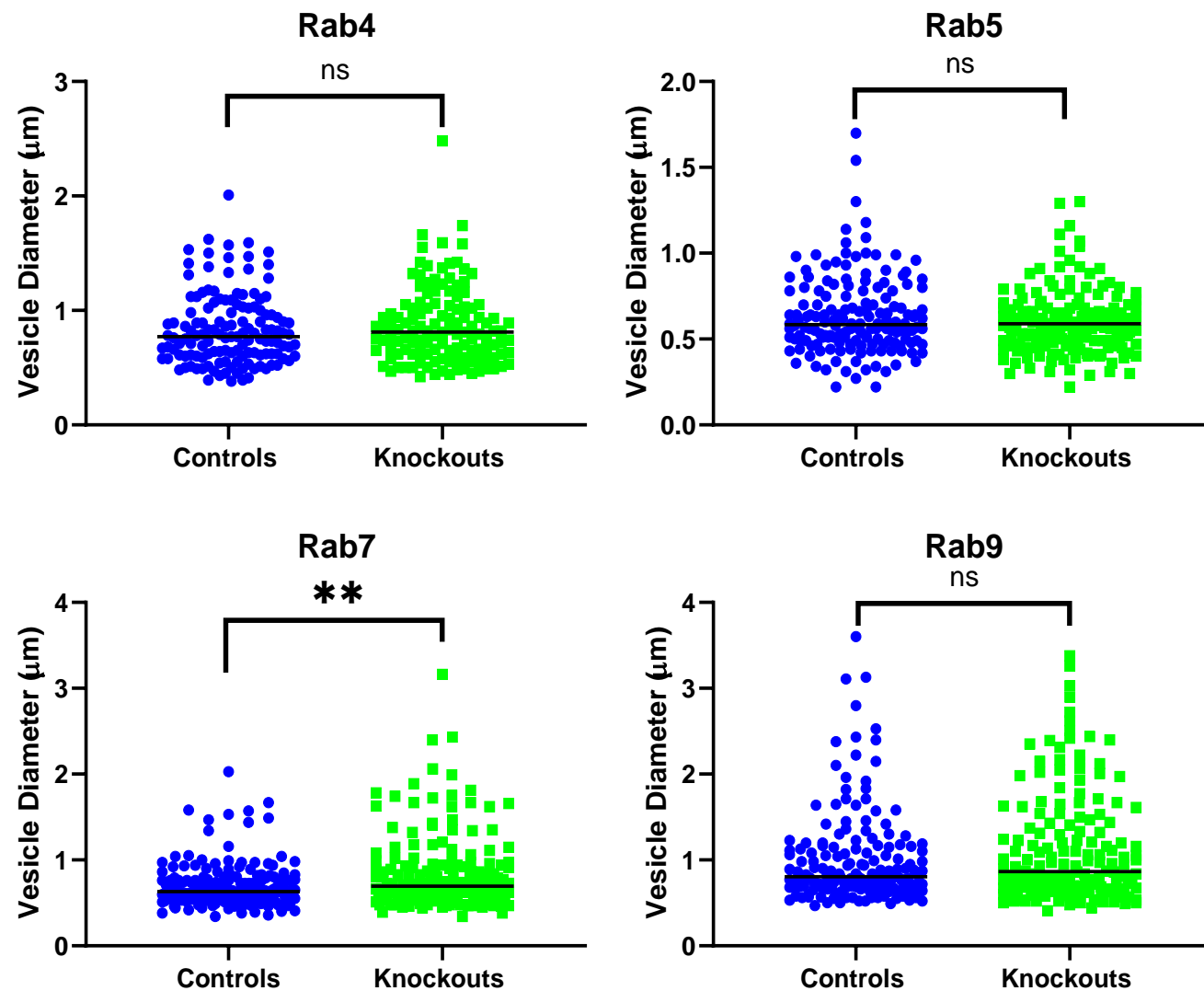


Figure 4.40. Vesicle diameter of Rab surrounded vesicles in control and SPG21 knockout cells. Scatter plots show median line and statistical significance determined by Mann-Whitney test where ns=not significant and **= $p < 0.01$. Rab4 $p=0.42$, Rab5 $p=0.34$, Rab7 $p=0.0017$ and Rab9 $p=0.23$. Rab4 control $n=137$ and knockout $n=127$, both from 14 cells. Rab5 both control and knockout $n=160$ from 16 cells. Rab7 both control and knockout $n=180$ from 18 cells. Rab9 both control and knockout $n=170$ from 17 cells. All from 3 independent experiments.

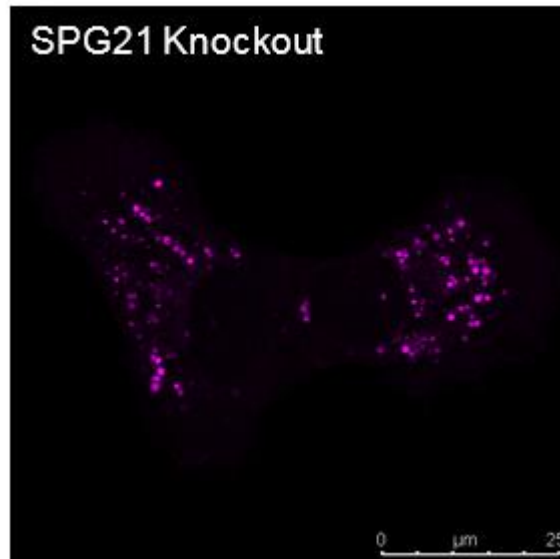
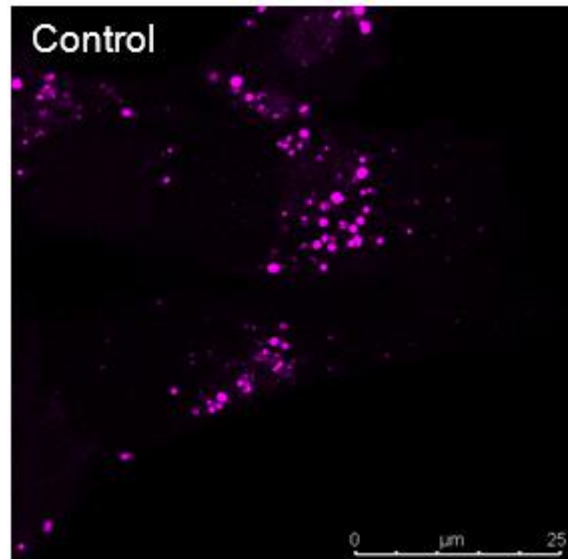
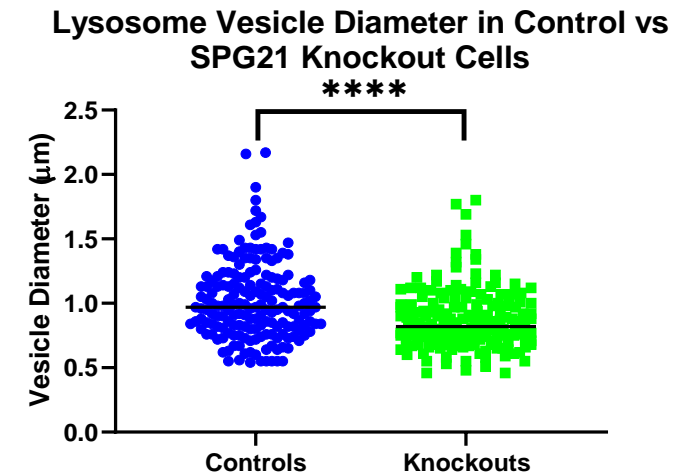
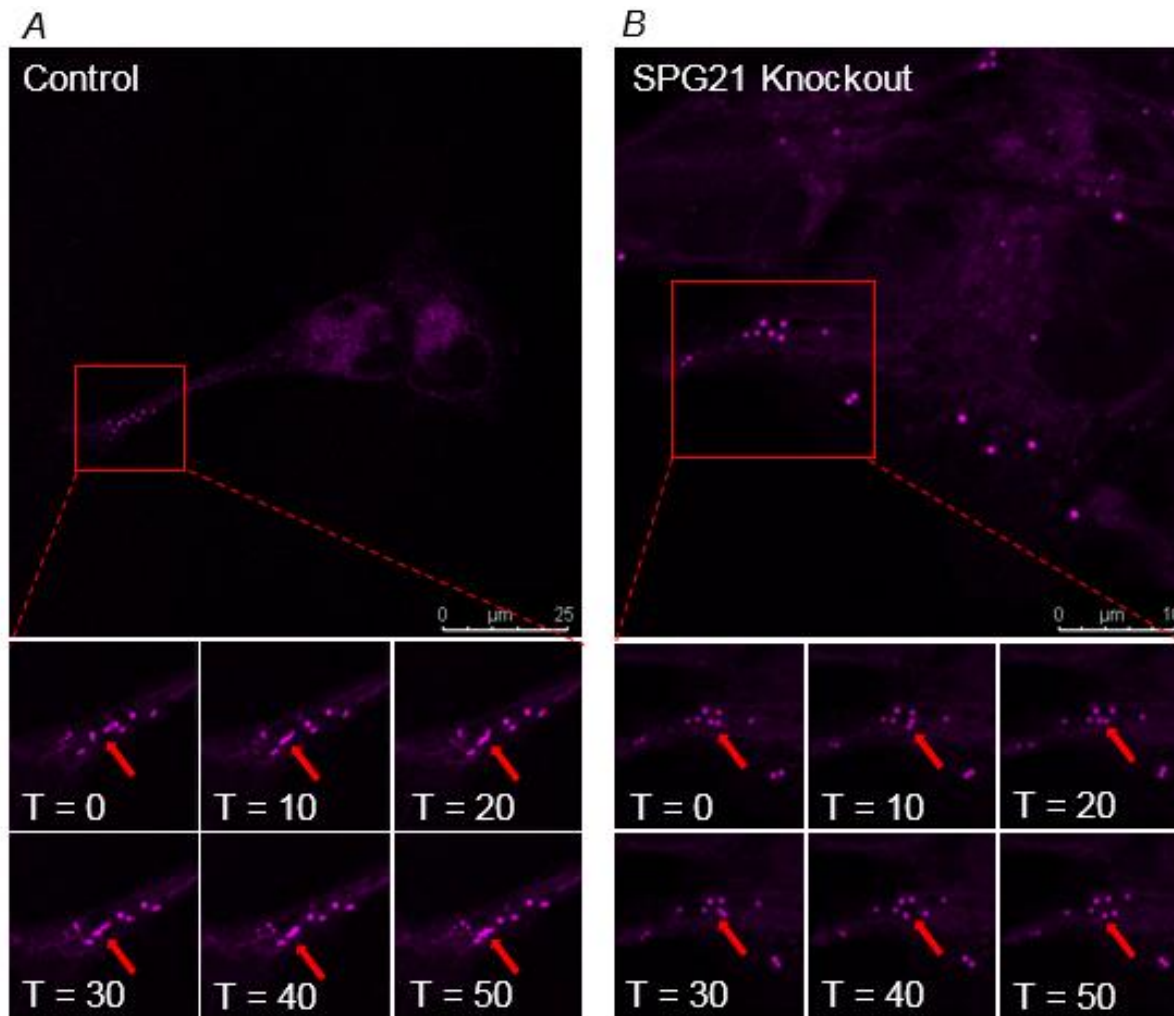
A**B**

Figure 4.41. Lysosome size and distribution in control and SPG21 knockout SH-SY5Y cells. Cells stained with lysosomal stain (ab112137) and imaged by confocal live cell microscopy. **A)** Control and SPG21 knockout cells. The lysosomes were shown to move very slowly, see videos in Appendix E, media 9 and 10. **B)** The diameter of lysosomes in control and SPG21 knockout cells are significantly different in size with a reduced diameter in SPG21 knockout cells. Scatter plot shows the median line with both control and knockouts $n=180$ lysosomes from 18 cells over three individual experiments. ****= $p<0.0001$ determined by Mann-Whitney test.

The size of lipid droplets was also investigated between control and *SPG21* knockout cells revealing no significant difference between the two, Figure 4.42. Lipid droplets were mostly observed towards the cellular periphery and moving quickly whilst interacting with one another, videos in Appendix E, media 7 and 8.



C
Lipid Droplet Diameter in Control vs SPG21 Knockout Cells

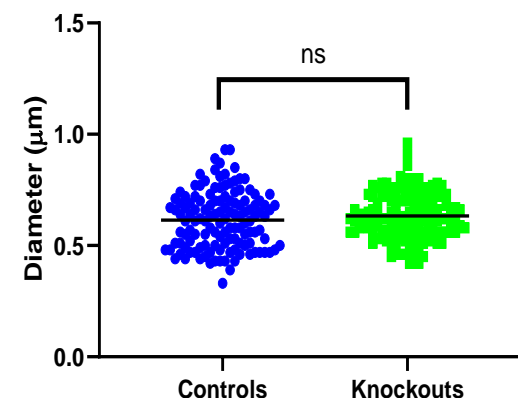


Figure 4.42. Lipid droplet size and interaction in control and SPG21 knockout cells. Cells stained with Nile Red lipid droplet stain and imaged by confocal live cell microscopy. Control **(A)** and SPG21 knockout **(B)** cell LD distribution including images showing LD interactions over 50 seconds, highlighted by red arrows. **(C)** The diameter of LDs in control and SPG21 knockout cells do not differ. Scatter plot show mean with control $n=130$ LDs from 19 cells and knockout $n=122$ LDs from 16 cells over three individual experiments. ns =not significant ($p=0.204$) determined by Mann-Whitney test. Videos in Appendix E, media 7 and 8.

The mitochondrial structure was also investigated given its proximity to maspardin surrounded vesicles (section 4.2.6.5), by staining control and knockout cells with Mitotracker and observing them using live cell imaging. Although no quantitative analysis was undertaken, no obvious mitochondrial structural abnormalities were observed, Figure 4.43.

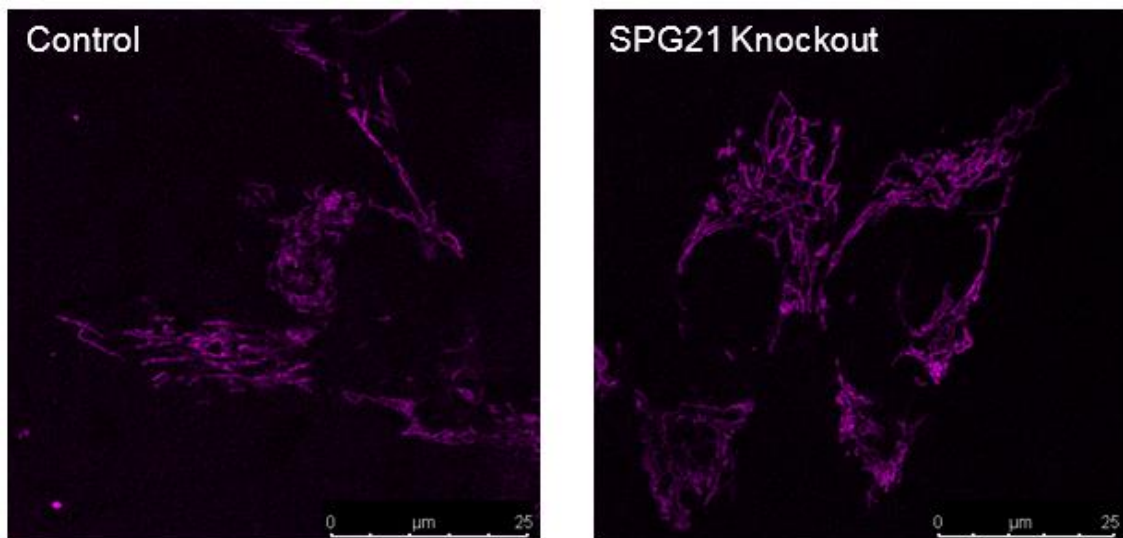


Figure 4.43. *Mitotracker stained control and SPG21 knockout SH-SY5Y cells. Live cell imaging using a confocal microscope; videos in Appendix E, media 11 and 12.*

4.3 Discussion

When using cell models to investigate proteins there are strengths and weaknesses associated with different techniques that should be considered, and the experimental techniques used in this study have highlighted some of the challenges involved. Antibody specificity is one such consideration, which appears to be the case for the available maspardin antibodies. In experiments involving knockout cell lines, confirmed genetically and by the lack of maspardin expression shown by Western blot and transcript analysis, there was still a considerable level of detection of protein in immunocytochemistry, suggesting the antibodies do not solely bind to maspardin. The three antibodies also showed differing cellular localisation distribution patterns. However despite this, the antibodies do detect maspardin as indicated by the tagged maspardin plasmids colocalising with the antibodies. To certify antibody reliability, commercial companies have started introducing standardised validation by generating knockout cell lines using CRISPR-Cas9 to ensure antibodies do not bind elsewhere. Unfortunately no such 'validated' antibody is currently available for maspardin.

In order to supplement the antibody experimental dataset, maspardin tagged gene constructs were generated. However, the use of plasmids is also not without disadvantages. Firstly, transfecting cells with plasmids grossly overexpresses (and potentially inappropriately expresses) that particular protein. Recently, a tool using CRISPR/Cas9 technology has been developed to knock-in a fluorescent tag to your endogenous protein of choice, potentially overcoming the issue of overexpression in cells studies [243]. However, the tag fused to the protein to aid detection may in itself potentially alter protein function, particularly as some polypeptide tags are sizeable; in this case the

YFP fluorescent protein is 238 amino acids in size, which is almost the same size of the 308 amino acid maspardin protein, although the myc and FLAG tags only add an additional 18 amino acid residues. However, fluorescently tagged maspardin enables live cell imaging to be undertaken, providing a powerful insight into the localisation and movement of the protein. This provided potentially important insight into maspardin function, revealing that it colocalised with Rab7 and localised to circular structures. When this plasmid was transfected into cells, fixed with PFA and mounted onto coverslips, it did not show the circular structures to the same clarity or resolution that could be observed when viewing the live cells via confocal microscopy. This highlights the limitations of fixing cells to observe protein localisation, and identifying potential interactors by colocalisation studies with other antibodies. Overall, this project showed that the most reliable localisation information could most likely be obtained using live cell imaging, and that cell studies using maspardin antibodies on fixed cells should be viewed with caution.

The primary aim of this chapter was to understand more about maspardin by exploring its' subcellular localisation, binding partners and the cellular consequences associated with the loss of maspardin. To date only a few studies have investigated the functional role of maspardin. Maspardin was previously thought to localise to endosomes and lysosomes and interact with Rab7 and ALDH16A1 [151, 211, 218]. Through live cell imaging in this work maspardin has been identified to localise to distinct circular structures revealed to be endosomes and lysosomes. The generation of an *SPG21* knockout cell line is an important tool for studying maspardin function as this enables exploration of cellular consequences due to maspardin loss which is replicable to loss of function Mast syndrome variants.

The colocalisation of maspardin on Rab7 surrounded vesicles is striking evidence for their association, particularly when maspardin is not obviously associating with other Rab 4, 5 and 9 surrounded vesicles. This association is further supported by mass spectrometry binding partner analysis identifying Rab7 as a potential binding partner, alongside other endosomal proteins. Given the strong association between maspardin and Rab7 it would be anticipated that Rab7 is detected following maspardin pull-down (and vice versa) when analysed by Western blot, however this was not the case. This could simply be due to the levels of protein that are required for detection by Western blot are too low, or the interaction between the two proteins are low affinity, but sensitive enough for liquid chromatography mass spectrometry detection. Alternatively, it could be due to the limitations of co-immunoprecipitation itself to identify protein-protein interactions. It is plausible that during the cell lysis or denaturation of the samples that the proteins could dissociate partially or entirely, therefore the interaction between the proteins is not easily detected. Further limitations surround the use of Rab proteins themselves in co-immunoprecipitation experiments as their association with membranes are dependent on a lipid anchor [244], therefore this anchor could easily be dissociated. Whereas these limitations are not present in live cell imaging to detect colocalisation of two proteins. To investigate whether the co-immunoprecipitation methodology is a limitation to detect the association of maspardin and Rab7 a known Rab7 interacting protein, such as ORP1L or Rab7-interacting lysosomal protein [245], could be used as a control.

Maspardin was also identified to surround a proportion of lysosomes, however the fluorescent vital dye used for this experiment stains lysosomes based on their pH so it is highly likely that other acidic vesicles are also stained. When

both maspardin and Rab7 were analysed against lysotracker it showed both surrounded lysotracker positive vesicles, suggesting that they associate with both lysosomes and late endosomes. The association between maspardin and lysosomes is further supported by the potential lysosomal localisation signals identified within the maspardin polypeptide sequence. In order to overcome the limitations of lysotracker potentially staining other acidic vesicles a more specific method would be needed. One option is to specifically label lysosomes with the LAMP1 marker, however the data presented here has identified that cells transfected with YFP-SPG21, fixed and stained reveal a more diffuse localisation without the clarity observed with live cell imaging. Alternatively, if a reliable maspardin antibody was available, LAMP1 could be co-immunostained with it or even tripled stained with a reliable Rab7 antibody to ascertain the proportion of vesicles maspardin associates with.

Additional lines of investigation pertaining to Rab7 expression in *SPG21* knockout cells found that its' protein expression is not altered by loss of maspardin. In support of this finding, a study by *Soderblom et al., 2010* determined that *Spg21* knockout mice do not exhibit changes in Rab7 mRNA expression in the brain [208]. The loss of maspardin has resulted in the disruption of Rab7 surrounded and lysotracker stained vesicles, however this cellular disruption was not evident in Rab4, 5 and 9 surrounded vesicles. This could suggest that maspardin is involved in maintaining the structure and function of these vesicles, and in the absence of maspardin inefficient transfer of vesicular cargo ensues resulting in altered vesicular size; potentially from late endosomes to lysosomes given the overall size increase in Rab7 surrounded vesicles and the size decrease in lysotracker stained vesicles. The decrease in lysosome size is more profound than the increase in Rab7 surrounded vesicles,

this could potentially be a result of reduced fission as its size is regulated by a balance between fission and fusion [246]. In addition to vesicle size, it would be beneficial to analyse the number of vesicles per cell and their rate of fission and fusion with other compartments to understand if any further alterations in endosomal/lysosomal functioning results from maspardin loss.

Maspardin has not previously been associated with mitochondria, however this work has identified that maspardin surrounded vesicles appear to transiently interact with mitochondria. In support of this, a number of mitochondrial proteins were detected in our binding partner analysis. Several members of the MICOS complex crucial for cristae formation and mitochondrial structure were identified as putative maspardin binding partners; this complex has also been associated with neurodegenerative disorders [234, 235]. Mitochondria and lysosomes are mutually functional organelles with approximately 15% of lysosomes contacting the mitochondria at any given time with transient tethering lasting around 60 seconds [247]. These contacts are crucial for maintaining cellular homeostasis by mediating nutrient exchange between the two organelles and Rab7 has emerged as playing a key role in tethering these contact sites [248].

The loss of maspardin appears to result in alterations of cellular homeostasis. This is apparent through the increase in cell death and the subsequent increase in metabolic activity to overcome the cellular impairment caused by maspardin loss. Altered cellular homeostasis is indicative of an unhealthy cell and the increase in cell death is reflective of neurodegeneration. Interestingly, the slight increase in ROS levels when treated with exogenous ROS, suggests cells may be unable to control and eliminate ROS as efficiently in absence of maspardin. As identified in section 1.3.3, aberrant ROS levels have been associated with a plethora of diseases, however it is likely that the increase in ROS/deficiencies in

combating ROS elevation in Mast syndrome is not directly impacted, but instead it is a secondary effect due to disruptions elsewhere as the difference between control and *SPG21* knockout cells are not profound.

Multiple forms of neurodegenerative disease including HSPs have been linked to the disruption of lysosomes and mitochondria [249]. Spatacsin and spastizin, associated with SPG11 and SPG15, are both localised to lysosomes and are critical for lysosomal generation [250]. Both SPG11 and SPG15 are clinically similar forms of HSP in which patients may also present with Parkinsonism, and enlarged lysosomes have been observed in patient-derived fibroblasts [251]. Another HSP associated with Parkinsonism is SPG78, due to mutations in the *ATP13A2* gene, which encodes a lysosomal membrane protein [252]. Furthermore, mutations in the *LYST* gene encoding lysosomal trafficking regulator protein involved in intracellular trafficking have also been found to be associated with HSP in two Japanese brothers [253].

HSP-associated genes encoding endosomal proteins is one of the largest subcellular groups within this group of conditions, many of which are directly associated with the ESCRT complex (section 1.4.4). EGF is crucial to the development and differentiation of neurones and it has been identified that endosomes may be central to proper functioning of EGF signalling to activate cell proliferation and survival pathways [254, 255]. Other studies have shown that EGF does not promote the growth and maturation of cortical neurones of *Spg21* knockout mice, unlike wildtype neurones [209]. This is consistent with the finding that maspardin also localises to endosomes, therefore its absence (through KO studies of gene mutation) may result in dysfunctional EGF downstream pathways, and consequently neurones are unable to develop efficiently. Furthermore, the multifunctional protein spartin (SPG20) is also

implicated in the degradation of the EGF receptor and spartin loss results in decreased EGF receptor degradation [256]. The accumulation of the endosomal EGF receptor induces apoptosis therefore it is crucial that the receptors are efficiently degraded when in excess to requirements [255]. Moreover, cell studies have demonstrated that excess EGF impairs the ESCRT-1 complex functionality [257]. Taken together, it is possible that the loss of maspardin could be impacting upon the EGF receptor within endosomes resulting in apoptosis.

4.3.1 Future Work

This data provides compelling evidence for the localisation of maspardin to Rab7 positive vesicular structures that transiently contact mitochondria, however the precise function and role of maspardin is yet to be fully elucidated. Future studies could delve into the 3D structure of the protein to understand how it may interact with other proteins, in particular Rab7, and how it may function. This work has identified maspardin surrounds vesicles, so it is important to investigate the cargo of these vesicles and then compare the cargo to Rab7 surrounded vesicles in *SPG21* knockout cells to better understand how the cargo may be impacted as a result of maspardin loss. Given that the size of Rab7 surrounded vesicles and lysosomes are significantly altered due to maspardin loss it would also be of great interest to understand the nature of the cargo that is transferred between these vesicles. To explore the vesicular cargo immunocytochemistry would be required, and for these experiments it is important to obtain or generate a reliable maspardin antibody. Another avenue of future work could employ the use of electron microscopy to explore the subcellular localisation of maspardin in much greater detail, with a particular focus on maspardin surrounded vesicles transiently contacting mitochondria.

The interaction between maspardin and Rab7 warrants further exploration to determine its precise nature and role. The findings presented in this thesis identified that Rab7 surrounded vesicles are altered in the absence of maspardin. It would be intriguing to understand the cellular effects of Rab7 depletion/dysfunction (by generating a *Rab7* knockout cell line) and whether this would impact the function or localisation of maspardin.

The generation of an *SPG21* knockout cell line will be invaluable for future studies to fully define the cellular implications of maspardin loss. A limitation of generating a knockout cell line by CRISPR/Cas9 is the potential to incorporate genetic off-target effects into the genome. To investigate these potential off-target effects the whole genome from multiple knockout clones and control SH-SY5Y cells could be sequenced. From the work carried out in this thesis *SPG21* knockout cells were found to have bioenergetic impairments. To expand upon these findings further mitochondrial experiments would be beneficial to understand mitochondrial impact, particularly given the association between maspardin and mitochondria. The Seahorse XF cell mito stress kit would provide a detailed insight into mitochondrial function. To completely understand the molecular basis of Mast syndrome it is crucial to fully define the function of maspardin, and then use this information alongside the knockout cell line to understand the pathways impaired, and how this leads to neurodegeneration. To explore the pathways implicated, qPCR could be utilised to understand the differences in gene regulation between wildtype and *SPG21* knockout cells whilst referring to the vast amount of putative maspardin binding partners identified by mass spectrometry, therefore giving an insight into altered biological pathways.

The effects of maspardin loss have been explored in this work which in essence replicates the two loss of function mutations that are seen in the Amish and Italian individuals. It would be interesting to investigate the cellular consequences that result from the Japanese missense mutation, this could be explored by site directed mutagenesis using the previously used fluorescent plasmid. This plasmid could be used to investigate how this particular variant impacts the protein's cellular localisation, and how the binding partners may differ by repeating mass spectrometry experiments. Given that maspardin is revealed to localise to Rab7 positive vesicles the exploration of how this interaction may differ due to the single base substitution would be insightful to understand the biomolecular basis of this genetic form of Mast syndrome.

Finally, to increase the impact of this work and confirm the significance to Mast syndrome patient induced pluripotent stem cells could be generated to investigate whether the same cellular abnormalities observed in *SPG21* knockout SH-SY5Y cells are also identified in patient derived cells.

Chapter 5

Investigating Lipid Profiles in Motor Neurone

Disease

Investigating Lipid Profiles in Motor Neurone Disease

5.1 Introduction

5.1.1 Cholesterol and the Bile Acid Pathway

Lipid imbalance, in particular abnormal cholesterol levels, is a common theme among neurodegenerative disorders. Cholesterol is a type of lipid hydrocarbon with its name deriving from ancient Greek (chole; bile, and stereos; solid), due to it being first identified as a component of gallstones [258]. The specific hydrocarbon properties of cholesterol make it particularly well suited for its role as an important constituent of cellular membranes where it is typically found in high concentration [259]. This is particularly the case in the brain, the most cholesterol rich organ [53], in which cholesterol is an integral component of myelin. Myelin is vital for electrically insulating neurones for rapid signal transduction and accounts for ~80% of brain cholesterol, [260]. However as peripheral circulating cholesterol does not cross the blood-brain barrier, the brain must synthesise its own cholesterol. As, in adults, the rate of synthesis exceeds requirements, cholesterol must be metabolised and removed from the brain to prevent toxic build-up [261]. Cholesterol metabolism involves the bile acid synthesis pathway, which predominantly takes place in the liver through the 'classical' pathway, although neuronal cholesterol clearance is achieved via an 'alternative' branch of the bile acid synthesis pathway, Figure 5.1 [262]. The classical pathway accounts for ~90% of bile acid production under physiological conditions, whereas the alternative pathways contributes just ~10% of bile acid synthesis, however liver damage or cirrhosis leads to the increased utilisation of the alternative pathways [263, 264]. In this process cholesterol is converted into primary bile acids, cholic acid and chenodeoxycholic acid, by a cascade of 16 distinct enzymes with primary sites of action in the ER, mitochondria,

peroxisomes and cytosol [265, 266]. In the liver these enzymes enable bile acid extrusion via a series of bile acid oxysterol intermediate derivatives [267], however the enzymatic primary site of action may differ compared to the same enzymes in the brain [266].

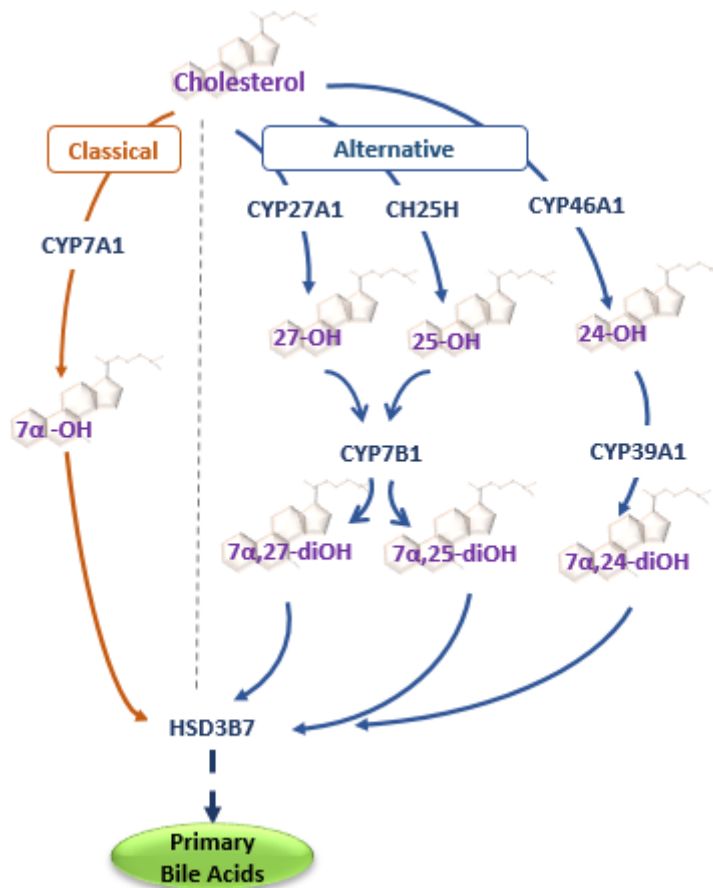


Figure 5.1. The classical and alternative bile acid pathways. The classical pathway is initiated by CYP7A1 in the liver whereas the three alternative pathways are initiated by either CYP27A1, CH25H or CYP46A1. CYP46A1 is the main pathway for the extrusion of cholesterol from the brain. The alternative and classical pathways converge after oxysterol 7α-hydroxylation in the common pathway to produce primary bile acids after further enzymatic steps.

The first and the rate-limiting step of the pathway is initiated by cytochrome P450 cholesterol 7α-hydroxylase (CYP7A1) in the liver as part of the classical pathway. The alternative pathway comprises three enzymatic outcomes, all of which firstly modify cholesterol side-chains prior to pathway to re-convergence [268-270]. The first of these pathways is initiated by the cytochrome P450 sterol

27-hydroxylase (CYP27A1), catalysing the conversion of cholesterol to 27-hydroxycholesterol (27-OH). This molecule primarily functions within mitochondria, and it is widely distributed in most tissues [270]. This initial step requires mitochondrial cholesterol import, primarily via the ER and lipid droplets, mediated by steroidogenic acute regulatory protein (StAR) and StAR-related lipid transfer domain (StarD) proteins [271]. The liver microsomal enzyme sterol 25-hydroxylase (CH25H) also initiates an arm of the alternative pathway, converting cholesterol to 25-hydroxycholesterol (25-OH). Both 27-OH and 25-OH are 7 α -hydroxylated by the ER cytochrome P450 oxysterol 7 α -hydroxylase (CYP7B1), forming 7 α ,27-dihydroxycholesterol (7 α ,27-diOH) and 7 α ,25-dihydroxycholesterol (7 α ,25-diOH), prior to entry into the common bile acid pathway [269, 270]. While the primary site of action of CYP7B1 is within the ER other studies indicate that this molecule may also be active within brain mitochondria [272, 273]. A final arm of the alternative pathway takes place in the brain, where cytochrome P450 sterol 24-hydroxylase (CYP46A1) catalyses the conversion of cholesterol to 24-hydroxycholesterol (24-OH), which is able to cross the blood brain barrier and is the major pathway for cholesterol elimination from the brain [274]. 24-OH is then 7 α -hydroxylated by the liver microsomal cytochrome P450 oxysterol 7 α -hydroxylase II (CYP39A1) to 7 α ,24-dihydroxycholesterol (7 α ,24-diOH), which subsequently enters the common bile acid pathway [269, 275]. The various initial arms of the oxysterol cascade then converge with the involvement of 3 β -hydroxysteroid dehydrogenase (HSD3B7), which catalyses the first step of the common bile acid pathway initiating the subsequent steps leading to the primary bile acids chenodeoxycholic and cholic acid [268]. Despite an enzyme's specificity for certain oxysterols it is known that other oxysterols are also able to fit into the catalytic site with differing

specificities, for example CYP27A1 is a multifunctional enzyme that catalyses the hydroxylation of different oxysterols (Figure 5.2). Recent studies have shown that CYP27A1 is also able to hydroxylate cholesterol to 25-OH and 24-OH, in addition to 27-OH [263].

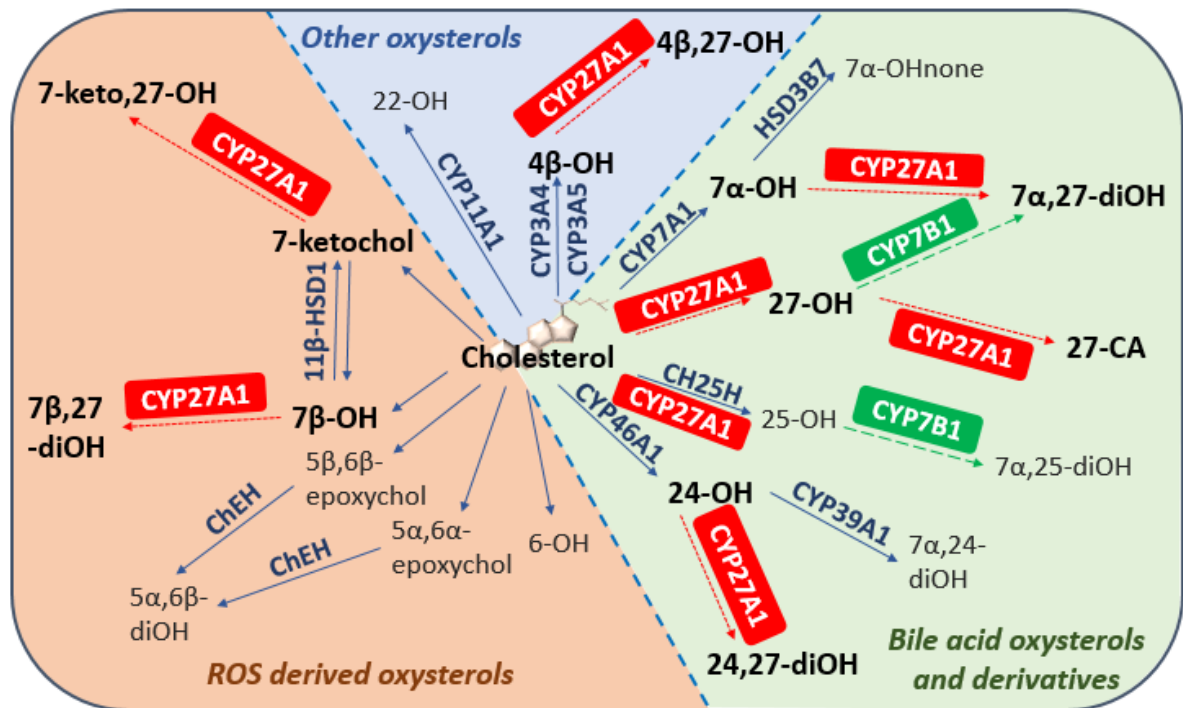


Figure 5.2. The multifunctional CYP27A1 enzyme in cholesterol and oxysterol metabolism. Green segment outlines bile acid derived oxysterols, red segment shows reactive oxygen species (ROS) derived oxysterols and the blue segment shows other oxysterols formed by CYP27A1. ChEH = cholesterol epoxide hydrolase; CA = cholestanic acid; HSD = hydroxysteroid dehydrogenase; none = cholestenone. Figure adapted from Mutemberezi et al., 2016.

5.1.2 Oxysterol Function

As well as comprising bile acid intermediates for cholesterol extrusion the oxysterols entail a large family of lipids which have been found over recent years to be important for a plethora of physiological processes including cell/nuclear receptor-mediated signalling, glucose homeostasis, and immune response [267]. In particular, oxysterols are important for regulating levels of cholesterol which must be constrained within narrow limits within the cell to

sustain appropriate membrane permeability, fluidity, and function [276]. One mechanism of oxysterol regulation involves the processing of sterol regulatory element-binding proteins (SREBPs) which are a family of transcription factors that regulate lipid homeostasis [277]. SREPB-2 is considered the master regulator of cholesterol biosynthesis which multiple oxysterols are known to inhibit and therefore cholesterol synthesis is not activated [278]. Oxysterols also bind to and activate liver X receptors (LXRs) to induce cholesterol efflux, and eliminate and limit lipoprotein cholesterol uptake [276, 279]. While the precise mechanism of oxysterol transport remains to be determined, a group of conserved proteins including oxysterol binding protein (OSBP) and OSBP-related proteins (ORPs) bind and traffic oxysterols to illicit multiple cellular processes [276, 280]. In particular, 27-OH, 25-OH and 24-OH are potent inhibitors of cholesterol synthesis in the brain, and notably alterations in these oxysterols have been implicated in a range of neurodegenerative diseases [278, 281, 282].

5.1.3 Oxysterols and Apoptosis

Oxysterols have been shown to trigger cell death through a number of mechanisms by inducing both the intrinsic and extrinsic apoptotic pathways [283]. A study by *Lee and Chau, 2001* demonstrated that 25-OH upregulates death mediators and apoptosis [284]. Upon oxysterol treatment the loss of mitochondrial membrane potential and the subsequent release of cytochrome c resulting in apoptosis has been identified [283]. A co-culture of human SH-SY5Y neuroblastoma and rat C6 glioma cell lines were used by *Wang et al., 2016* in order to investigate the cytotoxicity of 27-OH on neurones. These cells were shown to have reduced mitochondrial membrane potential and increased apoptosis [285]. Distinct oxysterols and cell types vary in their ability to induce

apoptosis and there is not a common pathway that oxysterols follow to execute apoptosis [276].

5.1.4 Oxysterol Imbalance and Motor Neurone Disease

A key finding highlighting a central role of altered oxysterol metabolism in motor neurone degeneration, is the association of mutations within core enzymatic components of the cascade with MND outcomes. Mutations in *CYP7B1* cause the pure autosomal recessive SPG5 [286], the analysis of cerebrospinal fluid (CSF) and blood plasma from patients with SPG5 found altered levels of several oxysterols in the bile acid pathway including the accumulation of metabolic precursor substrates (25-OH and 27-OH) [263, 287, 288]. A 6-9-fold increase in 27-OH levels are seen in the plasma of patients whereas a 30-50-fold increase is seen in the CSF compared with a huge 100-fold increase in 25-OH levels in CSF when compared to control individuals [289]. The cholesterol levels in *Cyp7b1* knockout mice do not show altered cholesterol levels compared to wildtype mice in brain tissue and plasma, however there is a build-up in the enzymatic precursors, 25-OH and 27-OH as seen in patients with SPG5 [278].

Mutations in a second enzyme in the oxysterol cascade; *CYP27A1*, responsible for the immediate precursor enzymatic step to *CYP7B1* in the alternative mitochondrial arm of the bile acid pathway, have also been associated with overlapping neurodegenerative outcomes. Mutations in the *CYP27A1* gene result in cerebrotendinous xanthomatosis (CTX), a well-defined rare autosomal recessive lipid storage disorder characterised by tendinous xanthomas, presenile cataract and diarrhoea [290]. While CTX is also characterised by a wide range of neurological outcomes including intellectual disability, dementia,

ataxia, epilepsy and psychiatric symptoms [291], spasticity (and HSP) are considered cardinal and often the presenting clinical features [292, 293].

In post-mortem brain tissue from CTX patients a significant increase in brain cholesterol and cholestanol has been shown, in particular within the cerebellum [294]. This has also been observed in *Cyp27a1* knockout mice however, it is important to note that these mice do not present with a distinct CTX phenotype [294]. It has been found that the mouse specific CYP3A11 can also hydroxylate 7 α -OH in the 27 position in *Cyp27a1* knockout mice therefore circumnavigating the clinical phenotypes that are observed in CTX individuals as bile acids are still produced [264]. The devastating effects of CYP27A1 dysfunction or depletion in humans is likely to be due to the enzyme hydroxylating so many oxysterols (Figure 5.2) and due to it being widely expressed in all tissues in the body, unlike CYP7A1 which is solely expressed in the liver [264].

5.1.5 The Role of Mitochondria and ER in Bile Acid Synthesis

The mitochondria and ER are both crucial to the bile acid pathway as the site of action of several of the enzymes is within these organelles. The mitochondria is particularly important for the CYP27A1 initiated arm of the alternative pathway, as this enzyme is located on the IMM [263]. Mitochondria are one of the least abundant areas of cellular cholesterol, with 40-fold less than the plasma membrane and 4.5-fold less than the ER. The majority of mitochondrial cholesterol is obtained from the ER which is first transported to the plasma membrane and then to the mitochondria via StarD1, however a smaller proportion is directly imported from the ER via ER-mitochondria contact sites [295]. Cholesterol delivery to CYP27A1 is considered the rate limiting step of the pathway [263]. Overexpression of *Cyp27a1* in mice only slightly increases

oxysterol levels, but overexpression of *StarD1* significantly increases oxysterol and bile acid synthesis [263].

As the enzymes required for bile acid synthesis are located in different organelles, this necessitates the efficient transport of oxysterols between subcellular compartments. Up to 20% of the mitochondria are in contact with the ER forming the mitochondria-associated ER membrane (MAM), which is enriched in cholesterol [295]. This specialised contact site allows the tethering and subsequent transfer of molecules such as lipids and calcium between the two membranes. The MAM is also important for maintaining structural integrity to the two organelle membranes in addition to regulating autophagy and cell survival [295, 296]. ORP5 and ORP8 are localised to the MAM and are known to mediate the transport of phosphatidylserine from the ER to mitochondria. Both ORP5 and ORP8 have been shown to be linked to the MICOS complex, a multiprotein assemblage of molecules spanning the IMM and OMM necessary for cristae formation, illustrated in Figure 5.3 [297]. It is likely that the oxysterol intermediates of the bile acid pathway are transported between the two membranes by ORPs and associated transport proteins using the MAM as a scaffold for transport.

There are four main tethering mechanisms regulating the mitochondria-ER contact site (Figure 5.3):

(i) mitochondrial mitofusin 1 (MFN1) interacting with ER mitofusin 2 (MFN2), with tethering also via MNF2 – MFN2 homodimers mediated through a pool of the molecule present on the mitochondrial membrane [298],

- (ii) mitochondrial tyrosine phosphatase-interacting protein 51 (PTPIP51) interacting with ER vesicle associated membrane protein-associated protein B (VAPB) [299],
- (iii) mitochondrial voltage-dependent anion channel 1 (VDAC1) complex formation important for calcium ion exchange with 75 kDa glucose-regulated protein (GRP75) and Sigma 1 receptor (SIGMAR1), and ER 1,4,5-triphosphate receptor 3 (IP3R3),
- (iv) ER B-cell receptor-associated protein 31 (BAP31) complex formation with mitochondrial fission protein FIS1 (fission 1 homolog) and the phosphofurin acidic cluster sorting protein-2 (PACS-2), important for apoptotic processes [300].

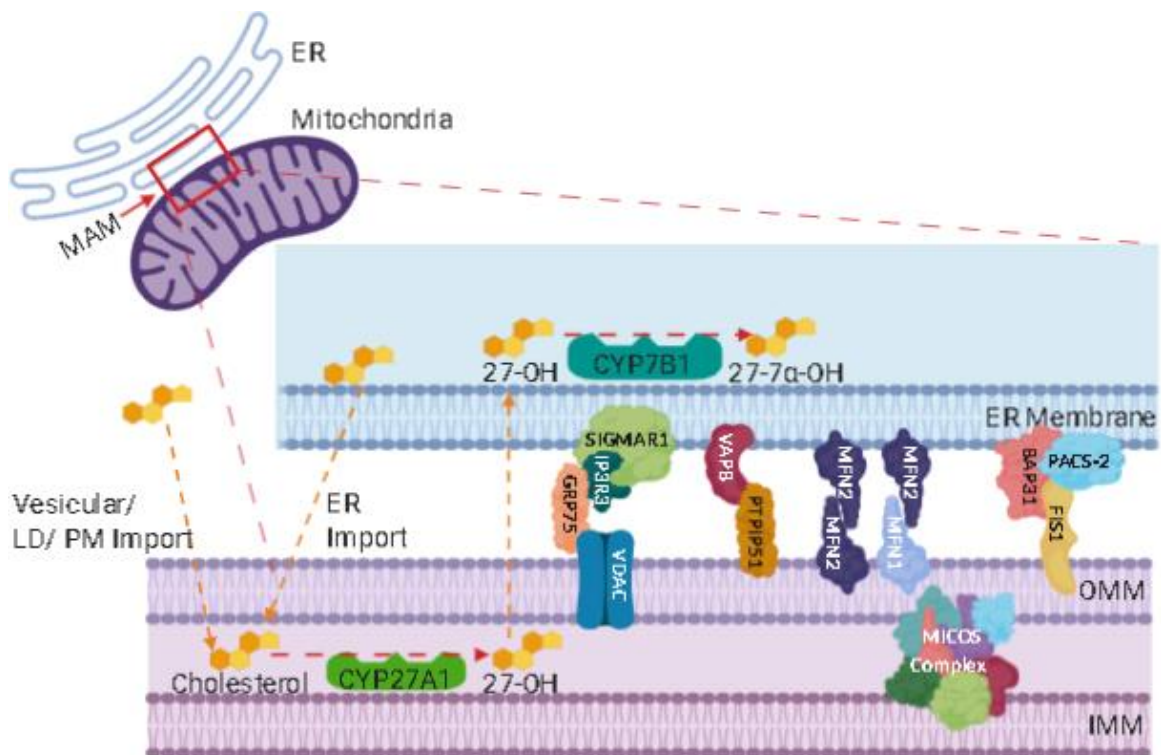


Figure 5.3. The mitochondria-associated ER membrane (MAM). The four main tethers required to maintain the integrity of the MAM are depicted, in addition to the MICOS complex which is required for mitochondrial cristae formation and membrane integrity. The first steps of the mitochondrial alternative arm of the bile acid synthesis pathway are shown including the mitochondrial import of cholesterol to CYP27A1 and the transport of its product, 27-OH across the MAM to CYP7B1. Made using BioRender.

5.1.6 Mutations in the Mitochondria-Associated ER Membrane Tethers Associated with Motor Neurone Disease

Several mutations in genes encoding ER-mitochondrial membrane tethers have been found to be associated with MND, most notably in *MFN2*, *SIGMAR1* and *VAPB*. Mutations in *MFN2* have been associated with a broad range of motor neurone phenotypes including CMT2A2, hereditary motor sensory neuropathy (HMSN) with pyramidal features (HMSN V), HMSN with optic atrophy (HMSN VIA) and/or cognitive impairment, and spasticity [301-303]. In support of this, studies of an *Mfn2* transgenic mouse model harbouring a pathogenic CMT2A mutation (*MFN2*^{R94Q}) identified a notable reduction in ER-mitochondria contacts, a finding that was also replicated in cells of CMT2A patient fibroblasts [304]. *SIGMAR1* gene mutations have again been associated with a range of MND subtypes including early and late-onset ALS and dHMN with no additional neurological abnormalities [305-307]. As with *MFN2*^{R94Q}, studies of cells expressing pathogenic *SIGMAR1* mutations (E138Q and E150K) revealed a reduction in total ER-mitochondria contacts, and incorrect targeting of mutant protein [305]. Mutations in another tethering molecule, *VAPB*, also result in similar MAM abnormalities and is mutated in MND phenotypes; mutations are associated with late-onset SMA and ALS [308, 309].

5.1.7 Lipidome imbalance in MNDs

Taken together, it is clear that abnormalities and imbalances in lipid homeostasis in addition to the cellular architecture crucial for these metabolic processes may form a key and common basis in MNDs. More specifically, gene mutations impairing molecules important for the functionality of bile acid pathways and the transport of lipids across the MAM, may result in general cellular and mitochondrial lipid imbalance leading to MNDs/HSP. Therefore, in addition to core metabolic enzymes of these pathways, auxiliary molecules

important for their function such as transporters, chaperones and structural proteins that provide a scaffold for their transport are likely to impact lipid homeostasis when dysfunctional.

To explore the hypothesis that mitochondrial lipid imbalance is observed more widely within MNDs this chapter describes the development of methodologies to detect the very low levels of oxysterols by mass spectrometry in mitochondrial-enriched subcellular fractions obtained from both cultured cells and blood samples. Thus far, oxysterols have not been investigated on a subcellular basis in relation to MND, instead studies have focussed on CSF and blood plasma, therefore this work is novel. These investigations were undertaken in collaboration with Professor Helen Griffiths from the University of Surrey, in addition to Dr Irundika Dias from the University of Aston. Alongside this an *SPG21* knockout cell line was developed and utilised to investigate lipid profiles in cells in the absence of maspardin.

5.2 Method and Results

A core aspect of this component of my PhD entailed the modification and development of existing laboratory methods to define the lipidomic profiles of subcellular fractions obtained from small (<10ml) blood samples, as well as CRISPR-Cas9 cell models of disease. As such this work, detailed below, is presented as a joint methods-results section.

5.2.1 Method Development

5.2.1.1 Obtaining Enriched Mitochondrial Fractions

In order to explore this hypothesis is it important to reliably obtain mitochondrial fractions from both cultured cells and blood samples. Standard mitochondrial extraction protocols contain a series of homogenisation and centrifugation steps to remove unwanted cellular material to obtain a mitochondrial pellet.

5.2.1.2 Starting Cellular Material

The first step is to obtain cellular starting material. Cell lines grown in a monolayer on a 15cm cell culture dish were washed with 10ml PBS, detached with 2ml trypsin, neutralised with 5ml of the relevant cell culture media and multiple dishes combined into one 50ml tube. The cell suspension was then centrifuged at 1000g for 5 minutes to obtain a cell pellet. Six 15cm cell culture dishes (~90% confluency) were found to be sufficient.

10ml blood samples are first taken from an individual in an EDTA tube for subcellular fractionation. To separate out peripheral blood mononuclear cells (PBMCs) from the plasma and red blood cells (RBCs) the blood sample is diluted 1:1 in RPMI+GlutaMAX and then carefully layered onto 8ml of Histopaque-1077 in a universal tube and centrifuged at 1000g for 30 minutes with the brake off. Figure 5.4 shows the layers that form after centrifugation and

the PBMC 'buffy coat' layer is extracted and pelleted at 1000g for 5 minutes. An initial challenge faced during this part of the protocol was that the PBMCs adhered to the sides of the plastic universal tube, so a condensed cell pellet was not formed. It was found that the type of plastic that the universal tubes were made from altered cell adherence to the tube, polypropylene tubes allowed more defined pellets to be formed than polystyrene universal tubes.

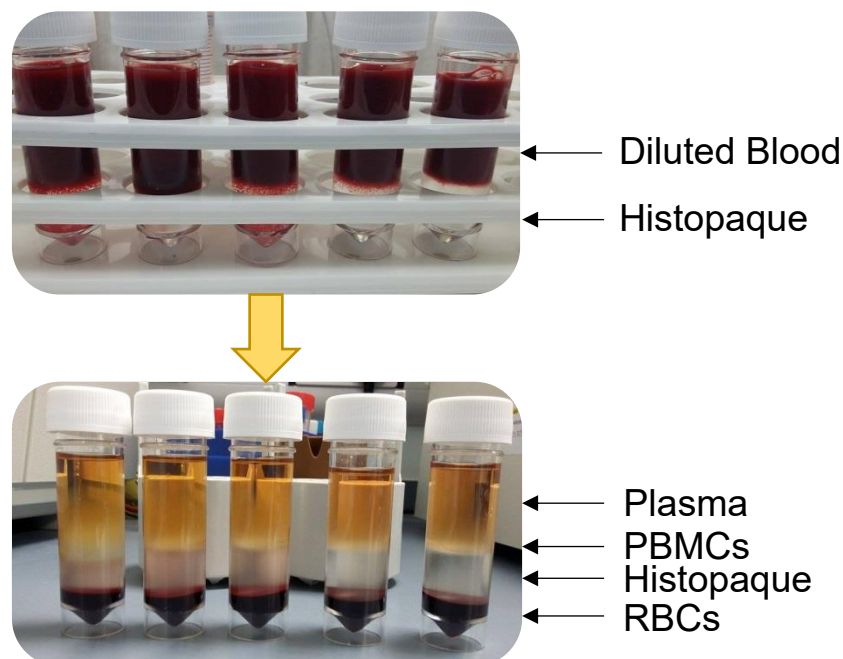


Figure 5.4. The separation of PBMCs from whole blood. The top image shows whole diluted blood layered onto Histopaque-1077. The bottom image is after centrifugation showing the central PBMC layer with the separated plasma at the top and the RBCs at the bottom beneath the clear Histopaque layer.

5.2.1.3 First Mitochondrial Extraction Protocol

The protocol adopted initially comprised of homogenisation and several centrifugation steps to remove unwanted cellular material to obtain a mitochondrial pellet, conducted on ice, with centrifugation at 4°C. The homogenisation buffer used for this protocol was made up of 0.32M sucrose, 1mM EDTA, 10mM Tris and protease inhibitors (1:500 dilution). Cell pellets were resuspended in 2ml of homogenising buffer and transferred to a glass

homogeniser where the cells were broken apart by 30 grinding repetitions. The subsequent steps of this protocol involve centrifugation using microcentrifuges as outlined in Figure 5.5. 400µl of the homogenised cell suspension was set aside and the remainder divided into microcentrifuge tubes and centrifuged for 10 minutes at 1000g. The supernatant was then centrifuged again under the same conditions whereas the pellet was kept. The pellet from the second spin was also kept and the supernatant was then centrifuged for 20 minutes at 13,000g. The supernatant was kept, and the pellet was resuspended in 200µl of homogenising buffer and centrifuged for a further 10 minutes at 13,000g. This final centrifugation step produced the mitochondrial pellet, and the supernatant was transferred to a fresh microcentrifuge tube. All pellets were resuspended in 200µl of homogenising buffer and stored at -80°C until Western blot analysis.

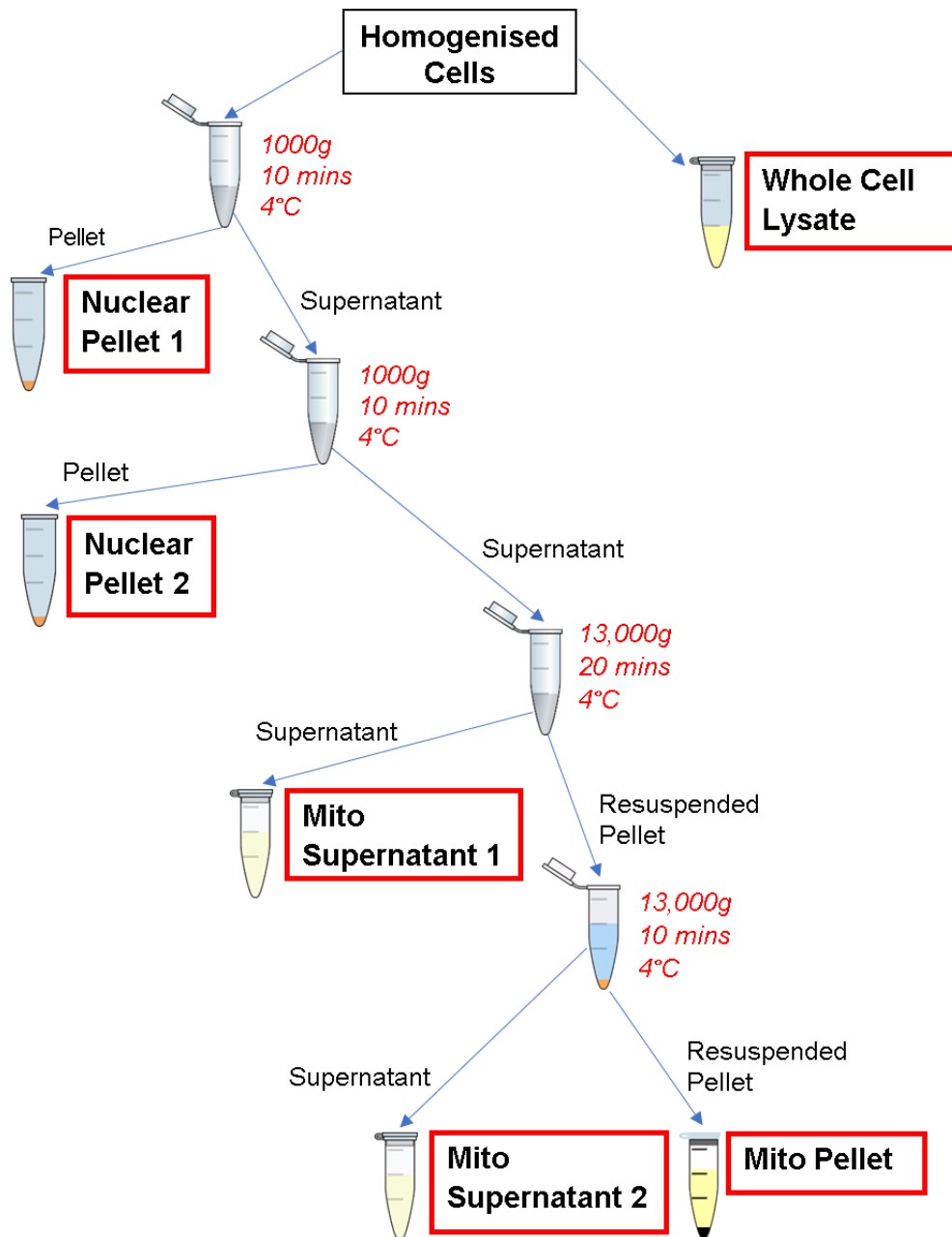


Figure 5.5. Diagram outlining the protocol to obtain mitochondria from homogenised cellular material. Fractions highlighted by a red box were kept for further analysis.

To assess the cellular composition of each supernatant and pellet obtained a Western blot was performed. First, suitable subcellular antibody markers were required to assess the purity of mitochondrial fractions; calreticulin (PA3-900) was used as a marker for the ER and several antibodies were trialled to detect a mitochondrial marker including voltage dependant anion channel (Abcam,

ab15895; 1:1000 dilution in milk) and succinate dehydrogenase complex subunit A (Cell Signaling, 11998; 1:1000 dilution in milk) but only the cytochrome c oxidase complex IV (COX IV) antibody successfully detected protein. Figure 5.6 shows the cellular fractions from a mitochondrial extraction using HEK 293 cells as a starting material. Only the whole cell lysate and first mitochondrial pellet show detection of the mitochondrial and ER markers, whereas no protein is detected in the remaining fractions.

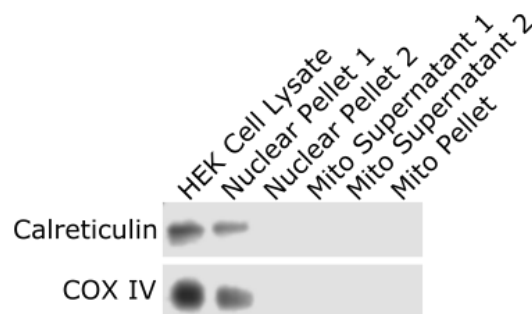


Figure 5.6. Western blot of cellular fractions obtained from mitochondrial extraction of HEK 293 cells. Absolute amounts of sample were probed with calreticulin (~57kDa) and COX IV (~17kDa) primary antibodies which were detected by HRP conjugated secondary antibodies and ECL.

This protocol proved to be unsuccessful as mitochondrial pellets were unable to be obtained from HEK 293 cells or PBMCs. Furthermore, COX IV was unable to be detected beyond the first few fractions of the protocol indicating the lack of mitochondrial sample where an enriched mitochondrial fraction is expected, perhaps due to inadequate sample yield.

5.2.1.4 Second Mitochondrial Extraction Protocol: Purity Matters

A second protocol was implemented based on a published method paper; 'Purity matters: A workflow for the valid high-resolution lipid profiling of mitochondria from cell samples' by Kappler *et al.*, 2016 [310], which details a method to isolate relatively pure mitochondria from cell samples. The major

difference with this protocol is the incorporation of an ultracentrifugation step toward the end of the protocol, to primarily detach mitochondria from the ER as the two organelles are tightly bound via their contact sites. The resulting mitochondrial pellet appears to be extremely enriched in mitochondria and almost pure, as confirmed by Western blot probing with mitochondrial ATP5A, ER calnexin, nuclear histone H3 and Golgi apparatus giantin markers. Figure 5.7 shows the blot taken from the paper which outlines three mitochondrial extraction protocols, indicating the ultracentrifugation (UC) method obtains the purest sample with little ER detection and no nuclear or Golgi apparatus detection. The density centrifugation (DC) method is the same methodology that is included in the UC method, however it lacks the final ultracentrifugation spin. This therefore demonstrates the effectiveness of ultracentrifugation to obtain a purer mitochondrial fraction.

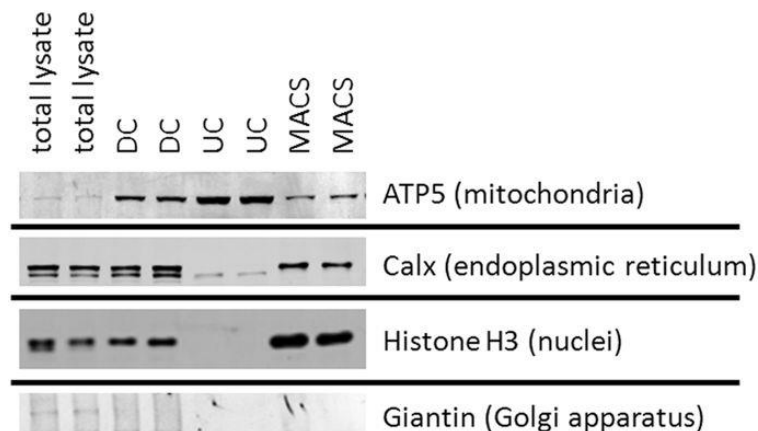


Figure 5.7. Comparative mitochondrial isolation techniques. Blot taken from Kappler et al., 2016 where the authors demonstrate the purity of the mitochondria isolated via the ultracentrifugation technique. The authors extract mitochondria from HEPG2 cells by three methods: density centrifugation (DC), ultracentrifugation (UC) and magnetic bead-assisted isolation (MACS). 30µg of protein was loaded for each sample and the UC method shows the least contamination.

Initial experiments with the protocol involved clarifying which supernatant layer the mitochondrial fraction was located in, and also establishing the most appropriate plasticware to use to perform the experiments (e.g. to aid visualisation of the supernatant layers, and adherence of pelleted material). Analyses were performed on extractions from various sections of the protocol to clarify the subcellular content and purity at different stages of the protocol. Figure 5.8 shows the Western blot image from these layers where '1' is from the bottom of the tube and '5' is the top, this blot reveals that there was only ER and mitochondrial protein detection at the top of the tube suggesting that the sample may not have travelled through the Percoll or another layer had not been extracted/detected. As expected, the 'whole cell lysate' contains both ER and mitochondria as determined by the detection of calreticulin and ATP5A, with the detection of calreticulin particularly abundant, whereas the 'DC lysate' component is abundant in mitochondria with less ER content. Despite the only detection present within the upper layer of the ultracentrifugation tube, calreticulin was not detected, although there was a strong ATP5A signal. The methodology was repeated using 50ml of blood as starting material as lower volumes of blood were unable to yield a sufficient mitochondrial fraction.

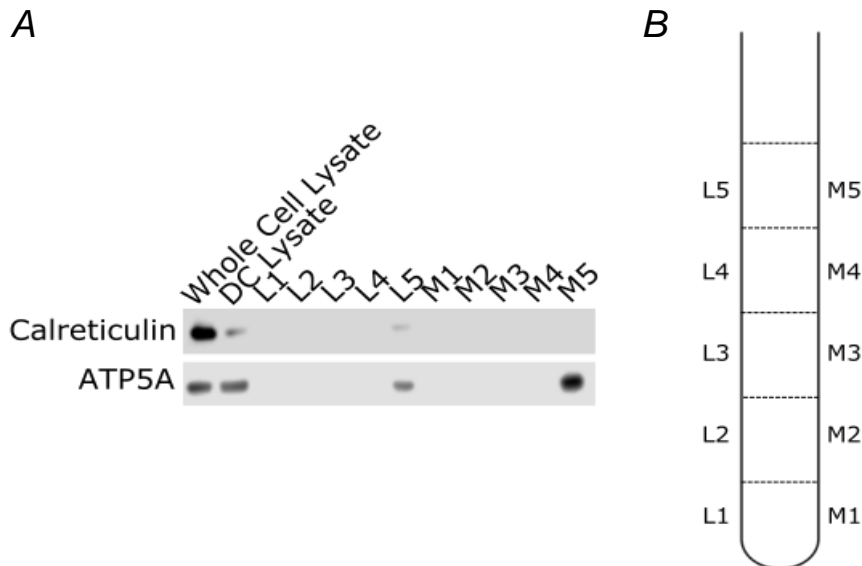


Figure 5.8. Identifying the portion of the ultracentrifugation tube containing cellular material. A) Mitochondrial extraction performed from HEK 293 cells and analysed by Western blot. L1-5 and M1-5 represent the layers of the tube as shown in (B) where ‘L’ represents whole cell lysate and ‘M’ represents the mitochondrial DC sample that was subjected to ultracentrifugation. Absolute amounts of sample were probed with calreticulin (~57kDa; (PA3-900)) and ATP5A (~56kDa) primary antibodies which were detected by HRP conjugated secondary antibodies and ECL.

To aid development of the protocol, arrangements were made for me to visit the group at the University of Tübingen to observe the methodology carried out by the author of the paper, Dr Lisa Kappler. Although the group had not previously isolated mitochondria from blood samples (only tissue and cell samples), the trip proved to be very helpful in defining the methodology to obtain mitochondrial samples from <30ml of blood. The knowledge and experience gained from the research team in Tübingen was invaluable to efficiently obtain mitochondrial samples, and this methodology continued to be adapted and optimised to efficiently isolate mitochondrial samples from blood.

5.2.1.5 Reducing Blood Volume

The next modification involved reducing the amount of starting material from 30ml to 10ml of blood, from which to still isolate a sufficient amount of

mitochondrial sample. 30ml, 20ml, and 10ml blood samples were used to determine whether extracting mitochondria from lower volumes of blood was feasible. Figure 5.9A shows that a 10ml blood sample contains enough sample to be detected by Western blot, including mitochondria. To increase yields from 10ml of blood several minor protocol adjustments were made, these included reducing wash steps, not keeping a sample of the DC pellet, and ensuring that all cellular material was transferred from tube to tube including both before and after ultracentrifugation. These protocol amendments enabled successful and reliable mitochondrial extractions from reduced blood volumes of just 7.5ml (Figure 5.9B).

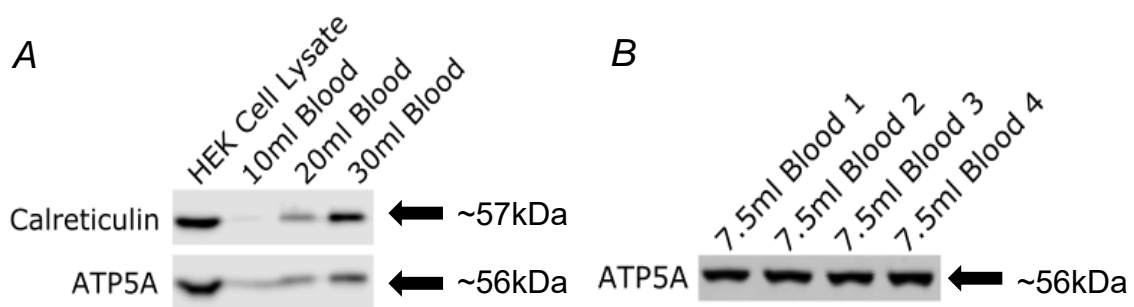


Figure 5.9. Mitochondrial detection and extraction reliability from low volumes of blood. A) Mitochondrial extraction performed on differing volumes of blood as starting material and Western blot probed with calreticulin (~57kDa; (PA3-900)) and ATP5A (~56kDa) primary antibodies. A HEK 293 cell lysate positive control was also added to the Western to confirm antibody detection. **B)** Western blot of four mitochondrial fractions extracted from the same individual and probed with ATP5A. Both blots detected using fluorescent secondary antibodies.

5.2.1.6 Antibodies to Assess Purity of Mitochondrial Fraction

Previous experiments during method development have relied on the use of antibodies to assess the composition of each cellular fraction, predominantly using calreticulin as an ER marker, and ATP5A as a mitochondrial marker. However, the intensity of calreticulin was high when compared to whole cell

lysate and the Western blot carried out by *Kappler et al., 2016* despite using the same mitochondrial extraction method. Calreticulin contains the ER localising KDEL signal, however studies have shown that calreticulin may also localise to the mitochondria/MAM [311-313]. Due to the possibility that calreticulin may also be localising to the mitochondria the calnexin protein was used to detect the presence of ER, which was also used in *Kappler et al., 2016*.

Mitochondrial samples were extracted from several SH-SY5Y cell samples as well as blood samples from six individuals for analysis. The protein content of each sample was quantified using the BCA assay and for each pair of whole cell lysate and mitochondrial fractions the samples were normalised and analysed by Western blot. The blots were then probed with calnexin (ab22595) and ATP5A antibodies to assess the ratio of mitochondria and ER within each fraction. This identified a significant enrichment in mitochondria in the mitochondrial fraction when compared to the whole cell lysate (Figure 5.10). Analyses of calnexin and ATP5A from SH-SY5Y cell samples (Figure 5.10B) shows ATP5A detection in all whole cell (WC) samples, unlike the PBMC samples, despite the very low levels of protein that were loaded. Calnexin was detected in all WC fractions from SH-SY5Y cells and only faintly in the mitochondrial samples where higher amounts of protein have been loaded. In PBMC whole cell lysates, ATP5A was not detected although it is present in the mitochondrial-enriched fraction (Figure 5.10A). Unlike in SH-SY5Y samples, two calnexin bands were detected in PBMCs at 90kDa and 75kDa; the 90kDa calnexin band corresponds with the expected calnexin band, however this is enriched in the mitochondrial fractions, whereas the detected 75kDa protein is enriched in the whole cell fractions. The detection of two calnexin bands in PBMCs may be most likely due to distinct calnexin isoforms being expressed in

different PBMC subcellular compartments, although post-translational modifications or the detection of other proteins cannot be conclusively excluded.

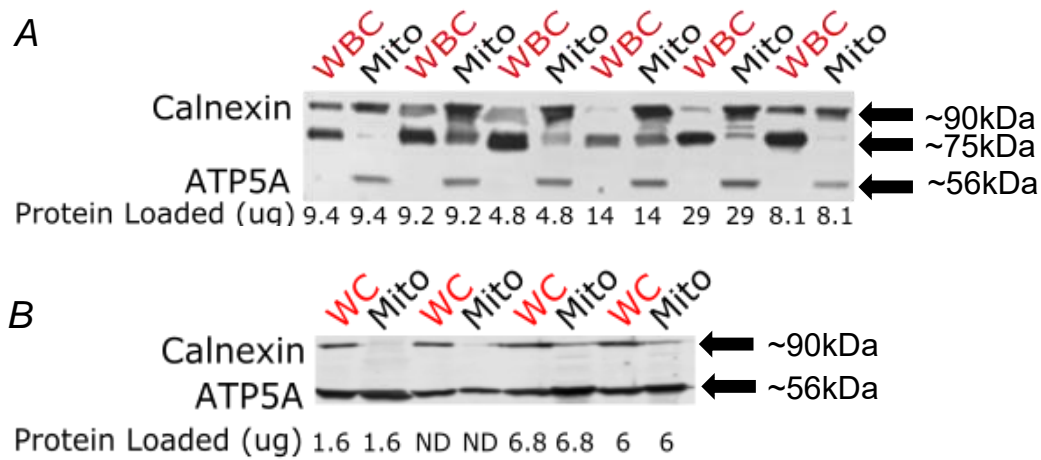


Figure 5.10. Mitochondrial and ER detection in whole cell lysate and mitochondrial fractions from PBMCs and SH-SY5Y cells. A) Whole blood cell lysate (WBC) and mitochondria (mito) extracted from 10ml blood from six individuals. **B)** Whole cell lysate (WC) and mitochondrial fractions from four individual SH-SY5Y cell samples. Whole cell and mitochondrial fractions were normalised and the amount of protein loaded (μg) per sample indicated. ND=no protein detected by BCA assay. Blots probed with calnexin ($\sim 90\text{kDa}$ and $\sim 75\text{kDa}$ in PBMCs; $\sim 90\text{kDa}$ SH-SY5Ys) and ATP5A ($\sim 56\text{kDa}$) and detected using fluorescent secondaries and detection.

5.2.1.7 The Optimised Mitochondrial Extraction Protocol

Thus with modifications to the protocol of *Kappler et al., 2016*, it was possible to obtain a mitochondrial pellet from a 10ml blood sample, or from cultured cells. Figure 5.11 outlines the main steps in the protocol to obtain a mitochondrial pellet, in addition to a whole cell lysate sample and an ER-mito fraction (remaining material after UC step) if required. The homogenising buffer used in this protocol is STE (250mM Sucrose, 5mM Iris and 2mM EDTA, pH7.4) which is made to be two times concentrated and then diluted 1:1 with ddH₂O and 0.5% BSA (Sigma Aldrich, A6003) added on the day of extraction. All steps are carried out on ice with ice-cold buffers and centrifugation steps are at 4°C. First,

cells are harvested from cell culture or PBMCs are extracted from blood as detailed in section 5.2.1.2. The cell pellets are then resuspended in 9ml STE + 0.5% BSA and transferred to a loose fitted 40ml Wheaton Dounce homogeniser containing an additional 9ml of STE + 0.5% BSA. The cell suspension is homogenised with 25 grinding repetitions and transferred to a 50ml centrifuge tube. To ensure all homogenate is removed the homogeniser is rinsed with 2ml STE + 0.5% BSA and added to the same tube. A 1ml whole cell lysate aliquot is taken before the homogenate is centrifuged at 1,000g for 10 minutes. The supernatant is transferred to a 50ml centrifuge tube (Fisher Scientific, 10460033) and the remaining pellet is resuspended, homogenised and centrifuged again to ensure complete cell homogenisation. The supernatant is added to the same 50ml centrifuge tube as before and the pellet containing larger cell components such as nuclei is discarded. The combined supernatant is centrifuged at 10,400g for 10 minutes to obtain a crude mitochondrial pellet. This pellet is then carefully resuspended in ~200 μ l of STE and layered onto a 9ml 25% Percoll gradient (25% Percoll (GE Healthcare), 25% 2xSTE and 50% STE + 0.5% BSA) and centrifuged at 80,000g for 20 minutes to break apart the ER-mitochondria contact sites. After centrifugation an upper ER (and mitochondria) and a lower mitochondrial layer is formed. These layers are then carefully removed using a Pasteur pipette (avoiding the uptake of excess Percoll) and transferred to a 50ml centrifuge tube. The tubes are then topped up with STE (~40ml) and centrifuged at 10,400g for 10 minutes to wash off the Percoll. If a pellet has not formed, then further washes are carried out to dilute the Percoll and allow the pellet to stick to the tube. The pellet is then resuspended in 1.5ml PBS, transferred to a microcentrifuge tube and centrifuged at 16,000g for 2 minutes, alongside the previously aliquoted whole

cell lysate fraction which is topped up with PBS. The PBS wash is repeated and then the final pellet is then resuspended in 100µl of molecular biology water and aliquoted into the required tubes for analysis: 5µl for protein quantification, 10µl for Western blotting, and the remaining ~85µl is for lipid analysis. The protein quantification and Western blotting aliquots are stored at -20°C until required and the lipid analysis aliquots are stored at -80°C until shipment on dry ice to the University of Surrey for oxysterol and cholesterol analysis.

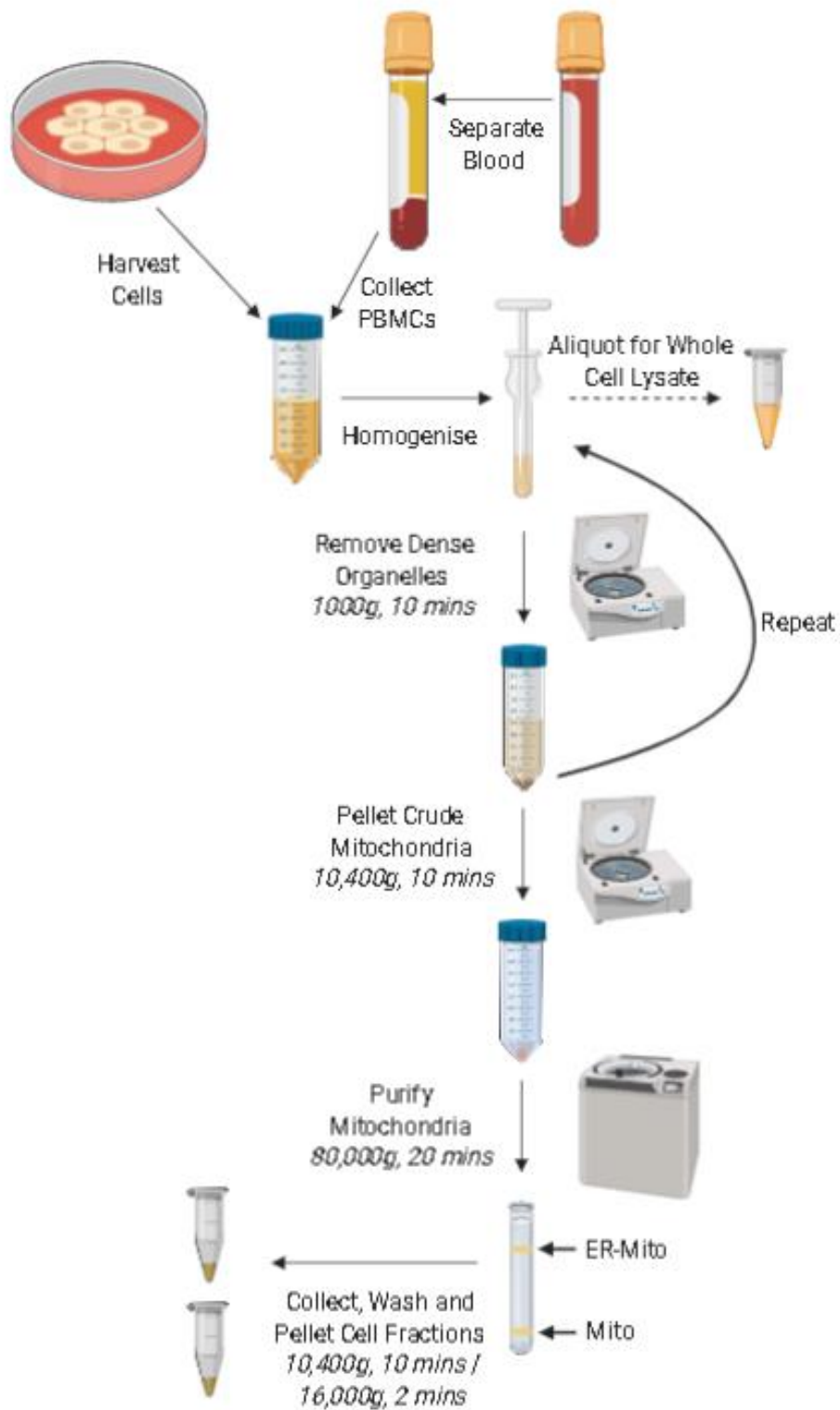


Figure 5.11. Diagram outlining the main steps of the optimised protocol to obtain a mitochondrial pellet from blood or cultured cell lines. Created using BioRender.

5.2.2 Oxysterol Analysis

Mitochondrial samples from both blood and cultured cell samples were able to be sufficiently obtained so the next step in method development was to analyse oxysterol levels in the mitochondrial and whole blood cell samples.

5.2.2.1 PBMC Oxysterol Analysis

The first oxysterol analysis was carried out by Dr Irundika Dias at the University of Aston following the methods outlined in *Dias et al., 2018*. This methodology includes the extraction of oxysterols from samples by solid phase extraction followed by liquid chromatography mass spectrometry to analyse five oxysterols: 24-OH, 25-OH, 27-OH, 7 β -OH and 7-ketocholesterol (7-KC). These oxysterols were previously used in *Dias et al., 2018*; 7 β -OH is formed by autoxidation, as is 7-KC which is formed via autoxidation from cholesterol and 7 α -OH therefore it is a good marker for autoxidation and oxidative stress. The oxysterol levels were analysed against spiked internal and authentic standards which were calculated against known concentrations of external standards.

Initial analyses examined oxysterol levels from whole cell lysate obtained from a single healthy individual 1 hour after blood draw and 24 hours after blood draw which was stored in the fridge, in addition to duplicate mitochondrial samples from each time point. For each sample protein quantification was performed and between 25-193 μ g of protein from 100 μ l of each sample was analysed, Figure 5.12C. Western blots were also performed on absolute and normalised samples which were probed with calreticulin and ATP5A (Figure 5.12D), however as identified in section 5.2.1.6 calreticulin has significant detection in mitochondrial samples. Despite this, the levels of ATP5A in samples when normalised show an overall increase in mitochondrial fractions compared to WBC samples. Figure 5.12 illustrates the results from this experiment showing both absolute

amounts of oxysterol (A), and normalised amounts per μg of protein (B) analysed. This revealed 25-OH to be the most prominent oxysterol within both the whole cell and mitochondrial samples. Despite the high protein content in whole cell samples the amount of all absolute oxysterols is very low other than 25-OH, and when normalised to protein there is a very low amount of oxysterols when compared to mitochondrial fractions. 27-OH is elevated in mitochondria compared to whole cell samples when compared to other oxysterols. 25-OH is also elevated in mitochondria compared to whole cell fractions, however one of the 'fresh' mitochondrial samples (fresh mito 2) contains particularly high amounts of 25-OH. In this analysis the most prominent difference between fresh and one day old blood is the increase in 7-KC by an average of 66%, likely to be the result of elevated autoxidation due to ROS in the stored blood. In the one-day old mitochondrial samples there is a reduction in 25-OH levels by an average of 58%, but this value may be due to the very high amount of 25-OH detected in one fresh mitochondrial sample. Importantly, the overall profiles of oxysterol levels between the two duplicate samples from both fresh and one day old mitochondria are similar suggesting that the methodology is reproducible between independent samples.

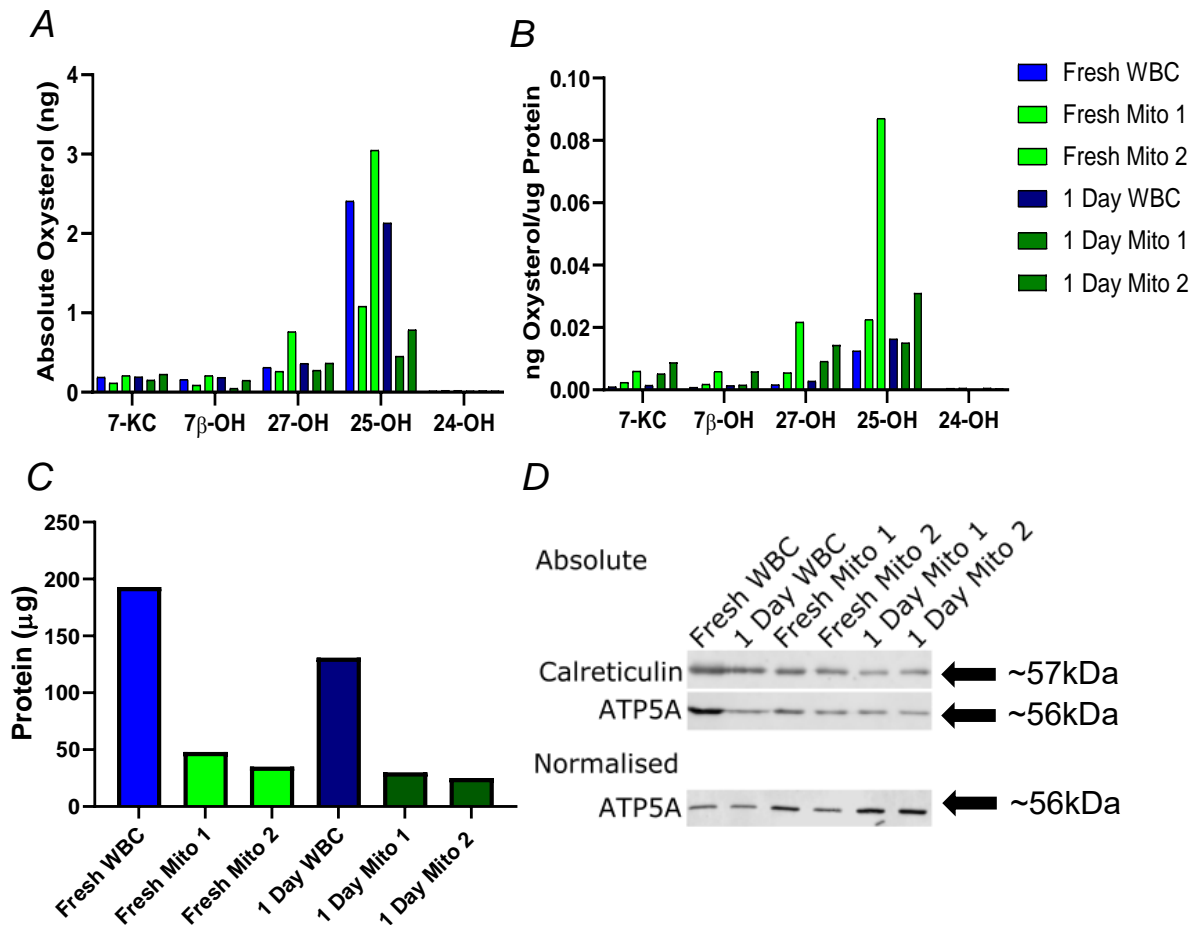


Figure 5.12. Oxysterol levels in PBMC whole cell lysate and mitochondrial fractions extracted from fresh and one day old blood stored at 4°C. **A)** Absolute values of five oxysterols, compared to values normalised to protein **(B)** and the protein content of each sample that was analysed by mass spectrometry **(C)**. Mass spectrometry performed by Dr Irundika Dias at the University of Aston. **D)** Western blot of samples probed with calreticulin (~57kDa; (PA3-900)) and ATP5A (~56kDa) with absolute sample loaded (top) and normalised samples (bottom) probed with just ATP5A. Blots detected using fluorescent secondary antibodies and detection.

Several key points were taken forward from this initial oxysterol analysis. Firstly, oxysterols were able to be successfully identified and quantified in mitochondria extracted from 10ml of blood. This experiment normalised oxysterol levels to the amount of protein that was analysed, however there is almost an 8-fold difference in the protein concentration analysed per sample (Figure 5.12C), this data indicates that a matrix effect may be a factor in oxysterol detection as a lower recovery of oxysterols is observed with higher loading of protein

concentration; this is particularly evident between the duplicate mitochondria fractions as the lower amount of protein that was analysed shows higher oxysterol levels. To mitigate the matrix effect the same amount of protein (50µg) was loaded per sample for analysis, instead of loading the same volume of sample with varying protein concentrations. A third methodological alteration was to normalise to cholesterol content rather than protein, as these oxysterols are derived from cholesterol. Internal cholesterol levels are able to be analysed by mass spectrometry, however given that the relative levels of cholesterol are much larger than oxysterol levels this would decrease the sensitivity of oxysterol detection. Thus, it was decided to use an independent cholesterol assay (Amplex red cholesterol assay kit; A12216, ThermoFisher) to measure the levels of cholesterol in each sample.

At the University of Surrey this methodology was adapted for use with another mass spectrometer and the protocol was refined to increase the sensitivity of oxysterol detection. To increase oxysterol detection a multistep analyte separation technique was incorporated into the protocol for oxysterol extraction rather than the previously used methanol lysis method. To further explore the alternative pathway the dihydroxycholesterols were also added to the analysis therefore giving a better insight into the metabolic flux through the various arms of the bile acid pathway. This improved methodology resulted in an average oxysterol recovery of 89% compared to that of just 9% (Figure in Appendix C) with the previously used methodology, therefore this allows the detection of oxysterols in small amounts of material. Further information of the optimisation and the newly devised method is outlined in Appendix C.

This method development was performed on both blood and SH-SY5Y cell samples prepared by myself and Dr Nikol Voutsina, in addition to mouse brain

tissue and THP-1 monocytes prepared at the University of Surrey. THP-1 cells were used to set up the methodology and perform reproducibility analysis. This new method also indicated reduced matrix effect that was observed in the initial analysis so inconsistent sample concentrations was no longer deemed to be an analytics issue.

5.2.3 Oxysterol Profiling

5.2.3.1 Whole Cell and Mitochondrial Fractions

Mitochondrial and whole cell lysate fractions from SH-SY5Y cells and PBMCs were prepared to profile oxysterol levels from each fraction. For this experiment mitochondrial extractions were performed on fresh blood from healthy individuals and cultured wildtype SH-SY5Y cells. The samples were analysed using the new oxysterol extraction and detection method, and normalised to cholesterol content (Figure 5.13). All seven oxysterols were detected in whole cell SH-SY5Y (A) fractions, but 27-diOH and 24-OH were not detected above the lower limit of quantitation in mitochondrial fractions. In PBMC fractions (B) only four oxysterols were detected in both samples as the dihydroxycholesterols and 24-OH were not detected above the lower limit of quantitation.

In whole cell and mitochondrial SH-SY5Y fractions 7-KC is the most abundant oxysterol detected. The second most abundant oxysterol is 7 α -OH in whole cell samples, whereas in mitochondrial fractions it is 27-OH. 7 α -OH and 7-KC both have the greatest difference between the two fractions with a 4-fold increase in whole cell fractions whereas 25-OH has a slight (1.2-fold) elevation and 27-OH has a 1.7-fold elevation in whole cell SH-SY5Y fractions compared to mitochondrial fractions. The only oxysterols where the mitochondrial content is higher than that of the whole cell fraction are two of the dihydroxycholesterols

which are detected together, 24S25diOH, where a 1.7-fold increase is observed in mitochondrial fractions.

In PBMC whole cell fractions 27-OH is the most abundant oxysterol whereas 7-KC is in the mitochondrial fraction. Between the two fractions the biggest difference is observed in 27-OH with a 3.2-fold increase in whole cell fractions, followed by a 3-fold increase in 7 α -OH, a 2.5-fold increase in 25-OH and 2-fold increase in 7-KC.

When comparing the PBMC to SH-SY5Y oxysterol profiles the mitochondrial profiles are very similar as 7-KC is the most abundant oxysterol, followed by 27-OH in both cell samples. Within SH-SY5Y cells a greater difference between whole cell and mitochondrial samples is detected in 7-KC than in PBMCs. In mitochondrial fractions of both sample types 27-diOH and 24-OH were unable to be detected to a quantifiable level, however very low amounts were detected in SH-SY5Y whole cell samples. Overall, this oxysterol cellular profiling will provide an important comparison for HSP cell models and PBMCs obtained from individuals with HSP.

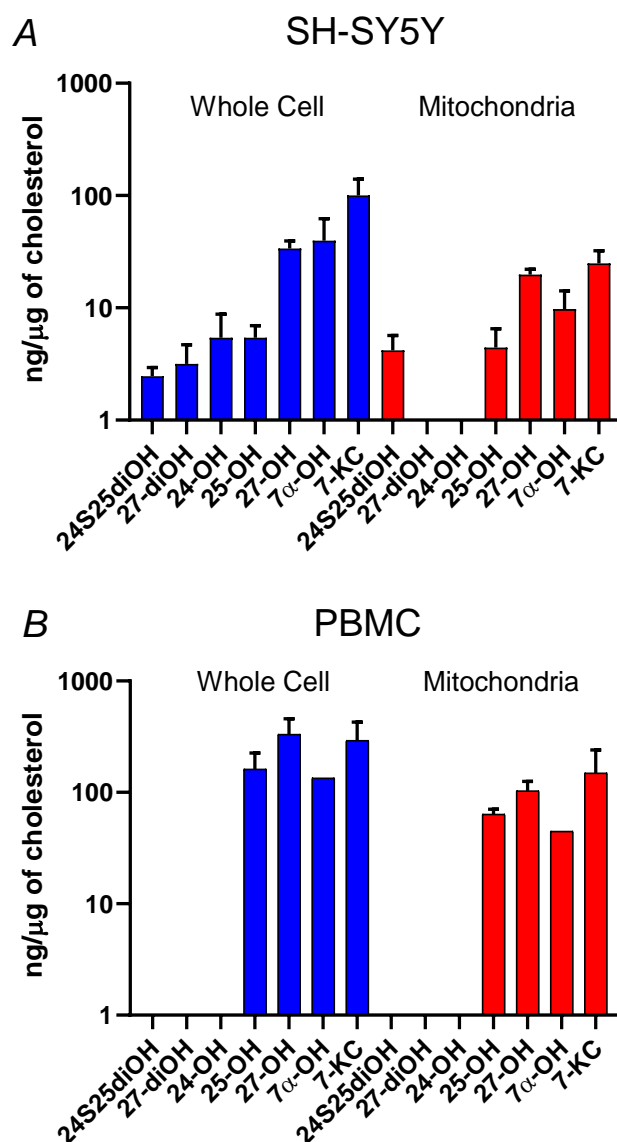
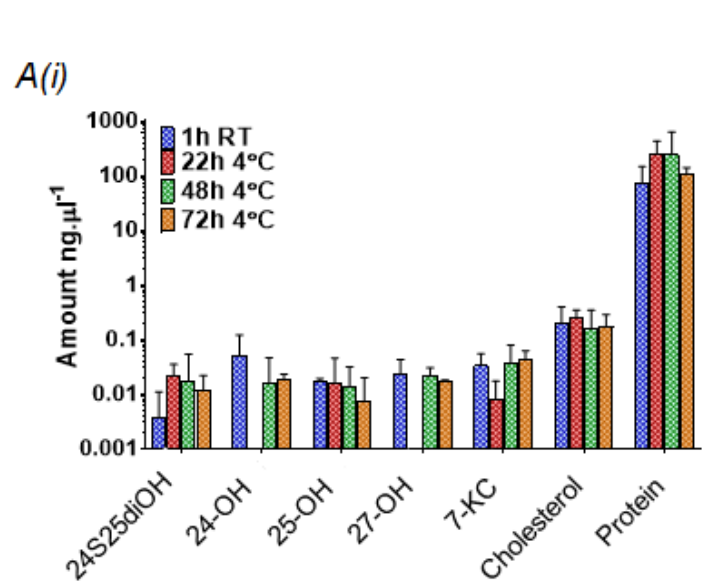


Figure 5.13. Oxysterol profiles in SH-SY5Y and PBMC whole cell and mitochondrial fractions. *n*=3 with values lower than the lower limit of quantitation are not included; all seven oxysterols were detected in SH-SY5Y (A) whole cell fractions and only five in the mitochondrial fraction. (B) Only four oxysterols in both PBMC fractions were detected with just one 7 α -OH value for each fraction. Columns represent mean values with error bars SEM.

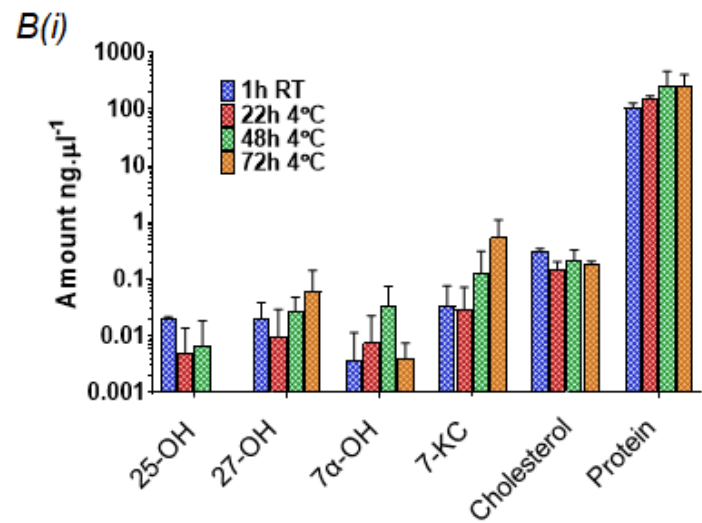
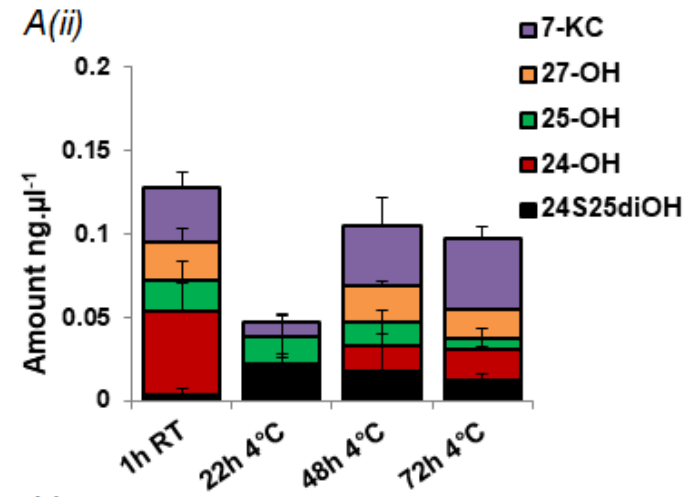
5.2.3.2 Increased Blood Storage Time Impacts Oxysterol Levels due to Autoxidation

A key area to explore and understand was the effect of blood sample storage time and the effects this would have on oxysterol recovery. This is important to ascertain as it would shape future blood collection and storage conditions when collecting patient and control samples. To explore this, blood was obtained from

four individuals and then whole cell and mitochondrial samples extracted at 24 hour intervals over a period of four days, with the first extraction being performed on fresh blood samples and the remaining blood samples were stored at 4°C until extraction. The oxysterol content was then analysed using the newly devised method and the results from this experiment are presented in Figure 5.14. The most significant finding from this experiment is the effect of autoxidation on mitochondrial samples overtime as shown by the increase in 7-KC (Figure 5.14B(ii)), indicating increased ROS and cell damage as a result of increased storage time. However, this increase is not observed in whole cell samples (Figure 5.14A(ii)). Figure 5.14A(i) and B(i) illustrate the absolute values of each oxysterol, in addition to cholesterol and protein quantification, both cholesterol and protein levels do not significantly differ between storage times. This data suggests that blood storage times need to be kept consistent in order to avoid autoxidation in mitochondrial samples.



Whole Cell



Mitochondria

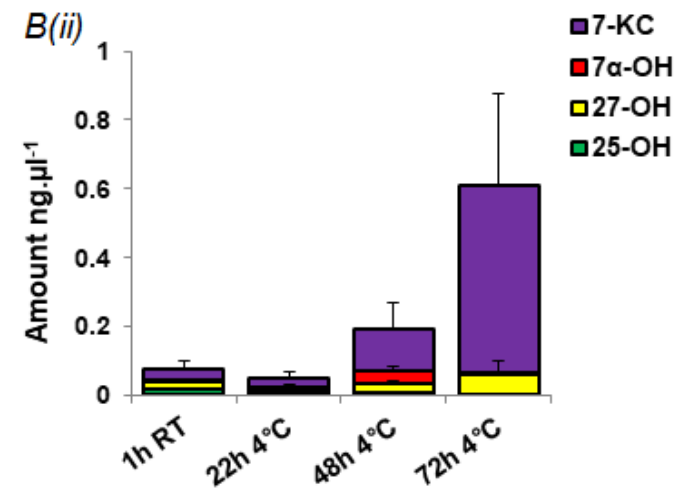


Figure 5.14. The effect of storage time on PBMC lysate (A) and mitochondrial (B) oxysterols. Blood samples were stored at the times indicated (0, 22, 48 and 72 hours) at 4°C until whole cell lysate and mitochondrial extraction. Figures A(i) and B(i) illustrate the absolute levels whereas A(ii) and B(ii) illustrate the proportion of each oxysterol relative to one another. Oxysterols were quantified using the newly described methodology, cholesterol quantified using cholesterol red assay and protein quantified using BCA assay. Only oxysterols that were above the lower limit of quantification are included. Absolute values are shown with mean \pm SEM from 2-4 samples. Oxysterol quantification and graphs by Dr Khushboo Borah.

5.2.4 Oxysterol Imbalance is Observed Between *SPG21* Knockout and Control Cells

To investigate the overarching hypothesis that imbalance within the oxysterol pathway is more common among HSPs the previously generated *SPG21* knockout SH-SY5Y cell line was utilised for this experiment. Therefore, this experiment would give an insight into whether oxysterol imbalance may be contributing to pathogenesis in Mast syndrome. To investigate this, *SPG21* knockout cells alongside control wildtype SH-SY5Y cells were cultured, whole cell lysate obtained, and the mitochondria extracted. For this experiment, a third fraction was also kept, this fraction comprised the upper layer from ultracentrifugation enriched in mitochondria. This 'ER-Mito' fraction was included for this experiment as it contains a higher proportion of cellular material than the final mitochondrial fraction, and it may give a further insight into subcellular oxysterol profiling as it contains ER where many of the bile acid pathway enzymes reside.

A Western blot was performed on the cell fractions obtained in the experiment from both control and *SPG21* knockout SH-SY5Y cell lysates. This blot was probed with calnexin and ATP5A to give a better understanding of the ratio of subcellular compartments within each fraction, Figure 5.15D. The results from this Western blot show that the 'ER-Mito' fraction contains a larger proportion of mitochondria than ER when compared to the whole cell (WC) fraction, however the detection of calnexin suggests that the ER is still present. In the mitochondrial (mito) fraction, ATP5A is only detected and not calnexin, therefore, as expected this fraction contains purer mitochondria. The absolute cholesterol levels in all control fractions are significantly higher than in *SPG21* knockout cell fractions, Figure 5.15C.

Oxysterol profiling of the three fractions between the control and *SPG21* knockout SH-SY5Y cells reveals oxysterol imbalance (Figure 5.15A and B), individual oxysterol comparisons in Appendix D. In the classical pathway cholesterol is metabolised to 7 α -OH, and a decrease of this oxysterol is observed in *SPG21* knockout cells in the whole cell fraction and significant in the ER/mito fraction, whereas the comparative levels of 7 α -OH in the mitochondrial fractions are low. 7 α -OH is autoxidated to 7-KC, and a similar profile is seen in this oxysterol as 7 α -OH with a decrease in the *SPG21* knockout cells.

In all three monohydroxycholesterols in the alternative arms of the bile acid pathway differences are observed between the control and *SPG21* knockout cells. An increase is especially evident in 25-OH which is elevated in all three of the *SPG21* knockout fractions but exemplified in the mitochondrial fraction. 24-OH was unable to be detected above the lower limit of quantitation in the control ER/mito and mitochondrial fraction, but it was detected in the all *SPG21* knockout fractions suggesting an increase in this monohydroxycholesterol. Conversely, a decrease in 27-OH in all cell fractions (significant in the whole cell fraction) is identified in *SPG21* knockout cells.

By mass spectrometry both the 24-diOH and 25-diOH are detected together and a decrease in these dihydroxycholesterols is revealed in *SPG21* knockout cells in both whole cell and ER/mito fractions but there was no detection above the lower limit of quantitation in the mitochondrial fraction. It is not clear whether there is an overall difference in 27-diOH as there is a slight decrease in the whole cell fraction in *SPG21* knockout cells, but no difference between the ER/mito fraction and there was no detection in the mitochondrial control fraction.

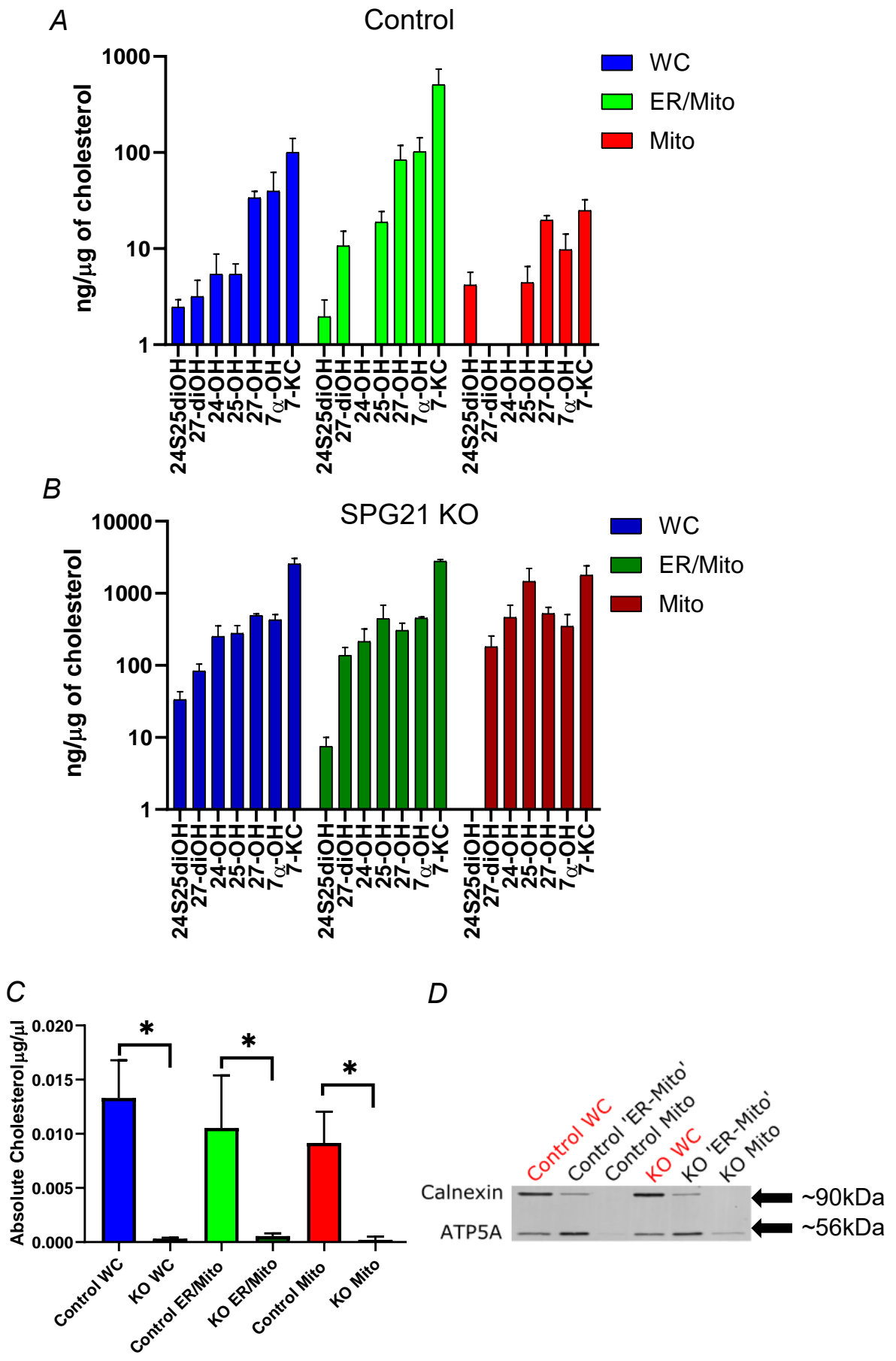


Figure 5.15. Oxysterol variation between control and SPG21 knockout SH-SY5Y cell fractions. **A)** Oxysterol profile in control SH-SY5Y cell fractions. **B)** Oxysterol profile in SPG21 knockout SH-SY5Y cell fractions. $n=3-6$ but values lower than the lower limit of quantitation are not included. The data shown in A and B are normalised to cholesterol with columns representing the mean with SEM error bars. **C)** Cholesterol levels in cell fractions from control and SPG21 knockout cells. Asterisks show statistical significance where $*= p<0.05$. **D)** Western blot of the three fractions analysed in this experiment from control and SPG21 knockout cell lysates ($3.75\mu\text{g}$ of protein loaded) that were normalised and probed with calnexin ($\sim 90\text{kDa}$) and ATP5A ($\sim 56\text{kDa}$), followed by fluorescent secondaries and detection.

5.3 Discussion

This aspect of my PhD entailed the development of methodology to robustly obtain consistent subcellular fractions, in particular mitochondrial fractions, from both cultured cells as well as 10ml blood samples. If the underlying hypotheses are proven to be correct, the ability to obtain and analyse subcellular fractions from just 10ml of blood may prove revolutionary in our understanding and diagnosing MND. Previous studies investigating oxysterol levels in MND/HSP patients have targeted specific genetic forms of disease entailing only the core metabolic (enzymatic) genes, in patient CSF and plasma. CSF limits the number of individuals that would be willing to take part as this requires a lumbar puncture which is much more invasive. Additionally, studies of CSF generally do not enable the investigation of cellular/subcellular oxysterol profiles. Whilst PBMCs are non-neuronal cells that are unaffected in the condition, the oxysterol profiles of both cell types are broadly overlapping and so disturbances to lipidomic processes are likely to be identified in PBMCs. To confirm that oxysterol imbalance is observed in blood, SPG5 patient samples can be analysed to verify oxysterol imbalance in the bile acid pathway. If present, the oxysterol profile relationship between blood and WT/KO cell models can be more precisely delineated, to enable profiling of other non-enzymatic forms of HSP/MND. Initial investigations will commence within the Amish community on the most common HSP subtype, SPG4, encoding spastin which is not a core metabolic enzyme. This study will be the largest patient-based oxysterol analysis to date.

An ongoing challenge during this work involves the normalisation of data to determine the best way to visualise lipidomic imbalance. Normalising oxysterol levels to protein levels was not considered the best approach, as oxysterols are

derived from cholesterol and there may be variability between protein and lipid levels in individuals. Similarly, normalisation of data to cholesterol levels may also be imperfect, as the measurements from subcellular samples are consistently at the bottom (and in some cases below) of the kit's lower limit of detectability so increased variability is likely. Furthermore, oxysterol imbalance may also influence cholesterol levels (and vice versa) due to cellular regulatory feedback mechanisms. Thus it may be important to consider the absolute amounts of oxysterol to gain a broader understanding of oxysterol profiles.

As identified in this work, additional complications to this analysis involve effects associated with the length of time that blood samples are stored before sample processing, in particular due to the effects of ROS in mitochondria. Ideally all patient and control samples would be extracted and stored under the exact same conditions. However, in some circumstances this may be hard to achieve due to the logistics of obtaining blood samples from patients that are in different geographical regions, for example obtaining samples from within the Amish community in Ohio, where certain forms of HSP are particularly prevalent. However, to overcome this the extraction process may be performed in nearby labs/facilities, or cell samples can be cryopreserved before extraction to ensure sample handling and storage conditions are kept as consistent as possible between affected and control individuals.

While more data is required from our initial findings, oxysterol imbalance appears to be present in *SPG21* knockout SH-SY5Y cells when compared to wildtype controls. Altered flux between the classical and alternative pathways was identified in *SPG21* knockout cells, with the reduction 7α -OH and 7-KC in the classical pathway, and an increase in the initial products in two of the three alternative pathways (24-OH and 25-OH), and a decrease in $7\alpha,24$ -diOH and

7 α ,25-diOH. If corroborated, these findings are profound as the functional role of maspardin is currently unknown, and no evidence exists to indicate that maspardin may possess a function within lipid metabolic processes. This may thus provide direct support for the lipidomic imbalance hypothesis in HSP. As such this lipid analysis was the first conducted on an *SPG21* knockout model, so there are no comparisons that can be drawn with existing data. However, data gathered from CSF and plasma samples from individuals with SPG5 reveal a significant increase in 25-OH and 27-OH but no change found in 24-OH levels; the remainder of the alternative and classical pathways are yet to be fully profiled [289, 314]. Between the data gathered in this work from *SPG21* knockout SH-SY5Y cells and published data on SPG5 the primary overlap appears to be an increase in 25-OH. It is important to note that these studies are performed on whole cell tissue samples, plasma and CSF, whereas this work outlined in this thesis is from whole cell and subcellular fractions.

The methodology established in this work will provide a tool to profile lipidomic outcomes in different forms of HSP/MND. This can also be applied to different cell types which are yet to be fully profiled, such as PBMCs and SH-SY5Y cells as outlined in this work, which provides a valuable insight into the differing oxysterol profiles of these tissue types. Upon validating this methodology to reliably detect lipid imbalance from subcellular fractions obtained from blood this will enable blood to be analysed to test for HSP.

5.3.2 Future Work

A range of future studies are planned including a focus on achieving a reliable and robust technique to quantify and characterise specific lipids from different cultured cell types and blood samples. To do this, more replicates of subcellular fractions are required to fully define their oxysterol profiles. Establishing a more

robust method for detecting low levels of cholesterol is also required. This may involve an alternative commercially available cholesterol assay, or the analysis of cholesterol alongside oxysterols in mass spectrometry. Another avenue of future work will investigate inter-individual variation within oxysterol profiles by considering age, gender, ethnicity and lifestyle variability. In the longer-term this analysis could be extended to other lipid pathways that are also commonly implicated in HSP/MND such as phospholipids, sphingolipids and fatty acids.

The mitochondrial extraction methodology results in considerably enriched mitochondrial fractions as determined by probing fractions with ATP5A, however in PBMCs calnexin detects two bands (unlike SH-SY5Y samples) revealing differing fraction enrichment. Future work will need to investigate this detection pattern and further explore the composition of enriched mitochondrial fractions using other subcellular markers, such as endosomal and lysosomal markers, to eliminate the possibility of contamination with these organelles.

To better understand the oxysterol imbalance due to maspardin loss, more *SPG21* knockout samples would need to be analysed to precisely define the oxysterol abnormalities present. This could be compared with data from blood samples from individuals with Mast syndrome. If the same oxysterol imbalance is observed in patient samples, this would provide extremely strong evidence that the oxysterol pathway is impacted in Mast syndrome, and confirm that knockout cell studies are representative of the condition.

Within our group the CRISPR-Cas9 technology has again been utilised to knockout other genes that are associated with HSP, including *CYP7B1*, *CYP2U1* and *SIGMAR1*. These and a wide range of other HSP-associated gene knockout cell lines will be invaluable to further test this hypothesis. In

particular, *CYP7B1* knockout cells will be important to profile given that this is a core enzyme of the bile acid pathway. *SIGMAR1* is an ER-mitochondrial tether, therefore this knockout cell line will be crucial to investigating the effects of impaired MAM tethering, and whether this is also associated with oxysterol imbalance. Little is known about *CYP2U1*, like maspardin, however it is thought to be involved in lipid metabolism. Investigating this and other HSP-associated molecules with a putative role in lipidomics (e.g. seipin, spartin and FA2H) will provide a greater insight into lipidomic imbalance in MND. By expanding this study into HSP-associated molecules with no currently defined role within lipid pathways, but detecting lipidomic imbalance in cell models of disease, would indicate that lipid pathways are impacted more widely in HSP. These findings, coupled with a better understanding of the precise subcellular compartments and molecules that aid the functioning of these pathways, could provide insights into therapeutic targets to slow or prevent onset of neurodegeneration in HSP/MND.

An additional study is planned in the coming months to investigate whether lipidomic abnormalities are present in SPG4-associated HSP. While SPG4 (*SPAST*) is known to be highly prevalent among the Amish community (Prof Crosby, personal communication), it represents the most common form of HSP worldwide. Due to the unique genetic and environmental homogeneity of the Amish, studies of SPG4 amongst community members provides an opportunity to understand the wider molecular basis of this form of HSP, and determine whether HSP-associated molecules that are not core enzymatic molecules may also adversely affect the bile acid pathway.

Ultimately, defining blood biomarkers for HSP/MND will be of ground-breaking importance, as it has considerable potential to pave the way for the commercial

development of a clinical diagnostic test for the condition. To date, there is not a diagnostic technique available to identify MND prior to clinical onset of symptoms and currently there is no treatment to reverse or significantly impede disease progression. Therefore, diagnosing MND earlier may allow improved clinical management and the opportunity for early intervention once a treatment is available, potentially to significantly increase an individual's lifespan or prevent the onset of symptoms.

Chapter 6

Closing Comments

Closing Comments

MND severely impacts the lives of people worldwide and represents a relatively increasing financial burden to healthcare services globally. For the vast majority of these conditions, the specific underlying biomolecular cause is unknown. Therefore, identifying and understanding how the associated proteins function, and in what biological pathways each genetic form of MND is involved, is crucial to understanding the pathogenesis underlying neurodegeneration, and for the development of new treatments. Furthermore, the availability of a diagnostic tool to identify individuals at risk of disease prior to the onset of symptoms may enable early intervention and clinical monitoring, to provide the best quality of life for affected individuals.

The work defined in this thesis has shown that it is possible to detect extremely small amounts of oxysterols from an enriched mitochondrial sample obtained from just 10ml of blood, or cultured cells. The development of this new methodological tool will enable the identification of lipidomic imbalance within HSP/MND and investigate the extent of imbalance within forms of MND where there may currently be no clear lipidomic link. This tool will empower the discovery of key MND biomarkers, which in turn will enable the development of a revolutionary new blood test to diagnose MND before the onset of physical symptoms. Patients who are at high risk of MND really want to know how their disease may progress and the age at which symptoms may develop, which is currently very difficult to predict, an important potential use of this blood test is as a prognostic tool. A further potential application of this tool includes drug testing whereby known (and newly developed) drugs/treatments are used to investigate the impact that they have on lipid pathways. Furthermore, understanding the precise alterations within lipidomic pathways will further our

understanding of disease progression and the key subcellular pathways involved in neurodegeneration.

Additionally, the work in this thesis has significantly contributed to scientific understanding of maspardin and the cellular consequences due to its loss, and generated a cell model resource important for future studies. Furthering our scientific understanding of the molecular role of maspardin and other HSP associated proteins, aided by cell models, will significantly contribute to our knowledge of disease progression and the cellular components involved in pathogenesis. Identifying subcellular pathways that are common to large groups of heterogeneous HSPs, and potentially other forms of neurodegeneration, represent a powerful means to aid a therapeutic target and drug discovery. As Mast syndrome involves a complex phenotype overlapping with other forms of neurodegenerative disease, in particular dementia, these findings are of relevance to other neurological disease. The mechanistic basis of *C19orf12* variants investigated in this work further highlights the complex genetic nature of MNDs. In addition, the overlapping clinical features between groups of MNDs, in particular NBIA and HSP, demonstrates the need for a test to identify biomarkers of disease to aid diagnosis in this large and clinically overlapping group of conditions.

Over recent years the Exeter research team and other research groups have discovered a number of genetic causes of MND. These discoveries have greatly aided our understanding of the molecular causes of the condition, which has enabled the development of a number of genetic tests to provide diagnoses for families with specific forms of MND. However, the genetic cause of many MNDs still remains unknown, and there are currently no single universal tests available that can determine an individuals' risk of developing the disease, or monitor

disease progression. Due to the complexity of MNDs, other specialised neurological (and other) tests may often be required to rule out other conditions with similar clinical features, and patients may face a difficult time in reaching a clear diagnosis of their condition. The work described in this thesis provides the foundations for the development of a blood test that would enable us to investigate how MND biomarkers relate to age of onset, the degree and extent of neurological damage, and the rate of development and progression of MND. This could be done by routinely analysing an individual's lipid levels to understand disease progression. Importantly this test will be based on biomarkers which we believe are common to many different genetic types of MND, irrespective of the genetic cause. This means that the test may also be of relevance to the many MND patients who don't yet have a genetic diagnosis due to lack of knowledge of all genetic causes of this condition. Lastly, and perhaps most fundamental would be the potential use of the methodology underlying this test for identifying candidate new drug treatments that may be effective in MND. This will allow us to assess scope for the development of new therapies to alter clinical course for ultimate evaluation in clinical trials, and potentially slow or halt progression, or prevent the onset, of disease.

Appendices

Appendix A:

Table A1. HSP associated proteins, the assigned SPG designation and mode of inheritance. SPG genes included in this table are discussed in chapter 1.

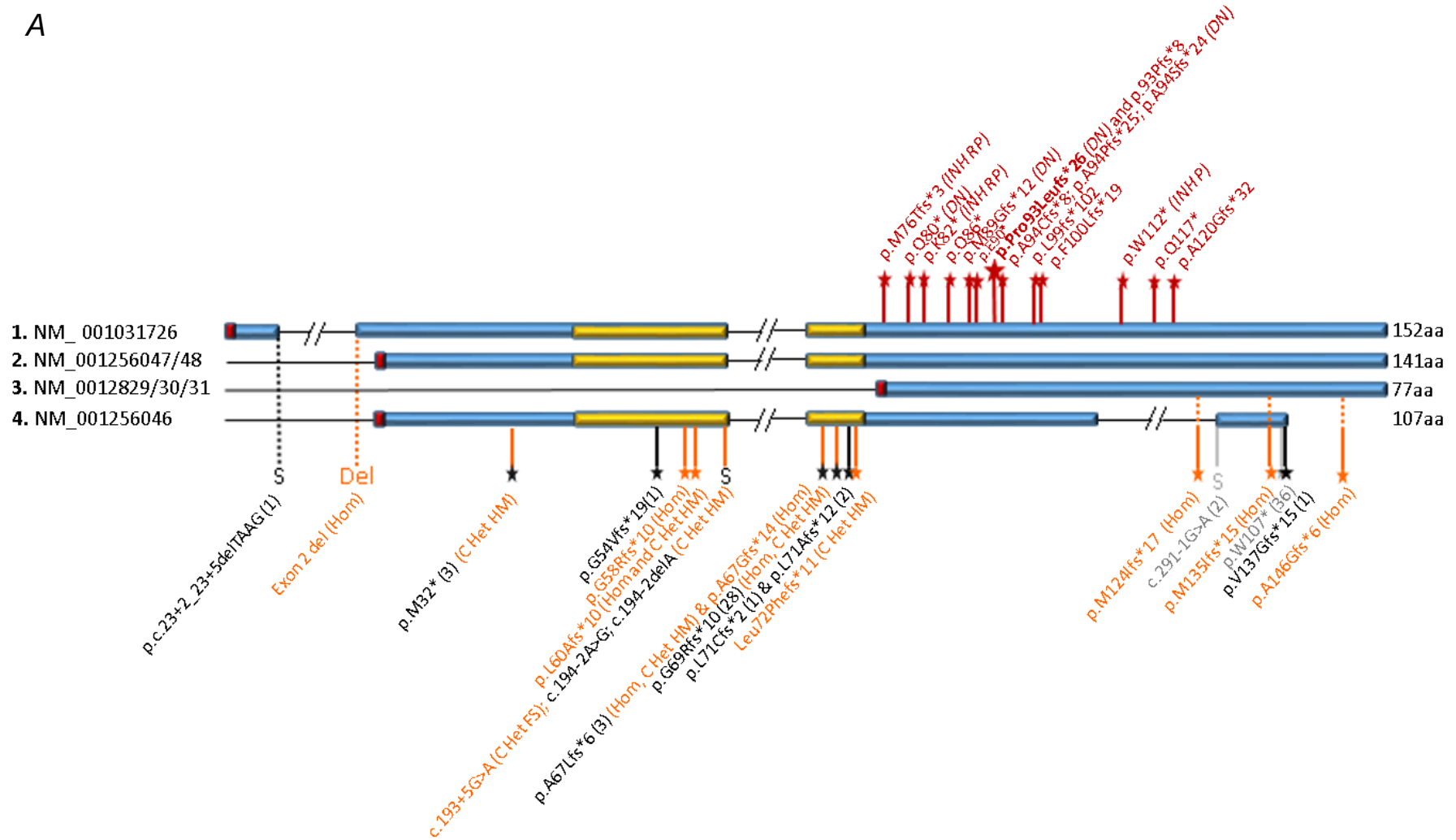
SPG Designation	Protein	Pure/Complicated; Inheritance
SPG1	L1 cell adhesion molecule	Complicated X-linked
SPG2	Proteolipid protein	Complicated X-linked
SPG3	Atlastin-1	Pure/complicated Autosomal dominant
SPG4	Spastin	Pure Autosomal dominant
SPG5	Cytochrome P450 family 7 subfamily B member 1 (CYP7B1)	Complicated Autosomal recessive
SPG6	Non imprinted in Prader-Willi/Angelman syndrome 1 (NIPA1)	Pure Autosomal dominant
SPG7	Paraplegin	Pure/complicated Autosomal recessive
SPG8	Strumpellin	Pure Autosomal dominant
SPG10	Kinesin family member 5A (KIF5A)	Pure/complicated Autosomal dominant
SPG11	Spasticsin	Complicated Autosomal recessive
SPG12	Reticulon 2	Pure Autosomal dominant
SPG13	60kDa heat shock protein (HSP60)	Pure Autosomal dominant
SPG15	Spastizin	Complicated Autosomal recessive
SPG17	Seipin	Complicated Autosomal dominant
SPG18	ER lipid raft-associated protein 2 (Erlin2)	Complicated Autosomal recessive
SPG20	Spartin	Complicated Autosomal recessive
SPG21	Maspardin	Complicated

		Autosomal recessive
SPG26	Beta-1,4-N-acetyl-galactosaminyltransferase 1 (B4GALNT1)	Complicated Autosomal recessive
SPG28	DDHD domain containing 1 (DDHD1)	Pure/complicated Autosomal recessive
SPG31	Receptor expression-enhancing protein1 (REEP1)	Pure/complicated Autosomal dominant
SPG35	Fatty acid-2 hydroxylase (FA2H)	Complicated Autosomal recessive
SPG39	Patatin like phospholipase domain containing 6 (PNPLA6)	Complicated Autosomal recessive
SPG44	Connexin 47	Complicated Autosomal recessive
SPG46	Glucosylceramidase beta 2 (GBA2)	Complicated Autosomal recessive
SPG47	Adaptor protein 4 subunit beta 1	Complicated Autosomal recessive
SPG48	Adaptor protein 5 subunit zeta 1	Complicated Autosomal recessive
SPG50	Adaptor protein 4 subunit mu 1	Complicated Autosomal recessive
SPG51	Adaptor protein 4 subunit epsilon 1	Complicated Autosomal recessive
SPG52	Adaptor protein 4 subunit sigma 1	Complicated Autosomal recessive
SPG53	Vacuolar protein sorting-associated protein 1 (VPS37A)	Complicated Autosomal recessive
SPG54	DDHD domain containing 2 (DDHD2)	Complicated Autosomal recessive
SPG55	Chromosome 12 open reading frame 65 (C12orf65)	Complicated Autosomal recessive
SPG56	Cytochrome P450 family 2 subfamily U member 1 (CYP2U1)	Complicated Autosomal recessive
SPG69	Rab3 GTPase activating protein subunit 2 (Rab3GAP2)	Complicated Autosomal recessive

SPG77	Phenylalanyl-tRNA synthetase 2 (FARS2)	Complicated Autosomal recessive
SPG80	Ubiquitin associated protein 1 (UBAP1)	Pure Autosomal dominant

Appendix B

A



B

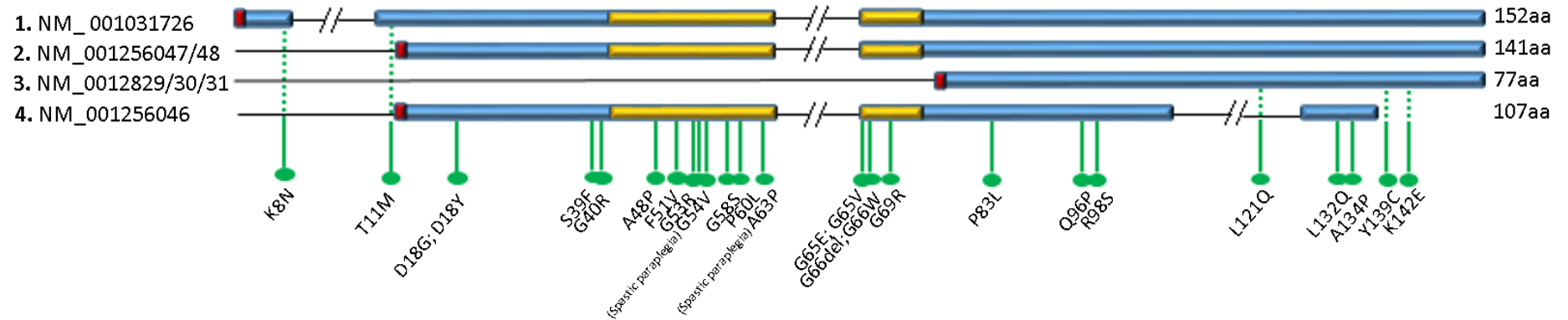


Figure A1. Schematic of C19orf12 genomic organisation, displaying reported dominant and recessively acting protein truncating variants (A) and missense mutations (B), in relation to gene exons, and protein domains and isoforms.

■ = proposed transmembrane domain. **■** = transcript initiation codon. Transcripts: **(1)** Canonical isoform, 152 amino acids (NM_001031726.3, ENST00000392278.2); **(2)** Isoform 2, 141 amino acids (NM_031448.6/NM_001256047.1, ENST00000323670.13); **(3)** Isoform 3, 77 amino acids (NM_001282929.1/NM_001282930.2/M_001282931.2, ENST00000392276.1); **(4)** Isoform 4, 107 amino acids (NM_001256046.2, ENST00000592153.5).

A) Red: Variants associated with autosomal dominant MPAN. **Orange:** Putative loss of function / splice junction variants associated with autosomal recessive MPAN. **Black:** Putative loss of function heterozygous variants present in the population database gnomAD. **Grey:** Variants predicted to be potentially loss of function in isoform 4 only. Number of individuals with the variant shown in brackets. **DN-** Proven de-novo in at least one pedigree; **INH RP-** Inherited with reduced penetrance/ later onset (i.e. variant inherited from unaffected parent or unaffected heterozygote > 60 years old in family); **INH P-** Inherited with apparent full penetrance. **B)** Missense mutations reported in recessively acting MPAN.

Appendix C

The methodology devised by Dr Irundika Dias used methanol lysis for sample and matrix disruption which worked well for plasma samples, but not cellular samples which only recovered ~20% of oxysterols from cells when compared to plasma recovery. Therefore, the sensitivity of the oxysterol analysis needed to be increased to confidently and efficiently analyse the relative abundance of each oxysterol within whole cell and subcellular fractions. To do this, different methods of lipid extraction and oxysterol analysis were investigated at The University of Surrey by building upon the established analysis to increase the sensitivity of oxysterol detection. Three methods for oxysterol extraction and quantification were compared for the quantification of oxysterols from cells, these three methods included the previously used methodology from *Dias et al., 2018*, methodology from *Bird et al., 2014* and a separate method established by Dr Khushboo Borah for this analysis. Figure A2 illustrates the results from the comparison of the three methods to quantify cellular oxysterols where M3 in Figure A2A and Figure A2D shows the chromatographic resolution of authentic standards and cellular yields from this newly developed oxysterol extraction and quantification. Figure A2A shows that the generated methodology (M3) has a significantly increased chromatographic resolution of authentic standards as observed by the larger peak areas when compared to the other two methods (M1 and M2). Figure A2B, C and D compare the recovery of authentic standards when using the three extraction methods compared to their whole cell lysates.

Figure A2B and C show a much smaller percentage of standards being recovered compared to the newly established methodology where there is at least a 70% recovery for each oxysterol with an average of 89% recovery for all

oxysterols compared to an average of 9% and 17% oxysterol recovery using the two previously described methods.

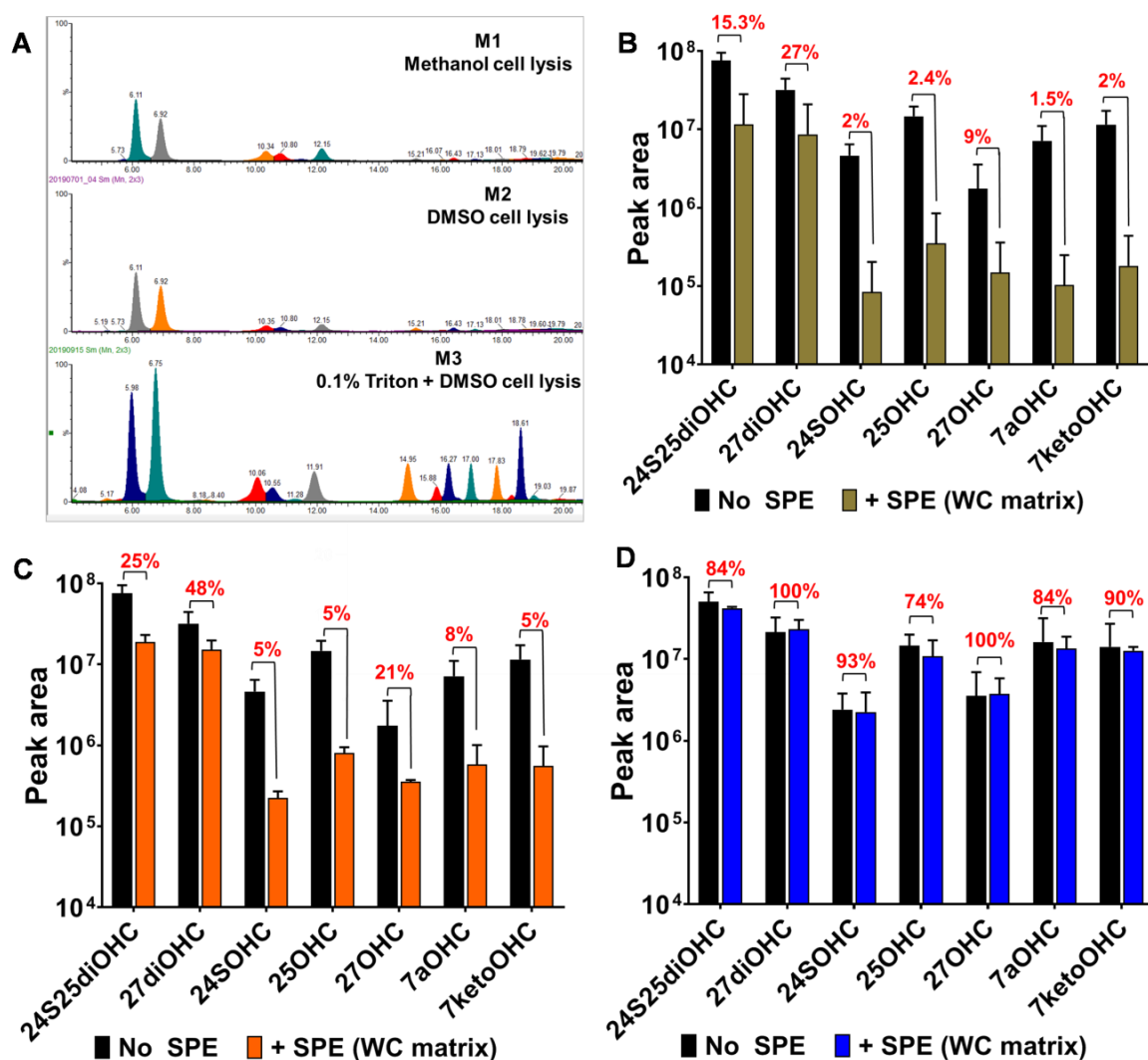


Figure A2. The comparative analysis of three methods for oxysterol extraction and subsequent quantification by LC-MS/MS. **A)** The comparative chromatographic resolution of authentic oxysterol standards when cellular material is extracted by the three methods (M1, Dias et al., 2018; M2, Bird et al., 2014; M3, the method developed in this study). Figures **B** (M1), **C** (M2) and **D** (M3) show the quantification from the peak areas shown in A and also comparing cellular lysates that have undergone solid phase extraction (SPE) and no SPE to compare the overall percentage recovery of each authentic oxysterol standard. Measurements were done using standards at 1ng.µl⁻¹ and are mean ± S.D. of 2-4 independent replicates. Data collected and graphs generated by Dr Khushboo Borah.

Instead of methanol lysis this newly developed methodology involves a multistep analyte separation. First, the samples are disrupted by sonication using a mixture of 70µl triton, 40µl DMSO and 5µl butylatedhydroxytoluene that was optimised for efficient cell lysis. Then, samples were pelleted and resuspended in the cell lysis mixture and sonicated for 20 minutes. The second step is required for the isolation of lipids from the samples, using a modified method outlined by Bligh and Dyer [315]. Cell lysates were mixed with 190µl methanol, 380µl dichloromethane and vortexed. Then 120µl of water was added to the solvent mixture, vortexed and incubated at room temperature for 10 minutes. The third step of the protocol involves phase separation to extract the lipids. After incubation the samples were centrifuged at 8000rpm for 10 minutes to induce phase separation then the bottom dichloromethane phase containing total lipids was collected. A portion of this lipid containing phase was used for cholesterol quantification using the cholesterol assay and the remainder was used for oxysterol extraction. Oxysterol extraction was achieved by the lipid phase being dried and resuspended in 40% methanol followed by SPE and elution with butyl acetate. The butyl acetate was dried, and the oxysterols reconstituted in 40% methanol for LC-MS/MS. The MS/MS method was developed using a Waters Triple quad mass spectrometer using targeted quantification of oxysterols. The LC multistep gradient methodology developed by *Dias et al., 2018* was modified for chromatographic analysis of both mono and dihydroxycholesterols for this analysis. Data analysis and quantification was performed in MassLynx software purchased from Waters.

Appendix D

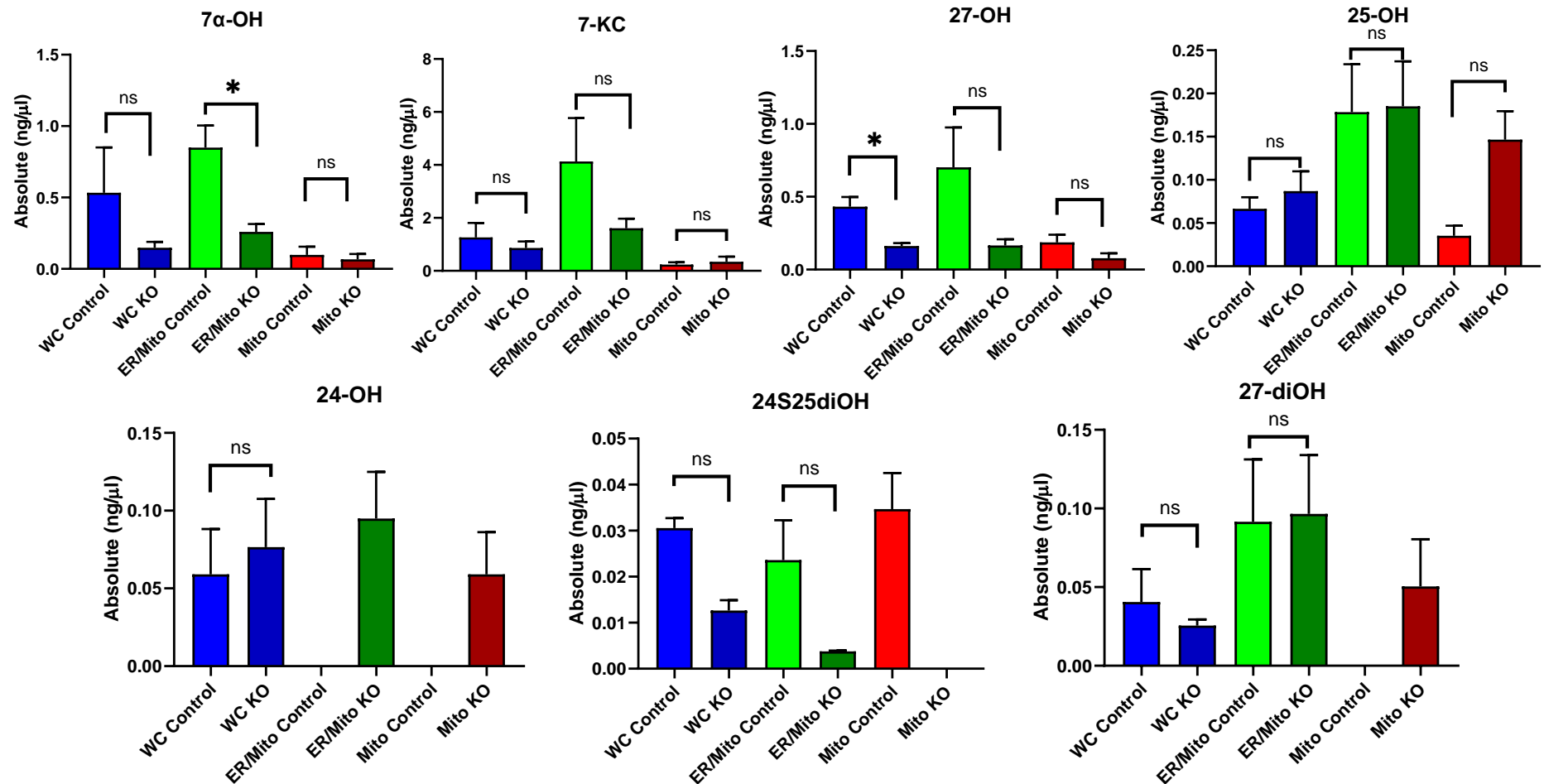


Figure A3. Individual oxysterol comparisons in control SH-SY5Y vs SPG21 knockout (KO) cells. $n=3-6$ but values lower than the lower limit of quantitation are not included. Absolute oxysterol values with columns representing the mean with SEM error bars. Significance determined by Mann-Whitney test and asterisks show statistical significance where $*=p<0.05$ and ns = not significant.

Appendix E

Media 1

Time-lapse film of 3T3 cells transfected with YFP-SPG21 and stained with Nile Red lipid droplet stain. Images were captured with a 63x oil immersion objective, every 9 seconds, for 5 minutes.

File name: YFP-SPG21 and Nile Red.

Media 2

Time-lapse film of 3T3 cells transfected with YFP-SPG21 and rab7. Images were captured with a 63x oil immersion objective, every 6 seconds, for 4 minutes 12 seconds.

File name: YFP-SPG21 and Rab7.

Media 3

Time-lapse film of 3T3 cells transfected with YFP-SPG21 and rab5. Images were captured with a 63x oil immersion objective, every 5 seconds, for 2 minutes.

File name: YFP-SPG21 and Rab5.

Media 4

Time-lapse film of 3T3 cells transfected with YFP-SPG21 and stained with lysotracker. Images were captured with a 63x oil immersion objective, every 5 seconds, for 2 minutes 10 seconds.

File name: YFP-SPG21 and LysoTracker.

Media 5

Time-lapse film of 3T3 cells transfected with YFP-SPG21 and rab7, and stained with lysotracker. Images were captured with a 63x oil immersion objective, every 10 seconds, for 5 minutes 10 seconds.

File name: YFP-SPG21, Rab7 and Lysotracker.

Media 6

Time-lapse film of 3T3 cells transfected with YFP-SPG21 and stained with Mitotracker. Images were captured with a 63x oil immersion objective, every 9 seconds, for 2 minutes 32 seconds.

File name: YFP-SPG21 and Mitotracker.

Media 7

Time-lapse film of control SH-SY5Y cells stained with Nile Red. Images were captured with a 63x oil immersion objective, every 5 seconds, for 5 minutes.

File name: Control SH-SY5Y and Nile Red.

Media 8

Time-lapse film of *SPG21* knockout SH-SY5Y cells stained with Nile Red. Images were captured with a 63x oil immersion objective, every 5 seconds, for 4 minutes 15 seconds.

File name: SPG21 Knockout SH-SY5Y and Nile Red.

Media 9

Time-lapse film of control SH-SY5Y cells stained with lysotracker. Images were captured with a 63x oil immersion objective, every 5 seconds, for 5 minutes 0 seconds.

File name: Control SH-SY5Y and Lysotracker.

Media 10

Time-lapse film of *SPG21* knockout SH-SY5Y cells stained with lysotracker. Images were captured with a 63x oil immersion objective, every 5 seconds, for 5 minutes 15 seconds.

File name: SPG21 Knockout SH-SY5Y and Lysotracker.

Media 11

Time-lapse film of control SH-SY5Y cells stained with Mitotracker. Images were captured with a 63x oil immersion objective, every 5 seconds, for 6 minutes 45 seconds.

File name: Control SH-SY5Y and Mitotracker.

Media 12

Time-lapse film of *SPG21* knockout SH-SY5Y cells stained with Mitotracker. Images were captured with a 63x oil immersion objective, every 5 seconds, for 6 minutes 10 seconds.

File name: SPG21 Knockout SH-SY5Y and Mitotracker.

Appendix F

Papers published and in submission from this work.

Paper 1

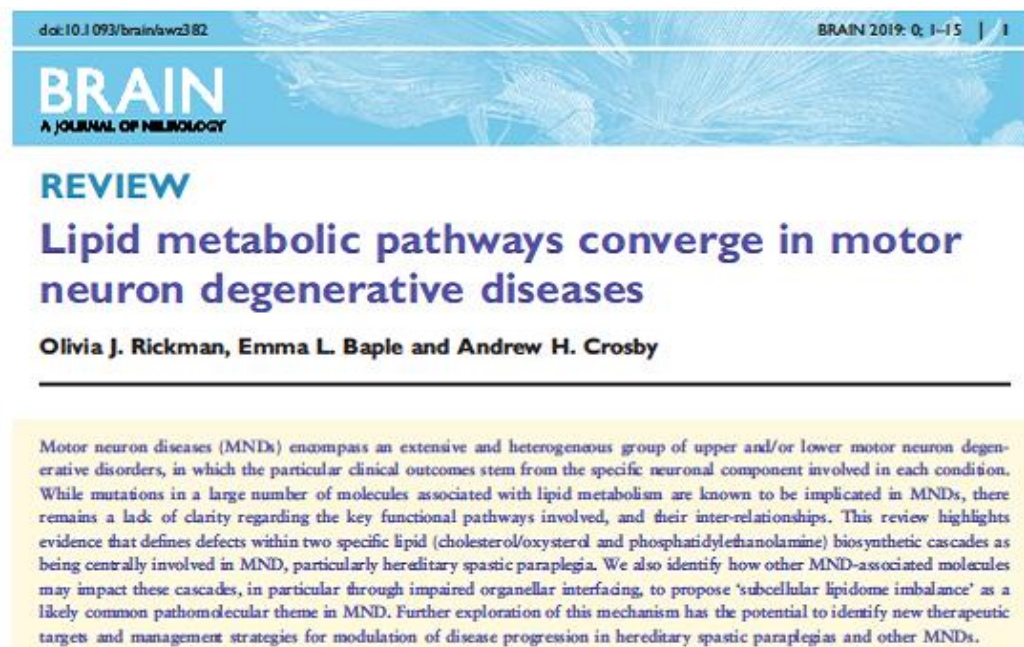
Title: Lipid metabolic pathways converge in motor neurone degenerative diseases

Authors: Olivia J Rickman, Emma L Baple and Andrew H Crosby

Journal: Brain, Volume 143, Issue 4, Pages 1073-1087

Date Published: Online: December 2019. Print: April 2020.

Altmetrics score: 248 (29/4/2020)



Paper 2

Title: Dominant mitochondrial membrane protein associated neurodegeneration (MPAN) variants cluster within a specific C19orf12 isoform

Authors: Olivia J Rickman, Claire G Salter, Adam C Gunning, James Fasham, Nikol Voutsina, Joseph S Leslie, Harold E Cross, James R Lupski, Emma L Baple and Andrew H Crosby

Journal: Parkinsonism & Related Disorders

Status: Submitted

Paper 3

Title: A quantitative LC-MS/MS method for analysis of mitochondrial specific oxysterol metabolism

Authors: Khushboo Borah, Olivia J Rickman, Nikol Voutsina, Isaac Ampong, Dan Gao, Emma L Baple, Irundika HK Dias, Andrew H Crosby and Helen Griffiths

Journal: Redox Biology

Status: Submitted

Bibliography

1. Nichols, E., et al., *Global, regional, and national burden of Alzheimer's disease and other dementias, 1990-2016: a systematic analysis for the Global Burden of Disease Study 2016*. The Lancet Neurology, 2019. **18**(1): p. 88-106.
2. Roehr, S., et al., *Is dementia incidence declining in high-income countries? A systematic review and meta-analysis*. Clinical epidemiology, 2018. **10**: p. 1233-1247.
3. Dorsey, E.R., et al., *Global, regional, and national burden of Parkinson's disease, 1990-2016: a systematic analysis for the Global Burden of Disease Study 2016*. The Lancet Neurology, 2018. **17**(11): p. 939-953.
4. Logroscino, G., et al., *Global, regional, and national burden of motor neuron diseases 1990-2016: a systematic analysis for the Global Burden of Disease Study 2016*. The Lancet Neurology, 2018. **17**(12): p. 1083-1097.
5. Jellinger, K.A., *Basic mechanisms of neurodegeneration: a critical update*. Journal of cellular and molecular medicine, 2010. **14**(3): p. 457-487.
6. Campanari, M.-L., A.-R. Bourefis, and E. Kabashi, *Diagnostic Challenge and Neuromuscular Junction Contribution to ALS Pathogenesis*. Frontiers in Neurology, 2019. **10**(68).
7. Saxena, S. and P. Caroni, *Mechanisms of axon degeneration: From development to disease*. Progress in Neurobiology, 2007. **83**(3): p. 174-191.
8. Jing Fan, T.M.D., Valina L. Dawson, *Cell Death Mechanisms of Neurodegeneration*. In: Beart P., Robinson M., Rattray M., Maragakis N. (eds) Neurodegenerative Diseases. Advances in Neurobiology,, 2017. **15**: p. 403-425.
9. Chi, H., H.-Y. Chang, and T.-K. Sang, *Neuronal Cell Death Mechanisms in Major Neurodegenerative Diseases*. International journal of molecular sciences, 2018. **19**(10): p. 3082.
10. Magrassi, L., K. Leto, and F. Rossi, *Lifespan of neurons is uncoupled from organismal lifespan*. Proceedings of the National Academy of Sciences of the United States of America, 2013. **110**(11): p. 4374-4379.
11. Fricker, M., et al., *Neuronal Cell Death*. Physiological reviews, 2018. **98**(2): p. 813-880.
12. Bear, M.F., B. Connors, and M. Paradiso, *Neuroscience : exploring the brain*. 2016: Fourth edition. Philadelphia: Wolters Kluwer, 2016.
13. Omar A, M.K., Bollu PC, *Physiology, Neuromuscular Junction*. [Updated 2019 Aug 10]. In: StatPearls [Internet]. Treasure Island (FL): StatPearls Publishing, 2019.
14. Longstaff, A., *BIOS Instant Notes in Neuroscience*. 2011.
15. Waxman, S.G., *Clinical neuroanatomy*. 2017.
16. Cappello, V. and M. Francolini, *Neuromuscular Junction Dismantling in Amyotrophic Lateral Sclerosis*. International journal of molecular sciences, 2017. **18**(10): p. 2092.
17. García, M.L., A. Fernández, and M.T. Solas, *Mitochondria, motor neurons and aging*. Journal of the Neurological Sciences, 2013. **330**(1): p. 18-26.

18. Statland, J.M., et al., *Patterns of Weakness, Classification of Motor Neuron Disease & Clinical Diagnosis of Sporadic ALS*. *Neurologic clinics*, 2015. **33**(4): p. 735-748.
19. Jawabri KH, S.S., *Physiology, Cerebral Cortex Functions*. . [Updated 2019 Jun 29]. In: StatPearls [Internet]. Treasure Island (FL): StatPearls Publishing, 2019.
20. Kantak, S.S., et al., *Rewiring the Brain: Potential Role of the Premotor Cortex in Motor Control, Learning, and Recovery of Function Following Brain Injury*. *Neurorehabilitation and Neural Repair*, 2012. **26**(3): p. 282-292.
21. Nachev, P., C. Kennard, and M. Husain, *Functional role of the supplementary and pre-supplementary motor areas*. *Nature Reviews Neuroscience*, 2008. **9**(11): p. 856-869.
22. Mukherjee, A. and A. Chakravarty, *Spasticity mechanisms - for the clinician*. *Frontiers in neurology*, 2010. **1**: p. 149-149.
23. Thau, L. and P. Singh, *Anatomy, Central Nervous System*. [Updated 2019 May 25]. In: StatPearls [Internet]. Treasure Island (FL): StatPearls Publishing, 2019.
24. Statland, J.M., et al., *Patterns of Weakness, Classification of Motor Neuron Disease, and Clinical Diagnosis of Sporadic Amyotrophic Lateral Sclerosis*. *Neurologic clinics*, 2015. **33**(4): p. 735-748.
25. McDermott, C.J. and P.J. Shaw, *Diagnosis and management of motor neurone disease*. *BMJ (Clinical research ed.)*, 2008. **336**(7645): p. 658-662.
26. Brown, R.H. and A. Al-Chalabi, *Amyotrophic Lateral Sclerosis*. *New England Journal of Medicine*, 2017. **377**(2): p. 162-172.
27. Ajroud-Driss, S. and T. Siddique, *Sporadic and hereditary amyotrophic lateral sclerosis (ALS)*. *Biochimica et Biophysica Acta (BBA) - Molecular Basis of Disease*, 2015. **1852**(4): p. 679-684.
28. Rosen, D.R., et al., *Mutations in Cu/Zn superoxide dismutase gene are associated with familial amyotrophic lateral sclerosis*. *Nature*, 1993. **362**(6415): p. 59-62.
29. Benatar, M., et al., *Presymptomatic ALS genetic counseling and testing: Experience and recommendations*. *Neurology*, 2016. **86**(24): p. 2295-2302.
30. Garg, N., et al., *Differentiating lower motor neuron syndromes*. *Journal of Neurology, Neurosurgery & Psychiatry*, 2017. **88**(6): p. 474-483.
31. Querin, G., et al., *Non-neural phenotype of spinal and bulbar muscular atrophy: results from a large cohort of Italian patients*. *Journal of Neurology, Neurosurgery & Psychiatry*, 2016. **87**(8): p. 810-816.
32. Rossor, A.M., et al., *The distal hereditary motor neuropathies*. *Journal of Neurology, Neurosurgery & Psychiatry*, 2012. **83**(1): p. 6-14.
33. Irobi, J., P. De Jonghe, and V. Timmerman, *Molecular genetics of distal hereditary motor neuropathies*. *Human Molecular Genetics*, 2004. **13**(suppl_2): p. R195-R202.
34. Szigeti, K. and J.R. Lupski, *Charcot-Marie-Tooth disease*. *European journal of human genetics : EJHG*, 2009. **17**(6): p. 703-710.
35. Magy, L. and J.-M. Vallat, *Therapeutic options in Charcot–Marie–Tooth diseases AU - Mathis, Stéphane*. *Expert Review of Neurotherapeutics*, 2015. **15**(4): p. 355-366.

36. Züchner, S. and J.M. Vance, *Mechanisms of Disease: a molecular genetic update on hereditary axonal neuropathies*. Nature Clinical Practice Neurology, 2006. **2**(1): p. 45-53.
37. Brugman, F., et al., *Differentiation of Hereditary Spastic Paraparesis From Primary Lateral Sclerosis in Sporadic Adult-Onset Upper Motor Neuron Syndromes*. JAMA Neurology, 2009. **66**(4): p. 509-514.
38. Ramanathan, R.S. and S. Rana, *Demographics and clinical characteristics of primary lateral sclerosis: case series and a review of literature*. Neurodegenerative Disease Management, 2018. **8**(1): p. 17-23.
39. Clark, M.G., et al., *Loss of functional connectivity is an early imaging marker in primary lateral sclerosis*. Amyotrophic lateral sclerosis & frontotemporal degeneration, 2018. **19**(7-8): p. 562-569.
40. Simonds, A.K., *Progress in respiratory management of bulbar complications of motor neuron disease/amyotrophic lateral sclerosis?* Thorax, 2017. **72**(3): p. 199-201.
41. McDermott, C., et al., *Hereditary spastic paraparesis: a review of new developments*. Journal of Neurology, Neurosurgery & Psychiatry, 2000. **69**(2): p. 150-160.
42. Nan, H., et al., *UBAP1 mutations cause juvenile-onset hereditary spastic paraplegias (SPG80) and impair UBAP1 targeting to endosomes*. Journal of Human Genetics, 2019. **64**(11): p. 1055-1065.
43. Noreau, A., P.A. Dion, and G.A. Rouleau, *Molecular aspects of hereditary spastic paraplegia*. Exp Cell Res, 2014. **325**(1): p. 18-26.
44. Lo Giudice, T., et al., *Hereditary spastic paraplegia: clinical-genetic characteristics and evolving molecular mechanisms*. Exp Neurol, 2014. **261**: p. 518-39.
45. Faber, I., L.M.T. Branco, and M.C. França Júnior, *Cognitive dysfunction in hereditary spastic paraplegias and other motor neuron disorders*. Dementia & neuropsychologia, 2016. **10**(4): p. 276-279.
46. Shribman, S., et al., *Hereditary spastic paraplegia: from diagnosis to emerging therapeutic approaches*. The Lancet Neurology, 2019. **18**(12): p. 1136-1146.
47. Hedera, P., *Hereditary Spastic Paraplegia Overview*. In: Adam MP, Ardinger HH, Pagon RA, et al., editors. GeneReviews®, 2000 Aug 15 [Updated 2018 Sep 27].
48. van Meer, G., D.R. Voelker, and G.W. Feigenson, *Membrane lipids: where they are and how they behave*. Nature reviews. Molecular cell biology, 2008. **9**(2): p. 112-124.
49. Raichle, M.E. and D.A. Gusnard, *Appraising the brain's energy budget*. Proceedings of the National Academy of Sciences of the United States of America, 2002. **99**(16): p. 10237-10239.
50. Panov, A., et al., *Fatty Acids in Energy Metabolism of the Central Nervous System*. BioMed Research International, 2014. **2014**: p. 22.
51. Jackman, N., A. Ishii, and R. Bansal, *Oligodendrocyte development and myelin biogenesis: parsing out the roles of glycosphingolipids*. Physiology (Bethesda, Md.), 2009. **24**: p. 290-297.
52. Schmitt, S., L. Cantuti Castelvetti, and M. Simons, *Metabolism and functions of lipids in myelin*. Biochimica et Biophysica Acta (BBA) - Molecular and Cell Biology of Lipids, 2015. **1851**(8): p. 999-1005.
53. Zhang, J. and Q. Liu, *Cholesterol metabolism and homeostasis in the brain*. Protein & cell, 2015. **6**(4): p. 254-264.

54. Hussain, G., et al., *Role of cholesterol and sphingolipids in brain development and neurological diseases*. *Lipids in Health and Disease*, 2019. **18**(1): p. 26.
55. Di Battista, A.M., N.M. Heinsinger, and G.W. Rebeck, *Alzheimer's Disease Genetic Risk Factor APOE-ε4 Also Affects Normal Brain Function*. *Current Alzheimer research*, 2016. **13**(11): p. 1200-1207.
56. Chung, J., et al., *Endosomal-Lysosomal Cholesterol Sequestration by U18666A Differentially Regulates Amyloid Precursor Protein (APP) Metabolism in Normal and APP-Overexpressing Cells*. *Molecular and Cellular Biology*, 2018. **38**(11): p. e00529-17.
57. Schneider, A., et al., *Cholesterol depletion reduces aggregation of amyloid-beta peptide in hippocampal neurons*. *Neurobiology of Disease*, 2006. **23**(3): p. 573-577.
58. Shahmoradian, S.H., et al., *Lewy pathology in Parkinson's disease consists of crowded organelles and lipid membranes*. *Nature Neuroscience*, 2019. **22**(7): p. 1099-1109.
59. Galvagnion, C., et al., *Lipid vesicles trigger α-synuclein aggregation by stimulating primary nucleation*. *Nature Chemical Biology*, 2015. **11**: p. 229.
60. Doria, M., et al., *Contribution of cholesterol and oxysterols to the pathophysiology of Parkinson's disease*. *Free Radical Biology and Medicine*, 2016. **101**: p. 393-400.
61. Ruipérez, V., F. Darios, and B. Davletov, *Alpha-synuclein, lipids and Parkinson's disease*. *Progress in Lipid Research*, 2010. **49**(4): p. 420-428.
62. Valenza, M., et al., *Dysfunction of the cholesterol biosynthetic pathway in Huntington's disease*. *The Journal of neuroscience : the official journal of the Society for Neuroscience*, 2005. **25**(43): p. 9932-9939.
63. Sipione, S., et al., *Early transcriptional profiles in huntingtin-inducible striatal cells by microarray analyses*. *Human Molecular Genetics*, 2002. **11**(17): p. 1953-1965.
64. Leoni, V. and C. Caccia, *The impairment of cholesterol metabolism in Huntington disease*. *Biochimica et Biophysica Acta (BBA) - Molecular and Cell Biology of Lipids*, 2015. **1851**(8): p. 1095-1105.
65. Lezi, E. and R.H. Swerdlow, *Mitochondria in neurodegeneration*. *Advances in experimental medicine and biology*, 2012. **942**: p. 269-286.
66. Vanhauwaert, R., V. Bharat, and X. Wang, *Surveillance and transportation of mitochondria in neurons*. *Current Opinion in Neurobiology*, 2019. **57**: p. 87-93.
67. Nguyen, T.T., et al., *Loss of Miro1-directed mitochondrial movement results in a novel murine model for neuron disease*. *Proceedings of the National Academy of Sciences*, 2014. **111**(35): p. E3631-E3640.
68. Barel, O., et al., *Deleterious variants in TRAK1 disrupt mitochondrial movement and cause fatal encephalopathy*. *Brain : a journal of neurology*, 2017. **140**(3): p. 568-581.
69. Lin, M.-Y., et al., *Releasing Syntaphilin Removes Stressed Mitochondria from Axons Independent of Mitophagy under Pathophysiological Conditions*. *Neuron*, 2017. **94**(3): p. 595-610.e6.
70. Johri, A. and M.F. Beal, *Mitochondrial Dysfunction in Neurodegenerative Diseases*. *The Journal of Pharmacology and Experimental Therapeutics*, 2012. **342**(3): p. 619-630.

71. Youle, R.J. and A.M. van der Bliek, *Mitochondrial fission, fusion, and stress*. Science (New York, N.Y.), 2012. **337**(6098): p. 1062-1065.
72. Di Meglio, C., et al., *Clinical and allelic heterogeneity in a pediatric cohort of 11 patients carrying MFN2 mutation*. Brain and Development, 2016. **38**(5): p. 498-506.
73. Waterham, H.R., et al., *A Lethal Defect of Mitochondrial and Peroxisomal Fission*. New England Journal of Medicine, 2007. **356**(17): p. 1736-1741.
74. Oliver, D. and P.H. Reddy, *Dynamics of Dynamin-Related Protein 1 in Alzheimer's Disease and Other Neurodegenerative Diseases*. Cells, 2019. **8**(9): p. 961.
75. Pathak, D., A. Berthet, and K. Nakamura, *Energy failure: does it contribute to neurodegeneration?* Annals of neurology, 2013. **74**(4): p. 506-516.
76. Cha, M.-Y., D.K. Kim, and I. Mook-Jung, *The role of mitochondrial DNA mutation on neurodegenerative diseases*. Experimental & molecular medicine, 2015. **47**(3): p. e150-e150.
77. Cowan, K., O. Anichtchik, and S. Luo, *Mitochondrial integrity in neurodegeneration*. CNS neuroscience & therapeutics, 2019. **25**(7): p. 825-836.
78. Itoh, K., et al., *Mitochondrial dynamics in neurodegeneration*. Trends in cell biology, 2013. **23**(2): p. 64-71.
79. Yoboue, E.D., R. Sitia, and T. Simmen, *Redox crosstalk at endoplasmic reticulum (ER) membrane contact sites (MCS) uses toxic waste to deliver messages*. Cell Death & Disease, 2018. **9**(3): p. 331.
80. Zorov, D.B., M. Juhaszova, and S.J. Sollott, *Mitochondrial reactive oxygen species (ROS) and ROS-induced ROS release*. Physiological reviews, 2014. **94**(3): p. 909-950.
81. Turrens, J.F., *Mitochondrial formation of reactive oxygen species*. The Journal of physiology, 2003. **552**(Pt 2): p. 335-344.
82. Kim, G.H., et al., *The Role of Oxidative Stress in Neurodegenerative Diseases*. Experimental neurobiology, 2015. **24**(4): p. 325-340.
83. Karch, J. and J.D. Molkentin, *Identifying the components of the elusive mitochondrial permeability transition pore*. Proceedings of the National Academy of Sciences, 2014. **111**(29): p. 10396-10397.
84. Smith, E.F., P.J. Shaw, and K.J. De Vos, *The role of mitochondria in amyotrophic lateral sclerosis*. Neuroscience Letters, 2017.
85. Volpe, C.M.O., et al., *Cellular death, reactive oxygen species (ROS) and diabetic complications*. Cell death & disease, 2018. **9**(2): p. 119-119.
86. Panth, N., K.R. Paudel, and K. Parajuli, *Reactive Oxygen Species: A Key Hallmark of Cardiovascular Disease*. Advances in medicine, 2016. **2016**: p. 9152732-9152732.
87. Liou, G.-Y. and P. Storz, *Reactive oxygen species in cancer*. Free radical research, 2010. **44**(5): p. 479-496.
88. Gaschler, M.M. and B.R. Stockwell, *Lipid peroxidation in cell death*. Biochemical and Biophysical Research Communications, 2017. **482**(3): p. 419-425.
89. Wong-ekkabut, J., et al., *Effect of Lipid Peroxidation on the Properties of Lipid Bilayers: A Molecular Dynamics Study*. Biophysical Journal, 2007. **93**(12): p. 4225-4236.
90. Li, X.-M., et al., *Conformation of an Endogenous Ligand in a Membrane Bilayer for the Macrophage Scavenger Receptor CD36*. Biochemistry, 2007. **46**(17): p. 5009-5017.

91. Shichiri, M., *The role of lipid peroxidation in neurological disorders*. Journal of clinical biochemistry and nutrition, 2014. **54**(3): p. 151-160.
92. Dixon, S.J., et al., *Ferroptosis: an iron-dependent form of nonapoptotic cell death*. Cell, 2012. **149**(5): p. 1060-1072.
93. Yang, W.S. and B.R. Stockwell, *Synthetic Lethal Screening Identifies Compounds Activating Iron-Dependent, Nonapoptotic Cell Death in Oncogenic-RAS-Harboring Cancer Cells*. Chemistry & Biology, 2008. **15**(3): p. 234-245.
94. Dolma, S., et al., *Identification of genotype-selective antitumor agents using synthetic lethal chemical screening in engineered human tumor cells*. Cancer Cell, 2003. **3**(3): p. 285-296.
95. Martinez, A.M., et al., *NSC-34 motor neuron-like cells are sensitized to ferroptosis upon differentiation*. FEBS open bio, 2019. **9**(4): p. 582-593.
96. Gandhi, S. and A.Y. Abramov, *Mechanism of oxidative stress in neurodegeneration*. Oxidative medicine and cellular longevity, 2012. **2012**: p. 428010-428010.
97. Brigelius-Flohé, R. and M. Maiorino, *Glutathione peroxidases*. Biochimica et Biophysica Acta (BBA) - General Subjects, 2013. **1830**(5): p. 3289-3303.
98. Yang, W.S., et al., *Regulation of Ferroptotic Cancer Cell Death by GPX4*. Cell, 2014. **156**(0): p. 317-331.
99. Pansarasa, O., et al., *SOD1 in Amyotrophic Lateral Sclerosis: "Ambivalent" Behavior Connected to the Disease*. International journal of molecular sciences, 2018. **19**(5): p. 1345.
100. McAlary, L., J.A. Aquilina, and J.J. Yerbury, *Susceptibility of Mutant SOD1 to Form a Destabilized Monomer Predicts Cellular Aggregation and Toxicity but Not In vitro Aggregation Propensity*. Frontiers in neuroscience, 2016. **10**: p. 499-499.
101. Tokuda, E., et al., *Wild-type Cu/Zn-superoxide dismutase is misfolded in cerebrospinal fluid of sporadic amyotrophic lateral sclerosis*. Molecular Neurodegeneration, 2019. **14**(1): p. 42.
102. Li, Y., et al., *Dilated cardiomyopathy and neonatal lethality in mutant mice lacking manganese superoxide dismutase*. Nature Genetics, 1995. **11**: p. 376.
103. Tomkins, J., et al., *Mutation screening of manganese superoxide dismutase in amyotrophic lateral sclerosis*. NeuroReport, 2001. **12**(11): p. 2319-2322.
104. Gongora, M.C., et al., *Loss of extracellular superoxide dismutase leads to acute lung damage in the presence of ambient air: a potential mechanism underlying adult respiratory distress syndrome*. The American journal of pathology, 2008. **173**(4): p. 915-926.
105. Stadelmann, C., et al., *Myelin in the Central Nervous System: Structure, Function, and Pathology*. Physiological Reviews, 2019. **99**(3): p. 1381-1431.
106. Blackstone, C., *Cellular pathways of hereditary spastic paraplegia*. Annu Rev Neurosci, 2012. **35**: p. 25-47.
107. Linneberg, C., et al., *L1cam-mediated developmental processes of the nervous system are differentially regulated by proteolytic processing*. Scientific Reports, 2019. **9**(1): p. 3716.
108. Potter, K.A., et al., *Central nervous system dysfunction in a mouse model of FA2H deficiency*. Glia, 2011. **59**(7): p. 1009-1021.

109. Abrams, C.K., *Diseases of connexins expressed in myelinating glia*. Neuroscience Letters, 2019. **695**: p. 91-99.
110. Park, S.H., et al., *Hereditary spastic paraplegia proteins REEP1, spastin, and atlastin-1 coordinate microtubule interactions with the tubular ER network*. The Journal of clinical investigation, 2010. **120**(4): p. 1097-1110.
111. Montenegro, G., et al., *Mutations in the ER-shaping protein reticulon 2 cause the axon-degenerative disorder hereditary spastic paraplegia type 12*. The Journal of clinical investigation, 2012. **122**(2): p. 538-544.
112. Pagac, M., et al., *SEIPIN Regulates Lipid Droplet Expansion and Adipocyte Development by Modulating the Activity of Glycerol-3-phosphate Acyltransferase*. Cell reports, 2016. **17**(6): p. 1546-1559.
113. Tian, W.-T., et al., *Novel Mutations in Endoplasmic Reticulum Lipid Raft-associated Protein 2 Gene Cause Pure Hereditary Spastic Paraplegia Type 18*. Chinese medical journal, 2016. **129**(22): p. 2759-2761.
114. Mancuso, G., et al., *Alternative splicing of Spg7, a gene involved in hereditary spastic paraplegia, encodes a variant of paraplegin targeted to the endoplasmic reticulum*. PloS one, 2012. **7**(5): p. e36337-e36337.
115. Hansen, J.J., et al., *Hereditary spastic paraplegia SPG13 is associated with a mutation in the gene encoding the mitochondrial chaperonin Hsp60*. American journal of human genetics, 2002. **70**(5): p. 1328-1332.
116. Blackstone, C., *Converging cellular themes for the hereditary spastic paraplegias*. Current opinion in neurobiology, 2018. **51**: p. 139-146.
117. Campbell, P.D., et al., *Unique function of Kinesin Kif5A in localization of mitochondria in axons*. The Journal of neuroscience : the official journal of the Society for Neuroscience, 2014. **34**(44): p. 14717-14732.
118. Nicolas, A., et al., *Genome-wide Analyses Identify KIF5A as a Novel ALS Gene*. Neuron, 2018. **97**(6): p. 1268-1283.e6.
119. Ramírez, O.A. and A. Couve, *The endoplasmic reticulum and protein trafficking in dendrites and axons*. Trends in Cell Biology, 2011. **21**(4): p. 219-227.
120. Schmidt, O. and D. Teis, *The ESCRT machinery*. Current biology : CB, 2012. **22**(4): p. R116-R120.
121. Vantaggiato, C., et al., *ZFYVE26/SPASTIZIN and SPG11/SPATACSIN mutations in hereditary spastic paraplegia types AR-SPG15 and AR-SPG11 have different effects on autophagy and endocytosis*. Autophagy, 2019. **15**(1): p. 34-57.
122. Hirst, J., C. Irving, and G.H.H. Borner, *Adaptor Protein Complexes AP-4 and AP-5: New Players in Endosomal Trafficking and Progressive Spastic Paraplegia*. Traffic, 2013. **14**(2): p. 153-164.
123. Goytain, A., et al., *NIPA1(SP6), the Basis for Autosomal Dominant Form of Hereditary Spastic Paraplegia, Encodes a Functional Mg²⁺ Transporter*. Journal of Biological Chemistry, 2007. **282**(11): p. 8060-8068.
124. Wali, G., et al., *Mechanism of impaired microtubule-dependent peroxisome trafficking and oxidative stress in SPAST-mutated cells from patients with Hereditary Spastic Paraplegia*. Scientific Reports, 2016. **6**(1): p. 27004.
125. Chang, C.-L., et al., *Spastin tethers lipid droplets to peroxisomes and directs fatty acid trafficking through ESCRT-III*. Journal of Cell Biology, 2019. **218**(8): p. 2583-2599.

126. Darios, F., F. Mochel, and G. Stevanin, *Lipids in the Physiopathology of Hereditary Spastic Paraplegias*. *Frontiers in Neuroscience*, 2020. **14**(74).
127. Salo, V.T., et al., *Seipin Facilitates Triglyceride Flow to Lipid Droplet and Counteracts Droplet Ripening via Endoplasmic Reticulum Contact*. *Developmental Cell*, 2019. **50**(4): p. 478-493.e9.
128. Craveiro Sarmiento, A.S., et al., *Exploring Seipin: From Biochemistry to Bioinformatics Predictions*. *International journal of cell biology*, 2018. **2018**: p. 5207608-5207608.
129. Eastman, S.W., M. Yassaee, and P.D. Bieniasz, *A role for ubiquitin ligases and Spartin/SPG20 in lipid droplet turnover*. *The Journal of cell biology*, 2009. **184**(6): p. 881-894.
130. Renvoisé, B., et al., *Spg20^{-/-} mice reveal multimodal functions for Troyer syndrome protein spartin in lipid droplet maintenance, cytokinesis and BMP signaling*. *Human Molecular Genetics*, 2012. **21**(16): p. 3604-3618.
131. Maruyama, T., et al., *Loss of DDHD2, whose mutation causes spastic paraplegia, promotes reactive oxygen species generation and apoptosis*. *Cell death & disease*, 2018. **9**(8): p. 797-797.
132. Synofzik, M., et al., *PNPLA6 mutations cause Boucher-Neuhäuser and Gordon Holmes syndromes as part of a broad neurodegenerative spectrum*. *Brain*, 2013. **137**(1): p. 69-77.
133. Durand, C.M., et al., *CYP2U1 activity is altered by missense mutations in hereditary spastic paraplegia 56*. *Human Mutation*, 2018. **39**(1): p. 140-151.
134. Arnoldi, A., et al., *Clinical phenotype variability in patients with hereditary spastic paraplegia type 5 associated with CYP7B1 mutations*. *Clinical Genetics*, 2012. **81**(2): p. 150-157.
135. Jaiswal, M.K., *Riluzole and edaravone: A tale of two amyotrophic lateral sclerosis drugs*. *Medicinal Research Reviews*, 2019. **39**(2): p. 733-748.
136. Marsden, J., et al., *The Effects of Functional Electrical Stimulation on Walking in Hereditary and Spontaneous Spastic Paraparesis*. *Neuromodulation: Technology at the Neural Interface*, 2013. **16**(3): p. 256-260.
137. Williams, J.R., et al., *Copper delivery to the CNS by CuATSM effectively treats motor neuron disease in SODG93A mice co-expressing the Copper-Chaperone-for-SOD*. *Neurobiology of Disease*, 2016. **89**: p. 1-9.
138. Farrowell, N.E., et al., *CuATSM Protects Against the In Vitro Cytotoxicity of Wild-Type-Like Copper-Zinc Superoxide Dismutase Mutants but not Mutants That Disrupt Metal Binding*. *ACS Chemical Neuroscience*, 2019. **10**(3): p. 1555-1564.
139. Wu, Y., M. Chen, and J. Jiang, *Mitochondrial dysfunction in neurodegenerative diseases and drug targets via apoptotic signaling*. *Mitochondrion*, 2019. **49**: p. 35-45.
140. Gowing, G. and C.N. Svendsen, *Stem cell transplantation for motor neuron disease: current approaches and future perspectives*. *Neurotherapeutics : the journal of the American Society for Experimental NeuroTherapeutics*, 2011. **8**(4): p. 591-606.
141. Kraybill, D., Olshan, Marc., *The Amish struggle with modernity* Hanover, NH : University Press of New England, 1994.
142. Rohrer, K. and L. Dundes, *Sharing the Load: Amish Healthcare Financing*. *Healthcare (Basel, Switzerland)*, 2016. **4**(4): p. 92.
143. *Amish Population Profile 2018*. Amish Studies The Young Center, Accessed 5.12.19(<https://groups.etown.edu/amishstudies/>).

144. Hou, L., et al., *Amish revisited: next-generation sequencing studies of psychiatric disorders among the Plain people*. Trends in genetics : TIG, 2013. **29**(7): p. 412-418.
145. Heima, M., M.-A. Harrison, and P. Milgrom, *Oral health and medical conditions among Amish children*. Journal of clinical and experimental dentistry, 2017. **9**(3): p. e338-e343.
146. Grant, P.R., *Founder effects and silvereyes*. Proceedings of the National Academy of Sciences of the United States of America, 2002. **99**(12): p. 7818-7820.
147. Francomano, C.A., V.A. McKusick, and L.G. Biesecker, *Medical genetic studies in the Amish: Historical perspective*. American Journal of Medical Genetics Part C: Seminars in Medical Genetics, 2003. **121C**(1): p. 1-4.
148. Cross, H.E. and V.A. McKusick, *The Troyer Syndrome: A Recessive Form of Spastic Paraplegia With Distal Muscle Wasting*. JAMA Neurology, 1967. **16**(5): p. 473-485.
149. CROSS, H.E. and V.A. McKUSICK, *The Mast Syndrome: A Recessively Inherited Form of Presenile Dementia With Motor Disturbances*. JAMA Neurology, 1967. **16**(1): p. 1-13.
150. Patel H, C.H., Proukakis C, Hershberger R, Bork P, Ciccarelli FD, Patton MA, McKusick VA, Crosby AH, *SPG20 is mutated in Troyer syndrome, an hereditary spastic paraplegia*. Nature Genetics, 2002. **31**(4): p. 347-348.
151. Simpson, M.A., et al., *Maspardin Is Mutated in Mast Syndrome, a Complicated Form of Hereditary Spastic Paraplegia Associated with Dementia*. American Journal of Human Genetics, 2003. **73**(5): p. 1147-1156.
152. Tsui, L., et al., *Cystic fibrosis locus defined by a genetically linked polymorphic DNA marker*. Science, 1985. **230**(4729): p. 1054-1057.
153. *Windows of Hope Project* Accessed 5.12.19(<https://wohproject.com/about/>).
154. Proukakis, C., et al., *Troyer syndrome revisited*. Journal of Neurology, 2004. **251**(9): p. 1105-1110.
155. Bizzari, S., et al., *Novel SPG20 mutation in an extended family with Troyer syndrome*. Metabolic Brain Disease, 2017. **32**(6): p. 2155-2159.
156. Dardour, L., et al., *SPG20 mutation in three siblings with familial hereditary spastic paraplegia*. Cold Spring Harbor molecular case studies. **3**(4): p. a001537.
157. Renvoisé, B., et al., *Reep1 null mice reveal a converging role for hereditary spastic paraplegia proteins in lipid droplet regulation*. Human molecular genetics, 2016. **25**(23): p. 5111-5125.
158. Joshi, D.C. and J.C. Bakowska, *SPG20 protein spartin associates with cardiolipin via its plant-related senescence domain and regulates mitochondrial Ca²⁺ homeostasis*. PloS one, 2011. **6**(4): p. e19290-e19290.
159. Harlalka, G.V., et al., *Mutations in B4GALNT1 (GM2 synthase) underlie a new disorder of ganglioside biosynthesis*. Brain : a journal of neurology, 2013. **136**(Pt 12): p. 3618-3624.
160. Dad, R., et al., *Febrile ataxia and myokymia broaden the SPG26 hereditary spastic paraplegia phenotype*. Neurology. Genetics, 2017. **3**(3): p. e156-e156.

161. Wilkinson, P.A., et al., *A new locus for autosomal recessive complicated hereditary spastic paraplegia (SPG26) maps to chromosome 12p11.1-12q14*. Journal of medical genetics, 2005. **42**(1): p. 80-82.
162. Boukhris, A., et al., *Alteration of ganglioside biosynthesis responsible for complex hereditary spastic paraplegia*. American journal of human genetics, 2013. **93**(1): p. 118-123.
163. Simpson, M.A., et al., *Infantile-onset symptomatic epilepsy syndrome caused by a homozygous loss-of-function mutation of GM3 synthase*. Nature Genetics, 2004. **36**(11): p. 1225-1229.
164. Crosby, A.H., et al., *Defective mitochondrial mRNA maturation is associated with spastic ataxia*. American journal of human genetics, 2010. **87**(5): p. 655-660.
165. Tesson, C., et al., *Alteration of Fatty-Acid-Metabolizing Enzymes Affects Mitochondrial Form and Function in Hereditary Spastic Paraplegia*. American Journal of Human Genetics, 2012. **91**(6): p. 1051-1064.
166. Towbin, H., T. Staehelin, and J. Gordon, *Electrophoretic transfer of proteins from polyacrylamide gels to nitrocellulose sheets: procedure and some applications*. Proceedings of the National Academy of Sciences of the United States of America, 1979. **76**(9): p. 4350-4354.
167. Mullis, K., et al., *Specific enzymatic amplification of DNA in vitro: the polymerase chain reaction*. Cold Spring Harbor symposia on quantitative biology, 1986. **51 Pt 1**: p. 263-273.
168. Hunt, S.E., et al., *Ensembl variation resources*. Database, 2018. **2018**.
169. Untergasser, A., et al., *Primer3--new capabilities and interfaces*. Nucleic acids research, 2012. **40**(15): p. e115-e115.
170. Kent, W.J., *BLAT--the BLAST-like alignment tool*. Genome research, 2002. **12**(4): p. 656-664.
171. Kent, W.J., et al., *The human genome browser at UCSC*. Genome research, 2002. **12**(6): p. 996-1006.
172. Yang, Y., et al., *Clinical whole-exome sequencing for the diagnosis of mendelian disorders*. The New England journal of medicine, 2013. **369**(16): p. 1502-1511.
173. Smith, H.O. and K.W. Welcox, *A Restriction enzyme from Hemophilus influenzae: I. Purification and general properties*. Journal of Molecular Biology, 1970. **51**(2): p. 379-391.
174. Gellert, M., *Formation of covalent circles of lambda DNA by E. coli extracts*. Proceedings of the National Academy of Sciences, 1967. **57**(1): p. 148-155.
175. Cohen, S.N., et al., *Construction of biologically functional bacterial plasmids in vitro*. Proceedings of the National Academy of Sciences of the United States of America, 1973. **70**(11): p. 3240-3244.
176. Crowley, L.C., et al., *Measuring Cell Death by Propidium Iodide Uptake and Flow Cytometry*. Cold Spring Harbor Protocols, 2016. **2016**(7): p. pdb.prot087163.
177. Pietkiewicz, S., J.H. Schmidt, and I.N. Lavrik, *Quantification of apoptosis and necroptosis at the single cell level by a combination of Imaging Flow Cytometry with classical Annexin V/propidium iodide staining*. Journal of Immunological Methods, 2015. **423**: p. 99-103.
178. Di Meo, I. and V. Tiranti, *Classification and molecular pathogenesis of NBIA syndromes*. European Journal of Paediatric Neurology, 2018. **22**(2): p. 272-284.

179. Hogarth, P., et al., *New NBIA subtype: genetic, clinical, pathologic, and radiographic features of MPAN*. *Neurology*, 2013. **80**(3): p. 268-275.
180. Strokin, M. and G. Reiser, *Mitochondria from a mouse model of the human infantile neuroaxonal dystrophy (INAD) with genetic defects in VIA iPLA2 have disturbed Ca²⁺ regulation with reduction in Ca²⁺ capacity*. *Neurochemistry International*, 2016. **99**: p. 187-193.
181. Zöller, I., et al., *Absence of 2-Hydroxylated Sphingolipids Is Compatible with Normal Neural Development But Causes Late-Onset Axon and Myelin Sheath Degeneration*. *The Journal of Neuroscience*, 2008. **28**(39): p. 9741-9754.
182. Hartig, Monika B., et al., *Absence of an Orphan Mitochondrial Protein, C19orf12, Causes a Distinct Clinical Subtype of Neurodegeneration with Brain Iron Accumulation*. *The American Journal of Human Genetics*, 2011. **89**(4): p. 543-550.
183. Horvath, R., et al., *SCP2 mutations and neurodegeneration with brain iron accumulation*. *Neurology*, 2015. **85**(21): p. 1909-1911.
184. Jaber, E., et al., *Identification of mutation in GTPBP2 in patients of a family with neurodegeneration accompanied by iron deposition in the brain*. *Neurobiology of Aging*, 2016. **38**: p. 216.e11-216.e18.
185. Arber, C.E., et al., *Review: Insights into molecular mechanisms of disease in neurodegeneration with brain iron accumulation: unifying theories*. *Neuropathology and applied neurobiology*, 2016. **42**(3): p. 220-241.
186. Dick, K.J., et al., *Mutation of FA2H underlies a complicated form of hereditary spastic paraplegia (SPG35)*. *Human Mutation*, 2010. **31**(4): p. E1251-E1260.
187. Landouré, G., et al., *Hereditary spastic paraplegia type 43 (SPG43) is caused by mutation in C19orf12*. *Human mutation*, 2013. **34**(10): p. 1357-1360.
188. Estrada-Cuzcano, A., et al., *Loss-of-function mutations in the ATP13A2/PARK9 gene cause complicated hereditary spastic paraplegia (SPG78)*. *Brain : a journal of neurology*, 2017. **140**(2): p. 287-305.
189. Ozes, B., et al., *PLA2G6 mutations associated with a continuous clinical spectrum from neuroaxonal dystrophy to hereditary spastic paraplegia*. *Clinical genetics*, 2017. **92**(5): p. 534-539.
190. Koh, K., et al., *PLA2G6-associated neurodegeneration presenting as a complicated form of hereditary spastic paraplegia*. *Journal of Human Genetics*, 2019. **64**(1): p. 55-59.
191. Paul, B.T., et al., *Mitochondria and Iron: current questions*. *Expert review of hematology*, 2017. **10**(1): p. 65-79.
192. Wang, Z.-B., et al., *Neurodegeneration with brain iron accumulation: Insights into the mitochondria dysregulation*. *Biomedicine & Pharmacotherapy*, 2019. **118**: p. 109068.
193. Gregory, A., et al., *Autosomal dominant mitochondrial membrane protein-associated neurodegeneration (MPAN)*. *Molecular genetics & genomic medicine*, 2019. **7**(7): p. e00736-e00736.
194. Hayflick, S.J., M.A. Kurian, and P. Hogarth, *Chapter 19 - Neurodegeneration with brain iron accumulation*, in *Handbook of Clinical Neurology*, D.H. Geschwind, H.L. Paulson, and C. Klein, Editors. 2018, Elsevier. p. 293-305.

195. Gregory A, H.M., Prokisch H, Kmiec T, Hogarth P, Hayflick SJ, *Mitochondrial Membrane Protein-Associated Neurodegeneration*, in *GeneReviews*, M.P. Adam, et al., Editors. 2014: Seattle (WA).
196. Venco, P., et al., *Mutations of C19orf12, coding for a transmembrane glycine zipper containing mitochondrial protein, cause mis-localization of the protein, inability to respond to oxidative stress and increased mitochondrial Ca²⁺*. *Frontiers in genetics*, 2015. **6**: p. 185-185.
197. Lonsdale, J., et al., *The Genotype-Tissue Expression (GTEx) project*. *Nature Genetics*, 2013. **45**(6): p. 580-585.
198. Monfrini, E., et al., *A de novo C19orf12 heterozygous mutation in a patient with MPAN*. *Parkinsonism & Related Disorders*, 2018. **48**: p. 109-111.
199. Gagliardi, M., et al., *C19orf12 gene mutations in patients with neurodegeneration with brain iron accumulation*. *Parkinsonism Relat Disord*, 2015. **21**(7): p. 813-6.
200. Tariq, H., et al., *Are some C19orf12 variants monoallelic for neurological disorders?* *Parkinsonism & Related Disorders*, 2019. **65**: p. 267-269.
201. Incecik, F., et al., *Mitochondrial membrane protein-associated neurodegeneration in a Turkish patient*. *Journal of pediatric neurosciences*, 2016. **11**(3): p. 288-289.
202. Karczewski, K.J., et al., *Variation across 141,456 human exomes and genomes reveals the spectrum of loss-of-function intolerance across human protein-coding genes*. *bioRxiv*, 2019: p. 531210.
203. Hogarth, P., et al., *New NBIA subtype: genetic, clinical, pathologic, and radiographic features of MPAN*. *Neurology*, 2013. **80**(3): p. 268-75.
204. Panteghini, C., et al., *C19orf12 and FA2H mutations are rare in Italian patients with neurodegeneration with brain iron accumulation*. *Semin Pediatr Neurol*, 2012. **19**(2): p. 75-81.
205. Ishiura, H., et al., *Molecular epidemiology and clinical spectrum of hereditary spastic paraplegia in the Japanese population based on comprehensive mutational analyses*. *Journal Of Human Genetics*, 2014. **59**: p. 163.
206. Scarlato, M., et al., *Exome sequencing reveals a novel homozygous mutation in ACP33 gene in the first Italian family with SPG21*. *Journal of Neurology*, 2017. **264**(9): p. 2021-2023.
207. Chertemps, T., et al., *Characterization of maspardin, responsible for human Mast syndrome, in an insect species and analysis of its evolution in metazoans*. *Naturwissenschaften*, 2012. **99**(7): p. 537-543.
208. Soderblom, C., et al., *Targeted disruption of the Mast syndrome gene SPG21 in mice impairs hind limb function and alters axon branching in cultured cortical neurons*. *Neurogenetics*, 2010. **11**(4): p. 369-378.
209. Davenport, A., et al., *Loss of Maspardin Attenuates the Growth and Maturation of Mouse Cortical Neurons*. *Neurodegener Dis*, 2016. **16**(3-4): p. 260-72.
210. Zeitlmann, L., et al., *Cloning of ACP33 as a Novel Intracellular Ligand of CD4*. *Journal of Biological Chemistry*, 2001. **276**(12): p. 9123-9132.
211. Hanna, M.C. and C. Blackstone, *Interaction of the SPG21 protein ACP33/maspardin with the aldehyde dehydrogenase ALDH16A1*. *Neurogenetics*, 2009. **10**(3): p. 217-228.
212. Vasiliou, V., et al., *ALDH16A1 is a novel non-catalytic enzyme that may be involved in the etiology of gout via protein-protein interactions with HPRT1*. *Chemico-Biological Interactions*, 2013. **202**(1): p. 22-31.

213. Liu, L.-K. and J.J. Tanner, *Crystal Structure of Aldehyde Dehydrogenase 16 Reveals Trans-Hierarchical Structural Similarity and a New Dimer*. Journal of Molecular Biology, 2019. **431**(3): p. 524-541.
214. Koh, K., et al., *Novel mutations in the ALDH18A1 gene in complicated hereditary spastic paraplegia with cerebellar ataxia and cognitive impairment*. Journal of Human Genetics, 2018. **63**(9): p. 1009-1013.
215. Coutelier, M., et al., *Alteration of ornithine metabolism leads to dominant and recessive hereditary spastic paraplegia*. Brain, 2015. **138**(8): p. 2191-2205.
216. Panza, E., et al., *ALDH18A1 gene mutations cause dominant spastic paraplegia SPG9: loss of function effect and plausibility of a dominant negative mechanism*. Brain, 2015. **139**(1): p. e3-e3.
217. Magini, P., et al., *P5CS expression study in a new family with ALDH18A1-associated hereditary spastic paraplegia SPG9*. Annals of clinical and translational neurology, 2019. **6**(8): p. 1533-1540.
218. McCray, B.A., E. Skordalakes, and J.P. Taylor, *Disease mutations in Rab7 result in unregulated nucleotide exchange and inappropriate activation*. Human Molecular Genetics, 2010. **19**(6): p. 1033-1047.
219. Zhen, Y. and H. Stenmark, *Cellular functions of Rab GTPases at a glance*. Journal of Cell Science, 2015. **128**(17): p. 3171-3176.
220. Rink, J., et al., *Rab Conversion as a Mechanism of Progression from Early to Late Endosomes*. Cell, 2005. **122**(5): p. 735-749.
221. Guerra, F. and C. Bucci, *Multiple Roles of the Small GTPase Rab7*. Cells, 2016. **5**(3): p. 34.
222. Jimenez-Orgaz, A., et al., *Control of RAB7 activity and localization through the retromer-TBC1D5 complex enables RAB7-dependent mitophagy*. The EMBO journal, 2018. **37**(2): p. 235-254.
223. BasuRay, S., et al., *Rab7 Mutants Associated with Charcot-Marie-Tooth Disease Cause Delayed Growth Factor Receptor Transport and Altered Endosomal and Nuclear Signaling*. Journal of Biological Chemistry, 2013. **288**(2): p. 1135-1149.
224. Spinosa, M.R., et al., *Functional Characterization of Rab7 Mutant Proteins Associated with Charcot-Marie-Tooth Type 2B Disease*. The Journal of Neuroscience, 2008. **28**(7): p. 1640-1648.
225. Deinhardt, K., et al., *Rab5 and Rab7 Control Endocytic Sorting along the Axonal Retrograde Transport Pathway*. Neuron, 2006. **52**(2): p. 293-305.
226. Ishino, Y., et al., *Nucleotide sequence of the iap gene, responsible for alkaline phosphatase isozyme conversion in Escherichia coli, and identification of the gene product*. Journal of Bacteriology, 1987. **169**(12): p. 5429-5433.
227. Cong, L., et al., *Multiplex Genome Engineering Using CRISPR/Cas Systems*. Science, 2013. **339**(6121): p. 819-823.
228. Jinek, M., et al., *A Programmable Dual-RNA-Guided DNA Endonuclease in Adaptive Bacterial Immunity*. Science, 2012. **337**(6096): p. 816-821.
229. Uhlén, M., et al., *Proteomics. Tissue-based map of the human proteome*. Science, 2015. **347**(6220): p. 1260419.
230. Szklarczyk, D., et al., *STRING v11: protein-protein association networks with increased coverage, supporting functional discovery in genome-wide experimental datasets*. Nucleic acids research, 2019. **47**(D1): p. D607-D613.
231. Fabregat, A., et al., *The Reactome Pathway Knowledgebase*. Nucleic acids research, 2018. **46**(D1): p. D649-D655.

232. Hershenson, J., et al., *Mutations in the autoregulatory domain of β -tubulin 4a cause hereditary dystonia*. *Annals of neurology*, 2013. **73**(4): p. 546-553.
233. Collins, C.S. and S.J. Gould, *Identification of a common PEX1 mutation in Zellweger syndrome*. *Human Mutation*, 1999. **14**(1): p. 45-53.
234. Van Laar, V.S., et al., *Potential Role of Mic60/Mitofilin in Parkinson's Disease*. *Frontiers in Neuroscience*, 2019. **12**(898).
235. Imai, Y., et al., *Twin CHCH Proteins, CHCHD2, and CHCHD10: Key Molecules of Parkinson's Disease, Amyotrophic Lateral Sclerosis, and Frontotemporal Dementia*. *International journal of molecular sciences*, 2019. **20**(4): p. 908.
236. Guo, Y., et al., *Lipid droplets at a glance*. *Journal of Cell Science*, 2009. **122**(6): p. 749-752.
237. Pennetta, G. and M.A. Welte, *Emerging Links between Lipid Droplets and Motor Neuron Diseases*. *Developmental Cell*, 2018. **45**(4): p. 427-432.
238. Wandinger-Ness, A. and M. Zerial, *Rab proteins and the compartmentalization of the endosomal system*. *Cold Spring Harbor perspectives in biology*, 2014. **6**(11): p. a022616-a022616.
239. Hu, Y.-B., et al., *The endosomal-lysosomal system: from acidification and cargo sorting to neurodegeneration*. *Translational neurodegeneration*, 2015. **4**: p. 18-18.
240. King, B.R. and C. Guda, *ngLOC: an n-gram-based Bayesian method for estimating the subcellular proteomes of eukaryotes*. *Genome biology*, 2007. **8**(5): p. R68-R68.
241. Negi, S., et al., *LocSigDB: a database of protein localization signals*. *Database : the journal of biological databases and curation*, 2015. **2015**: p. bav003.
242. Liu, Z., et al., *Oxidative Stress in Neurodegenerative Diseases: From Molecular Mechanisms to Clinical Applications*. *Oxidative medicine and cellular longevity*, 2017. **2017**: p. 2525967-2525967.
243. Willems, J., et al., *ORANGE: A CRISPR/Cas9-based genome editing toolbox for epitope tagging of endogenous proteins in neurons*. *bioRxiv*, 2019: p. 700187.
244. Tamura, N. and J. Mima, *Membrane-anchored human Rab GTPases directly mediate membrane tethering *in vitro**. *Biology Open*, 2014. **3**(11): p. 1108-1115.
245. Ma, X., et al., *A non-canonical GTPase interaction enables ORP1L-Rab7-RILP complex formation and late endosome positioning*. *J Biol Chem*, 2018. **293**(36): p. 14155-14164.
246. Durchfort, N., et al., *The Enlarged Lysosomes in beigej Cells Result From Decreased Lysosome Fission and Not Increased Lysosome Fusion*. *Traffic*, 2012. **13**(1): p. 108-119.
247. Wong, Y.C., D. Ysselstein, and D. Krainc, *Mitochondria-lysosome contacts regulate mitochondrial fission via RAB7 GTP hydrolysis*. *Nature*, 2018. **554**(7692): p. 382-386.
248. Todkar, K., H.S. Ilamathi, and M. Germain, *Mitochondria and Lysosomes: Discovering Bonds*. *Frontiers in Cell and Developmental Biology*, 2017. **5**(106).
249. Lie, P.P.Y. and R.A. Nixon, *Lysosome trafficking and signaling in health and neurodegenerative diseases*. *Neurobiology of disease*, 2019. **122**: p. 94-105.

250. Chang, J., S. Lee, and C. Blackstone, *Spastic paraplegia proteins spastizin and spatacsin mediate autophagic lysosome reformation*. The Journal of Clinical Investigation, 2014. **124**(12): p. 5249-5262.
251. Renvoisé, B., et al., *Lysosomal abnormalities in hereditary spastic paraplegia types SPG15 and SPG11*. Annals of clinical and translational neurology, 2014. **1**(6): p. 379-389.
252. Usenovic, M., et al., *Deficiency of ATP13A2 leads to lysosomal dysfunction, α -synuclein accumulation, and neurotoxicity*. The Journal of neuroscience : the official journal of the Society for Neuroscience, 2012. **32**(12): p. 4240-4246.
253. Shimazaki, H., et al., *Autosomal-recessive complicated spastic paraplegia with a novel *lysosomal trafficking regulator* gene mutation*. Journal of Neurology, Neurosurgery & Psychiatry, 2014. **85**(9): p. 1024-1028.
254. Wang, Y., et al., *Endosomal signaling of epidermal growth factor receptor stimulates signal transduction pathways leading to cell survival*. Molecular and cellular biology, 2002. **22**(20): p. 7279-7290.
255. Rush, J.S., et al., *Endosomal accumulation of the activated epidermal growth factor receptor (EGFR) induces apoptosis*. The Journal of biological chemistry, 2012. **287**(1): p. 712-722.
256. Bakowska, J.C., et al., *Troyer syndrome protein spartin is mono-ubiquitinated and functions in EGF receptor trafficking*. Molecular biology of the cell, 2007. **18**(5): p. 1683-1692.
257. Quinney, K.B., et al., *Growth factor stimulation promotes multivesicular endosome biogenesis by prolonging recruitment of the late-acting ESCRT machinery*. Proceedings of the National Academy of Sciences, 2019. **116**(14): p. 6858-6867.
258. de Oliveira Andrade, L., *Understanding the role of cholesterol in cellular biomechanics and regulation of vesicular trafficking: The power of imaging*. Biomedical Spectroscopy and Imaging, 2016. **5**(S1): p. S101-S117.
259. Goluszko, P. and B. Nowicki, *Membrane cholesterol: a crucial molecule affecting interactions of microbial pathogens with mammalian cells*. Infection and immunity, 2005. **73**(12): p. 7791-7796.
260. Saher, G. and S.K. Stumpf, *Cholesterol in myelin biogenesis and hypomyelinating disorders*. Biochimica et Biophysica Acta (BBA) - Molecular and Cell Biology of Lipids, 2015. **1851**(8): p. 1083-1094.
261. Dietschy, J.M. and S.D. Turley, *Thematic review series: Brain Lipids. Cholesterol metabolism in the central nervous system during early development and in the mature animal*. Journal of Lipid Research, 2004. **45**(8): p. 1375-1397.
262. Russell, D.W., *Fifty years of advances in bile acid synthesis and metabolism*. J Lipid Res, 2009. **50 Suppl**: p. S120-5.
263. Kakiyama, G., et al., *Mitochondrial oxysterol biosynthetic pathway gives evidence for CYP7B1 as controller of regulatory oxysterols*. The Journal of Steroid Biochemistry and Molecular Biology, 2019.
264. Pandak, W.M. and G. Kakiyama, *The acidic pathway of bile acid synthesis: Not just an alternative pathway*. Liver Research, 2019. **3**(2): p. 88-98.
265. Russell, D.W., *The Enzymes, Regulation, and Genetics of Bile Acid Synthesis*. Annual Review of Biochemistry, 2003. **72**(1): p. 137-174.

266. Hedlund, E., J.A. Gustafsson, and M. Warner, *Cytochrome P450 in the Brain ; A Review*. Current Drug Metabolism, 2001. **2**(3): p. 245-263.
267. Mutemberezi, V., O. Guillemot-Legris, and G.G. Muccioli, *Oxysterols: From cholesterol metabolites to key mediators*. Progress in Lipid Research, 2016. **64**: p. 152-169.
268. Chiang, J.Y.L., *Bile Acid Metabolism and Signaling*. Comprehensive Physiology, 2013. **3**(3): p. 1191-1212.
269. Norlin, M., et al., *Oxysterol 7 α -Hydroxylase Activity by Cholesterol 7 α -Hydroxylase (CYP7A)*. Journal of Biological Chemistry, 2000. **275**(44): p. 34046-34053.
270. Schwarz, M., et al., *Alternate pathways of bile acid synthesis in the cholesterol 7 α -hydroxylase knockout mouse are not upregulated by either cholesterol or cholestyramine feeding*. Journal of Lipid Research, 2001. **42**(10): p. 1594-1603.
271. Scharwey, M., T. Tatsuta, and T. Langer, *Mitochondrial lipid transport at a glance*. J Cell Sci, 2013. **126**(Pt 23): p. 5317-23.
272. Pandak, W.M., et al., *Regulation of oxysterol 7 α -hydroxylase (CYP7B1) in primary cultures of rat hepatocytes*. Hepatology, 2003. **35**(6): p. 1400-1408.
273. Li, A. and J.C. Bigelow, *The 7-hydroxylation of dehydroepiandrosterone in rat brain*. Steroids, 2010. **75**(6): p. 404-410.
274. Lütjohann, D., et al., *Cholesterol homeostasis in human brain: evidence for an age-dependent flux of 24S-hydroxycholesterol from the brain into the circulation*. Proceedings of the National Academy of Sciences of the United States of America, 1996. **93**(18): p. 9799-9804.
275. Li-Hawkins, J., et al., *Expression Cloning of an Oxysterol 7 α -Hydroxylase Selective for 24-Hydroxycholesterol*. Journal of Biological Chemistry, 2000. **275**(22): p. 16543-16549.
276. Olkkonen, V.M., O. Beaslas, and E. Nissila, *Oxysterols and their cellular effectors*. Biomolecules, 2012. **2**(1): p. 76-103.
277. Radhakrishnan, A., et al., *Sterol-regulated transport of SREBPs from endoplasmic reticulum to Golgi: Oxysterols block transport by binding to Insig*. Proceedings of the National Academy of Sciences, 2007. **104**(16): p. 6511-6518.
278. Meljon, A., et al., *Mining for Oxysterols in Cyp7b1(-/-) Mouse Brain and Plasma: Relevance to Spastic Paraplegia Type 5*. Biomolecules, 2019. **9**(4): p. 149.
279. Janowski, B.A., et al., *An oxysterol signalling pathway mediated by the nuclear receptor LXR α* . Nature, 1996. **383**(6602): p. 728-731.
280. Raychaudhuri, S. and W.A. Prinz, *The diverse functions of oxysterol-binding proteins*. Annu Rev Cell Dev Biol, 2010. **26**: p. 157-77.
281. Ali, Z., et al., *On the regulatory role of side-chain hydroxylated oxysterols in the brain. Lessons from CYP27A1 transgenic and Cyp27a1(-/-) mice*. Journal of lipid research, 2013. **54**(4): p. 1033-1043.
282. Testa, G., et al., *Changes in brain oxysterols at different stages of Alzheimer's disease: Their involvement in neuroinflammation*. Redox biology, 2016. **10**: p. 24-33.
283. Lordan, S., J.J. Mackrill, and N.M. O'Brien, *Oxysterols and mechanisms of apoptotic signaling: implications in the pathology of degenerative diseases*. J Nutr Biochem, 2009. **20**(5): p. 321-36.
284. Lee, T.-S. and L.-Y. Chau, *Fas/Fas ligand-mediated death pathway is involved in oxLDL-induced apoptosis in vascular smooth muscle cells*.

- American Journal of Physiology-Cell Physiology, 2001. **280**(3): p. C709-C718.
285. Wang, H., et al., *The cytotoxicity of 27-hydroxycholesterol in co-cultured SH-SY5Y cells and C6 cells*. Neuroscience Letters, 2016. **632**: p. 209-217.
286. Tsaousidou, M.K., et al., *Sequence alterations within CYP7B1 implicate defective cholesterol homeostasis in motor-neuron degeneration*. Am J Hum Genet, 2008. **82**(2): p. 510-5.
287. Abdel-Khalik, J., et al., *Identification of 7 α ,24-dihydroxy-3-oxocholest-4-en-26-oic and 7 α ,25-dihydroxy-3-oxocholest-4-en-26-oic acids in human cerebrospinal fluid and plasma*. Biochimie, 2018. **153**: p. 86-98.
288. Marelli, C., et al., *Plasma oxysterols: biomarkers for diagnosis and treatment in spastic paraplegia type 5*. Brain, 2018. **141**(1): p. 72-84.
289. Schüle, R., et al., *Marked accumulation of 27-hydroxycholesterol in SPG5 patients with hereditary spastic paresis*. Journal of lipid research, 2010. **51**(4): p. 819-823.
290. Saxena, V. and P. Pradhan, *Cerebrotendinous xanthomatosis; a genetic condition: Clinical profile of three patients from a rural Indian family and review of literature*. Journal of Clinical Orthopaedics and Trauma, 2016. **7**(2): p. 122-126.
291. Nie, S., et al., *Cerebrotendinous xanthomatosis: a comprehensive review of pathogenesis, clinical manifestations, diagnosis, and management*. Orphanet Journal of Rare Diseases, 2014. **9**: p. 179.
292. Ismail, M.-A.-M., et al., *27-Hydroxycholesterol impairs neuronal glucose uptake through an IRAP/GLUT4 system dysregulation*. The Journal of Experimental Medicine, 2017. **214**(3): p. 699-717.
293. Mignarri, A., et al., *Clinical relevance and neurophysiological correlates of spasticity in cerebrotendinous xanthomatosis*. J Neurol, 2011. **258**(5): p. 783-90.
294. Mast, N., et al., *Cytochrome P450 27A1 Deficiency and Regional Differences in Brain Sterol Metabolism Cause Preferential Cholesterol Accumulation in the Cerebellum*. Journal of Biological Chemistry, 2017. **292**(12): p. 4913-4924.
295. Martin, L.A., B.E. Kennedy, and B. Karten, *Mitochondrial cholesterol: mechanisms of import and effects on mitochondrial function*. Journal of Bioenergetics and Biomembranes, 2016. **48**(2): p. 137-151.
296. Vance, J.E., *MAM (mitochondria-associated membranes) in mammalian cells: Lipids and beyond*. Biochimica et Biophysica Acta (BBA) - Molecular and Cell Biology of Lipids, 2014. **1841**(4): p. 595-609.
297. Rochin, L., et al., *ORP5 Regulates Transport of Lipids and Calcium to Mitochondria at Endoplasmic Reticulum-Mitochondria Membrane Contact Sites*. bioRxiv, 2019: p. 695577.
298. Filadi, R., D. Pendin, and P. Pizzo, *Mitofusin 2: from functions to disease*. Cell death & disease, 2018. **9**(3): p. 330-330.
299. Gomez-Suaga, P., et al., *The ER-Mitochondria Tethering Complex VAPB-PTPIP51 Regulates Autophagy*. Current Biology, 2017. **27**(3): p. 371-385.
300. Bernard-Marissal, N., R. Chrast, and B.L. Schneider, *Endoplasmic reticulum and mitochondria in diseases of motor and sensory neurons: a broken relationship?* Cell Death & Disease, 2018. **9**(3): p. 333.

301. Ando, M., et al., *Clinical and genetic diversities of Charcot-Marie-Tooth disease with MFN2 mutations in a large case study*. Journal of the peripheral nervous system : JPNS, 2017. **22**(3): p. 191-199.
302. Chung, K.W., et al., *Early onset severe and late-onset mild Charcot-Marie-Tooth disease with mitofusin 2 (MFN2) mutations*. Brain, 2006. **129**(8): p. 2103-2118.
303. Feely, S.M.E., et al., *MFN2 mutations cause severe phenotypes in most patients with CMT2A*. Neurology, 2011. **76**(20): p. 1690-1696.
304. Bernard-Marissal, N., et al., *Altered interplay between endoplasmic reticulum and mitochondria in Charcot-Marie-Tooth type 2A neuropathy*. Proceedings of the National Academy of Sciences, 2019: p. 201810932.
305. Vettori, A., et al., *Loss-of-function mutations in the SIGMAR1 gene cause distal hereditary motor neuropathy by impairing ER-mitochondria tethering and Ca²⁺ signalling*. Human Molecular Genetics, 2016. **25**(17): p. 3741-3753.
306. Al-Saif, A., F. Al-Mohanna, and S. Bohlega, *A mutation in sigma-1 receptor causes juvenile amyotrophic lateral sclerosis*. Annals of Neurology, 2011. **70**(6): p. 913-919.
307. Ullah, M.I., et al., *In silico analysis of SIGMAR1 variant (rs4879809) segregating in a consanguineous Pakistani family showing amyotrophic lateral sclerosis without frontotemporal lobar dementia*. neurogenetics, 2015. **16**(4): p. 299-306.
308. Nishimura, A.L., et al., *A mutation in the vesicle-trafficking protein VAPB causes late-onset spinal muscular atrophy and amyotrophic lateral sclerosis*. American journal of human genetics, 2004. **75**(5): p. 822-831.
309. Dong, R., et al., *Endosome-ER Contacts Control Actin Nucleation and Retromer Function through VAP-Dependent Regulation of PI4P*. Cell, 2016. **166**(2): p. 408-423.
310. Kappler, L., et al., *Purity matters: A workflow for the valid high-resolution lipid profiling of mitochondria from cell culture samples*. Sci Rep, 2016. **6**: p. 21107.
311. Shan, H., et al., *Calreticulin is localized at mitochondria of rat cardiomyocytes and affected by furazolidone*. Molecular and Cellular Biochemistry, 2014. **397**(1): p. 125-130.
312. Shigaeva, M.I., et al., *A role for calreticulin in functioning of mitochondrial ATP-dependent potassium channel*. Biophysics, 2014. **59**(5): p. 721-726.
313. Ma, J.H., et al., *Comparative Proteomic Analysis of the Mitochondria-associated ER Membrane (MAM) in a Long-term Type 2 Diabetic Rodent Model*. Scientific Reports, 2017. **7**(1): p. 2062.
314. Schöls, L., et al., *Hereditary spastic paraplegia type 5: natural history, biomarkers and a randomized controlled trial*. Brain, 2017. **140**(12): p. 3112-3127.
315. Bligh, E.G. and W.J. Dyer, *A RAPID METHOD OF TOTAL LIPID EXTRACTION AND PURIFICATION*. Canadian Journal of Biochemistry and Physiology, 1959. **37**(8): p. 911-917.